

University of Alberta

pH Changes Localized to the Surface of Membrane Transport Proteins

by

Danielle Elaine Johnson

A thesis submitted to the Faculty of Graduate Studies and Research
in partial fulfillment of the requirements for the degree of

Doctor of Philosophy

Department of Physiology

©Danielle Elaine Johnson

Spring 2011
Edmonton, Alberta

Permission is hereby granted to the University of Alberta Libraries to reproduce single copies of this thesis and to lend or sell such copies for private, scholarly or scientific research purposes only. Where the thesis is converted to, or otherwise made available in digital form, the University of Alberta will advise potential users of the thesis of these terms.

The author reserves all other publication and other rights in association with the copyright in the thesis and, except as herein before provided, neither the thesis nor any substantial portion thereof may be printed or otherwise reproduced in any material form whatsoever without the author's prior written permission.

Examining Committee

Dr. Joseph Casey, Physiology and Biochemistry

Dr. James Young, Physiology

Dr. Larry Fliegel, Biochemistry

Dr. Todd Alexander, Physiology and Pediatrics

Dr. Gergely Lukacs, McGill University, Department of Physiology

Abstract

Intracellular pH was monitored at the cytosolic surface of plasma membrane solute transporters (Na^+/H^+ /nucleoside co-transporters, or $\text{Cl}^-/\text{HCO}_3^-$ exchangers), using pH-sensitive fluorescent proteins (FPs), dual emission green FP (deGFP4) and a monomeric red FP Nectarine (mNect), whose development and characterization are also reported here.

Human concentrative nucleoside transporter, hCNT3, mediates Na^+/H^+ /nucleoside co-transport. We describe a new approach to monitor H^+ /uridine co-transport in HEK293 cells. pH changes at the intracellular surface of hCNT3 were monitored by fusing mNect to the cytoplasmic N-terminus of hCNT3 (mNect.hCNT3) or an inactive hCNT3 mutant (mNect.hCNT3-F563C). Cells were incubated at the permissive pH for H^+ -coupled nucleoside transport, pH 5.5, under both Na^+ -free and Na^+ -containing conditions. In mNect.hCNT3-expressing cells (but not under negative control conditions) the rate of acidification increased in media containing 0.5 mM uridine, providing the first direct evidence for H^+ -coupled uridine transport. At pH 5.5, there was no significant difference in uridine transport rates (coupled H^+ flux) in the presence or absence of Na^+ . This suggests that in acidic Na^+ -containing conditions, 1 Na^+ and 1 H^+ are transported/uridine molecule, while in acidic Na^+ -free conditions, 1 H^+ alone is transported/uridine. In acid environments, including renal proximal tubule and intestine, H^+ /nucleoside co-transport may drive nucleoside accumulation by hCNT3.

Microdomains, discrete regions of altered cytosolic solute concentration, are enhanced by rapid solute transport and slow diffusion rates. pH-regulatory membrane transporters, like the $\text{Cl}^-/\text{HCO}_3^-$ exchanger AE1, could nucleate H^+ microdomains, since AE1 has a rapid transport rate and cytosolic H^+ diffusion is slow. As AE1 drives $\text{Cl}^-/\text{HCO}_3^-$ exchange, differences in pH, near and remote from AE1, were monitored simultaneously by deGFP4 fused to AE1 (deGFP4.AE1) and mNect.hCNT3-F563C. deGFP4.AE1-mNect.hCNT3-F563C distance was varied by co-expression of different amounts of the two proteins in HEK293 cells. As the deGFP4.AE1-mNect.hCNT3-F563C distance increased, mNect.hCNT3-F563C detected the cytosolic pH change with a time delay and reduced rate of pH change, compared to deGFP4.AE1. Carbonic anhydrase activity was essential for H^+ microdomain formation. H^+ diffusion along the plasma membrane was 60-fold slower than to the cytosolic ER-surface. During physiological HCO_3^- transport, a H^+ microdomain 0.3 μm in diameter develops around AE1, which will affect nearby pH-sensitive processes.

Acknowledgements

Firstly, I wish to thank my two high school biology teachers for igniting my love of science and biology. Mrs. Dunn and Mr. Wasylenico were truly inspirational, and motivated me to always ask questions and seek answers. They were amazing mentors and friends and taught me to strive to be the best I could be.

Dr. Bill Cole was instrumental in inspiring me to pursue a career in research. I appreciate his support both before and after choosing this career path.

I thank Dr. Joe Casey for giving me the opportunity to work in his lab. I have learned how to be a scientist from him, and have learned a lot about myself. It has been a journey that I have been very happy to have experienced. I truly value the lessons I have learned and the growth I have experienced, both as a scientist, and as a person.

I have developed so many close friendships during my time in the lab. Anita Quon has been there for my entire journey. I will be forever indebted for her help around the lab, and will always treasure our friendship. Haley Shandro and Heather McMurtrie were two of my first friends in Edmonton, and their friendship will always mean a lot to me. Patricio Morgan, as well as an excellent scientist, is a wonderful friend who could always make me laugh. Bernardo and Veronica Alvarez were like a second family for me here in Edmonton. Kate Witkowska has been a great friend from the very beginning, and I have valued knowing her and sharing this journey of friendship and science with her. Pamela Bonar is a great friend, and my experience would not have been the same without

her. She has always been here for me - whether its for a good party, a shoulder to cry on, or a scientific discussion. Gonzalo Vilas is also a great friend and scientist, and has helped me in so many ways. Karli Moncrief, Adrienne Huxtable, Shereen Hamza, and Ras Mulinta have also been invaluable to me, with their friendship and advice.

Niels Sorensen has always supported me, believed in me, and encouraged me to be the best I could be. His love and support have meant everything to me.

Words cannot express my love and gratitude to my family. I could not have done this without the support of my parents, Roxanne and Cliff, and my sister, Amber. They have always encouraged me, loved me, and believed in me.

Table of Contents

| | |
|---|-----------|
| Chapter 1: General Introduction | 1 |
| 1.1 Thesis Overview | 2 |
| 1.2 Bicarbonate and Bicarbonate Transport..... | 3 |
| 1.2.1 Biochemistry of Bicarbonate | 3 |
| 1.2.2 Carbonic anhydrases | 4 |
| 1.2.3 Bicarbonate Transport Proteins | 5 |
| 1.2.4 The Bicarbonate Transport Metabolon | 11 |
| 1.2.4.1 Overview..... | 11 |
| 1.2.4.2 AE/CA Interactions - Initial Characterization | 12 |
| 1.2.4.3 AE/CA Interactions - Physiological Significance | 16 |
| 1.2.4.4 NBC/CA Interactions..... | 22 |
| 1.2.4.5 SLC26/CA Interactions | 25 |
| 1.2.4.6 Bicarbonate Transport Metabolon Controversies | 26 |
| 1.2.4.7 Bicarbonate Transport Metabolon Summary..... | 29 |
| 1.2.5 Other Acid/Base Transporter Carbonic Anhydrase Metabolons | 30 |
| 1.2.5.1 Na ⁺ /H ⁺ exchanger and CAII | 30 |
| 1.2.5.2 Monocarboxylate Transporter 1 (MCT1) and CAII | 33 |
| 1.2.5.3 N-type sodium-dependent neutral amino acid transporter isoform 3 (SNAT3) and CAII | 36 |
| 1.2.6 Acid/Base Transporters in Cell Volume Regulation | 37 |
| 1.3 Physiological Roles of pH..... | 38 |
| 1.3.1 General pH Discussion | 38 |
| 1.3.2 Intracellular Buffering, H ⁺ Diffusion Rates and Intracellular Buffer Shuttles | 40 |
| 1.3.3 H ⁺ as an Intracellular Signal | 43 |
| 1.3.4 Solute Microdomains..... | 45 |
| 1.3.5 H ⁺ gradients and H ⁺ microdomains | 47 |
| 1.3.6 Dual Roles of Carbonic Anhydrase in H ⁺ microdomain formation..... | 49 |
| 1.3.7 pH-Sensitive Proteins | 50 |
| 1.3.8 Role of pH in Cell Migration..... | 51 |
| 1.4 Nucleoside Transport | 52 |
| 1.5 Fluorescent proteins | 57 |
| 1.6 Thesis Objectives | 62 |

| | |
|---|------------|
| Chapter 2: Materials and Methods | 80 |
| 2.1 Materials | 81 |
| 2.2 Methods | 84 |
| 2.2.1 mNectarine mutagenesis, library construction, and screening | 84 |
| 2.2.2 Construction of fusion proteins | 85 |
| 2.2.3 Protein purification and characterization | 89 |
| 2.2.4 Photostability measurements | 90 |
| 2.2.5 Tissue culture | 90 |
| 2.2.6 Peptide: N-Glycosidase F (PNGaseF) Treatment | 91 |
| 2.2.7 Immunodetection | 92 |
| 2.2.8 Measurement of fluorescence in intact HEK293 cells | 93 |
| 2.2.9 Spectral characterization of deGFP4 and mNectarine expressed in HEK293 cells | 94 |
| 2.2.10 Fluorescence quenching | 95 |
| 2.2.11 Calibration of fluorescence values for pH | 96 |
| 2.2.12 Photobleaching correction | 97 |
| 2.2.13 H ⁺ /uridine co-transport activity assay | 97 |
| 2.2.14 Kinetics of H ⁺ /uridine co-transport | 98 |
| 2.2.15 Cl ⁻ /HCO ₃ ⁻ exchange activity assay | 99 |
| 2.2.16 Measurement of intrinsic buffer capacity and flux of proton equivalents | 100 |
| 2.2.17 Measuring the time of initial pH rise | 101 |
| 2.2.18 Quantification of ER-associated fluorescence in PM ROI | 102 |
| 2.2.19 Perfluorooctanoic acid polyacrylamide gel electrophoresis (PFO- PAGE) | 102 |
| 2.2.20 Cell surface processing assay | 103 |
| 2.2.21 Distribution of deGFP4.AE1, mNect.hCNT3 and mNect.hCNT3- F563C at the plasma membrane | 104 |
| 2.2.22 Calculation of average distance between deGF4P.AE1 and mNect.hCNT3-F563C molecules | 105 |
| 2.2.23 Statistical analysis | 106 |
| Bibliography | 107 |
| | |
| Chapter 3: Red Fluorescent Protein pH Biosensor to Detect Concentrative Nucleoside Transport | 110 |
| 3.1 Introduction | 111 |

| | |
|--|------------|
| 3.2 Results | 114 |
| 3.2.1 Engineering mNectarine | 114 |
| 3.2.2 pH sensitivity of mNectarine | 117 |
| 3.2.3 mNectarine.hCNT3 fusion proteins | 120 |
| 3.2.4 Spectral characterization of mNectarine expressed in HEK293 cells | 124 |
| 3.2.5 Correction for mNectarine photobleaching | 126 |
| 3.2.6 Measurement of cytosolic pH by mNect, mNect.hCNT3 and BCECF | 128 |
| 3.2.7 H ⁺ /uridine co-transport | 130 |
| 3.3 Discussion | 140 |
| Bibliography | 146 |
| | |
| Chapter 4: Cytosolic H⁺ Microdomain Developed During Ion Transport.. | 151 |
| 4.1 Introduction | 152 |
| 4.2 Results | 154 |
| 4.2.1 Construction and characterization of pH-reporter fusion proteins | 154 |
| 4.2.2 Halide sensitivity of FP fluorescence | 163 |
| 4.2.3 Correction for FP photobleaching | 166 |
| 4.2.4 Discrimination of ER and plasma membrane fluorescence..... | 171 |
| 4.2.5 Measurement of the rate of H ⁺ diffusion from plasma membrane to | 173 |
| cytosolic surface of ER..... | |
| 4.2.6 Measurement of the rate of H ⁺ diffusion along the cytosolic surface | 175 |
| of the plasma membrane | |
| 4.2.7 Estimation of the size of the H ⁺ microdomain..... | 183 |
| 4.2.8 Role of carbonic anhydrase in H ⁺ microdomain formation..... | 185 |
| 4.3 Discussion | 190 |
| 4.3.1 Size of the H ⁺ microdomain..... | 190 |
| 4.3.2 Role of carbonic anhydrase in H ⁺ microdomain formation..... | 193 |
| 4.3.3 Rates of H ⁺ diffusion | 194 |
| 4.3.4 Potential physiological significance of H ⁺ microdomains and observed | 197 |
| low rates of H ⁺ diffusion..... | |
| Bibliography | 201 |
| | |
| Chapter 5: Summary and Future Directions | 208 |
| 5.1 Summary | 209 |

| | |
|---|------------|
| 5.1.1 Red Fluorescent Protein Biosensor to Detect Concentrative Nucleoside Transport..... | 209 |
| 5.1.2 Cytosolic H ⁺ Microdomain Developed During Ion Transport | 211 |
| 5.2 Future Directions | 214 |
| Bibliography | 220 |

List of Tables

| | | |
|------------|--|------------|
| Table 1.1. | Bicarbonate transport proteins and carbonic anhydrase interactions..... | 7 |
| Table 2.1 | Reagents..... | 81 |
| Table 2.2 | DNA Modifying Enzymes..... | 82 |
| Table 2.3 | Antibodies..... | 83 |
| Table 3.1. | Properties of mNectarine and related variants..... | 116 |
| Table 4.1. | Quantification of ER-associated fluorescence in PM ROI..... | 174 |

List of Figures

| | | |
|--------------|--|-----|
| Figure 1.1. | Phylogenetic tree of human bicarbonate transporter genes.... | 6 |
| Figure 1.2. | AE1 topology model..... | 8 |
| Figure 1.3. | The bicarbonate transport metabolon..... | 13 |
| Figure 1.4. | Noncatalytic role of membrane-associated CAII..... | 35 |
| Figure 1.5. | Effect of pH on buffer capacity..... | 41 |
| Figure 1.6. | hCNT3 topology model..... | 56 |
| Figure 1.7. | Crystal structure of wild-type <i>Aequorea Victoria</i> green fluorescent protein..... | 58 |
| Figure 3.1. | Sequence alignment of mNectarine and related variants..... | 118 |
| Figure 3.2. | pH-dependence of mNectarine fluorescence..... | 119 |
| Figure 3.3. | Representative example of the results from the global four-component linear regression analysis of the absorbance spectra recorded at various pH..... | 121 |
| Figure 3.4. | Expression of mNect.hCNT3 in HEK293 cells and analysis of glycosylation status..... | 123 |
| Figure 3.5. | Spectral characterization of mNectarine expressed in HEK293 cells..... | 125 |
| Figure 3.6. | Correction for mNectarine photobleaching..... | 127 |
| Figure 3.7. | Measurement of intracellular pH, using cytosolic mNectarine, mNect.hCNT3 and BCECF..... | 129 |
| Figure 3.8. | hCNT3 mediated H⁺/uridine co-transport measured by mNectarine-hCNT3..... | 131 |
| Figure 3.9. | Plasma membrane localization of mNect.hCNT3 and mNect.hCNT3-F563C..... | 134 |
| Figure 3.10. | Kinetics of H⁺/uridine co-transport in HEK293 cells..... | 136 |
| Figure 3.11. | Effect of Na⁺ on H⁺/uridine co-transport..... | 137 |

| | | |
|--------------|---|------------|
| Figure 3.12. | Intracellular pH immediately prior to addition of uridine in mNect.hCNT3 and mNect.hCNT3-F563C expressing cells..... | 139 |
| Figure 4.1. | deGFP4.AE1 and mNect.hCNT3 topology model..... | 156 |
| Figure 4.2. | Spectral characterization of deGFP4 expressed in HEK293 cells..... | 157 |
| Figure 4.3. | Cl⁻/HCO₃⁻ exchange activity of AE1 and deGFP4.AE1..... | 159 |
| Figure 4.4. | Intracellular buffer capacity..... | 161 |
| Figure 4.5. | Assessment of crosstalk during simultaneous measurement of deGFP4 and mNectarine fluorescence..... | 162 |
| Figure 4.6. | Assessment of fluorescence resonance energy transfer (FRET) between deGFP4 and mNectarine..... | 164 |
| Figure 4.7. | Fluorescence quenching of deGFP4 and mNectarine by H⁺ and Cl⁻..... | 165 |
| Figure 4.8. | Photobleaching correction for deGFP4 and mNectarine..... | 167 |
| Figure 4.9. | pH and response time measured using cytosolic deGFP4 and mNectarine during AE1-mediated Cl⁻/HCO₃⁻ exchange..... | 169 |
| Figure 4.10. | Cytosolic deGFP4 and mNectarine temporal responsiveness to pH changes induced by NH₄Cl..... | 172 |
| Figure 4.11. | Lag time associated with Cl⁻/HCO₃⁻ exchange: measurement at plasma membrane and endoplasmic reticulum..... | 176 |
| Figure 4.12. | Quantification of deGFP4.AE1, mNect.AE1 and cell number standards..... | 178 |
| Figure 4.13. | Cell surface processing of deGFP4.AE1 and mNect.hCNT3-F563C..... | 179 |
| Figure 4.14. | Oligomeric state of mNect.hCNT3-F563C and AE1 assessed by PFO-PAGE..... | 180 |
| Figure 4.15. | Distribution of deGFP4.AE1 and mNect.hCNT3-F563C at the plasma membrane..... | 182 |

| | | |
|--------------|---|------------|
| Figure 4.16. | Evidence for a H⁺ microdomain around AE1..... | 184 |
| Figure 4.17. | Equilibrium plateau pH after Cl/HCO₃⁻ exchange reported by deGFP4.AE1 and mNect.hCNT3..... | 186 |
| Figure 4.18. | Role of CAII in H⁺ microdomain formation around AE1..... | 188 |
| Figure 4.19. | Effect of temperature on the H⁺ microdomain around AE1..... | 189 |
| Figure 4.20. | Model for H⁺ diffusion and H⁺ microdomain around AE1... | 191 |

List of Symbols, Nomenclature, Abbreviations

| | |
|----------------------------|--|
| β_{CO_2} | CO ₂ -dependent buffer capacity |
| $\beta_{\text{intrinsic}}$ | intrinsic buffer capacity |
| β_{total} | total buffer capacity |
| λ_{em} | emission wavelength |
| λ_{ex} | excitation wavelength |
| μm | micrometer |
| μM | micromolar |
| AE | Cl ⁻ /HCO ₃ ⁻ anion exchanger |
| AE1,2,3 | Cl ⁻ /HCO ₃ ⁻ anion exchanger isoform 1,2,3 |
| AE1-Ct | a purified GST fusion protein containing the last 40 amino acids (residues 872-911) of human AE1 |
| AE1-LDAAA | a human AE1 mutant unable to bind CAII |
| AE1-P652C | a functionally inactive mutant of human AE1 |
| AE1-WT | wild type AE1 (also referred to as AE1) |
| AQP | aquaporin |
| ATP | adenosine triphosphate |
| A.U. | arbitrary units |
| avGFP | <i>Aequorea victoria</i> green fluorescent protein |
| BCA | bicinchoninic acid |
| BCECF-AM | 2',7'-Bis(2-carboxyethyl)-5(6)-carboxyfluorescein acetoxymethyl ester |
| C | concentrative |

| | |
|--------------|--|
| CA | carbonic anhydrase |
| CAII, IV, IX | carbonic anhydrase isoform II, IV, IX |
| CAII-HEX | an N-terminal CAII mutant unable to bind AE1 |
| CAII-V143Y | a catalytically inactive CAII mutant |
| CAII-WT | wild type carbonic anhydrase isoform II (also referred to as CAII) |
| CAB | carbonic anhydrase binding site |
| CaM | calmodulin |
| cAMP | cyclic adenosine monophosphate |
| cDNA | complementary deoxyribonucleic acid |
| CFP | cyan fluorescent protein |
| ChCl | choline chloride |
| CHE | Cl ⁻ /OH ⁻ exchanger |
| CIP | calf intestinal alkaline phosphatase |
| CNT | concentrative nucleoside transporter |
| CNX | calnexin |
| CNX.mNect | mNectarine fused to the C-terminus of CNX |
| cpGFP | circularly permuted GFP |
| CS | calf serum |
| Ct | C-terminal |
| deGFP4 | dual emission green fluorescent protein 4 |
| deGFP4.AE1 | deGFP4 fused to the N-terminus of AE1 |

| | |
|-----------------|--|
| deGFP4-Y66L.AE1 | a non-fluorescent deGFP4 mutant fused to the N-terminus of AE1 |
| DIDS | 4,4'-Diisothiocyano-2,2'-stilbenedisulfonic acid |
| DMEM | Dulbecco's modified Eagle media |
| DNA | deoxyribonucleic acid |
| DNSA | dansylsulfonamide |
| dRTA | distal renal tubular acidosis |
| DsRed | tetrameric <i>Discosoma</i> RFP |
| DTT | dithiothreitol |
| E | equilibrative |
| eAE1 | erythrocyte AE1 |
| EDTA | ethylenediaminetetraacetic acid |
| EGFP | enhanced GFP |
| EIPA | 5-(N-ethyl-N-isopropyl)-amiloride |
| ELISA | enzyme-linked immunosorbent assay |
| em. | emission |
| ex. | excitation |
| ENT | equilibrative nucleoside transporter |
| ER | endoplasmic reticulum |
| F ₀ | initial fluorescence intensity |
| F | fluorescence intensity at a given time |
| FBS | fetal bovine serum |
| FP | fluorescent protein |

| | |
|------------------|--|
| FRET | fluorescence resonance energy transfer |
| GAPDH | glyceraldehyde 3-phosphate dehydrogenase |
| GFP | green fluorescent protein |
| GPA | glycophorin A |
| GPB | glycophorin B |
| GPI | glycosylphosphatidyl inositol |
| GST | glutathione S-transferase |
| h | human |
| Hb | hemoglobin |
| hCNT3 | human concentrative nucleoside transporter isoform 3 |
| HEK293 cells | human embryonic kidney 293 cells |
| HEPES | 4-(2-hydroxyethyl)-1-piperazineethanesulfonic acid |
| HRP | horseradish peroxidase |
| IC ₅₀ | half-maximal inhibitor concentration |
| ILK | integrin-linked kinase |
| I _{max} | highest fluorescence intensity at a given pH |
| I _{NBC} | NBC current |
| I _{pH} | fluorescence intensity at any pH |
| kAE1 | kidney AE1 |
| KCC | K ⁺ -Cl ⁻ co-transporter |
| K _m | substrate concentration that yields the half-maximal reaction rate |

| | |
|-------------------|--|
| K_{SV} | Stern-Volmer constant; relates the quenching of fluorescence to quencher concentration |
| LB-AMP | Luria-Bertani medium supplemented with 0.1 mg/ml ampicillin and 0.02% w/v L-arabinose |
| m | monomeric |
| M | molar |
| MCT1 | monocarboxylate transporter isoform 1 |
| MES | 2-(N-morpholino)ethanesulfonic acid |
| min | minute |
| mM | millimolar |
| mNect | mNectarine |
| mNect.AE1 | mNect fused to the N-terminus of AE1 |
| mNect.hCNT3 | mNect fused to the N-terminus of hCNT3 |
| mNect.hCNT3-F563C | mNect fused to the N-terminus of an inactive hCNT3 mutant |
| NaCl | sodium chloride |
| NBC | $\text{Na}^+/\text{HCO}_3^-$ co-transporter |
| ND | not determined |
| NHE1 | Na^+/H^+ exchanger isoform 1 |
| NKCC | $\text{Na}^+ - \text{K}^+ - 2\text{Cl}^-$ co-transporter |
| nM | nanomolar |
| N.S. | not significant |
| NT | nucleoside transport protein |

| | |
|-----------------|---|
| p | plasmid |
| PBS | phosphate-buffered saline |
| PCR | polymerase chain reaction |
| PEPT1/2 | proton-dependent oligopeptide transporter isoforms 1/2 |
| PFK | phosphofructokinase |
| PFO | perfluorooctanoic acid |
| PFO-PAGE | perfluorooctanoic acid polyacrylamide gel electrophoresis |
| pH _i | intracellular pH |
| pH _o | extracellular pH |
| PKA | cAMP-dependent protein kinase A |
| pK _a | logarithmic measure of acid dissociation constant |
| PM | plasma membrane |
| PNGaseF | Peptide: N-Glycosidase |
| PSG | penicillin-streptomycin-glutamine |
| Q | quencher |
| r | distance between centres of two chromophores during FRET |
| R ₀ | distance at which FRET is 50% efficient |
| RBC | red blood cell |
| RFP | red fluorescent protein |
| ROI | region of interest |
| RVD | regulatory volume decrease |
| RVI | regulatory volume increase |

| | |
|------------------|---|
| s | second |
| S | substrate |
| sAC | soluble adenylyl cyclase |
| SAO | Southeast Asian ovalocytosis |
| SDS | sodium dodecyl sulfate |
| SDS-PAGE | sodium dodecyl sulfate polyacrylamide gel electrophoresis |
| SGLT1 | Na ⁺ /glucose cotransporter isoform 1 |
| SLC | solute carrier |
| SNAT3 | N-type sodium-dependent neutral amino acid transporter isoform 3 |
| SPR | surface plasmon resonance |
| t | time |
| T | total |
| tmAC | transmembrane adenylyl cyclase |
| TMD | transmembrane domain |
| U | unbound |
| V | velocity |
| V _{max} | velocity at maximal substrate concentration |
| WT | wild type |
| YFP | yellow FP |
| °C | degrees Celsius |

Chapter 1: General Introduction

Portions of this chapter have been published in Johnson, D. E., and Casey, J. R. 2009. Bicarbonate Transport Metabolons. in *Drug Design of Zinc-Enzyme Inhibitors: Functional, Structural and Disease Applications*, Supuran, C.T. and Winnum, J. Eds, Wiley Chapter 20, pp 415-437. (Reproduced with permission)

1.1 Thesis Overview

The objective of this thesis is to examine pH changes at the intracellular surface of transport proteins during AE1-mediated $\text{Cl}^-/\text{HCO}_3^-$ exchange or hCNT3-mediated Na^+/H^+ /nucleoside co-transport. Intracellular pH was monitored with the pH-sensitive fluorescent proteins (FPs), dual emission green FP (deGFP4) fused to the N-terminus of AE1 (deGFP4.AE1) and a monomeric red FP Nectarine (mNect) fused to the N-terminus of hCNT3 (mNect.hCNT3) or an inactive hCNT3 mutant (mNect.hCNT3-F563C). Ultimately, we want to answer the question of whether a H^+ microdomain (a region of discontinuous cytosolic H^+ concentration) forms around AE1 as it exchanges Cl^- for HCO_3^- .

Solute microdomain formation is enhanced by rapid solute transport rate. Carbonic anhydrase (CA) activity is essential to AE1's rapid $\text{Cl}^-/\text{HCO}_3^-$ exchange rate, so the introduction begins with a discussion of the bicarbonate transport metabolon, with AE1 and other pH-regulatory membrane transport proteins. Physiological roles of pH are discussed, to illustrate the importance of pH regulation, and possible implications of H^+ microdomain formation. pH at the intracellular surface of hCNT3 was monitored in two separate studies. Both mNect.hCNT3 and mNect.hCNT3-F563C were utilized to investigate H^+ /nucleoside co-transport, while mNect.hCNT3-F563C also served as a control for the investigation of H^+ microdomain formation. Nucleoside transport is therefore discussed. Fluorescent proteins as intracellular indicators are also discussed, as they were utilized throughout all of the experiments presented in this thesis.

1.2 Bicarbonate and Bicarbonate Transport

1.2.1 Biochemistry of Bicarbonate

Bicarbonate (HCO_3^-) is an interesting and important molecule. It is a labile substrate, as its form changes subject to the coupled reactions: CO_2 (gas) \Leftrightarrow CO_2 (dissolved) + $\text{H}_2\text{O} \Leftrightarrow \text{H}_2\text{CO}_3 \Leftrightarrow \text{HCO}_3^- + \text{H}^+ \Leftrightarrow \text{CO}_3^{2-} + 2\text{H}^+$ [1]. The reaction $\text{CO}_2 + \text{H}_2\text{O} \Leftrightarrow \text{H}_2\text{CO}_3$ is catalyzed by carbonic anhydrase enzymes, while dissociation of H_2CO_3 to $\text{HCO}_3^- + \text{H}^+$ occurs spontaneously. The equilibrium between gaseous and dissolved CO_2 varies with partial pressure of CO_2 , temperature and pH, adding further complexity to the system. As bicarbonate changes form, solution pH does too, so understanding the chemistry behind this molecule is necessary to understanding pH and pH regulation.

HCO_3^- is involved in pH and cell volume regulation, and carbon dioxide (CO_2) metabolism. Precise regulation of pH is essential to whole body homeostasis, as biochemical processes occur within a narrow optimal pH window [1]. The $\text{CO}_2/\text{HCO}_3^-$ system serves as the cell's main pH buffer to limit changes in intra- and extra-cellular pH. Intracellular buffering will be discussed in greater detail in section 1.3.2. Under physiological conditions, cellular HCO_3^- levels are around 25 mM and metabolic acid will be consumed by the conversion of HCO_3^- to CO_2 [1]. CO_2 is membrane permeant, and can cross the plasma membrane of mammalian cells by diffusion. HCO_3^- , on the other hand, is membrane impermeant and requires bicarbonate transporters to move across the membrane. Transport of the base, HCO_3^- , into a cell will alkalinize it, while movement of

HCO_3^- out of a cell will acidify it. Since HCO_3^- has such key biological functions, translocation of HCO_3^- across cell membranes is carefully controlled by HCO_3^- transport proteins.

1.2.2 Carbonic anhydrases

Carbonic anhydrases are zinc metalloenzymes that catalyze the reversible reaction of $\text{CO}_2 + \text{H}_2\text{O} \rightleftharpoons \text{H}_2\text{CO}_3$. They are present in prokaryotes and eukaryotes and are encoded by four evolutionarily unrelated gene families [2]. α -CAs are present in vertebrates, bacteria, algae and in the cytoplasm of green plants, and are the most extensively studied CAs to date. There are at least 16 α -CAs isoforms, with different catalytic activity, tissue distribution and subcellular localization [2, 3]. α -CAs include cytosolic, membrane-bound forms, mitochondrial, and secreted isoforms [2]. The active site of the α -CAs is a Zn(II) ion coordinated by three histidine residues and a water molecule/hydroxide ion that acts as a nucleophile [3]. The metal ion stabilizes the highly reactive hydroxide ion [4]. α -CAs are inhibited by two classes of compounds: 1) metal complexing anions and 2) sulfonamides [3]. There are currently over 25 clinically used drugs, including diuretics, anti-glaucoma drugs, anticonvulsants, anti-cancer agents, anti-obesity drugs, and antimicrobials that target CAs [3]. β -CAs exist mainly in bacteria, algae and chloroplasts of monocotyledons and dicotyledons; γ -CAs are found in archaea and some bacteria, while the δ -CAs are present in some marine diatoms [2]. The β - and γ -CAs have similar mechanisms

of action as the α -CAs, but some of the β -CAs do not have water directly coordinated to the metal ion [3].

1.2.3 Bicarbonate Transport Proteins

Bicarbonate transport proteins facilitate the movement of membrane-impermeant bicarbonate across biological membranes [1]. Human bicarbonate transport proteins cluster phylogenetically into three classes: electroneutral $\text{Cl}^-/\text{HCO}_3^-$ exchangers of the SLC4 family (solute carrier 4), Na^+ -coupled HCO_3^- cotransporters (SLC4 family), and anion transporters of the SLC26 family (Fig. 1.1) [5]. These bicarbonate transport proteins differ in their tissue localization and mechanism of action (Table 1.1).

The SLC4 anion exchanger (AE) family is composed of three isoforms (AE1, AE2 and AE3) that share 65% amino acid sequence identity in their transmembrane regions [4-6]. AEs facilitate the electroneutral exchange of Cl^- for HCO_3^- across the plasma membrane of mammalian cells [6]. AEs also transport some other small inorganic and organic anions, including bromide, fluoride, iodide, phosphate, and sulphate, with varying physiological rates of exchange [6].

Human AE1 is comprised of a 43 kDa amino-terminal cytoplasmic domain that interacts with cytoskeletal proteins and glycolytic enzymes [7], a 55 kDa membrane spanning domain, responsible for $\text{Cl}^-/\text{HCO}_3^-$ exchange activity [8, 9], and a short 33 amino acid cytoplasmic carboxyl-terminal domain that contains the binding site for CAII (Fig. 1.2) [8, 10]. AE1 is expressed in the erythrocyte

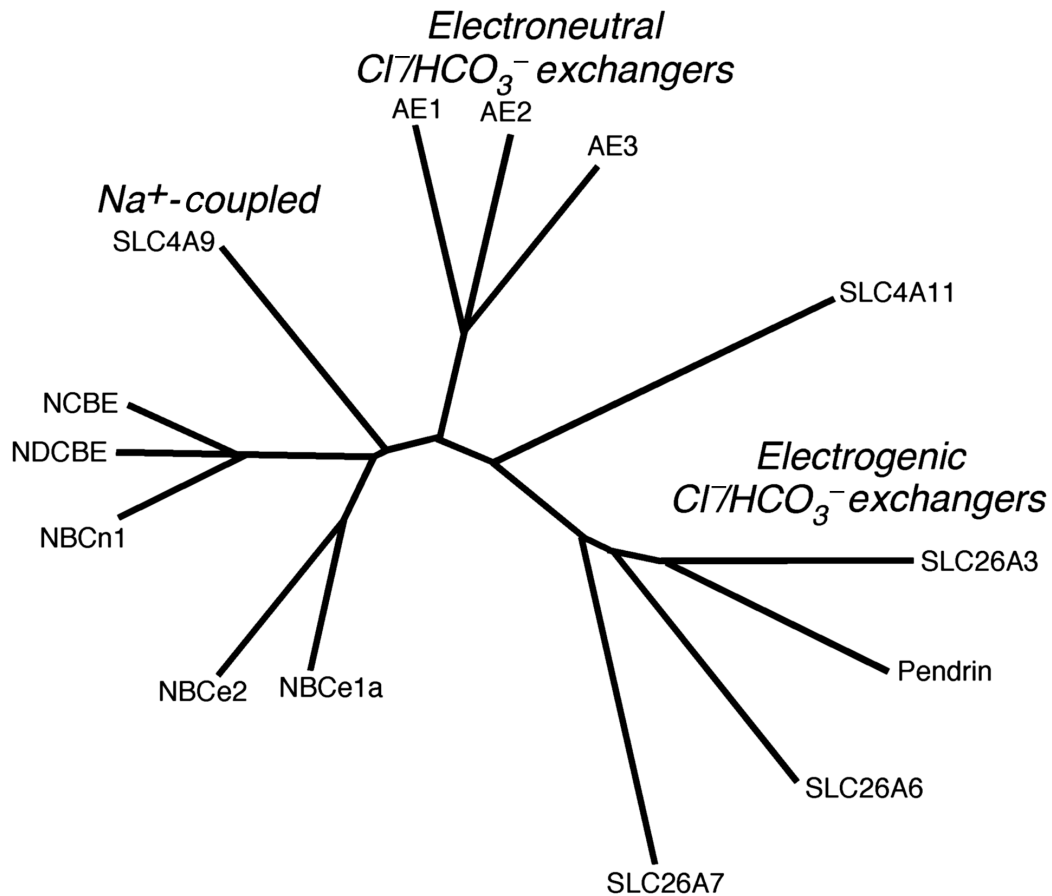


Figure 1.1. **Phylogenetic tree of human bicarbonate transporter genes.** Amino acid sequences corresponding to human bicarbonate transporter genes were aligned using Clustal W software (<http://align.genome.jp/>). Phylogenetic relationships were established using Clustal W software. The length of each line in the plot denotes relative evolutionary distance. The three families of bicarbonate transporters are labeled.

Table 1.1. **Bicarbonate transport proteins and carbonic anhydrase interactions.** Bracketed names are not generally accepted, but are found in the literature.

| Transport protein | Other names | Identified CA Interactions | Mechanism/ Charge Movement | Citations |
|--------------------------|-----------------------------------|-----------------------------------|---|------------------|
| AE1 | SLC4A1, Band 3, kAE1, eAE1 | CAII, CAIV, CAIX | Cl ⁻ /HCO ₃ ⁻ exchange/ electroneutral | [8-15] |
| AE2 | SLC4A2 | CAII, CAIV, CAIX | Cl ⁻ /HCO ₃ ⁻ exchange / electroneutral | [8, 9, 13-15] |
| mAE3 | SLC4A3 AE3c, AE3fl | CAII, CAIV, CAIX, CAXIV | Cl ⁻ /HCO ₃ ⁻ exchange / electroneutral | [9, 13-16] |
| NBCe1 | SLC4A4, NBC1, hhNBC, pNBC,, kNBC1 | CAII, CAIV | Na ⁺ /HCO ₃ ⁻ co-transport/ -2 or -1 | [17-20] |
| NBCe2 | NBC4, SLC4A5 | | Na ⁺ /HCO ₃ ⁻ co-transport/ -1 or 0 | |
| NBCn1 | SLC4A7, NBC3, (NBC2, SLC4A6) | CAII | Na ⁺ /HCO ₃ ⁻ co-transport/ electroneutral | [21] |
| SLC4A9 | AE4 | | Na ⁺ /HCO ₃ ⁻ co-transport electroneutral | |
| NDCBE | SLC4A8, NDAE1 (kNBC-3) | | Na ⁺ -dependent Cl ⁻ /HCO ₃ ⁻ exchange and (electroneutral NBC: splice variant)/electroneutral | |
| NCBE | SLC4A10 NBCn2 | | Na ⁺ -dependent Cl ⁻ /HCO ₃ ⁻ exchange or Na ⁺ /HCO ₃ ⁻ co-transport/ electroneutral | |
| SLC4A11 | BTR1, NaBC1 | | Na ⁺ /H ₂ BO ₄ ⁻ co-transport? HCO ₃ ⁻ transport?/ electrogenic | |
| SLC26A3 | DRA, CLD | CAII (functional only) | Cl ⁻ /HCO ₃ ⁻ exchange/ electroneutral | [15] |
| Pendrin | SLC26A4, PDS | | Cl ⁻ /HCO ₃ ⁻ exchange; also I ⁻ / electroneutral | |
| SLC26A6 | PAT-1, CFEX | CAII | Cl ⁻ /HCO ₃ ⁻ exchange; also oxalate and formate/ electroneutral | [22] |
| SLC26A7 | SLC26A7 | CAII (functional only) | Cl ⁻ /HCO ₃ ⁻ exchange | [15] |

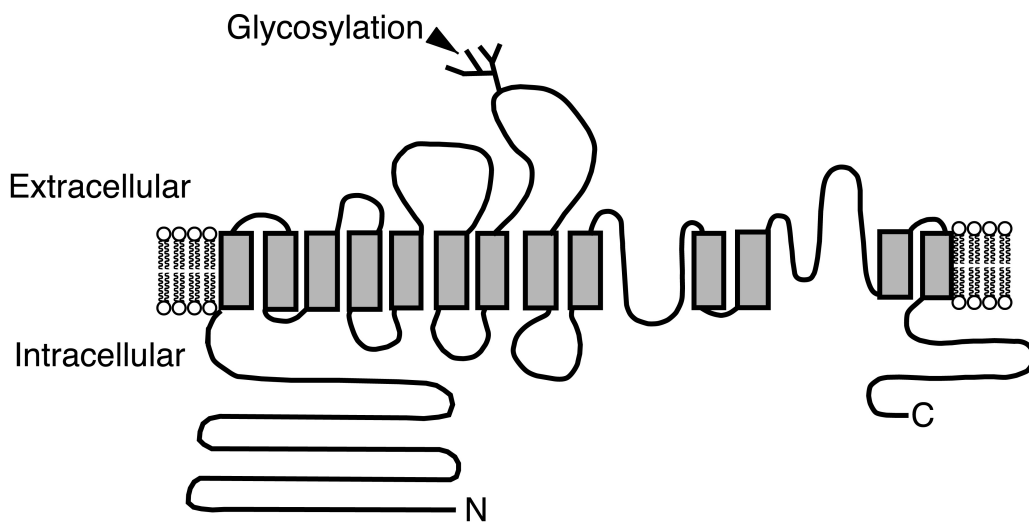


Figure 1.2. **AE1 topology model.** Topology model of AE1, drawn to approximate scale. The amino (N) and carboxyl (C) termini of AE1 are marked. The branched structure on the fourth extracellular loop represents the glycosylation site of AE1.

plasma membrane (eAE1) where it makes up 50% of the integral membrane protein, and contributes to CO₂ removal [23]. CO₂, the waste product of mitochondrial respiratory oxidation, is continuously produced by mammalian cells, and must be removed [1]. In peripheral tissues, membrane permeant CO₂ diffuses into the erythrocyte where its hydration is catalyzed by cytosolic carbonic anhydrase II. The resulting membrane-impermeant HCO₃⁻ is transported into the plasma by the Cl⁻/HCO₃⁻ exchanger, AE1, thus increasing blood's CO₂ carrying capacity. In the lungs, the process is reversed and HCO₃⁻ is transported back into the erythrocyte, dehydrated, and the resulting CO₂ diffuses across the erythrocyte and alveolar membranes, and is exhaled [8, 9]. Each erythrocyte contains ~10⁶ copies of CAII and 1.2 x10⁶ copies of AE1 [9], and maximal Cl⁻/HCO₃⁻ exchange in erythrocytes is dependent on CAII [9, 24]. The kidney isoform, kAE1, is expressed in the basolateral membrane of α-intercalated cells [25]. kAE1 lacks the N-terminal 65 amino acids of eAE1 [5]. Mutations in the human AE1 gene cause autosomal dominant spherocytic anemia, Southeast Asian Ovalocytosis, and distal renal tubular acidosis [26].

AE2 is the most widely expressed isoform and is found in the basolateral membrane of many epithelial cells [5]. AE2 activity is strongly inhibited by protons, but activated by hypertonicity and low concentrations of ammonium ions, whereas AE1 activity is unaffected by all of these parameters [5]. AE1/AE2 chimera studies demonstrated that the pH response of AE2 activity is due to the transmembrane domain (“sensor domain”), and that the cytoplasmic domain (“modifier domain”) serves to increase sensitivity to protons [5].

AE3 is expressed predominantly in excitable tissues, including brain, heart and retina, and throughout the gastrointestinal tract [5]. Two alternative transcripts of AE3 are generated by alternative promoter usage: AE3 full length (AE3fl) and AE3 cardiac (AE3c) [6]. AE3fl and AE3c differ in their N-termini: 270 amino acids in AE3fl are replaced by a unique sequence of 73 amino acids in AE3c [27, 28]. Both are expressed in heart and retina [29].

The $\text{Na}^+/\text{HCO}_3^-$ co-transporters (NBCs) of the SLC4 family facilitate the co-transport of Na^+ and HCO_3^- across the plasma membrane with either an electroneutral (NBC3/NBCn1) or electrogenic ($2/3 \text{ HCO}_3^-:1 \text{ Na}^+$) (NBCe1, NBC4/NBCE2) mechanism [4]. The Na^+ -coupled HCO_3^- transporter family is composed of NBCe1, NBCe2, NBCn1, NDCBE and NCBE [19]. Splicing variant NBCe1a (kNBCe1) plays the central role in HCO_3^- reabsorption in the basolateral membranes of the proximal tubule in conjunction with the luminal Na^+/H^+ exchanger, NHE3, and a H^+ -ATPase, which secrete acid [17]. NBCe1a thus mediates HCO_3^- efflux from the cell to the blood, and normally works with a stoichiometry of 3 HCO_3^- per Na^+ . NBCe1b (pNBCe1) is expressed in the basolateral membranes of pancreatic duct cells where it transports HCO_3^- into the cell and functions with a 2 HCO_3^- per Na^+ stoichiometry [17]. NBCs have a widespread tissue distribution including pancreas, kidney, skeletal muscle and heart [17].

Four members of the SLC26 family have established $\text{Cl}^-/\text{HCO}_3^-$ exchange activity. Individual paralogs differ significantly in their substrate specificity [30]. SLC26A4 (Pendrin) is insensitive to intra- and extracellular pH, while SLC26A3

(DRA) is inhibited by intracellular acidification and activated by intracellular alkalization, ammonium and hypertonicity [5]. SLC26A6 carries out both $\text{Cl}^-/\text{HCO}_3^-$ and Cl^-/OH^- exchange and is the predominant anion exchanger in the heart [31]. SLC26A6 is involved in NaCl reabsorption in the renal proximal tubule, and in secretion of basic pancreatic fluid in pancreatic duct cells [32]. SLC26A6 also transports several other anions, including sulfate, formate, oxalate, nitrate and iodide [32]. SLC26A7 is a $\text{Cl}^-/\text{HCO}_3^-$ exchanger localized predominantly in the basolateral membrane of gastric parietal cells [32].

1.2.4 The Bicarbonate Transport Metabolon

1.2.4.1 Overview

A metabolon is a physical complex of enzymes in a linked metabolic pathway that functions to maximize flux of substrate through the pathway by the direct transfer of an intermediate between the active site of two enzymes that catalyze sequential reactions, thereby limiting the loss of substrate through diffusion [9, 33-35]. This is also known as substrate channeling [36]. Metabolons include coupled enzymes in glycolysis, the citric acid cycle and the urea cycle, as well as DNA, RNA and protein biosynthesis [33, 34].

The linked physiological function (catalysis and transport of HCO_3^-) and the widespread tissue distribution of both bicarbonate transporters and carbonic anhydrases suggests that they could form a complex; CAs both supply the HCO_3^- substrate for transport and remove HCO_3^- following transport [37]. A bicarbonate

transport metabolon, composed of a bicarbonate transporter and a CA protein, has thus been proposed on the basis of physical and functional interactions between bicarbonate transporters and carbonic anhydrases (Fig. 1.3) [8-10, 12, 13, 33].

1.2.4.2 AE/CA Interactions - Initial Characterization

An interaction between AE1 and CAII in erythrocytes was initially found by examining the effect of the extracellular stilbene-disulfonate inhibitor (DIDS) of AE1 on the fluorescence of a labeled bovine CAII incorporated into erythrocyte ghosts [11]. In this experiment, the kinetics of CAII binding to the CA inhibitor, dansylsulfonamide (DNSA), were measured fluorimetrically with increasing amounts of DIDS. Binding of DIDS to AE1 increased the forward rate constant and apparent ligand binding constant of CAII-DNSA binding, indicating that AE1 inhibition alters CAII conformation [11]. This suggests that CAII/AE1 form a physical and functional complex.

A direct, physical interaction between CAII and the C-terminus of AE1 was later shown in erythrocytes or erythrocyte ghost membranes by immunolocalization, co-immunoprecipitation, and microtitre plate assays [8, 10]. Co-localization between AE1 and CAII was suggested by immunofluorescence experiments performed on tomato lectin-clustered AE1 ghost membranes (tomato lectin binds the extracellular sugar moieties present on the extracellular surface of AE1); immunofluorescence revealed parallel clustering of CAII at the cytosolic membrane surface [10]. This indicates that CAII is physically tethered to AE1 in the membrane. CAII and AE1 were also co-immunoprecipitated from solubilized erythrocyte membranes [10]. Moreover, full length AE1 or AE1 membrane

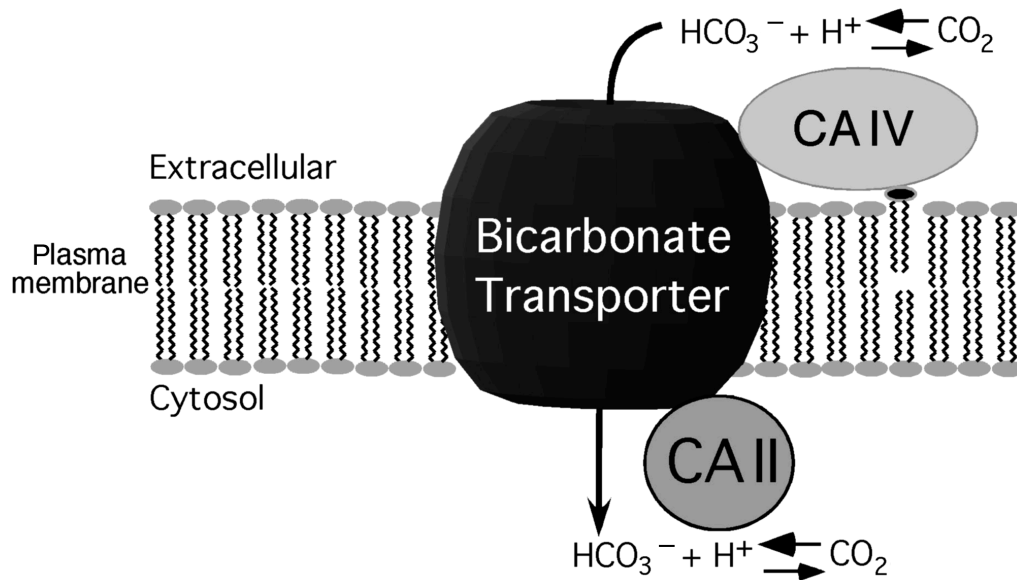


Figure 1.3. **The bicarbonate transport metabolon.** Carbonic anhydrases (CAs) catalyze the reversible conversion of CO_2 to HCO_3^- and H^+ . Some bicarbonate transporters directly bind both the soluble cytosolic enzyme CA II and the extracellular enzyme CA IV, anchored to the cell surface via a glycosylphosphatidyl inositol linkage. These direct interactions facilitate the rate of HCO_3^- transport by preventing depletion of HCO_3^- at the *cis* side of the transporter and minimizing it on the *trans* side, thereby maintaining the magnitude of the transmembrane HCO_3^- gradient. This gradient is the primary driving force for HCO_3^- transport.

domain bound saturably to CAII immobilized on microtitre plates in a solid phase binding assay [10]. AE1-CAII binding was decreased when the C-terminus of AE1 was blocked by pre-incubation with an antibody directed against the C-terminus of AE1. To further investigate the AE1-CAII interaction, a GST-fusion protein encoding the C terminal region of AE1 (residues 879-911) (AE1-Ct) was used as a probe in an affinity blotting assay, a solid phase binding assay and in affinity chromatography [10]. These experiments all showed that the AE1-Ct bound CAII with high affinity, and suggest that the C-terminus of AE1 directly binds CAII [8, 10].

A series of truncation mutants of the AE1-Ct sequence were characterized to narrow the region of AE1-Ct involved in association with CAII [8]; amino acids 879-890 of human AE1 were sufficient to bind CAII [8]. This carbonic anhydrase binding (CAB) site is immediately adjacent to the lipid bilayer, as the last transmembrane segment of AE1 is predicted to end at position 877, and thus CAII binding would bring CAII within close proximity to the bicarbonate translocation mechanism of AE1. CAII would then be ideally located to hydrate incoming CO₂ and supply AE1 with HCO₃⁻ for transport [8].

An electrostatic interaction between CAII and the AE1 C-terminus was suggested by the pH and ionic strength dependence of their interaction [8, 12]. Tantalizingly, the C-terminus of AE1 contains three short acidic regions. Among these, the most membrane proximal was identified as responsible for CAII binding. Further point mutations showed that a precise acidic cluster of residues (D⁸⁸⁷ADD) was required for CAII binding [8]. Within this sequence, at least two

out of three acidic residues are necessary for CAII-binding, as DADA, DAAD, and AADD mutants still bound CAII with similar levels to DADD. A conserved leucine residue (L886) in AE1 was also found to be essential for the AE1-CAII interaction, and indicates that both ionic and nonpolar interactions are involved [12]. The consensus CAII binding motif on AE1 was thus refined to consist of a hydrophobic amino acid followed by four residues, at least two of which are acidic.

What part of CAII binds AE1? The electrostatic nature of their interaction and the requirement for an acid region on AE1 suggested a complementary basic region on CAII that would form the binding site. The CAII crystal structure reveals that the amino terminal region of CAII contains multiple histidine residues along with lysine and arginine residues, that together form a basic patch extending from the surface of CAII that could interact with the highly acidic C-terminus of AE1 [8, 10, 38]. A series of truncation and point mutants of CAII showed that five histidine residues in CAII (His3, -4, -10, -15, -17) were required for binding to AE1-Ct in a microtitre plate binding assay [12]. This data indicates that the AE1 binding site in CAII is located within the first 17 amino acids, and that the association is mediated by electrostatic interactions involving histidine residues [12]. The histidine-rich region may act as an “electrostatic highway” to funnel HCO_3^- or Cl^- to and from the active sites of CAII and AE1 [36].

AE2 has 60% C-terminal sequence identity with AE1, but the corresponding acidic cluster in AE2 is LDANE [8]. Mutation of AE1’s LDADD sequence to LDANE did not affect AE1 binding to CAII, and a GST fusion

protein containing the C terminus of AE2 was able to bind CAII, demonstrating that CAII physically interacts with both AE1 and AE2 [8].

Erythrocytes express both CAII and CAI, but CAI does not bind AE1 despite possessing 60% sequence identity to CAII [12]. This is likely due to the absence of the basic histidine patch found in CAII [12].

1.2.4.3 AE/CA Interactions - Physiological Significance

The physiological role of the CAII/AE1 interaction was investigated by monitoring changes in intracellular pH associated with AE1-mediated $\text{Cl}^-/\text{HCO}_3^-$ exchange in transfected HEK293 cells [9]. Firstly, AE1-mediated $\text{Cl}^-/\text{HCO}_3^-$ exchange was inhibited by 50-60% in the presence of the sulfonamide CA inhibitor, acetazolamide, which indicates that CAII activity is required for full HCO_3^- transport activity [9]. Acetazolamide inhibits CA enzymatic activity without directly affecting AE1 anion exchange [24, 39]. Further, fusion of CAII to the AE1 C-terminus increases the AE1-mediated $\text{Cl}^-/\text{HCO}_3^-$ exchange rate [40]. Secondly, transport activity of AE1 mutants that were previously shown as unable to bind CAII (CAB mutants LNANN, LAAAA) [8] was assessed. AE1-WT had about ten times the $\text{Cl}^-/\text{HCO}_3^-$ exchange activity as the mutants, yet the mutants had similar total amounts of protein expression, and equal or greater plasma membrane localization; the decrease in $\text{Cl}^-/\text{HCO}_3^-$ exchange was thus not attributable to defects in processing the mutants to the cell surface, but might arise from a failure to associate with CAII [9]. A 20-fold over-expression of CAII had no effect on wild type or mutant AE1-mediated $\text{Cl}^-/\text{HCO}_3^-$ exchange, indicating

that endogenous levels of CAII are not rate-limiting, and that over-expression was not able to rescue the activity of the mutants [9].

To further examine the nature and importance of the CAII/AE1 interaction, a catalytically inactive CAII mutant (CAII-V143Y) [41] was over-expressed in HEK293 cells in conjunction with AE1 [9]. CAII-WT and CAII-V143Y bound AE1-Ct with similar affinities in a microtitre plate assay and expression of AE1 was not altered with varying levels of wild type or mutant CAII. Cells co-transfected with AE1 and increasing amounts of CAII-V143Y cDNA decreased AE1-mediated $\text{Cl}^-/\text{HCO}_3^-$ rates by up to 60% [9]. Alternatively, increasing amounts of CAII-WT cDNA had no effect [9]. This suggests that over-expressed CAII-V143Y displaces endogenous CAII-WT from the binding site on AE1 [4]. AE2 and AE3c contain similar acidic C-terminal sequences to AE1, and their exchange activity was also decreased by co-expression with CAII-V143Y [9]. Taken together, these results indicate that CAII physically interacts with AE1-3, to accelerate the rate of HCO_3^- transport.

Some members of the CA family have their catalytic sites anchored to the extracellular surface [16, 42, 43]. Cell surface glycosylphosphatidyl inositol (GPI)-anchored carbonic anhydrase IV (CAIV) has a high degree of similarity to the cytosolic CAs and shares 36% sequence identity with CAII [42]. In addition, CAIV has comparable catalytic activity to CAII [42]. Studies to isolate the role of CAIV in AE-mediated $\text{Cl}^-/\text{HCO}_3^-$ exchange were hindered by the impossibility of using pharmacological inhibitors of CAII, as membrane permeant compounds would also block extracellular CAIV activity. To circumvent this problem, the

inactive CAII-V143Y mutant was used to suppress endogenous CAII activity [13]. While AE-mediated $\text{Cl}^-/\text{HCO}_3^-$ exchange activity in HEK293 cells co-transfected with AE1, AE2, or AE3 and CAII-V143Y is impaired by ~50%, overexpression of CAIV in these cells rescued AE1, AE2, and AE3 $\text{Cl}^-/\text{HCO}_3^-$ exchange activity [13]. Rescue was specific to CA activity, as treatment with the CA inhibitor, acetazolamide, abolished the increase in transport rate. Together, these data indicate that there is a functional interaction between the anion exchangers and CAIV [13].

A physical association of AE1, AE2 and AE3, with CAIV was demonstrated by blot overlay assays [13]. The AE1/CAIV interaction was further confirmed by co-migration of AE1 and CAIV on sucrose gradients of membranes expressing the two proteins [13]. GST pull-down assays demonstrated that CAIV binds specifically to the fourth extracellular loop of AE1 (EC4), which is the largest extracellular loop in AE1 [13]. In addition, it has been proposed that a region in EC4 (Arg656-Ile661) forms the outer vestibule that funnels anions to and from the transport site [13, 44]. Thus, CAIV localizes close to the active site of AE1, where it can be most effective in dehydrating HCO_3^- and maximizing the transmembrane HCO_3^- gradient, thereby forming the extracellular component of a bicarbonate transport metabolon. The structure of AE2 and AE3 differ somewhat from AE1 in that EC3 is larger than EC4 [45, 46], but it is possible that a similar physical interaction exists [13].

AE3, CAII and CAXIV (another extracellular-linked CA isoform) are involved in pH_i , $[\text{Cl}^-]$, $[\text{HCO}_3^-]$ and volume regulation in the Müller and

horizontal cells of the human retina [16]. The retina is a highly metabolically active tissue that produces large amounts of CO_2 and H^+ , which must be eliminated in order to maintain intracellular and extracellular pH. Studies using ae3 knockout mice demonstrate that ae3 is essential for normal retinal function [16]. Furthermore, in ae3-null mice nbce1, caii and caxiv expression is upregulated, suggesting an attempt to compensate for the absence of $\text{Cl}^-/\text{HCO}_3^-$ activity [16]. A caxiv-deficient mouse has similar retinal deficiencies, suggesting a link between ae3 and caxiv [16]. Further, immunoprecipitation experiments using mouse brain and retinal lysates demonstrate a physical association between AE3 and CAXIV, and co-expression of CAXIV with AE3 in HEK293 cells maximizes AE3-mediated $\text{Cl}^-/\text{HCO}_3^-$ exchange activity [47]. Together, these data provide evidence for a physical and functional interaction between AE3 and CAXIV.

The CAIX catalytic domain is anchored to the extracellular surface of cells by a single transmembrane segment [15]. In normal tissues, CAIX is expressed in gastric, intestinal and gallbladder mucosa where it may play a role in acid secretion [43]. AE2 is also highly expressed in the stomach and, like CAIX, is localized to the basolateral membrane of parietal cells where it mediates the uptake of Cl^- destined for HCl secretion and extrusion of HCO_3^- generated intracellularly during acid secretion [48]. Does CAIX interact with AE2? In HEK293 cells, CAIX increased AE-mediated $\text{Cl}^-/\text{HCO}_3^-$ exchange when coexpressed with AE1, AE2, and AE3 [15]. Further, AE2-mediated $\text{Cl}^-/\text{HCO}_3^-$ exchange was decreased by CAII-V143Y overexpression, and this decrease was

rescued by coexpression with CAIX, thereby supporting a functional interaction between CAIX and AE2 [15].

Immunoprecipitation experiments demonstrated that CAIX physically interacts with AE1, AE2 and AE3 [15]. CAIX is a transmembrane protein, consisting of four domains: an N-terminal proteoglycan-like domain (amino acids 53-111), an extracellular catalytic domain (amino acids 135-391), a single transmembrane domain (amino acids 415-436) and a short intracellular C-terminal tail (amino acids 436-459) [15, 43]. Constructs encoding CAIX lacking the catalytic domain (Δ C-CAIX) and the proteoglycan domain (Δ PG-CAIX) were used to determine which portion(s) of CAIX bind AE2 [15]. Co-immunoprecipitation and GST pull-down approaches demonstrated that AE2 binds the catalytic domain of CAIX.

Additionally, CAIX is expressed in many types of carcinomas; CAIX activity leads to acidification of the extracellular space, thus facilitating tumor growth and maintenance of cytosolic pH [49, 50].

Two possible mechanisms may explain the increased $\text{Cl}^-/\text{HCO}_3^-$ exchange activity of SLC4 transport proteins when bound to CAII [26]. CAII could contribute to substrate channeling to and/or from the anion translocation pathway, as proposed [9], or it could possibly allosterically up-regulate AE1 activity at the cell surface by altering the conformational state of the bicarbonate transporter [26]. The latter possibility is not supported by the finding that catalytically inactive CAII (CAII-V143Y), able to bind AE1, *decreased* AE1 transport activity [26]. The allosteric mechanism was further tested by measuring the effect that

kAE1 C-terminal mutations had on $\text{Cl}^-/\text{HCO}_3^-$ and Cl^-/Cl^- exchange in *Xenopus* oocytes [26]. The rationale behind these experiments was that a change in Cl^-/Cl^- exchange rate upon CAII activation would be evidence of a CAII-induced conformational change. The distal renal tubular acidosis (dRTA) truncation mutant, AE1-901X, preserved Cl^-/Cl^- and $\text{Cl}^-/\text{HCO}_3^-$ exchange, while further truncations (891X, 896X) and AE1 CAB-site missense mutants showed no $\text{Cl}^-/\text{HCO}_3^-$ exchange, but preserved Cl^-/Cl^- exchange. Further, CAII enhanced kAE1-WT $\text{Cl}^-/\text{HCO}_3^-$ exchange rates, but did not alter Cl^-/Cl^- exchange rates [26]. In parallel, CA inhibition decreased kAE1-WT $\text{Cl}^-/\text{HCO}_3^-$ exchange rates, but did not alter Cl^-/Cl^- exchange rates. Together, these data do not support the hypothesis that CAII binding allosterically alters the conformation of AE1, but remain consistent with the channeling hypothesis [26].

Co-expression studies of wild type and mutant AE1 proteins further probed metabolon behaviour; AE1 forms dimers in which each AE1 subunit is sufficient for HCO_3^- transport function [51, 52]. The heterozygous AE1 mutant (AE1 Δ 400-408, SAO), associated with Southeast Asian ovalocytosis and dRTA, is completely devoid of $\text{Cl}^-/\text{HCO}_3^-$ exchange activity despite being expressed at the cell surface [26]. Engineered mutant, AE1-E699Q, is also expressed at the cell surface and exhibits severely impaired $\text{Cl}^-/\text{HCO}_3^-$ exchange. Both of these mutants retain the CAII binding site. When the mutants were co-expressed in *Xenopus* oocytes with AE1-LDAAA, which cannot bind CAII, they were able to rescue the $\text{Cl}^-/\text{HCO}_3^-$ exchange activity of AE1-LDAAA by 50% [26]. The ability of the heterodimers (homodimers presumably remain inactive) of

SAO/LDAAA and E699Q/LDAAA to rescue $\text{Cl}^-/\text{HCO}_3^-$ exchange is attributable to the functional proximity of the C-terminal tail of one protomer (SAO, E699Q) to the anion translocation pathway in the adjacent one (LDAAA) [26]. In other words, the CAII molecule does not need to be bound to the same protomer that is catalyzing transport; CAII binding at the adjacent monomer within the dimer unit suffices to activate $\text{Cl}^-/\text{HCO}_3^-$ exchange.

Another mechanism by which metabolon interaction facilitates coupled flux is that association of CAII with AE proteins activates the CAII catalytic rate. Di-/tri-/tetrapeptides containing all or part of the LDADD motif increased CAII activity over 5-fold [53]. This data strengthens the CA/AE metabolon hypothesis.

1.2.4.4 NBC/CA Interactions

CA interactions with NBC family members NBCn1 and NBCe1 have also been investigated. CAIV and NBCe1 co-localize in mammalian kidney, pancreas and heart, and can be co-immunoprecipitated from lysates of mouse kidney [17]. CAIV over-expression increases the rate of recovery from acid load in HEK293 cells co-transfected with NBCe1 and CAIV cDNA [17]. Mutation of NBCe1 in the fourth extracellular loop (NBCe1-G767T) abolished the CAIV induced increase in transport, and abrogated physical binding in GST pull down assays, indicating that this loop mediates the interaction with CAIV [17]. Membrane-permeant acetazolamide and a membrane impermeant CA inhibitor both reduced NBCe1 activity. Together these data suggest that CAIV interacts physically and functionally with NBCe1 in a manner similar to AE1 [13], and together form a bicarbonate transport metabolon.

Intracellular CAII also has a role in maximizing NBCe1 activity. Two acidic motifs in NBCe1 (L⁹⁵⁸DDV and D⁹⁸⁶NDD) are involved in binding CAII, as demonstrated by GST pull down assays [20]. CAII activity enhanced flux through NBCe1 in a mouse proximal convoluted tubule cell line (mPCT) [18, 20], and in *Xenopus laevis* oocytes [19] expressing NBCe1. Pharmacological CA inhibition or co-expression with CAII-V143Y, decreased flux through the co-transporter, suggesting that CA activity is necessary [18-20]. Taken together, this data indicates that NBCe1 physically and functionally interacts with both CAII and CAIV to form a bicarbonate transport metabolon.

Phosphorylation by cAMP-dependent protein kinase A (PKA) also plays a role in modulating NBCe1 transport activity, possibly working through a bicarbonate transport metabolon. The transport stoichiometry of NBCe1a is shifted from 3:1 HCO₃⁻:Na⁺ to 2:1 by phosphorylation of Ser⁹⁸² (NBCe1a) [18]. Three aspartate residues (D⁹⁸⁶NDD) involved in binding CAII are close to the PKA phosphorylation site, and acetazolamide decreases NBCe1a activity only when the transporter is unphosphorylated (3:1 stoichiometry) [18]. This suggests that PKA has an effect on CAII interaction with NBCe1a, and thus activity [18]. PKA-dependent phosphorylation of NBCe1a in the proximal tubule also reduces transport activity of NBCe1a [54].

The increased negative charge on NBCe1a-Ser⁹⁸²-phosphate may shift the stoichiometry by interfering with the binding of HCO₃⁻ to NBCe1a by modification of the electric field around the binding site [18]. The nearby D⁹⁸⁶NDD acidic cluster might also play a role in the shift in stoichiometry.

Mutation of all three aspartate residues in the D⁹⁸⁶NDD motif to asparagines (N⁹⁸⁶NNN) decreased CAII binding by ~90%, confirming the physical interaction between CAII and NBCe1a [20]. Furthermore, 8-Br-cAMP (a PKA activator) had no effect on the stoichiometry of the N⁹⁸⁶NNN mutant, suggesting that the D⁹⁸⁶NDD motif is indeed required for the shift in stoichiometry. Moreover, the PKA-induced shift in stoichiometry is dependent on D986 and D988, but not D989 [18, 20]. The PKA-induced shift in stoichiometry from 3:1 HCO₃⁻:Na⁺ to 2:1 is thus dependent on the phosphorylation of Ser⁹⁸² and requires the presence of D986 and D988 of the CAII-binding motif. This shift in stoichiometry decreases NBCe1a transport and renders the transporter's activity insensitive to acetazolamide, thus suggesting that phosphorylation interferes with CAII binding. Gross *et al.* propose that CAII binds to NBCe1a when the transporter functions in the 3:1 mode (NBCe1a-Ser⁹⁸² unphosphorylated) [18]. Upon phosphorylation of NBCe1a-Ser⁹⁸², CAII dissociates from the transporter. This explains the decreased effect of CA inhibition.

Like other bicarbonate transporters, a region in the C-terminus of NBCn1 (D1135-D1136) bound CAII, and this interaction was essential for maximal HCO₃⁻ transport [21]. CA activity was also necessary for maximal transport, as CA inhibition decreased NBCn1 activity [21]. Further, 8-bromoadenosine, a PKA activator, also decreases NBCn1 activity in a phosphorylation independent manner [21].

1.2.4.5 SLC26/CA Interactions

Amino acid sequence alignment reveals that the C-terminal tails of all known bicarbonate transport proteins (Fig. 1.1) except for SLC26A3 and SLC26A7, contain at least one CAII-binding motif consisting of a hydrophobic residue followed by a cluster of acidic residues [55]. A GST fusion protein consisting of the 42 C-terminal amino acids of SLC26A3 was able to bind immobilized CAII with a much lower affinity and capacity than AE1 [55]. SLC26A3-mediated $\text{Cl}^-/\text{HCO}_3^-$ exchange activity was not altered by over-expression of CAII-V143Y, but was decreased by inhibition of endogenous CAII with acetazolamide, suggesting that global CAII activity is required to enhance $\text{Cl}^-/\text{HCO}_3^-$ exchange activity [55]. SLC26A7 has been proposed to contribute to HCl secretion in the parietal cell along with AE2 and CAIX [32]. In HEK293 cells, SLC26A7 $\text{Cl}^-/\text{HCO}_3^-$ exchange activity was unchanged by either CAIX or CAII-V143Y expression [15]. Treatment of cells with acetazolamide, however, decreased SLC26A7 $\text{Cl}^-/\text{HCO}_3^-$ exchange activity [15]. Together these data suggest that while global CA activity is necessary for maximal SCL26A3- and SCL26A7-mediated $\text{Cl}^-/\text{HCO}_3^-$ exchange activity, CAII binding is not required.

Possible interactions between SLC26A6 and CA were investigated, as other SLC26 anion exchangers interact functionally, but not physically with CAII and/or CAIV [15, 55]. Glutathione S-transferase (GST) fusion proteins corresponding to various regions of the C-terminal cytoplasmic domain of SLC26A6 revealed that SLC26A6 D546-F549 region bound CAII [22]. The physiological significance of this binding was tested in HEK293 cells

endogenously expressing CAII; $\text{Cl}^-/\text{HCO}_3^-$ exchange activity assays were conducted in the absence or presence of acetazolamide [22]. As with other anion exchange proteins, CAII inhibition decreased exchange activity by approximately 50%, thus indicating that functional CAII is required for full SLC26A6 transport activity [22]. Over-expression of CAII-V143Y also decreased transport rates, consistent with a required physical interaction between SLC26A6 and CAII. Further to this, mutating the SLC26A6 CAII binding site decreased anion transport activity, but not cell surface processing efficiency [22]. Together, these data indicate that SLC26A6 interacts physically and functionally with CAII.

1.2.4.6 Bicarbonate Transport Metabolon Controversies

Some controversy surrounds the bicarbonate transport metabolon [56]. Lu *et al.* were unable to show a difference in NBC current (I_{NBC}) in NBCe1 expressing *Xenopus* oocytes co-injected with either CAII protein or Tris buffer [57]. Nor have they been able to see a difference in I_{NBC} when NBC was fused to the N-terminus of CAII. Thus, they conclude that CAII does not enhance the current carried by NBC, but instead only accelerates the intracellular hydration of CO_2 [57]. Note that in renal proximal tubule cells the $\text{HCO}_3^-:\text{Na}^+$ stoichiometry is 3:1, while in oocytes, the stoichiometry is 2:1 [57], which is significant in the context of the work of Gross *et al.*, discussed above. Furthermore, in other cells types when unphosphorylated NBCe1 works with a 3:1 $\text{HCO}_3^-:\text{Na}^+$ stoichiometry its transport is decreased with acetazolamide treatment. When phosphorylated, NBCe1 works with a 2:1 $\text{HCO}_3^-:\text{Na}^+$ stoichiometry, and is not sensitive to acetazolamide treatment. CAII may then only interact physically and functionally

with NBCe1, when functioning with the 3:1 stoichiometry; the lack of CAII-enhanced activity of NBCe1 in these experiments with *Xenopus* oocytes may be due to the transporter operating with a 2:1 stoichiometry. Becker *et al.*, however, showed that injection or co-expression of CAII did not change the reversal potential in NBCe1 expressing oocytes, suggesting that NBCe1 in oocytes still operates in the 2:1 mode when interacting with CAII [19].

The physical interaction between three SLC4 members (AE1, NBCe1, and NDCBE) and CAII was further investigated using an ELISA (enzyme-linked immunosorbent) assay [58]. GST-SLC4-Ct fusion proteins and pure SLC4-Ct peptides (similar constructs with GST cleaved off) were used. Consistent with previous results, the GST-SLC4-Ct fusion proteins bound immobilized CAII better than GST alone, but no binding between CAII and the pure SLC4-Ct peptides was observed. When the orientation was reversed, and SLC4-Ct pure peptides, GST or GST-fusion proteins were immobilized, CAII bound GST to a greater extent than the fusion proteins [58]. In addition, surface plasmon resonance (SPR) was also unable to detect an interaction between CAII and the SLC4-Ct peptides [58]. The SPR experiment is, however, potentially confounded by the way that CAII was immobilized to the SPR chip. CAII was coupled using amine-directed chemistry, which would have linked CAII to the SPR chip via both the primary amine at the CAII N-terminus, and at lysines 9 and 24. All three of the amines reside in the N-terminal region required for AE1 binding, thus presenting significant steric constraint to AE1 binding. The authors conclude that a bicarbonate transport metabolon may exist, but that CAII may not bind directly

to the bicarbonate transporters [58]. These results disagree with the findings of other groups [8-10, 12].

Recently, the interaction between NBCe1 and CAII was further investigated by expressing NBCe1 in *Xenopus* oocytes, with and without injected or co-expressed CAII [19]. Two CAII mutants were used, CAII-V143Y, and an N-terminal mutant with 6 exchanged amino acids in the N-terminal tail (CAII-HEX), which prevents binding to AE1. Co-transport activity of NBCe1 was determined by simultaneously measuring the membrane current, $[Na^+]_i$ and $[H^+]_i$ (calculated from pH) of voltage-clamped oocytes during a switch from HEPES-buffer to CO_2/HCO_3^- buffer [19]. Membrane conductance was also determined. CAII (either injected or co-expressed) increased membrane current, membrane conductance and the rate of cytosolic $[Na^+]$ and $[H^+]$ change in NBCe1 expressing oocytes following a switch to CO_2/HCO_3^- buffer to a greater extent than NBCe1 alone. Incubation with CA inhibitor 6-ethoxy-2-benzothiazolesulfonamide abolished these increases. Co-expression with CAII-V143Y also abolished these increases, suggesting that a physical interaction is necessary. CAII-HEX expressing oocytes showed similar responses to CAII-WT injected, suggesting that this mutant can still interact with NBCe1.

These results differ from the Lu *et al.*, report which analyzed membrane current only in terms of its slope conductance which was not changed by injection of CAII [57]. There were several differences between the Becker and Lu studies related to amount of CAII injected, the amplitude of slope conductance, and the level of NBC expression [19]. Becker *et al.* were able to detect an additional

current of 2.2 μS in CAII/NBCe1 expressing oocytes, which could have been missed in the Lu *et al.* study due to their higher slope conductance and lack of multiple approaches to measuring current [19]. In summary, the results of Becker *et al.* demonstrate that CAII enhances the activity of NBCe1 and supports the conclusion that NBCe1 forms a bicarbonate transport metabolon with CAII [18-20].

1.2.4.7 Bicarbonate Transport Metabolon Summary

Intracellular and extracellular carbonic anhydrases interact physically and/or functionally with many bicarbonate transport proteins (Table 1.1). Cytosolic CAII is able to physically interact with AE1, AE2, AE3, NBCe1, NBCn1, and SLC26A6, but not SLC26A3 or SLC26A7. Extracellular GPI-linked CAIV physically interacts with AE1, AE2, AE3, and NBCe1. Extracellular CAIX interacts with AE1, AE2, AE3, but not SLC26A7. CAXIV interacts with AE3. The physical interaction of all of the above CAII/bicarbonate transporter pairs is able to enhance bicarbonate transport activity. Global CAII activity is also required to maximize SLC26A3 and SLC26A7 activity.

A metabolon is a physical complex of enzymes in a linked metabolic pathway that functions to maximize flux of substrate through the pathway. There is extensive evidence supporting a bicarbonate transport metabolon (Fig. 1.3). This metabolon would maximize HCO_3^- flux through the bicarbonate transporter by maximizing the transmembrane HCO_3^- gradient local to the bicarbonate transporter. In HCO_3^- efflux mode, this would be accomplished by bringing cytosolic CAII within close proximity to the membrane, where CAII would be

ideally located to hydrate incoming CO_2 and supply the transporter with HCO_3^- for transport [8]. CAII would ensure that there is a continued pool of substrate available for transport. For example, AE1 has a high turnover rate of $5 \times 10^4 \text{ s}^{-1}$ and could rapidly deplete substrate without CAII, which has an even greater turnover rate of 10^6 s^{-1} [9]. Extracellular membrane-linked CAs (CAIV, CAIX) will rapidly deplete extruded HCO_3^- by conversion to CO_2 , thus maximizing the transmembrane HCO_3^- flux, and maximizing transport [13]. In HCO_3^- influx mode (such as during our experiments), extracellular membrane-linked CAs provide HCO_3^- for transport, while intracellular CAII catalyzes the conversion of H_2CO_3 to CO_2 and H_2O , where CO_2 can act as a rapidly diffusible H^+ equivalent.

In conclusion, the interaction of bicarbonate transporters with intracellular and extracellular carbonic anhydrases is a universal component of bicarbonate transport physiology, and that such interactions with linked metabolic enzymes suggests a general mechanism to modulate membrane transport activity that extends beyond bicarbonate transporters [17].

1.2.5 Other Acid/Base Transporter Carbonic Anhydrase

Metabolons

1.2.5.1 Na^+/H^+ exchanger and CAII

Na^+/H^+ exchangers (NHEs) mediate the electroneutral exchange of one intracellular proton for one extracellular sodium ion, thereby playing essential roles in the regulation of intracellular pH, cell volume and sodium flux [59].

NHEs are also involved in cytoskeletal organization, heart disease (ischemia and reperfusion injury, and cardiac hypertrophy) and cancer [60, 61]. Among the nine isoforms of mammalian NHEs, the ubiquitously expressed NHE1 is the most thoroughly characterized. NHE1 is composed of an N-terminal membrane domain that mediates Na^+/H^+ exchange, and a large C-terminal cytoplasmic domain that regulates the exchange activity and mediates cytoskeletal interactions [59, 60]. NHE1 is activated by angiotensin, endothelin and α_1 -adrenergic stimulation, all of which increase phosphorylation of the C-terminal domain by protein kinases [59].

Since carbonic anhydrases catalyze proton production and consumption, it is reasonable to hypothesize that an association between NHEs and CAs could facilitate proton removal [62]. Indeed, early studies demonstrated that the CA inhibitor, acetazolamide, caused a decrease in NHE activity [63]. NHE1 and CAII were also found to co-localize in oligodendrocytes [64]. A solid phase binding assay revealed that there was a physical interaction between the C-terminus of NHE1 (tagged with an N-terminal GST, or a C-terminal polyhistidine tag) and CAII, and that this interaction was increased in acidic medium, presumably by increasing electrostatic interactions [62]. This interaction is specific, since an antibody against the C-terminal 178 amino acids of NHE1 blocked the association. Results were confirmed using an affinity blotting technique and immunoprecipitation of lysates from stably-transfected cells. The physiological relevance of the NHE1/CAII interaction was examined by measuring pH_i recovery after acid load in AP1 cells (which contain endogenous

CAII) overexpressing NHE1, or NHE1 and CAII [62]. CAII overexpression increased NHE1 activity, and this effect was abolished by treatment with acetazolamide [62]. Co-transfection of NHE1 with the dominant negative CAII-V143Y decreased NHE1 activity. These results show that there is a physical interaction between NHE1 and CAII, and that this interaction is required for maximal Na^+/H^+ exchange.

Gel overlay assays, GST pull-down assays and solid phase binding assays using fusion proteins of C-terminal regions of NHE1, established that CAII binds the penultimate 13 amino acids on the cytoplasmic tail of NHE1 (⁷⁹⁰RIQRCLSDPGPHP⁸⁰²) [61]. Interestingly, the R790-P802 region does not contain the acidic stretch of amino acids (⁷⁵³EEDEDDD⁷⁵⁹) that were predicted to bind CAII based on their similarity to the acidic stretch of amino acids in AE1, and mutation of E753-D759 to neutral residues had no effect on CAII binding. Of the penultimate 13 amino acids, S796 and D797 are essential for CAII binding [61]. Phosphorylation of the last 26 amino acids of NHE1 did not affect CAII binding, although, as reported previously, phosphorylation of a larger portion of the C-terminal tail increased CAII binding [61, 62]. These results indicate that although S796 can be phosphorylated, phosphorylation at a more proximal site is responsible for increased CAII binding. There may be a region in the C-terminus of NHE1 that is involved in the reduction of CAII binding by blocking the CAII binding site, and phosphorylation of NHE1 appears to prevent this blockage [61]. NHE1 and CAII physically and functionally interact to form a transport metabolon, and this metabolon is regulated by phosphorylation of NHE1.

1.2.5.2 Monocarboxylate Transporter 1 (MCT1) and CAII

Monocarboxylate transporters (MCTs) transport lactate or pyruvate in an electroneutral 1 H⁺: 1 organic anion transport mode [65]. The 14 MCT isoforms in the SLC16 gene family are expressed in most tissues, with special importance in metabolically active tissues, like muscle and brain [65]. In the brain, MCT1 and MCT2 work in concert to shuttle lactate from glial cells to neurons; MCT1 facilitates the export of lactate, which is then taken up by MCT2 [66]. In skeletal muscle, MCT1, found in oxidative slow twitch fibers, mediates the import of lactate that is released from glycolytic fast twitch muscle cells via MCT3 and MCT4 [65, 67].

MCT1, when expressed in *Xenopus laevis* oocytes, mediates the import of lactate and H⁺ in both HEPES and CO₂/HCO₃⁻ buffer, and co-transport (measured by changes in pH_i upon application of lactate) is enhanced by the injection of CAII protein [66]. The increase in H⁺ flux, however, was insensitive to the CA inhibitor, ethoxzolamide, which suggests that the enzymatic activity of CAII is not required to enhance the transport activity of MCT. Further, co-expression with the catalytically inactive CAII-V143Y also caused an increase in transport activity [65]. Both the MCT1 protein and the MCT1-Δ56 C-terminal mutant (lacking the C-terminal 56 amino acids) bind immobilized CAII in pull-down assays [66]. This suggests that the C-terminal 56 amino acids of MCT1 (which include two acidic amino acid clusters: 456-458 and 489-491) are not involved in binding CAII, contrary to the CABs in bicarbonate transport proteins. The C-

terminus is, however, necessary for the enhanced transport in the presence of CAII, as no increase in transport is seen with the C-terminal mutant [66].

In another set of experiments, co-expression of MCT1 with CAII-HEX (an N-terminal CAII mutant unable to bind AE1) or injection of CAI (also unable to bind AE1) into MCT1-expressing oocytes, had no effect on MCT1 H⁺/lactate co-transport activity [65]. This demonstrates that increased amounts of CA catalytic activity are not sufficient to increase MCT1 activity, and suggests that the interaction between MCT1 and CAII is mediated by the same motif found with AE1 [65].

Together, these results suggest that CAII may accelerate the removal of protons from MCT1 at the inner face of the plasma membrane, to prevent H⁺ accumulation, which would dissipate the transmembrane H⁺ gradient local to MCT1, and slow H⁺/lactate co-transport (Fig. 1.4) [65]. Active CA is not necessary, as catalytically inactive CAII-V143Y was able to enhance MCT-mediated transport [65], although physical binding is required [65, 66]. Immunofluorescence reveals that CAII accumulates at the inner face of the plasma membrane, perhaps due to an accumulation of negative charges imparted by anionic phospholipids in the inner leaflet, and by physically interacting with acid/base transporters [65, 68]. Histidine residues on the surface of CAII could form dissociable sites for H⁺ binding. An interaction between CAII and the transporter would therefore form the initial component of a network of CAII molecules moving outward from the transporter (Fig. 1.4).

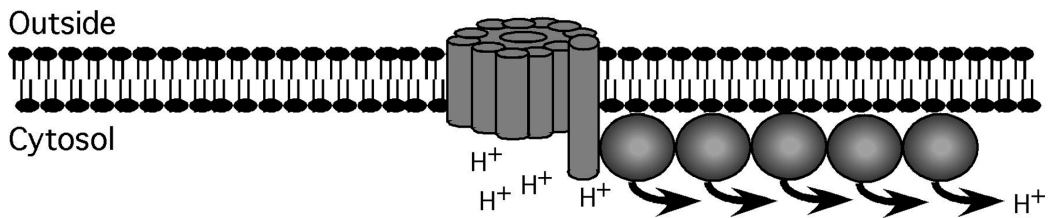


Figure 1.4. **Noncatalytic role of membrane-associated CAII.** CAII (gray filled ovals) associates with both the cytosolic surface of the plasma membrane, via electrostatic interaction with negative phospholipid head groups, and with the cytoplasmic regions of plasma membrane transporters. Histidine residues on the surface of CAII form ionizable groups to form an exchangeable H⁺ binding network. CAII thus facilitates the movement of H⁺ away from the transporter to prevent localized H⁺ accumulation that could slow down transmembrane substrate flux (as proposed from work on MCT1) [65].

The fate of H^+ imported by MCT1 was studied using the pH sensitive dye BCECF-AM to monitor the distribution of H^+ along the inner face of the oocyte membrane upon focal application of lactate to MCT1-expressing oocytes in the presence or absence of injected CAII [65]. In CAII-injected oocytes, the rate of rise of $[H^+]$ decayed to 50% at a distance of 323 μm away from the area of lactate application, while in H_2O -injected oocytes the rate decayed to 50% at 108 μm [65]. This supports the hypothesis that CAII is involved in removing H^+ from the inner face of MCT1 to prevent formation of a H^+ microdomain (discussed further in sections 1.3.5 and 1.3.6).

1.2.5.3 N-type sodium-dependent neutral amino acid transporter isoform 3 (SNAT3) and CAII

Transport of glutamine (non-neuroexcitatory amino acid) is essential to the glutamate-glutamine cycle in the brain, which is important for replenishing neuronal glutamate (neurotransmitter) stores [69]. SNAT3 catalyzes the electroneutral co-transport of 1 Na^+ and glutamine in exchange for 1 H^+ [70]. Glutamine transport is accompanied by substrate-induced uncoupled cation currents [70]. CAII-WT had no effect on SNAT3 glutamine transport in either HEPES or CO_2/HCO_3^- buffer, but CAII-WT and CAII-HEX (non-CAB-binding mutant) suppressed SNAT3-associated cation conductance in the presence of CO_2/HCO_3^- buffer [70]. The catalytic activity of CAII was required to suppress membrane conductance associated with SNAT3, as CAII-V143Y did not affect membrane conductance, and ethoxzolamide restored membrane conductance in the presence of CAII-WT [70]. CAII binding did not appear to be necessary,

since CAII-HEX suppressed cation conductance, and no CAII binding motifs were found in SNAT3 [70]. If there is a direct interaction between SNAT3 and CAII it does not occur through the canonical CAB motif. In conclusion, the catalytic activity of CAII affects SNAT3-associated cation conductance, and demonstrates yet another example wherein CAII activity is important for acid/base membrane transport.

1.2.6 Acid/Base Transporters in Cell Volume Regulation

As mentioned, acid/base transporters, such as AEs and NHEs, contribute to cell volume regulation as well as pH regulation [71]. Cell volume is perturbed by changes in intracellular changes in osmolarity caused by transepithelial transport and accumulation of nutrients and metabolic waste products [71]. In turn, volume changes regulate some physiological processes, including cell migration, programmed cell death, and cell proliferation [71].

After acute swelling or shrinking, cell volume is corrected by regulatory volume decrease (RVD) or regulatory volume increase (RVI), respectively [71]. Both mechanisms involve net movement of salt (KCl and NaCl) and H₂O (whose permeability is mediated by AQP expression). RVD involves the activation of swelling activated Cl⁻ and K⁺ channels, K⁺-Cl⁻ co-transporters (KCCs), and AEs. RVI is mediated by AEs, NHEs, Na⁺-K⁺-2Cl⁻ (NKCC) co-transporters, and Na⁺ channels, all of which are activated by cell shrinking. In RVI, the coordinated

activation of a $\text{Cl}^-/\text{HCO}_3^-$ exchanger and a Na^+/H^+ exchanger load cells with NaCl without a change in pH [1, 72].

1.3 Physiological Roles of pH

We have discussed the role of HCO_3^- transport, and acid/base transporter metabolons in great detail, but have not looked at the influence that pH-regulatory transporters (like AE1) may have on their immediate environment and pH-sensitive neighbouring proteins at the plasma membrane (e.g. ion channels and signaling proteins). The introduction continues with a discussion about the physiological roles of pH.

1.3.1 General pH Discussion

Virtually all proteins are pH-sensitive [73]. pH affects protein structure and function [73], and regulates receptor/ligand interactions [74]. pH alters the ionization state of amino acid side chains and phosphate groups, thereby affecting electrostatic interactions and conformational changes. Further, pH changes can alter the interaction of cationic signaling molecules (such as K-ras) or amphipathic proteins (such as Src kinase or phospholipase C) with anionic phospholipids in the plasma membrane, thereby affecting signaling [75]. Further, the fundamental energy transduction machinery of cells runs mainly on H^+ gradients and H^+ -coupled electron transfer reactions [76]. As such, pH regulates many cellular processes including signaling, trafficking, proliferation, apoptosis,

motility and migration [77-80]. Intracellular pH is thus very tightly regulated [73].

Cytosolic pH is generally more acidic than extracellular pH [73]. The membrane potential (-40 to -90 mV) across the plasma membrane (negative inside) drives the import of positively charged H^+ and the efflux of negatively charged bases such as HCO_3^- , and net acid equivalents are generated by metabolic reactions such glycolysis and oxidative phosphorylation [73]. As a result, cells must continuously extrude acid, or import base. While H^+ are extruded by various H^+ -ATPases, the main pH-regulatory transporters in mammalian cells are AEs, NBCs, NHEs, MCTs and Cl^-/OH^- exchangers (CHEs) [73]. The simultaneous operation of alkalinizing and acidifying pathways leads to precise control of pH. These proteins also contribute to volume regulation [71], which has been discussed in section 1.2.6.

Eukaryotic cells are compartmentalized, allowing for specific cellular functions to be localized within membrane-bound organelles [73]. While nuclear and peroxisomal pH appear to be similar to cytosolic pH, the pH within many other organelles differs substantially. The pH of the secretory pathway acidifies from the near-neutral endoplasmic reticulum to secretory granules with pH values of ~5.2 [81]. The luminal acidic pH is generated by the activity of vacuolar H^+ -ATPases (V-ATPases), multi-subunit transmembrane proteins that use the energy stored in ATP to import H^+ . The degree of organellar luminal acidification is regulated by variation in V-ATPase density and transport rate [73]. Parallel extrusion of cations (K^+) or influx of anions (Cl^-) is required to maintain constant

H⁺ influx, as buildup of intracellular positive charge would minimize H⁺ movement [82]. The progressive acidification of the endocytic pathway is regulated in a similar manner [73]. Na⁺/H⁺ exchangers are also involved in endosome acidification [83]. Conversely, mitochondrial pH is alkaline (pH ~8) due to H⁺ extrusion across the inner membrane [84].

1.3.2 Intracellular Buffering, H⁺ Diffusion Rates and Intracellular Buffer Shuttles

Cells are protected from acute changes in pH by intracellular buffers [73]. Total intracellular buffering (β_{total}) is comprised of intrinsic and extrinsic components. Intrinsic buffering ($\beta_{\text{intrinsic}}$) is provided by non-carbonic intracellular solutes and proteins, including amino acid side chains, phosphate groups, and weak intracellular acids and bases [73]. $\beta_{\text{intrinsic}}$ is relatively low at physiological pH [73]. CO₂-dependent buffer capacity (β_{CO_2}) arises from carbonic buffer governed by the equation $\text{CO}_2 + \text{H}_2\text{O} \rightleftharpoons \text{H}_2\text{CO}_3 \rightleftharpoons \text{HCO}_3^- + \text{H}^+$. $\beta_{\text{total}} = \beta_{\text{intrinsic}} + \beta_{\text{CO}_2}$, so β_{total} is increased by CO₂/HCO₃⁻ [85]. The values of $\beta_{\text{intrinsic}}$ and β_{CO_2} vary differently as pH varies [85], with $\beta_{\text{intrinsic}}$ increasing and β_{CO_2} decreasing with decreasing pH_i (Fig. 1.5) [85, 86]. Increased $\beta_{\text{intrinsic}}$ at acidic pH helps to protect against acute acid load, such as that seen during metabolic acidosis or ischemia [85].

As a result of high intracellular buffering capacity, H⁺ diffusion through the cytosol is two orders of magnitude slower than in water [86]. Rather than

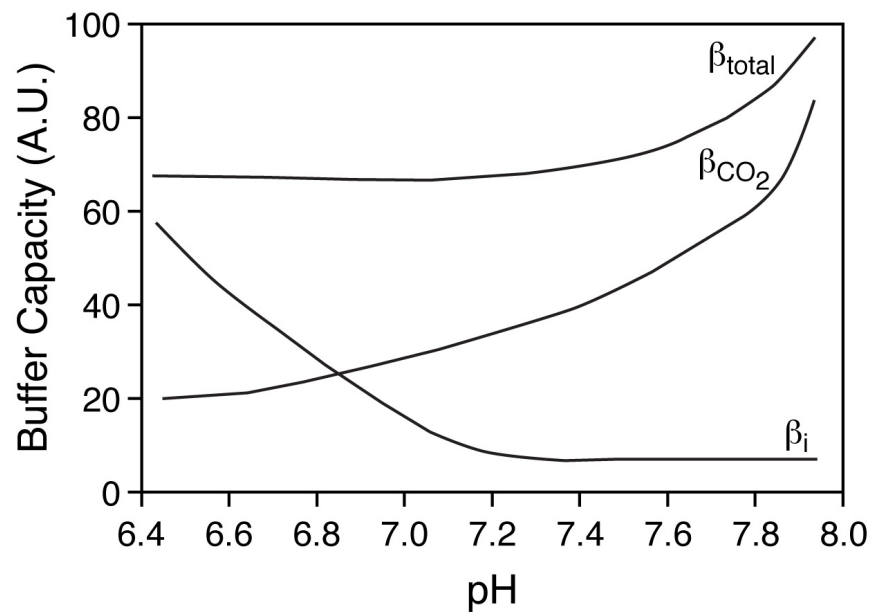


Figure 1.5. **Effect of pH on buffer capacity.** The effect of pH on intrinsic buffer capacity (β_i), CO_2 dependent buffer capacity (β_{CO_2}) and total buffer capacity (β_{total}) are depicted, based on [85, 87-90].

being able to diffuse freely, H^+ ions reversibly bind intracellular fixed or mobile buffers (such as CO_2/HCO_3^-), which hinder or promote H^+ diffusion, respectively [91-94]. Most cytosolic H^+ movement likely occurs via diffusive shuttling on intracellular buffers [94].

An intracellular buffer shuttle, composed of both intrinsic and extrinsic components, facilitates H^+ diffusion across the cytosol. In the intrinsic buffer shuttle system, H^+ bind buffer molecules (mainly low molecular weight proteins and histidine-containing dipeptides) and H^+ movement occurs via the diffusion of the protonated mobile buffers [95]. The H^+ will be unloaded once the mobile buffer reaches a more alkaline downstream region, and the buffer will be recycled. Fixed mobile buffers, such as large molecular weight proteins or subcellular organelles, are also a component of the intrinsic buffer shuttle, and restrict H^+ mobility [91]. Acid may still be shuttled longitudinally, however, by H^+ hopping along tracks of adjacent protonatable sites [86]. In the carbonic buffer shuttle, H^+ are buffered by HCO_3^- to form CO_2 , which diffuses along the length of a cell until it is re-hydrated to once again generate a H^+ . CO_2 acts as a rapidly diffusible H^+ -equivalent, and diffuses without binding to immobilized charged macromolecules [73]. Provided carbonic anhydrase is present, H^+ mobility is increased up to six-fold by the carbonic buffer shuttle [93]. Interestingly, H^+ mobility is greatly reduced during intracellular acidosis, whether in the presence or absence of carbonic buffer, due to increased intrinsic buffering capacity at acidic pH [96].

1.3.3 H⁺ as an Intracellular Signal

As a result of the high pH-sensitivity of proteins, it has been proposed that H⁺ have a role in intracellular signaling [73]. Specifically, localized changes in pH could initiate signaling due to the close proximity of pH-sensitive proteins to pH-regulatory proteins. For example, Ca⁺⁺-sensitive adenylyl cyclase activity is influenced by pH changes driven by NHE1 activity, both of which localize to lipid rafts and caveolae [97], and adenylyl cyclase generates cAMP, a classical intracellular second messenger [98]. NHE1 activity is also associated with recruitment of various signaling molecules to lipid rafts, which could lead to localized signaling [99].

AE1 may also be involved in H⁺ signaling, as both eAE1 and kAE1 form macromolecular complexes with the cytoskeleton and surrounding proteins. The N-terminus of eAE1 binds the spectrin-actin cytoskeleton via its association with ankyrin and protein 4.1 (adaptor proteins) [100]. Protein 4.1 also binds glycophorin A (GPA), which increases the maturation of AE1 to the cell surface and Cl⁻/HCO₃⁻ exchange rate in *Xenopus* oocytes [101], and rescues surface expression and activity of AE1 mutants defective in anion transport [102]. Further, ankyrin binds many other ion channels and transporters, including Na⁺K⁺-ATPase [100, 103]. Besides binding cytoskeletal elements, the N-terminus of eAE1 binds glycolytic enzymes, including the exquisitely pH-sensitive phosphofructokinase (PFK) [104]. Thus, cytoskeletal scaffolds could function to localize pH-sensitive proteins nearby to pH-regulatory proteins, thereby facilitating efficient and localized signaling.

eAE1 also forms an O₂/CO₂ gas exchange metabolon through association with the Rh protein complex, thus forming a macrocomplex where the individual components have linked functional and regulatory roles [105]. In addition to the associations described above, the N-terminus of AE1 also binds deoxy-hemoglobin, hemichromes, glyceraldehyde-3-phosphate dehydrogenase, and aldolase, while the C-terminus binds CAII [105]. CD47 (an integrin-associated protein), LW (cell adhesion molecule), GPA (which also binds AE1) and GPB all bind Rh proteins, which in turn directly binds AE1. Protein 4.2 binds ankyrin, AE1, and CD47, thereby providing another link between the Rh complex and the AE1 complex. The AE1/CAII metabolon at the surface of the red blood cell converts CO₂ to HCO₃⁻, which is exchanged for Cl⁻. The resulting H⁺ causes O₂ to be released from hemoglobin (Bohr effect). Rh proteins may function as non-specific CO₂/O₂ channels, which can function to channel CO₂ to and from AE1, and O₂ to and from hemoglobin. Thus, membrane localization and channeling provide efficient paths for O₂, CO₂, H⁺ and HCO₃⁻ exchange.

kAE1 binds integrin-linked kinase (ILK), which in turn binds paxillin and actopaxin (adaptor proteins), linking kAE1 to the cytoskeleton [25]. ILK increases the kAE1-mediated Cl⁻/HCO₃⁻ exchange rate by increasing the cell surface localization and basolateral targeting of kAE1, through mediating cytoskeleton interactions [25]. A kAE1/ILK complex has also been shown to bind nephrin in podocytes, and is suggested to have a unique role in the maintenance of the glomerular filtration barrier [106]. The intracellular domain of nephrin interacts with several podocyte and adaptor proteins to link the slit

diaphragm complex to the cytoskeleton, resulting in signal transduction. kAE1 may establish H^+ microdomains in the podocyte to modulate protein activity or signaling [106]. For example, pH-sensitive TRPC (transient receptor potential superfamily of non-selective cation channels) family members co-localize with nephrin in the podocyte [107], where kAE1 activity may alter TRPC activity [106]. H^+ microdomain formation will be discussed in section 1.3.5.

Thus, the association of AE1 with the cytoskeleton may be important for the formation of localized macromolecule signaling complexes [103, 108].

1.3.4 Solute Microdomains

Solute microdomains are discrete regions of altered cytosolic solute concentration that develop from the activity of ion channels or transporters. The diameter of these domains range in size from tens of nanometers (nanodomains) to hundreds of nanometers (microdomains) [109], although the terms are sometimes used interchangeably. Further, nanodomains are usually comprised of a single channel/transporter, while microdomains involve the assembly of multiple channels/transporters [110]. Due to rapid single channel opening, and decay of solute concentration over 100 nm distances, nanodomain formation leads to a more specific and rapid activation of nearby proteins [110].

Ca^{++} is an intracellular messenger that initiates a multitude of specific cellular responses including muscle contraction, exocytosis, gene transcription, and cell death [111]. Specificity of Ca^{++} signaling in space, time and amplitude is achieved by the formation of Ca^{++} microdomains, following opening of Ca^{++} -

release channels in the plasma membrane or intracellular organelles [112-114]. Formation of a Ca^{++} microdomain is enhanced by the high Ca^{++} buffering capacity of the cytosol leading to a slow diffusion rate, the existence of highly organized subcellular structures that both release and take up Ca^{++} and the clustering of Ca^{++} channels in the membrane [111]. Molecular crowding (the exclusion of solvent volume arising from the presence of a large number of solute particles) further slows Ca^{++} diffusion by creating steric, electrostatic and hydrophobic hindrances [115, 116]. The Ca^{++} concentration within a Ca^{++} microdomain can be several orders of magnitude greater than the bulk cytoplasmic $[\text{Ca}^{++}]$, leading to localized signaling responses [117]. Further, downstream signaling molecules (transcription factors and protein kinases), and integral membrane proteins (G-protein coupled receptors, IP_3 receptors, other Ca^{++} channels) localize near Ca^{++} channels to provide further specificity [111, 117]. Signals propagate from the source through diffusive movement of Ca^{++} in blips, puffs or sparks and waves [118-120]. A blip arises from the opening of a single Ca^{++} channel, while puffs and sparks originate from clusters of IP_3 receptors and ryanodine receptors, respectively [118-120]. Waves result from the summation of Ca^{++} puffs, and can spread rapidly throughout the cell. Interestingly, cytosolic Ca^{++} and H^+ diffusion rates are very similar [121], in part because both ions bind mobile and stationary intracellular protein buffers [118].

cAMP is another intracellular messenger, whose signaling specificity is derived from the formation of a solute microdomain. In cardiomyocytes, cAMP microdomains form as a result of the localization of transmembrane adenylyl

cyclases (tmACs, site of production of cAMP) within close proximity to anchored PKA molecules (cAMP target) and the physical separation from sarcoplasmic reticulum anchored phosphodiesterases (sites of cAMP degradation) [122-125]. cAMP microdomains may also develop in other cell types, such as at the basolateral membrane of proximal tubular cells where both transmembrane and soluble adenylyl cyclases (sAC) may function to form a complex signalling network [126].

1.3.5 H⁺ gradients and H⁺ microdomains

While Ca⁺⁺ and cAMP microdomains have been confirmed, whether or not H⁺ microdomains form has not been conclusively established. The objective of chapter 4 of this thesis is to determine if H⁺ microdomains form at the surface of AE1 during AE1-mediated Cl⁻/HCO₃⁻ exchange. Due to slow H⁺ diffusion, rapid flux of acid or base should cause a local accumulation or depletion of H⁺ [86]. Indeed, cytosolic H⁺ gradients as large as one pH unit, which persisted for minutes, were created in cardiomyocytes by local acid injection using cell-attached micropipettes [86, 93, 127], local microperfusion of extracellular membrane-permeant acids or bases [94], and flash photolysis-induced release of caged H⁺ [96]. Smaller H⁺ gradients were developed in cardiomyocytes by stimulation of sarcolemmal NHE activity [128]. Formation of a H⁺ gradient is dependent on the rate of H⁺ diffusion, which is in turn dependent on rate of H⁺ loading, buffer capacity and buffer mobility. Addition of CO₂/HCO₃⁻ (a mobile buffer) increases the rate of H⁺ diffusion, thus decreasing the formation of a

longitudinal H^+ gradient [93]. Inhibition of carbonic anhydrase largely suppressed carbonic anhydrase's influence on H^+ mobility. Interestingly, the ability of CO_2/HCO_3^- to diminish a H^+ gradient (by increasing H^+ diffusion) depends on the magnitude of the acid-equivalent flux [94]. Carbonic buffer enhances H^+ mobility to a greater extent during low rates of acid or base loading [94]. In situations with rapid acid-equivalent fluxes, the presence of carbonic buffer had virtually no effect on H^+ mobility [96]. This subject will be discussed in section 1.3.6, keeping in mind that AE1-mediated Cl^-/HCO_3^- exchange is rapid.

Cytosolic H^+ gradients have been found in cells other than cardiomyocytes. Longitudinal H^+ gradients in isolated mouse intestinal enterocytes result from the activity of apical proton-coupled dipeptide transporters [129]. Differential subcellular localization of Na^+/H^+ exchangers (NHEs), Na^+/HCO_3^- co-transporters and CAII in oligodendrocytes results in spatial non-uniformity of steady-state pH [64]. Extracellular H^+ microenvironments develop at the leading edge of tumor cells due to the up-regulation of pH-regulatory proteins, including AEs [130], NHEs [131], CAs [132], monocarboxylate transporters [133], and H^+ -ATPases [134]. A similar phenomenon is observed in microvascular endothelial cells [135].

1.3.6 Dual Roles of Carbonic Anhydrase in H⁺ microdomain formation

Two possible roles for carbonic anhydrase in the formation of a H⁺ microdomain have so far been discussed. Rapid transport rate is one prerequisite for microdomain formation, and CA activity is required for maximal AE1-mediated Cl⁻/HCO₃⁻ exchange [8-10, 12, 13, 33]. Conversely, CA increases H⁺ diffusion (by both catalytic and non-catalytic mechanisms), thereby contributing to dissipation of a H⁺ microdomain [65, 93].

As discussed in section 1.3.5, carbonic buffer/CA had virtually no effect on H⁺ mobility (and thus dissipation of a H⁺ microdomain) in situations with rapid acid-equivalent fluxes [94, 96]. Conversely, carbonic buffer enhances H⁺ mobility to a greater extent during low rates of acid or base loading [94]. For example, PepT1-generated H⁺ gradients were significantly attenuated by CA inhibition [129], and PepT1 has a very low turnover rate of 100 s⁻¹ [136]. Similarly, H⁺ diffusion away from MCT1 was enhanced by the presence of carbonic buffer/CA and MCT1 [65]; MCT1 has a turnover rate of only 12 s⁻¹ [137]. In comparison, AE1 has a rapid turnover rate of 5 x 10⁴ s⁻¹ [94], suggesting that CA may have a limited role in dissipating a H⁺ microdomain around AE1.

1.3.7 pH-Sensitive Proteins

pH elicits many cellular responses: it can modulate ion channel/transporter activity, affect protein-protein interactions, and is involved in the production of signaling molecules. For example, pH modulates aquaporin [138], connexin channel [139] and renal inwardly rectifying K^+ channel (Kir1.1) gating [140]. Gating of another K^+ channel, TASK-2, is regulated differentially by intracellular and extracellular pH [141]. Myocardial pH is regulated by four main pH-regulatory transporters, all of whose activities are sensitive to pH [85]. Decreased intracellular pH activates Na^+/H^+ exchange and Na^+/HCO_3^- co-transport [85, 142], while it inhibits Cl^-/HCO_3^- exchanger isoform 2 (AE2) and Cl^-/OH^- exchange activity [5, 85]. Activity of the Na^+/Ca^{++} exchanger is also extremely sensitive to pH [143], as is the activity of some carbonic anhydrase isoforms [96]. Phosphofructokinase activity increases 200-fold between pH 6.9 and 7.2, which enables pH to regulate metabolism effectively since PFK is rate limiting to glycolysis [144]. The binding affinity of many proteins for actin filaments is altered by changes in pH [145]. Endosomal V-ATPase subunits interact in an acidification-dependent manner with small GTPases involved in protein trafficking between early and late endosomes [74]. Ca^{++} binding to calmodulin is also pH-dependent [97]. HCO_3^- stimulates soluble adenylyl cyclase activity in a pH-dependent [146] and pH-independent [98] manner, leading to downstream signaling. Thus, it is evident that pH affects many diverse types of proteins, and pH regulation or dysregulation would affect many cellular processes.

1.3.8 Role of pH in Cell Migration

Cell migration is controlled by pH and volume changes, and is important for many cellular processes including immune defense, wound healing, angiogenesis, embryogenesis and formation of tumor metastases [130]. A change in cytosolic pH of 0.5 units or less affects the dynamic reorganization of the actin-based cytoskeleton, which is necessary for cell movement [77]. Steps in reorganization include 1) lamellipodia protrusion, 2) adhesion of leading edge to extracellular matrix and de-adhesion of cell body and rear, and 3) forward translocation [147].

Migrating cells are polarized, with lamellipodia at the front and cell body at the rear: Expression of membrane transport proteins is also polarized [130]. Na^+/H^+ exchanger isoform 1 (NHE1), $\text{Cl}^-/\text{HCO}_3^-$ exchanger isoform 2 (AE2) and aquaporin (AQP) isoforms 1,4 and 9 are localized to the leading edge of multiple migrating cell types including renal epithelium, endothelial cells, fibroblasts, MDCK cells and human leucocytes and neutrophils [130, 148, 149]. NHE1, AE2 and AQP1 together mediate lamellipodia protrusion via solute and water uptake, thus providing a force that extends the plasma membrane creating space for actin polymerization [130, 148, 149]. NHE1-mediated intracellular alkalinization is coincident with salt and water uptake, and activates cofilin, an actin-binding protein that promotes de-novo actin polymerization and recycling necessary for protrusion [148]. This remodeling in turn pushes the plasma membrane forward generating protrusion, and eventually whole cell movement. In contrast, a

decrease in pH_i stimulates gelsolin activity, which severs and caps actin filaments, thereby blocking their elongation [150].

Lamellipodia extension and leading edge cell swelling increases the surface tension of the plasma membrane, which activates Ca^{++} -permeable mechanosensitive cation channels resulting in a rise in intracellular Ca^{++} , with highest $[\text{Ca}^{++}]_i$ at the rear of the cell. Ca^{++} -sensitive K^+ channels in the rear of the cell are activated, resulting in K^+ efflux accompanied by rear shrinking, resulting in release of focal adhesion contacts and rear retraction. The $\text{Na}^+/\text{K}^+/\text{2Cl}^-$ co-transporter is localized to the trailing end of migrating cells, and is necessary to restore volume after K^+ channel-mediated cell shrinkage [130].

Formation and remodeling of focal adhesion contacts are pH-sensitive processes. Rear-retraction is rate-limiting in migrating cells: increased pH stimulates calpain (cysteine protease) activity which regulates de-adhesion by cleaving integrin-cytoskeleton linkages [108]. Further, focal adhesion protein talin (binds integrins and F-actin to tether adhesion complexes to cytoskeleton) may also be regulated by NHE1 activity [108]. NHE1 co-localizes with integrins at the leading edge of lamellipodia, and creates a H^+ rich environment in the immediate vicinity of integrins involved in focal adhesion complexes, thereby influencing the strength of cell adhesion and thus migration [149].

1.4 Nucleoside Transport

The objective of chapter 3 is to monitor pH changes at the cytosolic surface of hCNT3 during Na^+/H^+ /nucleoside co-transport. pH was monitored by

mNect (a pH-sensitive red fluorescent protein) fused to the N-terminus of hCNT3 (mNect.hCNT3) or an inactive hCNT3 mutant (mNect.hCNT3-F563C). mNect.hCNT3-F563C was also used as a spectator protein in the assessment of H⁺ microdomain formation (chapter 4). Information on nucleoside transport is thus provided as a background to both studies.

Nucleosides consist of a purine or pyrimidine nitrogenous base covalently bound to a ribose or 2-deoxyribose sugar [151]. Nucleosides can be phosphorylated by intracellular kinases to generate nucleotides, such as ATP, which are the building blocks of DNA and RNA. In addition to being nucleotide precursors, nucleosides have biochemical and physiological roles, including modulation of immune response, regulation of blood flow, platelet aggregation, renal function, neuromodulation and transmission, and muscle contraction [152]. Nucleosides can be produced by *de novo* synthesis pathways in the liver, or can be salvaged through ingestion and digestion of dietary nucleic acids.

Nucleosides are hydrophilic molecules that require nucleoside transport (NT) proteins to mediate their uptake into or release from cells [153]. NTs also transport anti-cancer and anti-viral drugs, and are thus vital to cancer therapy and the treatment of cardiovascular, parasitic and viral diseases [151, 154]. While NTs are found in both prokaryotic and eukaryotic organisms [155], only human (h) NTs will be discussed further. Most cells co-express several NTs, which mediate transport of nucleosides using either equilibrative (E) or concentrative (C) mechanisms [156]. ENTs mediate Na⁺-independent facilitated diffusion of nucleosides down their concentration gradient, while CNTs use either a Na⁺ or H⁺

gradient to accumulate nucleosides against their concentration gradient [157]. ENTs (primarily basolateral) and CNTs (primarily apical) work in tandem to facilitate transepithelial nucleoside flux to mediate absorption, distribution and elimination of nucleosides and nucleoside drugs [151, 158]. This process is especially important in the intestinal tract and renal tubule [159].

Equilibrative nucleoside transporters (ENTs) of the SLC29 family are expressed in most, if not all, cell types, and mediate low-affinity, bi-directional equilibrative nucleoside transport [158]. ENTs have a putative membrane topology consisting of 11 transmembrane domains (TMDs) with an intracellular N-terminus and extracellular C-terminus [155]. Additionally, ENTs contain two large loops: an extracellular loop with known glycosylation sites between TMD 1 and 2, and an intracellular loop between TMD 6 and 7. There are four hENT isoforms, hENT1-4, which are distinguished by their sensitivity to inhibitors. hENT1-3 are similar in their permeant selectivities and ubiquitous tissue distribution, while hENT4 is expressed only in heart, brain and liver, and only transports adenosine and organic cations. Interestingly, hENT2 can also transport nucleobases, and hENT3 and 4 are activated at low pH.

Concentrative nucleoside transporters (CNTs) of the SLC28 family divide into two phylogenetic subfamilies: hCNT1/2 belonging to one subfamily, and hCNT3 to the other [160-162]. hCNT1 and hCNT2 are 72% identical at the amino acid level, while hCNT3 exhibits only ~50% identity to hCNT1/2 [159]. All the CNTs have high substrate affinity (K_m values of 1-120 μM), with overlapping substrate selectivity [159]. All isoforms transport uridine: hCNT1

and hCNT2 are otherwise selective for pyrimidine and purine nucleosides, respectively, while hCNT3 is broadly selective for both [162]. All isoforms also display variable substrate selectivity with respect to nucleoside-analogues. CNTs have between 13 and 15 transmembrane segments [163, 164], with an intracellular N-terminus and extracellular glycosylated C-terminus (Fig. 1.6) [162]. Chimeric studies between hCNT1 and hCNT3 demonstrated that the C-terminal half of the protein is involved in determining nucleoside selectivity, and Na⁺- and H⁺-coupling [165].

hCNT cation:nucleoside stoichiometry can be determined by the simultaneous measurement of nucleoside-evoked transmembrane current and radiolabelled nucleoside uptake (charge to uptake coupling ratio) in the presence of different cations, using the *Xenopus laevis* oocyte expression system [160-162, 165-167]. hCNT1/2 couple nucleoside transport to the Na⁺ electrochemical gradient with a 1:1 stoichiometry, while hCNT3 can couple nucleoside transport to either the Na⁺ gradient (2 Na⁺: 1 nucleoside) or a H⁺ gradient (1 H⁺: 1 nucleoside) in the absence of Na⁺ [165, 166]. At acidic pH, hCNT3 also transports uridine in the presence of Na⁺ with a 2 cation: 1 nucleoside stoichiometry, suggesting that 1 H⁺ and 1 Na⁺ may be transported per nucleoside molecule in these conditions [165-168]. The 2:1 coupling ratio of hCNT3 allows it to develop a trans-membrane nucleoside concentration gradient up to 10-fold higher than that of hCNT1/2 [166, 168].

CNTs are expressed predominantly in intestinal and renal epithelia [151]. In the intestinal tract, hCNT1/2/3 are expressed in a proximal to distal gradient,

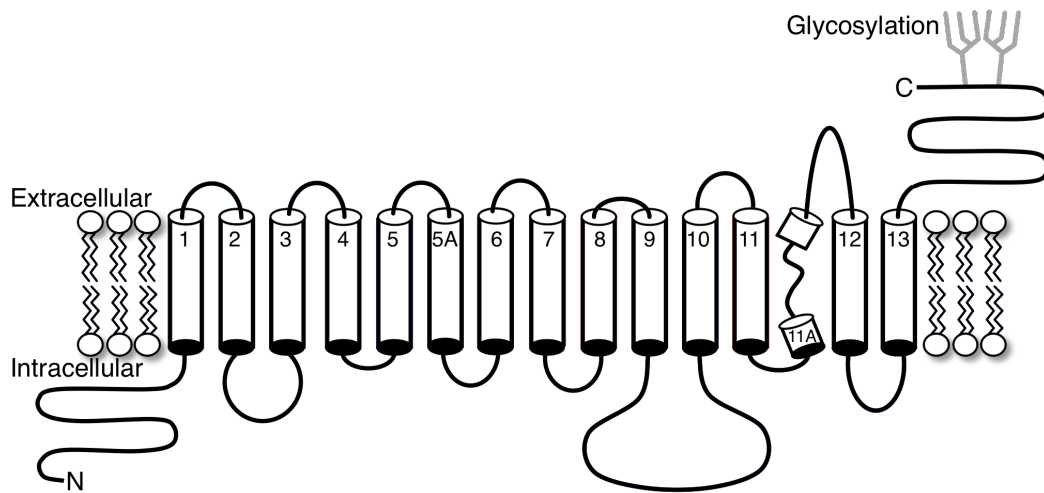


Figure 1.6. **hCNT3 topology model.** The amino (N) and carboxyl (C) termini of hCNT3 are marked. Numbers indicate transmembrane segments. The branched structures on the extracellular C-terminus represent the glycosylation sites of hCNT3.

with highest expression proximally [159, 169]. Renal expression is more complex. hCNT1-3 are expressed in the proximal tubule where they mediate nucleoside reabsorption. hCNT2/3 are expressed in the glomerulus and distal regions of the kidney, suggesting a secondary role in the regulation of renal function by modulating the abundance of tubular adenosine. H⁺-coupled nucleoside transport by hCNT3 may be physiologically and pharmacologically important in these tissues, as luminal contents can be acidic [166].

1.5 Fluorescent proteins

The objective of this thesis is to measure local changes in pH at the surface of membrane transport proteins as they undergo membrane transport. An ideal way to accomplish this task is to use fluorescent proteins, which have been engineered to report on intracellular environments, and can be easily fused to a protein of interest. The remainder of the introduction provides background information on fluorescent proteins, and their use as intracellular indicators.

The green fluorescent protein (GFP) from the jellyfish *Aequorea victoria* was discovered in 1962 [170], and has since become one of the most widely used scientific tools for studying biological processes in living organisms. GFP is an 11-stranded β -barrel with an α -helix containing the chromophore extending up into the centre of the cylinder where it is protected from bulk solvent (Fig. 1.7) [171]. The chromophore, which is responsible for GFP fluorescence, is formed from amino acids Ser65-Tyr66-Gly67 by a multistep mechanism of cyclization, dehydration and oxidation [171]. Many polar groups and structured water

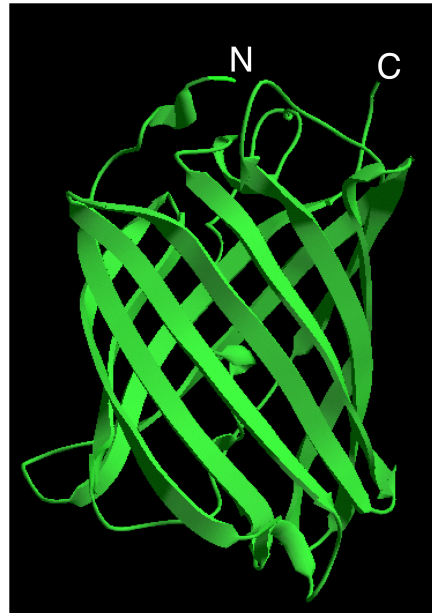


Figure 1.7. **Crystal structure of wild-type *Aequorea Victoria* green fluorescent protein.** (MMDB ID: 34112) [172]. Structure was rendered with Swiss-PdbViewer software. The amino (N) and carboxyl (C) termini of GFP are marked.

molecules are found adjacent to the chromophore, which are involved H⁺ transfer through a hydrogen bond network [171].

GFP variants are divided into multiple classes based on chromophore characteristics [171]. Variants of GFP have been generated by mutating amino acids involved in chromophore formation [173]. Altered excitation and emission wavelengths have resulted in yellow, cyan and blue FPs, with some gaining traits such as increased brightness and stability, and decreased anion sensitivity and photobleaching [171].

Longer-wavelength red fluorescent proteins (RFPs) are desirable for many cellular applications, as they provide greater tissue penetration and better spectral separation from autofluorescence [174]. First generation RFPs isolated from *Discosoma* coral (DsRed) were obligate tetramers, which is detrimental due to probable aggregation of fusion proteins [175]. Subsequent re-engineering using a combination of targeted and random mutagenesis led to the creation of first (monomeric RFP 1 (mRFP1)) [176] and second (mFruit series) [177] generation optimized RFPs, which are monomeric, but suffer from relatively low brightness relative to other common FPs. Third generation mRFPs (mApple and TagRFP-T) have improved fluorescent brightness values [178].

As mentioned, the rigid β -barrel structure of GFP shields the chromophore from environmental changes, but mutations to either the FP β -barrel or the chromophore itself render the fluorescence signal sensitive to external environmental signals by allowing solvent access to the chromophore. Further, disrupting the hydrogen bond network either by changing the distance between

important amino acid side chains or through ion interference has profound effects on excitation and emission spectra, and fluorescence environmental sensitivity. Thus, FPs can be adapted to report on a variety of environmental changes.

The degree to which FP fluorescence intensity is quenched (decreased) by environmental stimuli is quantified using the Stern-Volmer equation, which relates the relative change in fluorescence to the concentration of quencher [179]. The slope of the best-fit line is equal to the Stern-Volmer constant (K_{SV}), and the greater the constant, the greater the degree of quenching.

The excitation spectrum of native GFP is essentially unaltered between pH 5.5 and 10, but certain mutations show pH-sensitivity in the physiological range [173]. The fluorescence of the excitation ratiometric pHluorin, a pH-sensitive GFP mutant with a pK_a of 6.5, exhibits a spectral shift in addition to a change in intensity with changing pH [180-182]. Dual emission green fluorescent protein 4 (deGFP4) exhibits similar characteristics, with the difference that fluorescence is emission ratiometric, and deGFP4 has a pK_a of 7.3 [183]. Measurement of the ratio of fluorescence at two suitable chosen wavelengths, one pH-sensitive and one pH-insensitive (isobestic point), reports on pH independently of photobleaching, alteration of focal plane, absolute concentration of FP, thickness of the cell, brightness of excitation source, and absolute efficiency of detection [81, 171, 184].

Ca^{++} sensitive FPs (called camagros) were created by insertion of the Ca^{++} -binding protein calmodulin (CaM) in place of Tyr145 of yellow fluorescent protein (YFP) [174]. Camgaroo fluorescence increases seven-fold upon Ca^{++}

binding. [174]. Other Ca^{++} sensitive proteins were created through the generation of circularly permuted GFPs (cpGFP), in which the original amino and carboxyl termini are interchanged and reconnected by a short spacer, with new termini introduced near the chromophore [174]. Insertion of a cpGFP between CaM and a Ca^{++} -dependent CaM-binding protein (M13) results in Ca^{++} -sensitive indicators called pericams, which are more sensitive to $[\text{Ca}^{++}]$ than the camgaroos [185].

Fluorescence resonance energy transfer (FRET) occurs when two fluorophores are in close molecular proximity ($< 100 \text{ \AA}$) and the emission spectra of one fluorophore (donor) overlaps with the excitation spectra of the second fluorophore (acceptor) [171]. Any biochemical signal that changes the distance between the fluorophores will alter the efficiency of FRET. FRET efficiency is given by $R_0^6/(R_0^6 + r^6)$ where r is the actual distance between the centres of the chromophores and R_0 is the distance at which FRET is 50% efficient [171]. Currently, the best FRET pairs are cyan fluorescent protein (CFP) and YFP, although GFP-RFP pairs would be ideal [174]. FRET can be exploited to report on intracellular Ca^{++} concentrations. Cameleons, another class of Ca^{++} -indicators, consist of inserting a CaM-linker-M13 peptide between CFP and YFP [186]. Increased intracellular Ca^{++} switches on the affinity of CaM for M13, resulting in a change in orientation/distance between the two FPs and an increase in FRET. A similar strategy has also been employed to create reporters of tyrosine kinases [187, 188] and serine/threonine kinases [189]. A FRET-based voltage sensor was created by placing a truncated potassium channel amino terminal to both CFP and

YFP; voltage-dependent twists of the channel are proposed to rotate CFP with respect to YFP [190].

Other useful FP variants include a yellow FP, whose fluorescence is quenched by halide ions [191], a blue FP that has been engineered to bind and report on $[Zn^{++}]$ [192], and FPs that have been designed to sense redox potentials [174].

In summary, FPs have been engineered to report on pH, $[Ca^{++}]$, [halide], $[Zn^{++}]$, voltage, kinase activity, and redox potential. Further, FPs can be fused to proteins of interest to provide information on local intracellular environments.

1.6 Thesis Objectives

The objective of this thesis is to examine local intracellular pH changes during AE1-mediated Cl^-/HCO_3^- exchange or hCNT3-mediated Na^+/H^+ /nucleoside co-transport using pH-sensitive fluorescent proteins. Ultimately, we want to answer the question of whether a H^+ microdomain forms around AE1 as it exchanges Cl^- for HCO_3^- .

Chapter 2 details the experimental materials and methods used in this thesis. Chapter 3 describes the development of a new approach to directly monitor H^+ /uridine co-transport in HEK293 cells. We also report the development of a new pH sensitive monomeric red fluorescent protein, mNectarine (mNect). Using the H^+ -coupling characteristic of hCNT3, and the pH-sensitivity of mNect, we are able to provide insight into the mechanism of Na^+/H^+ /nucleoside co-transport. Chapter 4 extends upon the techniques

developed in chapter 3. pH at the surfaces of AE1 and hCNT3 was monitored simultaneously by deGFP4 and mNect. Validation of this technique required extensive control experiments, which are presented. Finally, we provide evidence that a H^+ microdomain forms around AE1 during Cl^-/HCO_3^- exchange.

Bibliography

1. Casey JR (2006) Why bicarbonate? *Biochem Cell Biol* **84**, 930-939.
2. Supuran CT (2008) Carbonic anhydrases: novel therapeutic applications for inhibitors and activators. *Nat Rev Drug Discov* **7**, 168-181.
3. Supuran CT (2008) Carbonic anhydrases-an overview. *Curr Pharm Des* **14**, 603-614.
4. McMurtrie HL, Cleary HJ, Alvarez BV, Loisel FB, Sterling D, Morgan PE, Johnson DE & Casey JR (2004) The bicarbonate transport metabolon. *J Enzyme Inhib Med Chem* **19**, 231-236.
5. Alper SL, Chernova MN & Stewart AK (2001) Regulation of Na⁺-independent Cl⁻/HCO₃⁻ exchangers by pH. *Jop* **2**, 171-175.
6. Sterling D & Casey JR (2002) Bicarbonate transport proteins. *Biochem Cell Biol* **80**, 483-497.
7. Low PS (1986) Structure and function of the cytoplasmic domain of band 3: center of erythrocyte membrane-peripheral protein interactions. *Biochim Biophys Acta* **864**, 145-167.
8. Vince JW & Reithmeier RA (2000) Identification of the carbonic anhydrase II binding site in the Cl⁻/HCO₃⁻ anion exchanger AE1. *Biochemistry* **39**, 5527-5533.
9. Sterling D, Reithmeier RA & Casey JR (2001) A transport metabolon. Functional interaction of carbonic anhydrase II and chloride/bicarbonate exchangers. *J Biol Chem* **276**, 47886-47894.
10. Vince JW & Reithmeier RA (1998) Carbonic anhydrase II binds to the carboxyl terminus of human band 3, the erythrocyte Cl⁻/HCO₃⁻ exchanger. *J Biol Chem* **273**, 28430-28437.
11. Kifor G, Toon MR, Janoshazi A & Solomon AK (1993) Interaction between red cell membrane band 3 and cytosolic carbonic anhydrase. *J Membr Biol* **134**, 169-179.
12. Vince JW, Carlsson U & Reithmeier RA (2000) Localization of the Cl⁻/HCO₃⁻ anion exchanger binding site to the amino-terminal region of carbonic anhydrase II. *Biochemistry* **39**, 13344-13349.
13. Sterling D, Alvarez BV & Casey JR (2002) The extracellular component of a transport metabolon. Extracellular loop 4 of the human AE1 Cl⁻/HCO₃⁻ exchanger binds carbonic anhydrase IV. *J Biol Chem* **277**, 25239-25246.

14. Waheed A, Zhu XL, Sly WS, Wetzel P & Gros G (1992) Rat skeletal muscle membrane associated carbonic anhydrase is 39-kDa, glycosylated, GPI-anchored CA IV. *Arch Biochem Biophys* **294**, 550-556.
15. Morgan PE, Pastorekova S, Stuart-Tilley AK, Alper SL & Casey JR (2007) Interactions of transmembrane carbonic anhydrase, CAIX, with bicarbonate transporters. *Am J Physiol Cell Physiol* **293**, C738-748.
16. Alvarez BV, Gilmour GS, Mema SC, Martin BT, Shull GE, Casey JR & Sauve Y (2007) Blindness caused by deficiency in AE3 chloride/bicarbonate exchanger. *PLoS ONE* **2**, e839.
17. Alvarez BV, Loisel FB, Supuran CT, Schwartz GJ & Casey JR (2003) Direct extracellular interaction between carbonic anhydrase IV and the human NBC1 sodium/bicarbonate co-transporter. *Biochemistry* **42**, 12321-12329.
18. Gross E, Pushkin A, Abuladze N, Fedotoff O & Kurtz I (2002) Regulation of the sodium bicarbonate cotransporter kNBC1 function: role of Asp(986), Asp(988) and kNBC1-carbonic anhydrase II binding. *J Physiol* **544**, 679-685.
19. Becker HM & Deitmer JW (2007) Carbonic anhydrase II increases the activity of the human electrogenic $\text{Na}^+/\text{HCO}_3^-$ cotransporter. *J Biol Chem* **282**, 13508-13521.
20. Pushkin A, Abuladze N, Gross E, Newman D, Tatishchev S, Lee I, Fedotoff O, Bondar G, Azimov R, Ngyuen M, et al. (2004) Molecular mechanism of kNBC1-carbonic anhydrase II interaction in proximal tubule cells. *J Physiol* **559**, 55-65.
21. Loisel FB, Morgan PE, Alvarez BV & Casey JR (2004) Regulation of the human NBC3 $\text{Na}^+/\text{HCO}_3^-$ cotransporter by carbonic anhydrase II and PKA. *Am J Physiol Cell Physiol* **286**, C1423-1433.
22. Alvarez BV, Vilas GL & Casey JR (2005) Metabolon disruption: a mechanism that regulates bicarbonate transport. *EMBO J* **24**, 2499-2511.
23. Fairbanks G, Steck TL & Wallach DFH (1971) Electrophoretic analysis of the major polypeptides of the human erythrocyte membrane. *Biochemistry* **10**, 2606-2617.
24. Cousin JL, Motais R & Sola F (1975) Transmembrane exchange of chloride with bicarbonate ion in mammalian red blood cells: evidence for a sulphamide-sensitive "carrier". *J Physiol* **253**, 385-399.
25. Keskanokwong T, Shandro HJ, Johnson DE, Kittanakom S, Vilas GL, Thorner P, Reithmeier RA, Akkarapatumwong V, Yenchitsomanus PT &

- Casey JR (2007) Interaction of integrin-linked kinase with the kidney chloride/bicarbonate exchanger, kAE1. *J Biol Chem* **282**, 23205-23218.
26. Dahl NK, Jiang L, Chernova MN, Stuart-Tilley AK, Shmukler BE & Alper SL (2003) Deficient HCO_3^- transport in an AE1 mutant with normal Cl^- transport can be rescued by carbonic anhydrase II presented on an adjacent AE1 protomer. *J Biol Chem* **278**, 44949-44958.
 27. Yannoukakos D, Stuart-Tilley A, Fernandez HA, Fey P, Duyk G & Alper SL (1994) Molecular cloning, expression, and chromosomal localization of two isoforms of the AE3 anion exchanger from human heart. *Circ Res* **75**, 603-614.
 28. Bonar PT & Casey JR (2008) Plasma membrane $\text{Cl}^-/\text{HCO}_3^-$ exchangers: Structure, mechanism and physiology. *Channels (Austin)* **2**, 337-345.
 29. Linn SC, Askew GR, Menon AG & Shull GE (1995) Conservation of an AE3 $\text{Cl}^-/\text{HCO}_3^-$ exchanger cardiac-specific exon and promoter region and AE3 mRNA expression patterns in murine and human hearts. *Circ Res* **76**, 584-591.
 30. Mount DB & Romero MF (2004) The SLC26 gene family of multifunctional anion exchangers. *Pflugers Arch* **447**, 710-721.
 31. Alvarez BV, Kieller DM, Quon AL, Markovich D & Casey JR (2004) Slc26a6: a cardiac chloride-hydroxyl exchanger and predominant chloride-bicarbonate exchanger of the mouse heart. *J Physiol* **561**, 721-734.
 32. Petrovic S, Ju X, Barone S, Seidler U, Alper SL, Lohi H, Kere J & Soleimani M (2003) Identification of a basolateral $\text{Cl}^-/\text{HCO}_3^-$ exchanger specific to gastric parietal cells. *Am J Physiol Gastrointest Liver Physiol* **284**, G1093-1103.
 33. Reithmeier RA (2001) A membrane metabolon linking carbonic anhydrase with chloride/bicarbonate anion exchangers. *Blood Cells Mol Dis* **27**, 85-89.
 34. Srere PA (1987) Complexes of sequential metabolic enzymes. *Annu Rev Biochem* **56**, 89-124.
 35. Srere PA (1985) The metabolon. *Trends in Biochemical Sciences* **10**, 109-110.
 36. Miles EW, Rhee S & Davies DR (1999) The molecular basis of substrate channeling. *J Biol Chem* **274**, 12193-12196.
 37. Sterling D, Reithmeier RA & Casey JR (2001) Carbonic anhydrase: in the driver's seat for bicarbonate transport. *Jop* **2**, 165-170.

38. Eriksson AE JT, Liljas A (1988) Refined structure of human carbonic anhydrase II at 2.0 Å resolution. *Proteins* **4**, 274-282.
39. Cousin JL & Motais R (1976) The role of carbonic anhydrase inhibitors on anion permeability into ox red blood cells. *J Physiol* **256**, 61-80.
40. Sowah D & Casey JR (2010) An Intramolecular Transport Metabolon: Fusion of Carbonic Anhydrase II to the C-terminus of the Cl⁻/HCO₃⁻ Exchanger, AE1. *J Biol Chem* **Submitted**.
41. Fierke CA, Calderone TL & Krebs JF (1991) Functional consequences of engineering the hydrophobic pocket of carbonic anhydrase II. *Biochemistry* **30**, 11054-11063.
42. Baird TT, Jr., Waheed A, Okuyama T, Sly WS & Fierke CA (1997) Catalysis and inhibition of human carbonic anhydrase IV. *Biochemistry* **36**, 2669-2678.
43. Pastorekova S, Parkkila S, Parkkila AK, Opavsky R, Zelnik V, Saarnio J & Pastorek J (1997) Carbonic anhydrase IX, MN/CA IX: analysis of stomach complementary DNA sequence and expression in human and rat alimentary tracts. *Gastroenterology* **112**, 398-408.
44. Tang XB, Fujinaga J, Kopito R & Casey JR (1998) Topology of the region surrounding Glu681 of human AE1 protein, the erythrocyte anion exchanger. *J Biol Chem* **273**, 22545-22553.
45. Zolotarev AS, Chernova MN, Yannoukakos D & Alper SL (1996) Proteolytic cleavage sites of native AE2 anion exchanger in gastric mucosal membranes. *Biochemistry* **35**, 10367-10376.
46. Kudrycki KE, Newman PR & Shull GE (1990) cDNA cloning and tissue distribution of mRNAs for two proteins that are related to the band 3 Cl⁻/HCO₃⁻ exchanger. *J Biol Chem* **265**, 462-471.
47. Casey JR, Sly WS, Shah GN & Alvarez BV (2009) Bicarbonate homeostasis in excitable tissues: role of AE3 Cl⁻/HCO₃⁻ exchanger and carbonic anhydrase XIV interaction. *Am J Physiol Cell Physiol* **297**, C1091-1102.
48. Gawenis LR, Ledoussal C, Judd LM, Prasad V, Alper SL, Stuart-Tilley A, Woo AL, Grisham C, Sanford LP, Doetschman T, et al. (2004) Mice with a targeted disruption of the AE2 Cl⁻/HCO₃⁻ exchanger are achlorhydric. *J Biol Chem* **279**, 30531-30539.
49. Swietach P, Vaughan-Jones RD & Harris AL (2007) Regulation of tumor pH and the role of carbonic anhydrase 9. *Cancer Metastasis Rev* **26**, 299-310.

50. Stock C & Schwab A (2009) Protons make tumor cells move like clockwork. *Pflugers Arch* **458**, 981-992.
51. Jennings ML (1984) Oligomeric structure and the anion transport function of human erythrocyte band 3 protein. *J Membr Biol* **80**, 105-117.
52. Wieth JO (1979) Bicarbonate exchange through the human red cell membrane determined with [^{14}C] bicarbonate. *J Physiol* **294**, 521-539.
53. Scozzafava A & Supuran CT (2002) Carbonic anhydrase activators: human isozyme II is strongly activated by oligopeptides incorporating the carboxyterminal sequence of the bicarbonate anion exchanger AE1. *Bioorg Med Chem Lett* **12**, 1177-1180.
54. Soleimani M & Burnham CE (2000) Physiologic and molecular aspects of the $\text{Na}^+/\text{HCO}_3^-$ cotransporter in health and disease processes. *Kidney Int* **57**, 371-384.
55. Sterling D, Brown NJ, Supuran CT & Casey JR (2002) The functional and physical relationship between the DRA bicarbonate transporter and carbonic anhydrase II. *Am J Physiol Cell Physiol* **283**, C1522-1529.
56. Boron WF (2010) Evaluating the role of carbonic anhydrases in the transport of HCO_3^- -related species. *Biochim Biophys Acta* **1804**, 410-421.
57. Lu J, Daly CM, Parker MD, Gill HS, Piermarini PM, Pelletier MF & Boron WF (2006) Effect of human carbonic anhydrase II on the activity of the human electrogenic $\text{Na}^+/\text{HCO}_3^-$ cotransporter NBCe1-A in *Xenopus* oocytes. *J Biol Chem* **281**, 19241-19250.
58. Piermarini PM, Kim EY & Boron WF (2007) Evidence against a direct interaction between intracellular carbonic anhydrase II and pure C-terminal domains of SLC4 bicarbonate transporters. *J Biol Chem* **282**, 1409-1421.
59. Fliegel L (2001) Regulation of myocardial Na^+/H^+ exchanger activity. *Basic Res Cardiol* **96**, 301-305.
60. Slepko ER, Rainey JK, Sykes BD & Fliegel L (2007) Structural and functional analysis of the Na^+/H^+ exchanger. *Biochem J* **401**, 623-633.
61. Li X, Liu Y, Alvarez BV, Casey JR & Fliegel L (2006) A novel carbonic anhydrase II binding site regulates NHE1 activity. *Biochemistry* **45**, 2414-2424.
62. Li X, Alvarez B, Casey JR, Reithmeier RA & Fliegel L (2002) Carbonic anhydrase II binds to and enhances activity of the Na^+/H^+ exchanger. *J Biol Chem* **277**, 36085-36091.

63. Wu Q, Pierce WM, Jr. & Delamere NA (1998) Cytoplasmic pH responses to carbonic anhydrase inhibitors in cultured rabbit nonpigmented ciliary epithelium. *J Membr Biol* **162**, 31-38.
64. Ro HA & Carson JH (2004) pH microdomains in oligodendrocytes. *J Biol Chem* **279**, 37115-37123.
65. Becker HM & Deitmer JW (2008) Nonenzymatic proton handling by carbonic anhydrase II during H⁺-lactate cotransport via monocarboxylate transporter 1. *J Biol Chem* **283**, 21655-21667.
66. Becker HM, Hirnet D, Fecher-Trost C, Sultemeyer D & Deitmer JW (2005) Transport activity of MCT1 expressed in *Xenopus* oocytes is increased by interaction with carbonic anhydrase. *J Biol Chem* **280**, 39882-39889.
67. Bergersen LH (2007) Is lactate food for neurons? Comparison of monocarboxylate transporter subtypes in brain and muscle. *Neuroscience* **145**, 11-19.
68. Yeung T & Grinstein S (2007) Lipid signaling and the modulation of surface charge during phagocytosis. *Immunol Rev* **219**, 17-36.
69. Broer S & Brookes N (2001) Transfer of glutamine between astrocytes and neurons. *J Neurochem* **77**, 705-719.
70. Weise A, Becker HM & Deitmer JW (2007) Enzymatic suppression of the membrane conductance associated with the glutamine transporter SNAT3 expressed in *Xenopus* oocytes by carbonic anhydrase II. *J Gen Physiol* **130**, 203-215.
71. Hoffmann EK, Lambert IH & Pedersen SF (2009) Physiology of cell volume regulation in vertebrates. *Physiol Rev* **89**, 193-277.
72. Mason MJ, Smith JD, Garcia-Soto JJ & Grinstein S (1989) Internal pH-sensitive site couples Cl⁻/HCO₃⁻ exchange to Na⁺/H⁺ antiport in lymphocytes. *Am J Physiol* **256**, C428-433.
73. Casey JR, Grinstein S & Orlowski J (2010) Sensors and regulators of intracellular pH. *Nat Rev Mol Cell Biol* **11**, 50-61.
74. Brown D, Breton S, Ausiello DA & Marshansky V (2009) Sensing, signaling and sorting events in kidney epithelial cell physiology. *Traffic* **10**, 275-284.
75. Yeung T, Gilbert GE, Shi J, Silvius J, Kapus A & Grinstein S (2008) Membrane phosphatidylserine regulates surface charge and protein localization. *Science* **319**, 210-213.

76. Garcia-Moreno B (2009) Adaptations of proteins to cellular and subcellular pH. *J Biol* **8**, 98.
77. Srivastava J, Barber DL & Jacobson MP (2007) Intracellular pH sensors: design principles and functional significance. *Physiology (Bethesda)* **22**, 30-39.
78. Pouyssegur J, Franchi A, L'Allemain G & Paris S (1985) Cytoplasmic pH, a key determinant of growth factor-induced DNA synthesis in quiescent fibroblasts. *FEBS Lett* **190**, 115-119.
79. Hayashi H, Aharonovitz O, Alexander RT, Touret N, Furuya W, Orłowski J & Grinstein S (2008) Na⁺/H⁺ exchange and pH regulation in the control of neutrophil chemokinesis and chemotaxis. *Am J Physiol Cell Physiol* **294**, C526-534.
80. Schelling JR & Abu Jawdeh BG (2008) Regulation of cell survival by Na⁺/H⁺ exchanger-1. *Am J Physiol Renal Physiol* **295**, F625-632.
81. Paroutis P, Touret N & Grinstein S (2004) The pH of the secretory pathway: measurement, determinants, and regulation. *Physiology (Bethesda)* **19**, 207-215.
82. Steinberg BE, Huynh KK, Brodovitch A, Jabs S, Stauber T, Jentsch TJ & Grinstein S (2010) A cation counterflux supports lysosomal acidification. *J Cell Biol* **189**, 1171-1186.
83. Orłowski J & Grinstein S (2007) Emerging roles of alkali cation/proton exchangers in organellar homeostasis. *Curr Opin Cell Biol* **19**, 483-492.
84. Szaszi K & Grinstein S (2005) Intracellular pH Measurement. In *Encyclopedia of Life Sciences*. John Wiley & Sons, Ltd.
85. Leem CH, Lagadic-Gossmann D & Vaughan-Jones RD (1999) Characterization of intracellular pH regulation in the guinea-pig ventricular myocyte. *J Physiol* **517 (Pt 1)**, 159-180.
86. Vaughan-Jones RD, Percy BE, Keener JP & Spitzer KW (2002) Intrinsic H⁺ ion mobility in the rabbit ventricular myocyte. *J Physiol* **541**, 139-158.
87. Sterling D & Casey JR (1999) Transport activity of AE3 chloride/bicarbonate anion-exchange proteins and their regulation by intracellular pH. *Biochem J* **344 Pt 1**, 221-229.
88. Wenzel E & Machen TE (1989) Intracellular pH dependence of buffer capacity and anion exchange in the parietal cell. *Am J Physiol* **20**, G741-G747.

89. Bischof G, Cosentini E, Hamilton G, Riegler M, Zacherl J, Teleky B, Feil W, Schiessel R, Machen TE & Wenzl E (1996) Effects of extracellular pH on intracellular pH-regulation and growth in a human colon carcinoma cell-line. *Biochim Biophys Acta* **1282**, 131-139.
90. Ch'en FF, Dilworth E, Swietach P, Goddard RS & Vaughan-Jones RD (2003) Temperature dependence of $\text{Na}^+\text{-H}^+$ exchange, $\text{Na}^+\text{-HCO}_3^-$ co-transport, intracellular buffering and intracellular pH in guinea-pig ventricular myocytes. *J Physiol* **552**, 715-726.
91. Swietach P, Camelliti P, Hulikova A, Kohl P & Vaughan-Jones RD (2010) Spatial regulation of intracellular pH in multicellular strands of neonatal rat cardiomyocytes. *Cardiovasc Res* **85**, 729-738.
92. Vaughan-Jones RD, Spitzer KW & Swietach P (2006) Spatial aspects of intracellular pH regulation in heart muscle. *Prog Biophys Mol Biol* **90**, 207-224.
93. Spitzer KW, Skolnick RL, Peercy BE, Keener JP & Vaughan-Jones RD (2002) Facilitation of intracellular H^+ ion mobility by $\text{CO}_2/\text{HCO}_3^-$ in rabbit ventricular myocytes is regulated by carbonic anhydrase. *J Physiol* **541**, 159-167.
94. Swietach P, Leem CH, Spitzer KW & Vaughan-Jones RD (2005) Experimental generation and computational modeling of intracellular pH gradients in cardiac myocytes. *Biophys J* **88**, 3018-3037.
95. Vaughan-Jones RD & Spitzer KW (2002) Role of bicarbonate in the regulation of intracellular pH in the mammalian ventricular myocyte. *Biochem Cell Biol* **80**, 579-596.
96. Swietach P, Spitzer KW & Vaughan-Jones RD (2007) pH-Dependence of extrinsic and intrinsic H^+ -ion mobility in the rat ventricular myocyte, investigated using flash photolysis of a caged- H^+ compound. *Biophys J* **92**, 641-653.
97. Willoughby D, Masada N, Crossthwaite AJ, Ciruela A & Cooper DM (2005) Localized Na^+/H^+ exchanger 1 expression protects Ca^{2+} -regulated adenylyl cyclases from changes in intracellular pH. *J Biol Chem* **280**, 30864-30872.
98. Orlov SN & Hamet P (2006) Intracellular monovalent ions as second messengers. *J Membr Biol* **210**, 161-172.
99. Bourguignon LY, Singleton PA, Diedrich F, Stern R & Gilad E (2004) CD44 interaction with $\text{Na}^+\text{-H}^+$ exchanger (NHE1) creates acidic microenvironments leading to hyaluronidase-2 and cathepsin B activation and breast tumor cell invasion. *J Biol Chem* **279**, 26991-27007.

100. Jons T & Drenckhahn D (1992) Identification of the binding interface involved in linkage of cytoskeletal protein 4.1 to the erythrocyte anion exchanger. *EMBO J* **11**, 2863-2867.
101. Groves JD & Tanner MJ (1992) Glycophorin A facilitates the expression of human band 3-mediated anion transport in *Xenopus* oocytes. *J Biol Chem* **267**, 22163-22170.
102. Tanphaichitr VS, Sumboonnanonda A, Ideguchi H, Shayakul C, Brugnara C, Takao M, Veerakul G & Alper SL (1998) Novel AE1 mutations in recessive distal renal tubular acidosis. Loss-of-function is rescued by glycophorin A. *J Clin Invest* **102**, 2173-2179.
103. Alper SL, Stuart-Tilley A, Simmons CF, Brown D & Drenckhahn D (1994) The fodrin-ankyrin cytoskeleton of choroid plexus preferentially colocalizes with apical Na⁺K⁺-ATPase rather than with basolateral anion exchanger AE2. *J Clin Invest* **93**, 1430-1438.
104. Campanella ME, Chu H & Low PS (2005) Assembly and regulation of a glycolytic enzyme complex on the human erythrocyte membrane. *Proc Natl Acad Sci U S A* **102**, 2402-2407.
105. Bruce LJ, Beckmann R, Ribeiro ML, Peters LL, Chasis JA, Delaunay J, Mohandas N, Anstee DJ & Tanner MJ (2003) A band 3-based macrocomplex of integral and peripheral proteins in the RBC membrane. *Blood* **101**, 4180-4188.
106. Wu F, Saleem MA, Kampik NB, Satchwell TJ, Williamson RC, Blattner SM, Ni L, Toth T, White G, Young MT, et al. (2010) Anion exchanger 1 interacts with nephrin in podocytes. *J Am Soc Nephrol* **21**, 1456-1467.
107. Cheng H & Harris RC (2010) The glomerulus--a view from the outside--the podocyte. *Int J Biochem Cell Biol* **42**, 1380-1387.
108. Denker SP & Barber DL (2002) Cell migration requires both ion translocation and cytoskeletal anchoring by the Na-H exchanger NHE1. *J Cell Biol* **159**, 1087-1096.
109. Yamashita T, Eguchi K, Saitoh N, von Gersdorff H & Takahashi T (2010) Developmental shift to a mechanism of synaptic vesicle endocytosis requiring nanodomain Ca²⁺. *Nat Neurosci* **13**, 838-844.
110. Muller A, Kukley M, Uebachs M, Beck H & Dietrich D (2007) Nanodomains of single Ca²⁺ channels contribute to action potential repolarization in cortical neurons. *J Neurosci* **27**, 483-495.
111. Rizzuto R & Pozzan T (2006) Microdomains of intracellular Ca²⁺: molecular determinants and functional consequences. *Physiol Rev* **86**, 369-408.

112. Meissner G & Henderson JS (1987) Rapid calcium release from cardiac sarcoplasmic reticulum vesicles is dependent on Ca^{2+} and is modulated by Mg^{2+} , adenine nucleotide, and calmodulin. *J Biol Chem* **262**, 3065-3073.
113. Choi HS, Trafford AW, Orchard CH & Eisner DA (2000) The effect of acidosis on systolic Ca^{2+} and sarcoplasmic reticulum calcium content in isolated rat ventricular myocytes. *J Physiol* **529 Pt 3**, 661-668.
114. Balnave CD & Vaughan-Jones RD (2000) Effect of intracellular pH on spontaneous Ca^{2+} sparks in rat ventricular myocytes. *J Physiol* **528 Pt 1**, 25-37.
115. McGuffee SR & Elcock AH (2010) Diffusion, crowding & protein stability in a dynamic molecular model of the bacterial cytoplasm. *PLoS Comput Biol* **6**, e1000694.
116. Dix JA & Verkman AS (2008) Crowding effects on diffusion in solutions and cells. *Annu Rev Biophys* **37**, 247-263.
117. Ng SW, Nelson C & Parekh AB (2009) Coupling of Ca^{2+} microdomains to spatially and temporally distinct cellular responses by the tyrosine kinase Syk. *J Biol Chem* **284**, 24767-24772.
118. Straube R & Ridgway D (2009) Investigating the effects of molecular crowding on Ca^{2+} diffusion using a particle-based simulation model. *Chaos* **19**, 037110.
119. Laude AJ & Simpson AW (2009) Compartmentalized signalling: Ca^{2+} compartments, microdomains and the many facets of Ca^{2+} signalling. *FEBS J* **276**, 1800-1816.
120. Wei C, Wang X, Chen M, Ouyang K, Zheng M & Cheng H (2010) Flickering calcium microdomains signal turning of migrating cells. *Can J Physiol Pharmacol* **88**, 105-110.
121. Gabso M, Neher E & Spira ME (1997) Low mobility of the Ca^{2+} buffers in axons of cultured Aplysia neurons. *Neuron* **18**, 473-481.
122. Zaccolo M & Pozzan T (2002) Discrete microdomains with high concentration of cAMP in stimulated rat neonatal cardiac myocytes. *Science* **295**, 1711-1715.
123. Neves SR & Iyengar R (2009) Models of spatially restricted biochemical reaction systems. *J Biol Chem* **284**, 5445-5449.
124. Schillace RV & Scott JD (1999) Organization of kinases, phosphatases, and receptor signaling complexes. *J Clin Invest* **103**, 761-765.

125. Dodge KL, Khouangsathiene S, Kapiloff MS, Mouton R, Hill EV, Houslay MD, Langeberg LK & Scott JD (2001) mAKAP assembles a protein kinase A/PDE4 phosphodiesterase cAMP signaling module. *EMBO J* **20**, 1921-1930.
126. Gerlyand AM & Sitar DS (2009) Protein kinase inhibition differentially regulates organic cation transport. *Can J Physiol Pharmacol* **87**, 821-830.
127. Spitzer KW, Ershler PR, Skolnick RL & Vaughan-Jones RD (2000) Generation of intracellular pH gradients in single cardiac myocytes with a microperfusion system. *Am J Physiol Heart Circ Physiol* **278**, H1371-1382.
128. Swietach P & Vaughan-Jones RD (2005) Spatial regulation of intracellular pH in the ventricular myocyte. *Ann N Y Acad Sci* **1047**, 271-282.
129. Stewart AK, Boyd CA & Vaughan-Jones RD (1999) A novel role for carbonic anhydrase: cytoplasmic pH gradient dissipation in mouse small intestinal enterocytes. *J Physiol* **516 (Pt 1)**, 209-217.
130. Klein M, Seeger P, Schuricht B, Alper SL & Schwab A (2000) Polarization of Na⁺/H⁺ and Cl⁻/HCO₃⁻ exchangers in migrating renal epithelial cells. *J Gen Physiol* **115**, 599-608.
131. Stuwe L, Muller M, Fabian A, Waning J, Mally S, Noel J, Schwab A & Stock C (2007) pH dependence of melanoma cell migration: protons extruded by NHE1 dominate protons of the bulk solution. *J Physiol* **585**, 351-360.
132. Swietach P, Wigfield S, Cobden P, Supuran CT, Harris AL & Vaughan-Jones RD (2008) Tumor-associated carbonic anhydrase 9 spatially coordinates intracellular pH in three-dimensional multicellular growths. *J Biol Chem* **283**, 20473-20483.
133. Halestrap AP & Meredith D (2004) The SLC16 gene family-from monocarboxylate transporters (MCTs) to aromatic amino acid transporters and beyond. *Pflugers Arch* **447**, 619-628.
134. Martinez-Zaguilan R, Raghunand N, Lynch RM, Bellamy W, Martinez GM, Rojas B, Smith D, Dalton WS & Gillies RJ (1999) pH and drug resistance. I. Functional expression of plasmalemmal V-type H⁺-ATPase in drug-resistant human breast carcinoma cell lines. *Biochem Pharmacol* **57**, 1037-1046.
135. Rojas JD, Sennoune SR, Maiti D, Bakunts K, Reuveni M, Sanka SC, Martinez GM, Seftor EA, Meininger CJ, Wu G, et al. (2006) Vacuolar-type H⁺-ATPases at the plasma membrane regulate pH and cell migration

- in microvascular endothelial cells. *Am J Physiol Heart Circ Physiol* **291**, H1147-1157.
136. Mackenzie B, Loo DD, Fei Y, Liu WJ, Ganapathy V, Leibach FH & Wright EM (1996) Mechanisms of the human intestinal H⁺-coupled oligopeptide transporter hPEPT1. *J Biol Chem* **271**, 5430-5437.
 137. Ovens MJ, Davies AJ, Wilson MC, Murray CM & Halestrap AP (2010) AR-C155858 is a potent inhibitor of monocarboxylate transporters MCT1 and MCT2 that binds to an intracellular site involving transmembrane helices 7-10. *Biochem J* **425**, 523-530.
 138. Tornroth-Horsefield S, Wang Y, Hedfalk K, Johanson U, Karlsson M, Tajkhorshid E, Neutze R & Kjellbom P (2006) Structural mechanism of plant aquaporin gating. *Nature* **439**, 688-694.
 139. Ek-Vitorin JF, Calero G, Morley GE, Coombs W, Taffet SM & Delmar M (1996) pH regulation of connexin43: molecular analysis of the gating particle. *Biophys J* **71**, 1273-1284.
 140. Schulte U & Fakler B (2000) Gating of inward-rectifier K⁺ channels by intracellular pH. *Eur J Biochem* **267**, 5837-5841.
 141. Niemeyer MI, Cid LP, Pena-Munzenmayer G & Sepulveda FV (2010) Separate gating mechanisms mediate the regulation of K2P potassium channel TASK-2 by intra- and extracellular pH. *J Biol Chem* **285**, 16467-16475.
 142. Lacroix J, Poet M, Maehrel C & Counillon L (2004) A mechanism for the activation of the Na/H exchanger NHE-1 by cytoplasmic acidification and mitogens. *EMBO Rep* **5**, 91-96.
 143. Philipson KD, Bersohn MM & Nishimoto AY (1982) Effects of pH on Na⁺-Ca²⁺ exchange in canine cardiac sarcolemmal vesicles. *Circ Res* **50**, 287-293.
 144. Meima ME, Mackley JR & Barber DL (2007) Beyond ion translocation: structural functions of the sodium-hydrogen exchanger isoform-1. *Curr Opin Nephrol Hypertens* **16**, 365-372.
 145. Pope BJ, Zierler-Gould KM, Kuhne R, Weeds AG & Ball LJ (2004) Solution structure of human cofilin: actin binding, pH sensitivity, and relationship to actin-depolymerizing factor. *J Biol Chem* **279**, 4840-4848.
 146. Akiba Y, Mizumori M, Guth PH, Engel E & Kaunitz JD (2007) Duodenal brush border intestinal alkaline phosphatase activity affects bicarbonate secretion in rats. *Am J Physiol Gastrointest Liver Physiol* **293**, G1223-1233.

147. Ananthakrishnan R & Ehrlicher A (2007) The forces behind cell movement. *Int J Biol Sci* **3**, 303-317.
148. Stock C & Schwab A (2006) Role of the Na/H exchanger NHE1 in cell migration. *Acta Physiol (Oxf)* **187**, 149-157.
149. Schwab A, Nechyporuk-Zloy V, Fabian A & Stock C (2007) Cells move when ions and water flow. *Pflugers Arch* **453**, 421-432.
150. Beaulieu V, Da Silva N, Pastor-Soler N, Brown CR, Smith PJ, Brown D & Breton S (2005) Modulation of the actin cytoskeleton via gelsolin regulates vacuolar H⁺-ATPase recycling. *J Biol Chem* **280**, 8452-8463.
151. King AE, Ackley MA, Cass CE, Young JD & Baldwin SA (2006) Nucleoside transporters: from scavengers to novel therapeutic targets. *Trends Pharmacol Sci* **27**, 416-425.
152. Young JD & Jarvis SM (1983) Nucleoside transport in animal cells. *Biosci Rep* **3**, 309-322.
153. Griffith DA & Jarvis SM (1996) Nucleoside and nucleobase transport systems of mammalian cells. *Biochim Biophys Acta* **1286**, 153-181.
154. Zhang J, Visser F, King KM, Baldwin SA, Young JD & Cass CE (2007) The role of nucleoside transporters in cancer chemotherapy with nucleoside drugs. *Cancer Metastasis Rev* **26**, 85-110.
155. Cabrita MA, Baldwin SA, Young JD & Cass CE (2002) Molecular biology and regulation of nucleoside and nucleobase transporter proteins in eukaryotes and prokaryotes. *Biochem Cell Biol* **80**, 623-638.
156. Young JD, Cheeseman, C.I., Mackey, J.R., Cass, C.E. and Baldwin, S.A. (2000) Molecular Mechanisms of Nucleoside and Nucleoside Drug Transport. In *Gastrointestinal Transport (Current Topics in Membranes)* (Barrett KE, and Donowitz, M., ed, pp. 329-378. Academic Press, San Diego.
157. Elwi AN, Damaraju VL, Baldwin SA, Young JD, Sawyer MB & Cass CE (2006) Renal nucleoside transporters: physiological and clinical implications. *Biochem Cell Biol* **84**, 844-858.
158. Young JD, Yao SY, Sun L, Cass CE & Baldwin SA (2008) Human equilibrative nucleoside transporter (ENT) family of nucleoside and nucleobase transporter proteins. *Xenobiotica* **38**, 995-1021.
159. Pastor-Anglada M, Cano-Soldado P, Errasti-Murugarren E & Casado FJ (2008) SLC28 genes and concentrative nucleoside transporter (CNT) proteins. *Xenobiotica* **38**, 972-994.

160. Ritzel MW, Yao SY, Huang MY, Elliott JF, Cass CE & Young JD (1997) Molecular cloning and functional expression of cDNAs encoding a human Na⁺-nucleoside cotransporter (hCNT1). *Am J Physiol* **272**, C707-714.
161. Ritzel MW, Yao SY, Ng AM, Mackey JR, Cass CE & Young JD (1998) Molecular cloning, functional expression and chromosomal localization of a cDNA encoding a human Na⁺/nucleoside cotransporter (hCNT2) selective for purine nucleosides and uridine. *Mol Membr Biol* **15**, 203-211.
162. Ritzel MW, Ng AM, Yao SY, Graham K, Loewen SK, Smith KM, Ritzel RG, Mowles DA, Carpenter P, Chen XZ, et al. (2001) Molecular identification and characterization of novel human and mouse concentrative Na⁺-nucleoside cotransporter proteins (hCNT3 and mCNT3) broadly selective for purine and pyrimidine nucleosides (system cib). *J Biol Chem* **276**, 2914-2927.
163. Slugoski MD, Ng AM, Yao SY, Smith KM, Lin CC, Zhang J, Karpinski E, Cass CE, Baldwin SA & Young JD (2008) A proton-mediated conformational shift identifies a mobile pore-lining cysteine residue (Cys-561) in human concentrative nucleoside transporter 3. *J Biol Chem* **283**, 8496-8507.
164. Slugoski MD, Ng AM, Yao SY, Lin CC, Mulinta R, Cass CE, Baldwin SA & Young JD (2009) Substituted cysteine accessibility method analysis of human concentrative nucleoside transporter hCNT3 reveals a novel discontinuous region of functional importance within the CNT family motif (G/A)XKX3NEFVA(Y/M/F). *J Biol Chem* **284**, 17281-17292.
165. Smith KM, Slugoski MD, Loewen SK, Ng AM, Yao SY, Chen XZ, Karpinski E, Cass CE, Baldwin SA & Young JD (2005) The broadly selective human Na⁺/nucleoside cotransporter (hCNT3) exhibits novel cation-coupled nucleoside transport characteristics. *J Biol Chem* **280**, 25436-25449.
166. Smith KM, Slugoski MD, Cass CE, Baldwin SA, Karpinski E & Young JD (2007) Cation coupling properties of human concentrative nucleoside transporters hCNT1, hCNT2 and hCNT3. *Mol Membr Biol* **24**, 53-64.
167. Slugoski MD, Smith KM, Mulinta R, Ng AM, Yao SY, Morrison EL, Lee QO, Zhang J, Karpinski E, Cass CE, et al. (2008) A conformationally mobile cysteine residue (Cys-561) modulates Na⁺ and H⁺ activation of human CNT3. *J Biol Chem* **283**, 24922-24934.
168. Damaraju VL, Elwi AN, Hunter C, Carpenter P, Santos C, Barron GM, Sun X, Baldwin SA, Young JD, Mackey JR, et al. (2007) Localization of broadly selective equilibrative and concentrative nucleoside transporters, hENT1 and hCNT3, in human kidney. *Am J Physiol Renal Physiol* **293**, F200-211.

169. Ngo LY, Patil SD & Unadkat JD (2001) Ontogenic and longitudinal activity of Na⁺-nucleoside transporters in the human intestine. *Am J Physiol Gastrointest Liver Physiol* **280**, G475-481.
170. Shimomura O, Johnson FH & Saiga Y (1962) Extraction, purification and properties of aequorin, a bioluminescent protein from the luminous hydromedusan, *Aequorea*. *J Cell Comp Physiol* **59**, 223-239.
171. Tsien RY (1998) The green fluorescent protein. *Annu Rev Biochem* **67**, 509-544.
172. van Thor JJ, Georgiev GY, Towrie M & Sage JT (2005) Ultrafast and low barrier motions in the photoreactions of the green fluorescent protein. *J Biol Chem* **280**, 33652-33659.
173. Zaccolo M & Pozzan T (2000) Imaging signal transduction in living cells with GFP-based probes. *IUBMB Life* **49**, 375-379.
174. Zhang J, Campbell RE, Ting AY & Tsien RY (2002) Creating new fluorescent probes for cell biology. *Nat Rev Mol Cell Biol* **3**, 906-918.
175. Matz MV, Fradkov AF, Labas YA, Savitsky AP, Zaraisky AG, Markelov ML & Lukyanov SA (1999) Fluorescent proteins from nonbioluminescent Anthozoa species. *Nat Biotechnol* **17**, 969-973.
176. Campbell RE, Tour O, Palmer AE, Steinbach PA, Baird GS, Zacharias DA & Tsien RY (2002) A monomeric red fluorescent protein. *Proc Natl Acad Sci U S A* **99**, 7877-7882.
177. Shaner NC, Campbell RE, Steinbach PA, Giepmans BN, Palmer AE & Tsien RY (2004) Improved monomeric red, orange and yellow fluorescent proteins derived from *Discosoma sp.* red fluorescent protein. *Nat Biotechnol* **22**, 1567-1572.
178. Shaner NC, Lin MZ, McKeown MR, Steinbach PA, Hazelwood KL, Davidson MW & Tsien RY (2008) Improving the photostability of bright monomeric orange and red fluorescent proteins. *Nat Methods* **5**, 545-551.
179. Eftink MR & Ghiron CA (1975) Dynamics of a protein matrix revealed by fluorescence quenching. *Proc Natl Acad Sci U S A* **72**, 3290-3294.
180. Miesenböck G, De Angelis DA & Rothman JE (1998) Visualizing secretion and synaptic transmission with pH-sensitive green fluorescent proteins. *Nature* **394**, 192-195.
181. Jankowski A, Kim JH, Collins RF, Daneman R, Walton P & Grinstein S (2001) In situ measurements of the pH of mammalian peroxisomes using the fluorescent protein pHluorin. *J Biol Chem* **276**, 48748-48753.

182. Yeung T, Touret N & Grinstein S (2005) Quantitative fluorescence microscopy to probe intracellular microenvironments. *Curr Opin Microbiol* **8**, 350-358.
183. Hanson GT, McAnaney TB, Park ES, Rendell ME, Yarbrough DK, Chu S, Xi L, Boxer SG, Montrose MH & Remington SJ (2002) Green fluorescent protein variants as ratiometric dual emission pH sensors. 1. Structural characterization and preliminary application. *Biochemistry* **41**, 15477-15488.
184. Bizzarri R, Arcangeli C, Arosio D, Ricci F, Faraci P, Cardarelli F & Beltram F (2006) Development of a novel GFP-based ratiometric excitation and emission pH indicator for intracellular studies. *Biophys J* **90**, 3300-3314.
185. Nagai T, Sawano A, Park ES & Miyawaki A (2001) Circularly permuted green fluorescent proteins engineered to sense Ca^{2+} . *Proc Natl Acad Sci U S A* **98**, 3197-3202.
186. Miyawaki A, Llopis J, Heim R, McCaffery JM, Adams JA, Ikura M & Tsien RY (1997) Fluorescent indicators for Ca^{2+} based on green fluorescent proteins and calmodulin. *Nature* **388**, 882-887.
187. Ting AY, Kain KH, Klemke RL & Tsien RY (2001) Genetically encoded fluorescent reporters of protein tyrosine kinase activities in living cells. *Proc Natl Acad Sci U S A* **98**, 15003-15008.
188. Sato M, Ozawa T, Inukai K, Asano T & Umezawa Y (2002) Fluorescent indicators for imaging protein phosphorylation in single living cells. *Nat Biotechnol* **20**, 287-294.
189. Zhang J, Ma Y, Taylor SS & Tsien RY (2001) Genetically encoded reporters of protein kinase A activity reveal impact of substrate tethering. *Proc Natl Acad Sci U S A* **98**, 14997-15002.
190. Sakai R, Repunte-Canonigo V, Raj CD & Knopfel T (2001) Design and characterization of a DNA-encoded, voltage-sensitive fluorescent protein. *Eur J Neurosci* **13**, 2314-2318.
191. Wachter RM & Remington SJ (1999) Sensitivity of the yellow variant of green fluorescent protein to halides and nitrate. *Curr Biol* **9**, R628-629.
192. Barondeau DP, Kassmann CJ, Tainer JA & Getzoff ED (2002) Structural chemistry of a green fluorescent protein Zn biosensor. *J Am Chem Soc* **124**, 3522-3524.

Chapter 2: Materials and Methods

2.1 Materials

During the completion of this work, the following materials were utilized. Standard lab reagents were from Fisher Scientific (Ontario, Canada), Sigma-Aldrich Canada (Oakville, Canada), BDH, Inc. (Toronto, ON, Canada) or EMD Chemicals (Gibbstown, NJ, USA). Less common reagents are listed in Table 2.1. DNA modifying enzymes are listed in Table 2.2. Antibodies are listed in Table 2.3.

Synthetic DNA oligonucleotides for cloning were purchased from Integrated DNA Technologies (Coralville, IA, USA).

The nucleotide sequence of mNectarine has been deposited in the GenBank nucleotide sequence database under accession number FJ439505.

Table 2.1 **Reagents**

| Name | Source |
|--|-------------------------------|
| 2',7'-Bis(2-carboxyethyl)-5(6)-carboxyfluorescein acetoxymethyl ester (BCECF-AM) | Sigma-Aldrich |
| 2-mercaptoethanol | EMD Chemicals |
| 5-(N-ethyl-N-isopropyl)-amiloride (EIPA) | Sigma-Aldrich |
| Acrylamide | Bio-Rad Laboratories |
| Ammonium persulfate | Bioshop Canada Inc. |
| BCA reagents | Thermo Fisher Scientific Inc. |
| Calf serum (CS) | Gibco-Invitrogen Corporation |
| Complete TM protease inhibitor cocktail tablets | Roche Applied Sciences |
| Dithiothreitol (DTT) | Sigma-Aldrich |
| Dulbecco's modified Eagle's medium (DMEM) | Gibco-Invitrogen Corporation |
| ECL chemiluminescent reagent | Perkin Elmer Life Sciences |
| Excitation and emission filters, cubes, beamsplitters | Chroma technology |

Table 2.1 Reagents (continued)

| Name | Source |
|---|-------------------------------|
| EZ-Link™ Sulfo-NHS-SS-Biotin (Sulfosuccinimidyl 2-(Biotinamido) Ethyl-1,3'Dithiopropionate) | Thermo Fisher Scientific Inc. |
| Fetal bovine serum (FBS) | Gibco-Invitrogen Corporation |
| GenCatch™ gel extraction kit | Epoch Biolabs |
| GeneJET™ Plasmid Miniprep Kit | Qiagen |
| HiSpeed® Plasmid Purification Kit | Qiagen |
| Immobilon-P PVDF membrane | Millipore |
| Nigericin sodium salt | Sigma-Aldrich |
| N,N,N',N',-tetramethylenediamine (TEMED) | Thermo Fisher Scientific Inc. |
| Penicillin-streptomycin-glutamine (PSG) | Gibco-Invitrogen Corporation |
| PNGaseF | New England Biolabs |
| Poly-L-lysine | Sigma-Aldrich |
| Precision Plus Protein™ Dual Color Standards | Bio-Rad Laboratories |
| QIAquick® Gel Extraction Kit | Qiagen |
| Round glass coverslips | Thermo Fisher Scientific Inc. |
| Sodium perfluorooctanoate (PFO) | Oakwood Products, Inc |
| Streptavidin agarose resin | Thermo Fisher Scientific Inc. |
| Trypsin-EDTA (0.25% w/v) | Gibco-Invitrogen Corporation |

Table 2.2 DNA Modifying Enzymes

| Enzyme | Source |
|--|---|
| Calf intestinal alkaline phosphatase (CIP) | New England BioLabs |
| DYEnamic ET kit | GE Healthcare |
| Platinum® <i>Pfx</i> DNA polymerase | Gibco-Invitrogen Corporation |
| Restriction Endonucleases | New England BioLabs or Gibco-Invitrogen Corporation |
| T4 DNA Ligase | New England BioLabs or Gibco-Invitrogen Corporation |
| T4 polynucleotide kinase | New England Biolabs |

Table 2.3 **Antibodies**

| Antibody | Source | Catalog number |
|--|--|-----------------------|
| Donkey anti-rabbit IgG-HRP | Santa Cruz Biotechnology, Inc. | SC-2317 |
| Mouse anti-AE1 monoclonal antibody (IVF12) | Dr. Mike Jennings, University of Arkansas [46] | N/A |
| Mouse anti-GAPDH monoclonal antibody | Santa Cruz Biotechnology, Inc. | SC-47724 |
| Rabbit anti-RFP polyclonal antibody | abcam | ab34771 |
| Sheep anti-mouse IgG-HRP | GE Healthcare UK Limited | NA93IV |

2.2 Methods

2.2.1 mNectarine mutagenesis, library construction, and screening

Mutagenesis of cDNA was performed by overlap extension PCR [1] or error-prone PCR [2]. PCR products and pBAD/His B vector were digested with XhoI and EcoRI, ligated, and used to transform electrocompetent *E. coli* strain DH10B (Invitrogen), which were then plated on Agar plates, containing LB-AMP (Luria-Bertani medium supplemented with 0.1 mg/ml ampicillin and 0.02% w/v L-arabinose). Plates were incubated for 14 h at 37 °C prior to library screening. Our previously described imaging system [3], was equipped with a 520–550 nm bandpass filter for excitation of red fluorescence from bacterial colonies plated on a 10 cm Petri dish. The fluorescence emission of individual colonies was screened by eye, using tinted plastic goggles that block light with a wavelength of less than 600 nm. In each round of screening, approximately 10^5 colonies were visually inspected and those with the most intense fluorescence (~10 to 20) were picked for further investigation. Colonies of interest were cultured overnight in 4 ml LB-AMP. The following day 0.1 ml of each culture was dispensed into individual wells of a clear bottom 96-well plate (Nunc, Rochester, NY, USA) and the full emission spectra of each variant measured with a Safire2 plate reader equipped with monochromators (Tecan, Mannedorf, Switzerland). Variants with the most intense red fluorescence emission were used as templates in the subsequent round of library construction. The resultant clone was called mNectarine in pBAD/His B.

2.2.2 Construction of fusion proteins

Mammalian expression constructs pJRC9 (AE1) and AE1-P652C were described previously [4, 5]. Calnexin in mammalian expression construct pcDNA3.1/zeo(+) was received from Dr. Marek Michalak, University of Alberta. Dual emission green fluorescent protein 4 in pEGFP/N1 (deGFP4) was received from Dr. Jim Remington, University of Oregon [6]. Mammalian expression construct mNectarine (pDEJ6) was generated by digestion of mNectarine in pBAD/His B with XhoI and EcoRI, and ligation into pcDNA3.1(-) (Invitrogen). hCNT3 in the mammalian expression vector pcDNA3.1(+) was generated by digestion of hCNT3 in yeast expression vector pYPGE15 [7] with KpnI and EcoRI, and ligation into pcDNA3.1(+) (Invitrogen). The mammalian expression construct for mNectarine.hCNT3 (pDEJ13) was constructed by two steps of PCR and cloning. The forward primer (5'-GCGGTACCGGTGGTGAGCTGAGGAGTACAGCAGC -3') annealed to the first 20 base pairs of hCNT3 and added a KpnI restriction site, and two glycine codons. The reverse primer (5'-GCCTCGAGTCAAAAATGTATTAGAGAT -3') annealed to the last 18 base pairs of hCNT3, and added an XhoI restriction site. The cDNA was generated by PCR (30 cycles of 94 °C for 30 s, 50-63 °C for 60 s, 72 °C for 120 s). The PCR product and pcDNA3.1(+) were cut with KpnI and XhoI and ligated to generate pDEJ11. The forward primer (5'-GCGCCAAGCTTATGGTGAGCAAGGGCGAGG -3') annealed to the first 19 base pairs of mNectarine, and added a HindIII restriction site. The reverse primer

(5'- GCGGTACCCTTGTACAGCTCGTCCATGCC -3') annealed to the last 21 base pairs of mNectarine, with the exception of the stop codon, which was removed. A KpnI site was also added to the 3' end of the primer. The cDNA was generated by PCR (30 cycles of 94 °C for 30 s, 63 °C for 60 s, 72 °C for 120 s) and was inserted into the HindIII and KpnI sites of pDEJ11 to generate pDEJ13 (mNectarine.hCNT3). The mammalian expression construct for mNectarine.hCNT3-F563C (pDEJ20) was constructed by digestion of pDEJ13 and hCNT3-F563C in oocyte expression vector pGEMHE (described previously) [8] by digestion with BamHI and EcoRV, and ligation. This introduced the F563C mutation into mNectarine.hCNT3. The mammalian expression construct for deGFP4.AE1 (pDEJ5) was generated through a three-step cloning process. pDEJ3 was generated by a single PCR step and cloning. Forward and reverse primers (5'- GCGCCATATGCTCGAGCAACTGGACACTCAGGACCAC -3' and 5'- GCGCGAGCAGAGGCTGTGAAGGAT -3', respectively) amplified a 591 base pair fragment of AE1 (pJRC9), and added 5' NdeI and XhoI restriction sites. The cDNA was generated by PCR (30 cycles of 94 °C for 30 s, 55 °C for 60 s, 72 °C for 120 s). pJRC9 and PCR product were cut with NdeI and BssHII and ligated to generate pDEJ3. pDEJ4 was generated by digestion of pDEJ3 and pcDNA3.1(-) with XhoI and HindIII, followed by ligation. pDEJ5 was constructed by two steps of PCR and cloning. The forward primer (5'- CCGCTCGAGATGGTGAGCAAGGGCGAGG -3') annealed to the first 19 base pairs of deGFP4 and added a 5' XhoI restriction site. The reverse primer (5'- CCATCATGTCTTCATAATCATCCTGCAGCTCCTCACCACCGCCACCCTT

GTACAGCTCGTCCATGCC -3') annealed to last 21 base pairs of deGFP4, with the exception of the stop codon, which was removed. The reverse primer also contained four glycine codons and the first 34 base pairs of AE1 (excluding the initial ATG). The cDNA was generated by PCR (30 cycles of 94 °C for 30 s, 56 °C for 60 s, 72 °C for 120 s). The second round of PCR included the original forward primer, a 1/50 dilution of the PCR product generated by the first round of PCR, pDEJ4 as template, and the reverse primer (5'-TGAGCCATGTAGGCATCTATGCGGAACACC -3'). The final PCR product and pDEJ4 were cut with XhoI and ClaI and ligated to generate pDEJ5 (deGFP4.AE1). The mammalian expression construct for mNectarine.AE1 (pDEJ14) was constructed using the same strategy as pDEJ5, except that pDEJ6 (mNectarine) was used as template in the first round of PCR instead of deGFP4. Mammalian expression construct deGFP4-Y66L.AE1 (pDEJ9) was generated through a two-step PCR strategy and cloning. The round one forward primer (5'-CCACTGCTTACTGGCTTATCG -3') and reverse primer (5'-TGCACGCCGAGGGTCAGGG -3') mutated TAC to CTC to render deGFP4 non-fluorescent. The cDNA was generated by PCR (30 cycles of 94 °C for 30 s, 53.7 °C for 30 s, 72 °C for 45 s). The second round of PCR included the original forward primer, a 1/50 dilution of the PCR product generated by the first round of PCR, pDEJ5 as template, and the reverse primer (5'-TCGTCCATCACCAGCTCC -3'). The final PCR product and pDEJ5 were digested with BmtI and BsrGI, and ligated to generate pDEJ9. Mammalian expression construct CNX.mNectarine (pDEJ19) was generated through a three-

step cloning process. First, pDEJ15 was generated by a single PCR step and cloning. The forward primer (5'-CCTTAGGATGGAAGGGAAGTGGTTACTGTGTTTG -3') annealed to the first 27 base pairs of calnexin. The reverse primer (5'-GCGGTACCCTCTCTTCGTGGCTTTCTGTTTCTTGG -3') annealed to the last 27 base pairs of calnexin, with the exception of the stop codon, which was removed. A KpnI site was also added to the 3' end of the primer. The cDNA was generated by PCR (30 cycles of 94 °C for 30 s, 63 °C for 60 s, 72 °C for 120 s), and then treated with T4 polynucleotide kinase to phosphorylate the 5' -OH of the PCR product. The treated PCR product was then ligated into pcDNA3.1(+) vector cut with EcoRV to generate pDEJ15. pDEJ17 was generated by a single PCR step and cloning. The forward primer (5'-GCGGTACCGGTGGTGTGAGCAAGGGCGAGGAGC -3') annealed to the first 18 base pairs of mNectarine (pDEJ6), with the exception of the start codon, which was removed. The primer also added a 5' KpnI restriction site, and two glycine codons. The reverse primer (5'-AGAATTCACTCTCTTCGTGGCTTTCTTGTACAGCTCGTCCATGCC -3') amplified the last 21 base pairs of mNectarine (pDEJ6), with the exception of the stop codon, which was removed. An ER-retention sequence (corresponding to amino acids RKPRRE) followed by a stop codon and an EcoRI restriction site were also added to the 3' end of the primer. The cDNA was generated by PCR (30 cycles of 94 °C for 30 s, 63 °C for 60 s, 72 °C for 120 s) and was inserted into the KpnI and EcoRI sites of pcDNA3.1(+) to generate pDEJ17. pDEJ15 and

pDEJ17 were then digested with KpnI and ligated to generate CNX.mNectarine (pDEJ19). Nucleotide sequences encoding fusion proteins were confirmed by sequencing (DNA Core Services Laboratory, University of Alberta, Department of Biochemistry).

2.2.3 Protein purification and characterization

For production of mNectarine protein, *E. coli* strain LMG194 was transformed with the pBAD/His B expression vector containing the FP gene of interest. A single colony was used to inoculate a 4 ml culture that was allowed to grow overnight (37 °C, 225 rpm) before being diluted into 1 l of LB-AMP. The culture was grown for 12 h before cells were harvested by centrifugation and lysed by French Press. Proteins were purified by Ni-NTA chromatography (GE Healthcare), and then dialyzed into 5 mM Tris buffer, pH 7.5. Absorption spectra were recorded on a DU-800 UV-visible spectrophotometer (Beckman Coulter, Mississauga, ON, Canada) and fluorescence excitation and emission spectra were recorded on a Safire2 plate reader. Fluorescence pK_a measurements were performed by diluting the dialyzed protein into a series of buffered solutions (200 mM imidazole, 200 mM citric acid, and 200 mM sodium phosphate), previously adjusted to various pHs. Quantum yields were determined using mTangerine as the reference standard [9]. Protein concentrations used for calculation of extinction coefficients were determined by the BCA method (Pierce).

2.2.4 Photostability measurements

For photostability measurements, microdroplets were formed by vortexing a solution of the purified protein (100 μ M protein in 5 mM Tris buffer, pH 7.5) mixed with mineral oil [10, 11]. A sample of this suspension (approximately 50 μ l) was sandwiched between a glass slide and a glass coverslip. The slide was imaged on an Axiovert 200M inverted fluorescence microscope (Zeiss) equipped with a 75 W xenon-arc lamp, a 20x objective, a 510-560 nm excitation filter, a 565 nm beamsplitter, a 573-648 nm emission filter, and a Retiga 2000R 12-bit cooled CCD camera (QImaging). Individual drops of protein solution considerably smaller than the field of view were identified by eye under low excitation light levels (2.5% neutral density filters). Digital image acquisition was then initiated and the neutral density filters removed. Collected images were processed using Image Pro (Media Cybernetics) to extract the fluorescence intensity as a function of time. Photobleaching curves were processed such that the bleaching half-time represents the time to bleach from an emission rate of 1000 photons/molecule/second to 500 photons/molecule/second [10]. mTangerine was subjected to bleaching under identical conditions and used as a reference standard [9].

2.2.5 Tissue culture

mNect, deGFP4, AE1, AE1-P652C, deGFP4.AE1, deGFP4-Y66L.AE1, mNect.AE1, mNect.hCNT3, mNect.hCNT3-F563, hCNT3, and CNX.mNect

constructs were expressed by transient transfection of HEK293 cells [12], using the calcium phosphate method [13]. Cells were grown at 37 °C in an air/CO₂ (19:1) environment in Dulbecco's modified Eagle media (DMEM, supplemented with 5% (v/v) fetal bovine serum, 5% (v/v) calf serum, and 1% (v/v) penicillin-streptomycin-glutamine).

In experiments where fluorescence of intact HEK293 cells was monitored, HEK293 cells grown on poly-L-lysine-coated 25 mm round coverslips were transiently transfected with the appropriate cDNA.

2.2.6 Peptide: N-Glycosidase F (PNGaseF) Treatment

HEK293 cells were transiently transfected with vector, mNect.hCNT3 or mNect.hCNT3-F563C cDNA. Cell lysates were harvested in IPB buffer (1% Ipegal CA-630, 5 mM EDTA, 0.15 M NaCl, 0.5% deoxycholate, 10 mM Tris, pH 7.5), supplemented with protease inhibitor cocktail. Samples (20 µg protein) were combined with 2 µL of glycoprotein denaturing solution (0.5% SDS, 40 mM dithiothreitol) and water to make a 20 µL reaction volume. Samples were denatured by heating to 100 °C for 10 min. Reactions were made to 40 µL by addition of 4 µL 10X G7 reaction buffer (50 mM sodium phosphate, pH 7.5), 4 µL 10% Ipegal CA-630, 1 µL PNGaseF enzyme and water. Samples were incubated at 37 °C for 1 h. One volume of 2x SDS-PAGE sample buffer (20% (v/v) glycerol, 2% (v/v) 2-mercaptoethanol, 4% (w/v) SDS, 1% (w/v) Bromophenol Blue, 150 mM Tris, 2x protease inhibitor cocktail, pH 6.8) was

added to each sample. Prior to analysis, samples were heated for 5 min at 65 °C, and sheared through 21 and 26-gauge needles (Becton Dickinson).

2.2.7 Immunodetection

HEK293 cells were transiently transfected with cDNA as described. Unless otherwise indicated, cells were rinsed with phosphate-buffered saline (PBS: 140 mM NaCl, 3 mM KCl, 6.5 mM NaH₂PO₄, 1.5 mM KH₂PO₄, pH 7.4) and harvested with IPB buffer, supplemented with protease inhibitor cocktail. Cell lysates were mixed with one volume of 2x SDS-PAGE sample buffer. Prior to analysis samples were heated for 5 min at 65 °C. Samples were resolved by SDS-PAGE on 6 or 7.5% acrylamide gels [14]. Proteins were transferred to PVDF membranes by electrophoresis for 1 h at 100 V at 20 °C [15]. PVDF membranes were blocked by incubation for 1 h at 20 °C in TBST-M buffer (TBST buffer (0.1% (v/v) Tween-20, 137 mM NaCl, 20 mM Tris, pH 7.5), containing 10% (w/v) non-fat dry milk) and then incubated at 4 °C for 16-18 h in TBST-M, containing 1:5000 or 1:10,000 diluted rabbit anti-RFP polyclonal antibody, 1:3000 diluted mouse anti-AE1 monoclonal antibody (IVF12), or 1:1000 diluted mouse anti-GAPDH polyclonal antibody. After successive washes with TBST, blots were incubated for 1 h with TBST-M, containing 1:3000 or 1:5000 diluted donkey anti-rabbit IgG conjugated to horseradish peroxidase or 1:3000 diluted sheep anti-mouse IgG conjugated to horseradish peroxidase. Blots were visualized, using ECL reagent and a Kodak Image Station 440CF (Kodak,

NY, USA). Densitometry analysis was performed with Kodak Molecular Imaging Software.

2.2.8 Measurement of fluorescence in intact HEK293 cells

HEK293 cells, grown and transfected on 25 mm glass coverslips were mounted in a 35 mm diameter Attofluor Cell Chamber (Molecular Probes). The chamber holds a custom-built insert, reducing the internal diameter to 13 mm and chamber volume to approximately 0.2 ml. During experiments the chamber was perfused at 3.5 ml/min. The chamber was placed on one of two microscope stages (defined in next two paragraphs).

For all experiments detailed in chapter 3, and experiments pertaining to Figs. 4.1 and 4.2) in chapter 4, the cell chamber was placed on the stage of a Leica DMIRB inverted microscope, equipped with a PTI (Photon Technologies International, London, Canada) D-104 microscope photometer. The light source, connected to the microscope via a fiber optic cable, was a 75 W xenon arc lamp in a PTI DeltaScan excitation monochromator, equipped with a chopper to enable dual excitation wavelength measurements. Excitation wavelengths were set to i) 400 nm (when monitoring deGFP4), or ii) 550 nm (when monitoring mNect), or iii) 440 and 502.5 nm (when monitoring BCECF). Wavelengths of emitted light were selected with i) a cube mounted in the microscope, containing a 425-nm beamsplitter, and a cube mounted in the photometer containing a 485-nm beamsplitter, a 445- to 475-nm emission filter, and a 495- to 525-nm emission filter (deGFP4 only), ii) a cube mounted in the microscope, containing a 570 nm

beamsplitter and a 575-625 nm emission filter (mNect), or iii) a cube mounted in the microscope containing a 515 nm beamsplitter and a 522.5-547.5 nm emission filter (BCECF). Fluorescence data was acquired at 1 point/s.

Alternatively, for the remainder of the experiments in chapter 4, the chamber was placed on the stage of Wave FX Spinning Disc Confocal Microscope (Quorum Technologies, Guelph, Canada), using the Yokogawa CSU10 scanning head complemented with an emission filterwheel (Ludl MAC5000) carrying a dual bandpass (500-535 nm and 568-616 nm) emission filter (Chroma). The Olympus IX81 motorized inverted microscope has a motorized XY stage with Piezo Focus Drive (ASI, MS-4000 XYZ Automated Stage) and live cell environment chamber (Chamlide, Korea), set to 24 °C or 37 °C. Acquisition was performed with Hamamatsu C9100-13 Digital Camera (EM-CCD), 20x objective (air immersion, numerical aperture 0.75), DAPI laser (404 nm, for deGFP4) and RFP laser (561 nm, for mNect). deGFP4 fluorescence data was acquired at 2 points/s, and mNect fluorescence data was acquired at 0.5 points/s (to minimize photobleaching). Lasers are from Spectral Applied Research Inc (Richmond Hill, ON, Canada). Image analysis was performed with Volocity 4.2 software (PerkinElmer, ON, Canada).

2.2.9 Spectral characterization of deGFP4 and mNectarine expressed in HEK293 cells

HEK293 cells, transiently transfected with deGFP4 or mNect cDNAs, were solubilised with 5% Triton X-100, 50 mM phosphate, pH 7.6 and lysates

collected following centrifugation for 2 min at 18 300 x g. Lysates were added to 50 mM phosphate, pH 7.6. Excitation and emission scans were collected at respective fixed emission and excitation wavelengths 510 and 400 nm (for deGFP4) and 590 and 550 nm (for mNect), with sample in the cuvette of a PTI fluorimeter. Scans were normalized by setting peak fluorescence to 1.0.

To measure spectral characteristics of intact HEK293 cells, cells were mounted on the microscope stage, as described above, and cytosolic pH was clamped to be the same as extracellular pH by perfusion in pH clamping buffer (5 mM glucose, 140 mM KCl, 5 mM potassium gluconate, 1 mM calcium gluconate, 1 mM MgSO₄, 2.5 mM sodium phosphate, 30 mM HEPES), containing 20 μM nigericin, with pH set to 6.5, 7.0, and 7.5. The photometer/microscope were configured for deGFP4 or mNect fluorescence measurements, as described above. Excitation scans from 340-450 nm (for deGFP4) and 505-565 nm (for mNect) were collected, and all data (deGFP4 or mNect, and vector alone transfected cells) was normalized to the peak fluorescence value found for FP-transfected cells clamped to pH 7.5.

2.2.10 Fluorescence quenching

HEK293 cells transiently transfected with deGFP4 or mNect cDNA were solubilised with 5% Triton X-100, 50 mM phosphate, pH 7.6 and lysates collected following centrifugation for 2 min at 18 300 x g. Lysates were titrated with 50 mM phosphate, pH 4.0 to assess fluorescence quenching by H⁺, and with 400 mM or 4.0 M NaCl to assess fluorescence quenching by Cl⁻. deGFP4 fluorescence

was monitored at $\lambda_{\text{ex}} = 400$ nm and $\lambda_{\text{em}} = 510$ nm, and mNect fluorescence was monitored at $\lambda_{\text{ex}} = 550$ nm and $\lambda_{\text{em}} = 573$ nm, in a PTI DeltaScan fluorimeter.

All fluorescence values were corrected for the added volume of quencher (Q). The relative fluorescence change F_0/F was plotted versus the quencher concentration for each experiment. The resulting plots were fitted to the Stern-Volmer relationship:

$$F_0/F = K_{\text{sv}}[Q] + 1$$

where the slope, K_{sv} , is the Stern-Volmer constant that relates the quenching of fluorescence to $[Q]$, F_0 is the initial fluorescence intensity, and F is fluorescence intensity in the presence of added quencher [16].

2.2.11 Calibration of fluorescence values for pH

To convert the fluorescence values observed for deGFP4 and mNect (including FP-fusions), and BCECF to pH, transfected HEK293 cells mounted on the microscope stage were sequentially perfused with pH clamping buffers, containing 20 μM nigericin, at known pH values of approximately 6.5, 7.0, and 7.5 [17]. To minimize the period of sample illumination, samples were perfused without illumination for 480 s in each solution prior to collecting fluorescence data. Fluorescence counts were measured, and in the case of deGFP4 and mNect fluorescence, data were corrected for photobleaching (see section 2.2.12). A calibration curve relating the average fluorescence of each pH-probe at each pH to the medium pH value was fitted to a straight line by linear regression. The

resulting equation for the line was used to transform fluorescence data to intracellular pH.

2.2.12 Photobleaching correction

HEK293 cells expressing cytosolic FPs, or FP-fusions were perfused with nigericin/high potassium solution, pH 7.0, to clamp cytosolic pH, and excited as described in section 2.2.8. Fluorescence values over time were converted to F/F_0 and fitted with an exponential decay equation of the form:

$$Y = \text{Span} * \exp(-K * X) + \text{Plateau}$$

where fluorescence starts at $\text{Span} + \text{Plateau}$ and decays to Plateau with rate constant K . The half life is $0.69/K$. The variables over five experiments were averaged, and the data for each subsequent experiment was multiplied by the average decay equation (photometer data). Alternatively, the variables over three photobleaching experiments, independently assessed for deGFP4 and mNect, were averaged for each day, and the data for each experiment that day was multiplied by the average decay equation (confocal data).

2.2.13 H^+ /uridine co-transport activity assay

Transfected HEK293 cells mounted on the microscope stage (attached to photometer), as described above, were perfused at 3.5 ml/min consecutively with Na^+ -free MBSS buffer (90 mM choline chloride (ChCl), 5.4 mM KCl, 0.4 mM $MgCl_2$, 0.4 mM $MgSO_4$, 5.5 mM glucose, 100 mM D-mannitol, 10 mM MES, pH

7.5), Na⁺-free MBSS buffer, pH 5.5 and Na⁺-free MBSS buffer, pH 5.5 with 0.5 μM uridine. Alternatively, cells were perfused consecutively with Na⁺-free MBSS buffer, pH 5.5, Na⁺-containing MBSS buffer (90 mM NaCl, 5.4 mM KCl, 0.4 mM MgCl₂, 0.4 mM MgSO₄, 5.5 mM glucose, 100 mM D-mannitol, 10 mM MES), pH 5.5 and Na⁺-containing MBSS buffer, pH 5.5 with 0.5 μM uridine. Some experiments contained 0.5 μM EIPA. At the end of each experiment, cells were subjected to pH calibration, using the nigericin/high potassium method (described in section 2.2.11). Between each experiment, the perfusion lines were rinsed sequentially with water, 100% ethanol and water to avoid nigericin contamination. Rates of pH_i change during the 20 s periods before and after addition of uridine were determined as the slope (dpH_i/dt) of the line fitted by the least squares method. Uridine induced pH_i change was calculated as: dpH_i/dt after addition of uridine minus dpH_i/dt before uridine addition. H⁺ flux, in units of dpH_i/dt, was converted to flux of proton equivalents/time by multiplying dpH_i/dt by the previously established intrinsic buffer capacity of HEK293 cells [18]. These experiments were performed in nominally CO₂/HCO₃⁻ free conditions, so it was assumed that the CO₂ buffer capacity would be negligible.

2.2.14 Kinetics of H⁺/uridine co-transport

Experiments were carried out as described in section 2.2.13, with various concentrations of uridine (0-960 μM). Transport rates were obtained as described above, and plotted in PRISM 4.0. Data were fitted with an equation of the form:

$$V = V_{\max} * [S] / (K_m + [S])$$

where V_{\max} is the velocity (V) at maximal substrate concentration ([S]) and K_m is the substrate concentration at which the rate is half-maximal.

2.2.15 Cl⁻/HCO₃⁻ exchange activity assay

Transfected HEK293 cells grown on glass coverslips and mounted on the microscope stage (confocal, or attached to photometer), as described in section 2.2.8, were perfused with Cl⁻-containing Ringer's buffer for 5 min before image acquisition to ensure that the pH of cells was at equilibrium. Cells were then perfused alternately with Ringer's buffer (5 mM glucose, 5 mM potassium gluconate, 1 mM calcium gluconate, 1 mM MgSO₄, 2.5 mM NaH₂PO₄, 25 mM NaHCO₃, and 10 mM HEPES, pH 7.4), containing either 140 mM NaCl or 140 mM sodium gluconate. Both buffers were continuously bubbled with 5% CO₂ (balance air) and a small shunt inserted into the custom-built insert allowed this gas mixture to be blown over the surface of the solution. At the end of each experiment, cells were subjected to pH calibration, using the nigericin/high potassium method (described in section 2.2.11). Between each experiment, the perfusion lines were rinsed sequentially with water, 100% ethanol and water to avoid nigericin contamination. Fluorescence of deGFP4 and mNect, or BCECF was monitored at the excitation and emission wavelengths described in section 2.2.8. Illumination was paused at times indicated during Cl⁻/HCO₃⁻ exchange to minimize photobleaching.

For confocal microscopy experiments, fluorescence values were obtained by using the freehand tool in Volocity 4.2 to select regions of interest (ROIs) on

fluorescent cells. Three to five cells from each coverslip were analyzed. In figure legends involving $\text{Cl}^-/\text{HCO}_3^-$ exchange, number of replicates, n , is defined as number of coverslips. Cytosolic ROIs were drawn to encompass the entire interior of cells. Plasma membrane (PM) ROIs were drawn as a thin boxed line around periphery of cells ($\sim 1 \mu\text{m}$ wide). Endoplasmic reticulum (ER) ROIs were drawn so that the centre of the ROI was about $4 \mu\text{m}$ away from the centre of the PM ROI. Background ROIs were selected in areas with no cells placed beside measured ROIs. The mean intensity of each ROI over time for the deGFP4 and mNect channels was determined using Volocity software. The mean background intensity was subtracted from the mean intensity of each FP, and photobleaching correction applied (see section 2.2.12). Corrected fluorescence values were converted to pH_i (as in section 2.2.11), and the $\text{Cl}^-/\text{HCO}_3^-$ exchange rates were calculated by linear regression of the initial rate of pH_i change (first 15 s after pH_i change detected) during perfusion with Cl^- -free Ringer's buffer (the slope (dpH_i/dt) of the line fitted by the least squares method).

2.2.16 Measurement of intrinsic buffer capacity and flux of proton equivalents

Intrinsic buffer capacity was measured using the ammonium chloride pulse method [19]. Briefly, HEK293 cells grown on glass coverslips and transfected with deGFP4.AE1 cDNA were mounted on the confocal microscope stage and perfused consecutively with $\text{CO}_2/\text{HCO}_3^-$ -free Ringer's buffer containing 50, 0, 1, 5, 10, and 20 mM NH_4Cl . At the end of each experiment, cells were

subjected to pH calibration, using the nigericin/high potassium method (described in section 2.2.11). deGFP4 fluorescence in PM ROIs was corrected for photobleaching and converted to pH_i , as described in sections 2.2.11 and 2.2.12. The intracellular NH_4Cl concentration ($[NH_4Cl]_i$) was calculated using the Henderson-Hasselbalch equation, and the intrinsic buffer capacity (β_i) was calculated as $\Delta([NH_4Cl]_i)/\Delta pH_i$ (mM/pH) [19]. Total buffer capacity (β_{total}) was calculated as $\beta_{total} = \beta_i + \beta_{CO_2}$, where $\beta_{CO_2} = 2.3 \times [HCO_3^-]$ [18]. Flux of proton equivalents (in $mM \cdot min^{-1}$) was then calculated as $dpH_i/dt \cdot \beta_{total}$ [18].

2.2.17 Measuring the time of initial pH rise

Cl^-/HCO_3^- exchange assays were carried out on transfected HEK293 cells, and analyzed as described in section 2.2.15. Transport rates were determined by linear regression of the initial rate of pH_i change upon switching to Cl^- -free Ringer's buffer. The baseline pH_i was also fitted by linear regression. The point at which the two lines intersect was determined mathematically and that point on the X-axis (time, s) was defined as the time at which each FP begins to detect a change in pH_i . The time at which the medium was switched to Cl^- -free Ringer's buffer was subtracted from this value to get the absolute time to detect the pH_i change. Alternatively, HEK293 cells transiently transfected with deGFP4.AE1 cDNA were perfused with CO_2/HCO_3^- -free Ringer's buffer containing 50 mM, then 0 mM NH_4Cl , and response time determined as above.

2.2.18 Quantification of ER-associated fluorescence in PM ROI

HEK293 cells were grown on 25 mm round coverslips, and co-transfected with deGFP4.AE1 and CNX.mNect cDNA, or deGFP4.AE1 and mNect.hCNT3-F563C cDNA. Cells were placed on the stage of a confocal microscope, and perfused continuously with Ringer's buffer, pH 7.4. Cells were illuminated as described above for 30 s. ROIs were drawn along the plasma membrane of the cell. The mean intensity of each ROI over time for the deGFP4 and mNect channels was determined using Volocity software. The mean background intensity was subtracted from the mean intensity of each FP. To correct for differences in ROI size and protein expression efficiency, fluorescence values were normalized to give the same deGFP4 fluorescence in both cell types. The intensity of mNect fluorescence in the ER was assumed to be the same for cells expressing CNX.mNect or mNect.hCNT3-F563C. In this way the % ER-associated mNect fluorescence in PM ROI = $\text{CNX.mNect fluorescence} / \text{mNect.hCNT3-F563C fluorescence} \times 100\%$.

2.2.19 Perfluorooctanoic acid polyacrylamide gel electrophoresis (PFO-PAGE)

The basic technique used was described previously [20-22]. HEK293 cells were transiently transfected with mNect.hCNT3 or AE1. Two days post-transfection, HEK293 cells were washed twice with PBS, supplemented with protease inhibitor cocktail. Cells were solubilised by the addition of 1% Igepal

(in PBS) for 20 min on ice. Cellular debris was removed by centrifugation at 4 °C for 10 min at 15 800 x g. Cell lysate (40 µg of protein) was mixed with one volume of 2x PFO sample buffer (20% (v/v) glycerol, 0.005% (w/v) bromophenol blue, 0-8% (w/v) PFO, 100 mM Tris, pH 8.0) with, or without 25 mM dithiothreitol (DTT). AE1 was analyzed with PFO sample buffer that contained DTT. Samples were mixed gently, and incubated at 4° C for 15 min prior to loading on a 6% polyacrylamide gel without SDS. Electrophoresis was carried out at 4° C at 100 V with 4° C running buffer (192 mM glycine, 0.5% (w/v) PFO, 25 mM Tris, pH 8.5).

2.2.20 Cell surface processing assay

HEK293 cells were transfected with varying ratios of deGFP4:AE1:mNect:hCNT3-F563C cDNA, or with empty vector. The same cDNA ratios used for Cl⁻/HCO₃⁻ exchange assays were used for cell surface processing. Two days post-transfection, HEK293 cells were placed on ice, washed twice with 4 °C PBS supplemented with protease inhibitors, washed with 4° C borate buffer (154 mM NaCl, 7.2 mM KCl, 1.8 mM CaCl₂, 10 mM boric acid, pH 9.0) and then incubated for 20 min at 4° C in borate buffer, containing 0.5 mg/ml Sulpho-NHS-SS-Biotin. Cells were washed three times with 4 °C quenching buffer (192 mM glycine, 25 mM Tris, pH 8.3) and then solubilised with IPB buffer, supplemented with protease inhibitor cocktail. Cell lysates were centrifuged for 20 min at 16 300 x g and supernatant collected. Half of the supernatant was retained for later SDS-PAGE analysis (total protein, T). The

remainder was incubated with streptavidin agarose resin (100 μ L of 50% slurry in PBS, containing 0.02% sodium azide) for 16 h at 4 °C, with gentle rotation. Samples were centrifuged for 2 min at 7 600 x g, and supernatant was collected (unbound protein, U). Equal volumes of biotin-free (U) and total (T) lysates were separated by SDS-PAGE, as described above. deGFP4.AE1, mNect.hCNT3-F563C and GAPDH (negative control) were detected by immunoblot as described above, using mouse anti-AE1 monoclonal antibody (IVF12), rabbit anti-RFP polyclonal antibody, or mouse anti-GAPDH monoclonal antibody, respectively. After densitometric quantification of the appropriate bands, the percentage of biotinylated protein was calculated as $(T-U)/T \times 100\%$.

2.2.21 Distribution of deGFP4.AE1, mNect.hCNT3 and mNect.hCNT3-F563C at the plasma membrane

HEK293 cells transfected with mNect.hCNT3 or mNect.hCNT3-F563C cDNA, or co-transfected with deGFP4.AE1 and mNect.hCNT3-F563C cDNAs were analyzed by confocal microscopy as described in section 2.2.8. The level of FP abundance across the entire cell (plasma membrane, cytosol, and plasma membrane), or along portions of the plasma membrane was analyzed with ImageJ software (National Institutes of Health). Pixel intensity versus distance was plotted, and the area under the curve was analyzed with PRISM software.

2.2.22 Calculation of average distance between deGF4P.AE1 and mNect.hCNT3-F563C molecules

HEK293 cells grown on glass coverslips were co-transfected with cDNA encoding deGFP4.AE1, mNect.hCNT3-F563C, and untagged hCNT3. Cl⁻/HCO₃⁻ exchange assays were carried out as described in section 2.2.15. Cells were harvested at the end of each experiment, and saved for later SDS-PAGE analysis. deGFP4.AE1 and mNect.hCNT3-F563C expression levels were quantified, using three standards that were run alongside all experimental protein samples on SDS-PAGE gels. The molar amount (per 10 μ L aliquot) of two of these standards, deGFP4.AE1 and mNect.AE1, were quantified by densitometry in comparison to a known amount of AE1-Ct standard (a purified GST fusion protein containing the last 40 amino acids (residues 872-911) of AE1) [23], using the anti-AE1 (IVF12) antibody. The third standard is a sample in which cells were harvested, counted, and a known amount used as a cell number standard on subsequent blots. The standards and experimental samples for each day were separated by SDS-PAGE and immunoblotted. Immunoblots were probed for GAPDH (as a measure of number of cells), AE1, and RFP, which enabled the number of molecules/cell for deGFP4.AE1 and mNect.hCNT3-F563C to be determined by densitometry. This value was multiplied by the percent of protein at the cell surface (as determined by cell surface processing assays) to determine the absolute number of deGFP4.AE1 dimers and mNect.hCNT3-F563C monomers at the cell surface/cell. The cell surface area of 2591 μ m² for HEK293 cells [24], did not take into account processes extending from the cell surface, which were detected by

electron microscopy, which increase surface area by 50.3%. We therefore estimated that HEK293 cell surface area as 3887 μm^2 [25]. The average deGFP4.AE1 dimer to mNect.hCNT3-F563C monomer distance was calculated as the square root of $(3887 \mu\text{m}^2 / (\text{number deGFP4.AE1 dimers} + \text{number of mNect.hCNT3-F563C monomers}))$.

2.2.23 Statistical analysis

Values are expressed \pm standard error of measurement. Statistical significance was determined using an unpaired t test (PRISM software), with $p < 0.05$ considered significant.

Bibliography

1. Campbell RE, Tour O, Palmer AE, Steinbach PA, Baird GS, Zacharias DA & Tsien RY (2002) A monomeric red fluorescent protein. *Proc Natl Acad Sci U S A* **99**, 7877-7882.
2. Griesbeck O, Baird GS, Campbell RE, Zacharias DA & Tsien RY (2001) Reducing the environmental sensitivity of yellow fluorescent protein. Mechanism and applications. *J Biol Chem* **276**, 29188-29194.
3. Ai HW, Henderson JN, Remington SJ & Campbell RE (2006) Directed evolution of a monomeric, bright and photostable version of Clavularia cyan fluorescent protein: structural characterization and applications in fluorescence imaging. *Biochem J* **400**, 531-540.
4. Casey JR, Ding Y & Kopito RR (1995) The role of cysteine residues in the erythrocyte plasma membrane anion exchange protein, AE1. *J Biol Chem* **270**, 8521-8527.
5. Tang XB, Fujinaga J, Kopito R & Casey JR (1998) Topology of the region surrounding Glu681 of human AE1 protein, the erythrocyte anion exchanger. *J Biol Chem* **273**, 22545-22553.
6. Hanson GT, McAnaney TB, Park ES, Rendell ME, Yarbrough DK, Chu S, Xi L, Boxer SG, Montrose MH & Remington SJ (2002) Green fluorescent protein variants as ratiometric dual emission pH sensors. 1. Structural characterization and preliminary application. *Biochemistry* **41**, 15477-15488.
7. Zhang J, Tackaberry T, Ritzel MW, Raborn T, Barron G, Baldwin SA, Young JD & Cass CE (2006) Cysteine-accessibility analysis of transmembrane domains 11-13 of human concentrative nucleoside transporter 3. *Biochem J* **394**, 389-398.
8. Slugoski MD, Ng AM, Yao SY, Smith KM, Lin CC, Zhang J, Karpinski E, Cass CE, Baldwin SA & Young JD (2008) A proton-mediated conformational shift identifies a mobile pore-lining cysteine residue (Cys-561) in human concentrative nucleoside transporter 3. *J Biol Chem* **283**, 8496-8507.
9. Shaner NC, Campbell RE, Steinbach PA, Giepmans BN, Palmer AE & Tsien RY (2004) Improved monomeric red, orange and yellow fluorescent proteins derived from *Discosoma sp.* red fluorescent protein. *Nat Biotechnol* **22**, 1567-1572.

10. Shaner NC, Steinbach PA & Tsien RY (2005) A guide to choosing fluorescent proteins. *Nat Methods* **2**, 905-909.
11. Ai HW, Shaner NC, Cheng Z, Tsien RY & Campbell RE (2007) Exploration of new chromophore structures leads to the identification of improved blue fluorescent proteins. *Biochemistry* **46**, 5904-5910.
12. Graham FL, Smiley J, Russell WC & Nairn R (1977) Characteristics of a human cell line transformed by DNA from human adenovirus type 5. *J Gen Virol* **36**, 59-74.
13. Ruetz S, Lindsey AE, Ward CL & Kopito RR (1993) Functional activation of plasma membrane anion exchangers occurs in a pre-Golgi compartment. *J Cell Biol* **121**, 37-48.
14. Laemmli UK (1970) Cleavage of structural proteins during the assembly of the head of bacteriophage T4. *Nature* **227**, 680-685.
15. Towbin H, Staehelin T & Gordon J (1979) Electrophoretic transfer of proteins from polyacrylamide gels to nitrocellulose sheets: procedure and some applications. *Proc Natl Acad Sci U S A* **76**, 4350-4354.
16. Eftink MR & Ghiron CA (1975) Dynamics of a protein matrix revealed by fluorescence quenching. *Proc Natl Acad Sci U S A* **72**, 3290-3294.
17. Thomas JA, Buchsbaum RN, Zimniak A & Racker E (1979) Intracellular pH measurements in Ehrlich ascites tumor cells utilizing spectroscopic probes generated in situ. *Biochemistry* **18**, 2210-2218.
18. Sterling D & Casey JR (1999) Transport activity of AE3 chloride/bicarbonate anion-exchange proteins and their regulation by intracellular pH. *Biochem J* **344 Pt 1**, 221-229.
19. Loiselle FB & Casey JR (2010) Measurement of Intracellular pH. *Methods Mol Biol* **637**, 311-331.
20. Ramjeesingh M, Huan LJ, Garami E & Bear CE (1999) Novel method for evaluation of the oligomeric structure of membrane proteins. *Biochem J* **342 (Pt 1)**, 119-123.
21. Penna A, Demuro A, Yeromin AV, Zhang SL, Safrina O, Parker I & Cahalan MD (2008) The CRAC channel consists of a tetramer formed by Stim-induced dimerization of Orai dimers. *Nature* **456**, 116-120.
22. Kedei N, Szabo T, Lile JD, Treanor JJ, Olah Z, Iadarola MJ & Blumberg PM (2001) Analysis of the native quaternary structure of vanilloid receptor 1. *J Biol Chem* **276**, 28613-28619.

23. Bonar P & Casey JR (2010) Purification of functional human Cl⁻/HCO₃⁻ exchanger, AE1, over-expressed in *Saccharomyces cerevisiae*. *Protein Expr Purif* **74**, 106-115.
24. Sommerhage F, Helpenstein R, Rauf A, Wrobel G, Offenhausser A & Ingebrandt S (2008) Membrane allocation profiling: a method to characterize three-dimensional cell shape and attachment based on surface reconstruction. *Biomaterials* **29**, 3927-3935.
25. Gentet LJ, Stuart GJ & Clements JD (2000) Direct measurement of specific membrane capacitance in neurons. *Biophys J* **79**, 314-320.

Chapter 3: Red Fluorescent Protein pH Biosensor to Detect Concentrative Nucleoside Transport

A version of this chapter has been published as Johnson, D.E., H.W. Ai, P. Wong, J.D. Young, R.E. Campbell, and J.R. Casey. 2009. Red Fluorescent Protein pH Biosensor to Detect Concentrative Nucleoside Transport. *J Biol Chem.* 284:20499-20511. (Reproduced with permission).

The work presented in this chapter represents a collaboration between the authors on the paper. D.E.J. performed all of the experiments and analysis except engineering mNectarine and characterization of purified mNectarine protein, which was performed by H.W.A. and P.W.

3.1 Introduction

Nucleosides are hydrophilic molecules that require transport proteins to mediate their movement across the plasma membrane [1]. Human (h) nucleoside transport (NT) proteins catalyze the vectorial transport of nucleosides, using either concentrative (C) or equilibrative (E) mechanisms [2]. hCNTs use either a Na^+ or H^+ gradient to accumulate nucleosides against their concentration gradient, while hENTs mediate facilitated diffusion of nucleosides down their concentration gradient [3]. Nucleoside transporters also transport anti-cancer and anti-viral drugs, and cellular expression of nucleoside transporters is important in cancer therapy as well as in the treatment of cardiovascular, parasitic and viral diseases [4, 5].

Members of the SLC28 family of concentrative nucleoside transporters (CNTs) divide into two phylogenetic subfamilies: hCNT1/2 belonging to one subfamily, and hCNT3 to the other [6-8]. Cation substitution and charge/flux ratio studies suggest that hCNT1/2 couple the inward movement of nucleoside to the Na^+ electrochemical gradient with a 1:1 stoichiometry, while hCNT3 can couple nucleoside transport to either the Na^+ gradient (2 Na^+ : 1 nucleoside) or a H^+ gradient (1 H^+ : 1 nucleoside) in the absence of Na^+ [9, 10]. The 2:1 coupling ratio of hCNT3 allows it to develop a trans-membrane nucleoside concentration gradient up to 10-fold higher than that of hCNT1 or hCNT2 [9, 11]. At pH 5.5, hCNT3 also transports uridine in the presence of Na^+ with a 2 cation: 1 nucleoside stoichiometry, which raises the possibility that 1 H^+ and 1 Na^+ may be transported

per nucleoside molecule in these conditions [9-12]. Up to this point, however, there has been no direct demonstration that hCNT3 can transport H^+ .

Concentrative nucleoside transport has previously been investigated using the *Xenopus laevis* oocyte expression system and both electrophysiology (two-microelectrode voltage-clamp technique) and radioisotope flux measurements [6-9, 12]. Electrophysiological experiments are advantageous in that they measure the current induced by addition of substrate in real time, but they are time consuming and require specialized equipment and skills. Radioisotope flux assays measure the accumulation of radiolabelled substrate. The need for radiolabelled substrate restricts the range of permeants able to be studied. In addition, radioisotope flux assays are not done in real time and are labour-intensive, requiring large numbers of oocytes.

An attractive alternative approach for the study of hCNT3 would be to measure pH in the immediate vicinity of its intracellular face during H^+ /nucleoside co-transport. These measurements could take advantage of the remarkable progress achieved in the development of genetically encoded fluorophores [13]. Indeed, all members of the extended family of homologues and variants of the *Aequorea victoria* green fluorescent protein (avGFP) exhibit pH-dependent changes in their fluorescent intensity. The spectral changes that occur upon a change in pH can be intensimetric [14], excitation ratiometric [14], emission ratiometric [15], or both excitation and emission ratiometric [16]. The apparent pK_a (equal to the pH at which the fluorescence is half maximal in intensity) for a specific fluorescent protein (FP) is acutely dependent on specific

amino acid substitutions in close proximity to the chromophore and can range from less than 3 [17, 18] to greater than 8 [19]. Variants with pK_a values that are relatively close to intracellular pH values (*i.e.*, ~ 7.3 for the mammalian cytosol [20]) are particularly useful as genetically encoded biosensors for dynamic measurement of proton concentrations in living cells.

A major development in the area of FP technology has been the identification [21] and subsequent optimization [22, 23] of red fluorescent protein (RFP) homologues of avGFP. The first (monomeric RFP 1 (mRFP1))[23] and second (the mFruit series) [22] generation optimized RFPs, derived from tetrameric *Discosoma* RFP (DsRed) [21], suffer from relatively low brightness relative to other common hues of FP. For example, of the three most red shifted second generation mFruit variants (mTangerine, mStrawberry, and mCherry) [22], the brightest (mStrawberry) has only 44% of the intrinsic brightness (proportional to the product of extinction coefficient (ϵ) and quantum yield (Φ)) of the popular yellow FP (YFP) Citrine [24] and 76% of the brightness of enhanced avGFP (EGFP). This limitation has been partially addressed by third generation mRFPs, specifically mApple and TagRFP-T with fluorescent brightness values on par with, or better than, that of EGFP [25].

Generally speaking, the most red-shifted RFPs derived from DsRed are relatively pH-insensitive, with the majority of variants having pK_a values < 5 [22, 25]. A notable exception is the recently reported mApple variant with a pK_a of 6.5 [25]. The more blue-shifted of the mFruit variants (*i.e.*, mOrange) also have

pK_a values of 6.5 [22]. Several variants of mRFP1 with pK_a values greater than 7.5 have been previously reported [26].

Here we report the engineering of a pH-sensitive mFruit variant through multiple rounds of directed evolution by random mutagenesis. This RFP, called mNectarine, is appropriate to measure physiological pH changes in mammalian cells, as it has a pK_a of 6.9. We have developed a new method to measure H^+ /nucleoside co-transport in mammalian cells, which utilizes hCNT3's H^+ coupling characteristics and mNectarine's pH sensitivity. We fused mNectarine to the cytosolic N-terminus of hCNT3 to generate mNect.hCNT3. Fusion of the fluorescent H^+ sensor to hCNT3 enabled measurement of pH at the intracellular surface of hCNT3, and provided insight into the mechanism of hCNT3 H^+ /uridine co-transport.

3.2 Results

3.2.1 Engineering mNectarine

With the goal of engineering an mRFP with improved brightness, we chose mTangerine (the Q66C/T147S/Q213L variant of mRFP1) [22] for further optimization by directed evolution. We selected mTangerine because: 1. it has the highest fluorescence quantum yield of the most red-shifted second generation mRFPs [22]; 2. its absorbance profile makes it well suited as a potential fluorescence resonance energy transfer (FRET) acceptor from a YFP donor; and 3. relatively little effort had been previously expended on its optimization [22].

We first transferred the characteristic mTangerine mutations (M66C and Q213L) to an engineered homologue that had already been subjected to extensive directed evolution for brightness and folding efficiency (mCherry2, the K92N/K138C/K139R/S147T/N196D/T202L variant of mCherry) (Nathan C. Shaner and Roger Y. Tsien, unpublished results) (Fig. 3.1). mCherry2-M66C/Q213L had a fluorescence hue similar to that of mTangerine, yet had intrinsic fluorescent brightness that was 1.1x that of mCherry and 1.5x that of mTangerine (Table 3.1). This variant was used as the template for the first of five iterative rounds of random mutagenesis and manual fluorescence-based screening of large randomized libraries (each on the order of 10^5 variants) expressed in bacterial colonies. In each round the brightest colonies were picked, plasmids isolated, and the pool of improved FP genes used as the template for the subsequent library. We have successfully applied this basic strategy to the optimization of a teal FP [27], blue FPs [17], and a YFP with violet excitation [28].

During this process, the protein accumulated four additional substitutions relative to the initial template: F91L, M141V, Y151H, and K162M. The resulting protein was an mRFP with intrinsic brightness (Table 3.1) that was considerably greater than that of mCherry and mTangerine [22] (1.6x and 2.3x, respectively) but still somewhat less than that of mApple and TagRFP-T [25] (0.71x and 0.78x, respectively). The excitation and emission maxima of the final variant (excitation maximum at 558 nm and emission maximum at 578 nm) were different enough

Table 3.1. **Properties of mNectarine and related variants.** Brightness is the product of extinction coefficient and quantum yield. For comparison, the brightness values of EGFP and mCherry are 34 and 16 $\text{mM}^{-1}\text{cm}^{-1}$, respectively [29]. Photobleaching half-time represents the time to bleach from an initial emission rate of 1000 photons/molecule/second to 500 photons/molecule/second. * measured in PBS (pH 8.0), using mTangerine as the reference. ND, not determined.

| | λ_{ex} (nm) maximum | λ_{em} (nm) maximum | Extinction coefficient ($\text{mM}^{-1}\text{cm}^{-1}$) | Fluorescence quantum yield | Brightness | pK_{a} | $t_{0.5}$ for maturation at 37 °C | $t_{0.5}$ for bleach (s) (arc lamp) |
|-------------------------|---------------------------------------|---------------------------------------|---|-------------------------------|------------|------------------------|---|---|
| mTangerine | 568 | 585 | 38 | 0.30 | 11 | 5.7 | 1.5 h | 5.1 |
| mCherry2- M66C/Q213L | 558 | 580 | 44* | 0.40* | 18 | ND | ND | ND |
| mNectarine | 558 | 578 | 58* | 0.45* | 26 | 6.9 | 30 min | 11 |

from that of mTangerine, and every other variant in the existing palette, that we decided to designate it with the name ‘mNectarine’ (Fig. 3.1).

3.2.2 pH sensitivity of mNectarine

Characterization of mNectarine revealed that its fluorescence was remarkably pH-sensitive, with an apparent pK_a of 6.9 (Fig. 3.2A-B). The data points shown in Figure 3.2B were fitted to a curve of the general form:

$$I_{pH} = \frac{I_{\max}}{10^{(pK_a - pH)} + 1}$$

where I_{pH} is the fluorescence intensity at a given pH and I_{\max} is the highest fluorescence intensity at any pH. An equation of similar form was used to fit the absorbance data points as shown in Figure 3.2D.

Absorbance spectra of mNectarine recorded at various pHs revealed a complex change in profile that appears to include a mixture of anionic cyan-absorbing ($\lambda_{\max} = 489$ nm) and orange-absorbing ($\lambda_{\max} = 558$ nm) forms of the protein at high pH and a mixture of protonated violet-absorbing ($\lambda_{\max} = 387$ nm) and blue-absorbing ($\lambda_{\max} = 453$ nm) forms of the protein at low pH (Fig. 3.2C). A reasonable explanation of these changes is that the purified and aged protein exists as a mixture of an orange-absorbing/red-fluorescing species and a ‘dead-end’ cyan-absorbing/non-fluorescent species with an avGFP-type chromophore. Accordingly, the cyan and violet species may represent two ionization states of one distinct form of an avGFP-type chromophore, while the orange and blue

```

1 2 3 3b 3c 4 5 6 6a 6b 7 8 9 10 11 12 13 14 15 16 17 18 19 20 21 22 23 24 25 26 27 28 29 30 31 32 33 34 35 36 37 38 39 40 41 42 43
M V S K G E E D N M A I I K E F M R F K V H M E G S V N G H E F E I E G E G R R P Y E G T Q T
mNectarine A K L K V T K K G T K G G P L P F A W D I L S P Q F C Y G S K A A V K H P A D I P D Y L K L S F P E G L
mCherry2 A K L K V T K K G T K G G P L P F A W D I L S P Q F C Y G S K A A V K H P A D I P D Y L K L S F P E G L
mCherry A K L K V T K K G T K G G P L P F A W D I L S P Q F C Y G S K A A V K H P A D I P D Y L K L S F P E G L
mTangerine A K L K V T K K G T K G G P L P F A W D I L S P Q F C Y G S K A A V K H P A D I P D Y L K L S F P E G L
44 45 46 47 48 49 50 51 52 53 54 55 56 57 58 59 60 61 62 63 64 65 66 67 68 69 70 71 72 73 74 75 76 77 78 79 80 81 82 83 84 85 86 87 88 89 90 91
mNectarine N W E R V M N F E D G G V V T V T T V T T Q D S L Q D D G E F I Y K V K L R G G T N F P S D G G P V M Q C R
mCherry2 N W E R V M N F E D G G V V T V T T V T T Q D S L Q D D G E F I Y K V K L R G G T N F P S D G G P V M Q C R
mCherry K W E R V M N F E D G G V V T V T T V T T Q D S L Q D D G E F I Y K V K L R G G T N F P S D G G P V M Q C R
mTangerine K W E R V M N F E D G G V V T V T T V T T Q D S L Q D D G E F I Y K V K L R G G T N F P S D G G P V M Q C R
140 141 142 143 144 145 146 147 148 149 150 151 152 153 154 155 156 157 158 159 160 161 162 163 164 165 166 167 168 169
V G W E A S T E R M H P E D G A L L K G E I M Q R L K L K D G G H Y D A E V K T T Y K A K K P V
mNectarine T M G W E A S T E R M H P E D G A L L K G E I M Q R L K L K D G G H Y D A E V K T T Y K A K K P V
mCherry2 T M G W E A S T E R M H P E D G A L L K G E I M Q R L K L K D G G H Y D A E V K T T Y K A K K P V
mTangerine T M G W E A S T E R M H P E D G A L L K G E I M Q R L K L K D G G H Y D A E V K T T Y K A K K P V
188 189 190 191 192 193 194 195 196 197 198 199 200 201 202 203 204 205 206 207 208 209 210 211 212 213 214 215 216 217 218 219 220 221 222 223 224 225 226 227 228 229 230 231
L P G A Y N V D I K L D I L S H N E D Y T I V E Q Y E R A E G R H S T G G M D E L Y K
mNectarine Q L P G A Y N V D I K L D I L S H N E D Y T I V E Q Y E R A E G R H S T G G M D E L Y K
mCherry2 Q L P G A Y N V D I K L D I L S H N E D Y T I V E Q Y E R A E G R H S T G G M D E L Y K
mTangerine Q L P G A Y N V D I K L D I L S H N E D Y T I V E Q Y E R A E G R H S T G G M D E L Y K

```

Figure 3.1. **Sequence alignment of mNectarine and related variants.** The chromophore forming residues are indicated with an enclosing box. Residues are numbered using the convention for mRFPs. Letters a, b, and c have been used to denote where additional residues have been inserted near the N-terminus, in order to keep the numbering through the rest of the protein consistent with the original DsRed variant. The accession numbers in the GenBank nucleotide sequence database are as follows: mNectarine FJ439505, mCherry AAV52164 and mTangerine AAV52170. Information for mCherry2 is from Nathan C. Shaner and Roger Y. Tsien (unpublished results).

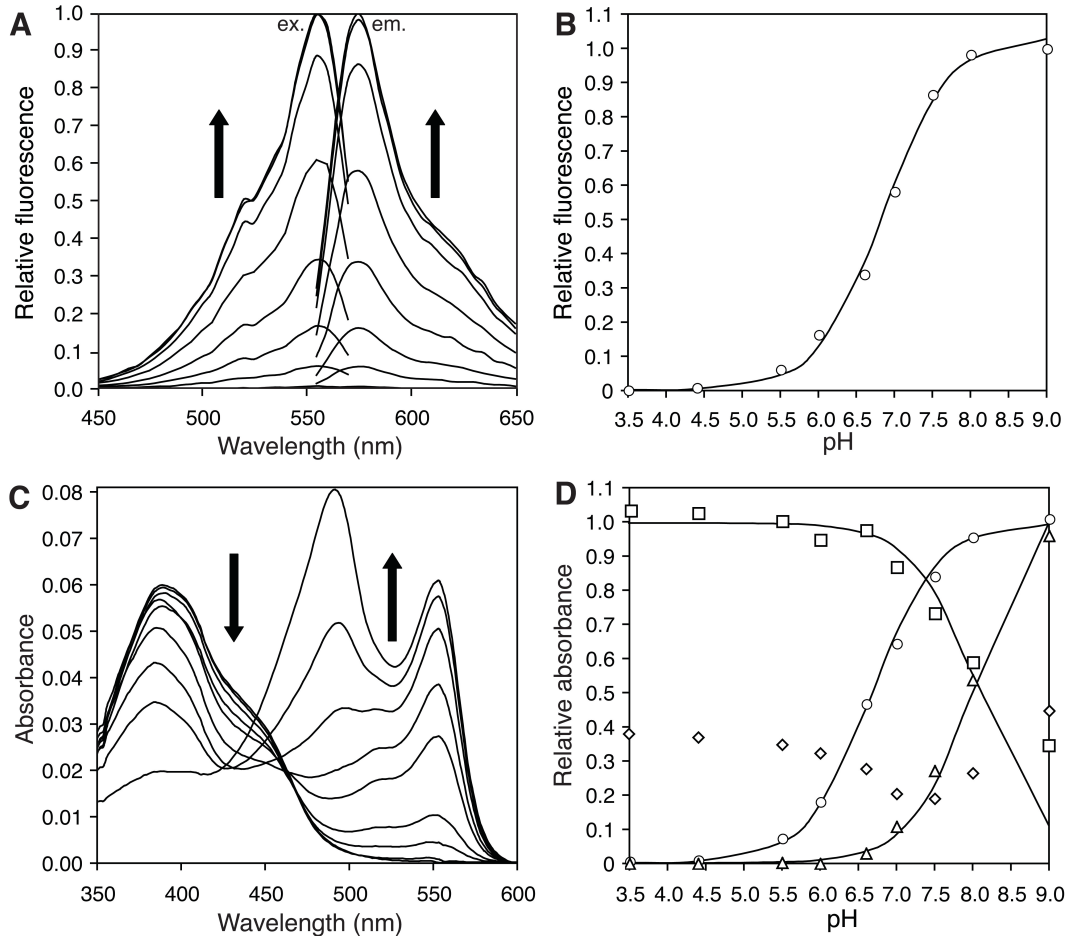


Figure 3.2. **pH-dependence of mNectarine fluorescence.** (A) Fluorescence excitation (left, emission at 600 nm) and emission (right, excitation at 550 nm) intensity for mNectarine, recorded at various pH (actual pH values presented in B). Arrows represent the direction of change with increasing pH. (B) Plot of relative fluorescence intensity versus pH for mNectarine, with excitation at 550 nm and emission at 600 nm. The curve represents the best of fit of the data obtained using a form of the Henderson–Hasselbalch equation. (C) Absorbance spectra of mNectarine at various pH. Arrows represent the direction of change with increasing pH. These spectra were subjected to a global four-component linear regression analysis (Fig. 3.3). (D) Relative absorbance intensities of each component of the spectra in C plotted as a function of pH. The four components are the red fluorescence excitation profile (○, orange-absorbing) and 3 Gaussian curves centered at 489 nm (△, cyan-absorbing), 453 nm (◇, blue-absorbing), and 387 nm (□, violet-absorbing).

species represent two ionization states of a DsRed-type (or possibly an mOrange-type, containing a third heterocycle [30]) chromophore. To investigate this hypothesis, we performed a multiple linear regression analysis of the spectra acquired at each pH in order to examine the relative contribution of each of these four components (Fig. 3.3). Efforts to fit the data with fewer than four components resulted in poor fits of the experimental data. This analysis revealed that pH dependent changes in the absorbance of the violet (decreasing with increasing pH) and cyan species (increasing with increasing pH) occur with pK_a values of approximately 8.1 (Fig. 3.2D), an observation consistent with the conclusion that these are indeed different ionization states of the same molecular species. The multiple regression analysis did not provide support for correlated changes in the orange and blue species as a function of pH, with the intensity of blue species remaining relatively constant as the intensity of orange species changed considerably. Two possible explanations for this discrepancy are that either the blue peak represents a distinct ‘dead-end’ species, or that our data is simply insufficient to enable separation of the overlapping contributions of the violet and blue peaks.

3.2.3 mNectarine.hCNT3 fusion proteins

We fused mNectarine to the N-terminus of the human nucleoside transporter, hCNT3. The N-terminus was chosen for the fusion, since the C-terminus is extracellular [8], and our goal was to measure pH at the intracellular



Figure 3.3. **Representative example of the results from the global four-component linear regression analysis of the absorbance spectra recorded at various pH.** The black circles represent the experimental data for the spectrum recorded at pH 8 (refer to Fig. 3.2). The four individual components are the red fluorescence excitation profile (orange line, orange-absorbing) and three Gaussian curves centred at 489 nm (cyan line, cyan-absorbing), 453 nm (blue line, blue-absorbing), and 387 nm (violet line, violet-absorbing). The sum of the four components is shown as a grey line.

surface of hCNT3. We wanted to use a specific and localized probe of $[H^+]$ because hCNT3 has a relatively low turnover rate (a value of 34 s^{-1} for hCNT3 was found in voltage-clamped oocytes at -150 mV [31]). Since the resting membrane potential of mammalian cells is $\sim -40\text{ mV}$, a turnover rate closer to 10 s^{-1} is to be expected.

Expression of mNect.hCNT3 fusion proteins was assessed on immunoblots (Fig. 3.4). hCNT3-F563C, a functionally inactive mutant [32], was fused to mNectarine to serve as a negative control (called mNect.hCNT3-F563C). HEK293 cells were transiently transfected with vector, mNect.hCNT3, or mNect.hCNT3-F563C cDNA. Lysates from the cells were treated with or without PNGaseF (an enzyme that removes N-linked glycosylation from proteins) [33]. Samples were immunoblotted, and probed with an anti-RFP antibody. hCNT3 alone migrates as a 75 kDa band [12] while mNectarine is 27 kDa . Untreated mNect.hCNT3 was detected as multiple bands around 100 kDa (Fig. 3.4). Upon treatment with PNGaseF, only a single band was detected for the two fusion proteins (Fig. 3.4). The multiple banding pattern is attributed to unglycosylated, core glycosylated and mature glycosylated bands. This is supported by the prediction that there are four putative glycosylation sites in the C-terminus of hCNT3, and both hCNT1 and hCNT3 exhibit multiple glycosylation states [12, 34, 35]. The presence of different glycoforms of hCNT3 will not affect the protein's function at the plasma membrane, since hCNT3 with all glycosylation sites absent is fully functional [12].

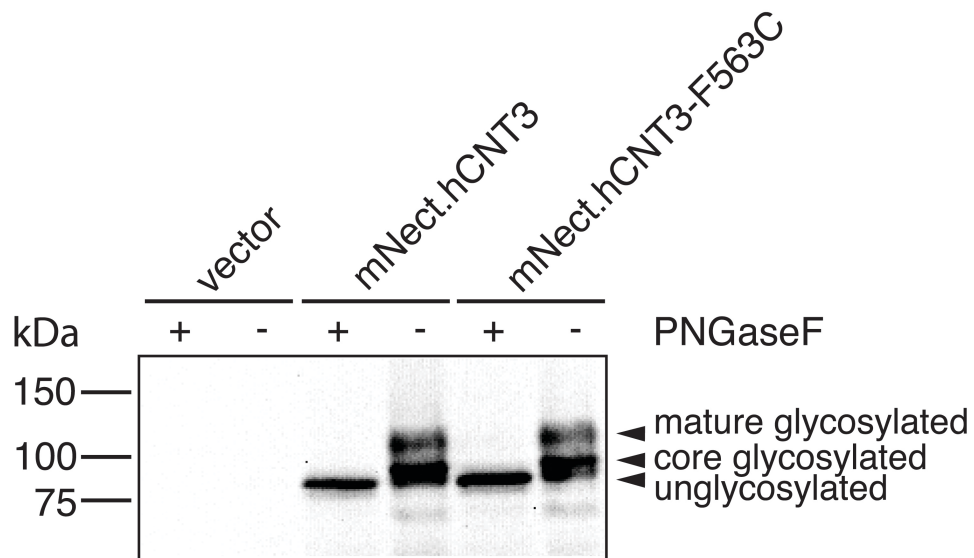


Figure 3.4. **Expression of mNect.hCNT3 in HEK293 cells and analysis of glycosylation status.** HEK293 cells were transiently transfected with vector (pcDNA3.1), mNect.hCNT3, or mNect.hCNT3-F563C cDNA. Lysates from the cells were treated with (+) or without (-) the deglycosylation enzyme, PNGaseF. Samples were immunoblotted and probed with a polyclonal anti-RFP antibody.

3.2.4 Spectral characterization of mNectarine expressed in

HEK293 cells

Fluorescence excitation and emission scans were obtained for lysates of mNect-transfected HEK293 cells (Fig. 3.5A). The peak fluorescence excitation wavelength was 558 nm and the peak emission wavelength was 573 nm. Fluorescence excitation spectra were collected for intact mNect-transfected HEK293 cells, or vector-alone transfected cells clamped at pH 7.5, 7.0, and 6.5 with nigericin/high potassium (Fig. 3.5B). mNectarine fluorescence decreased with decreasing pH (Fig. 3.5B), in a manner similar to that seen with purified mNectarine (Fig. 3.2A). In intact HEK293 cells the peak excitation wavelength was 558 nm at pH 6.5 and 7.0, and 557 nm at pH 7.5 (Fig. 3.5B). The observed fluorescence of mNect-transfected cells can be attributed to mNect fluorescence, as little fluorescence was observed when similar numbers of vector-alone transfected HEK293 cells were subjected to fluorescence excitation scans (Fig. 3.5B, lower curves). A plot of normalized fluorescence in intact mNect-transfected cells versus medium pH revealed a linear relationship over the pH 6.5-7.5 range (Fig. 3.5C). This indicates that mNect fluorescence, upon appropriate calibration, can be used as a reporter of cytosolic pH in intact cells.

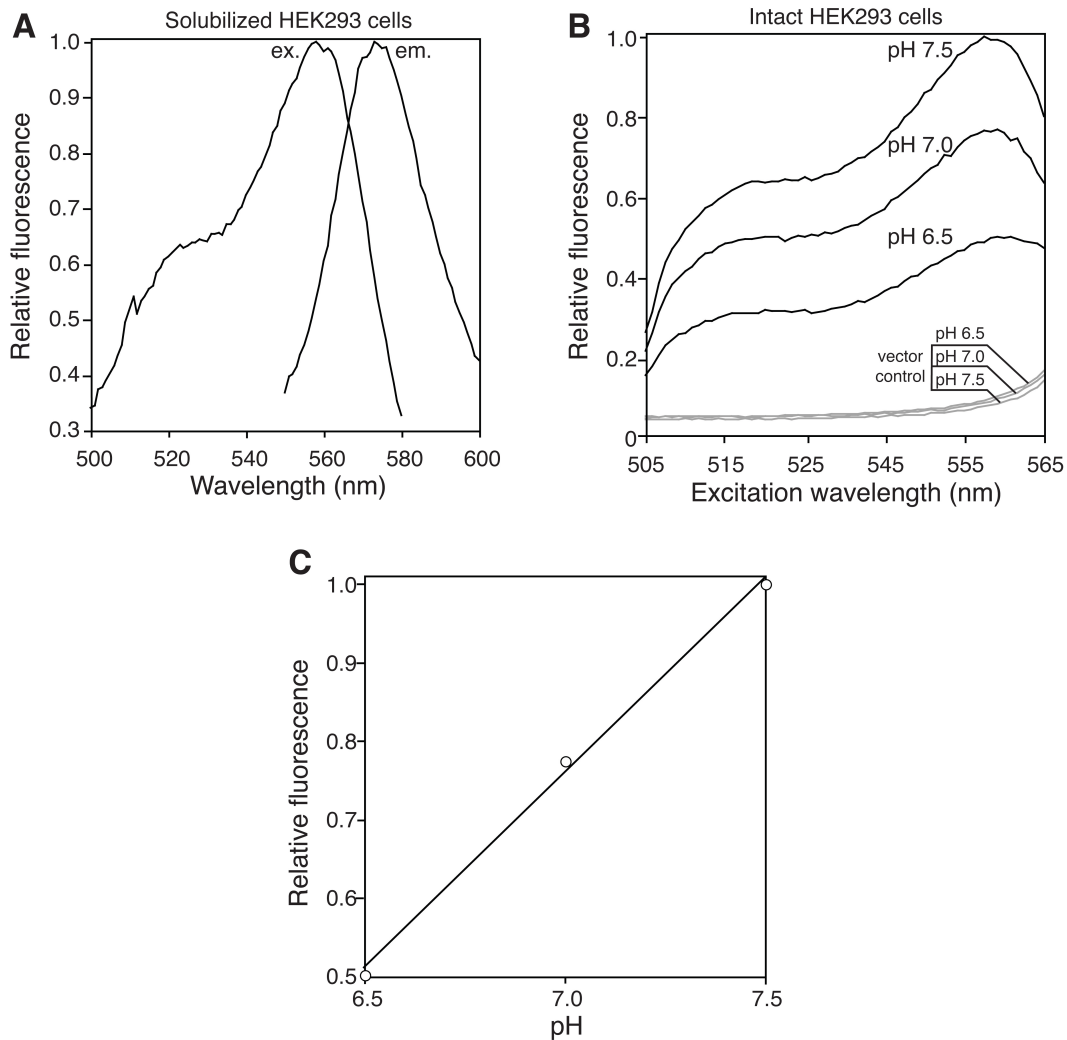


Figure 3.5. Spectral characterization of mNectarine expressed in HEK293 cells. HEK293 cells were transfected with mNectarine cDNA, and cell lysates were prepared. (A) Excitation (ex.) and emission (em.) scans of the lysates were collected at respective fixed emission and excitation wavelengths 590 and 550 nm. (B) Fluorescence excitation spectra ($\lambda_{em} = 573$ nm) of intact mNect-transfected HEK293 cells clamped at pH 7.5, 7.0, and 6.5 with nigericin/high potassium (black lines). Excitation spectra of vector alone transfected cells are shown as grey lines, with clamped pH values of experiments indicated. (C) Relationship between fluorescence ($\lambda_{ex} = 558$ nm and $\lambda_{em} = 573$ nm) and clamped cytosolic pH, in mNect transfected HEK293 cells (data from Panel B).

3.2.5 Correction for mNectarine photobleaching

Extended periods of illumination of mNect, under pH-clamped conditions, resulted in a continuous decrease of fluorescence, consistent with photobleaching (Fig. 3.6A). Examination of the kinetics of bleaching revealed they could be fitted by an exponential decay equation, which provides the basis for a method to correct for photobleaching. Under pH-clamped conditions mNect should report a constant fluorescence value, in the absence of photobleaching. The ability to correct photobleaching, by applying an exponential correction, was applied to pH 7.0-clamped cells (Fig. 3.6A-B). The data revealed that the continuous reduction in signal was substantially corrected, but not fully eliminated. To limit the effects of photobleaching and the need to apply corrections, in further experiments, steps were taken to minimize the time period during which mNect was illuminated.

The ability for mNect to report cytosolic pH accurately, following photobleaching correction, was assessed by clamping cytosolic pH to medium pH, using the nigericin/high potassium method (Fig. 3.6C-D). In these experiments pH was clamped sequentially to values near 7.0, 6.5, 7.5 and 7.0 (reported in Fig. 3.6C-D in the black bar) by perfusion with media of known pH. To calibrate fluorescence to cytosolic pH, a standard curve was generated, relating average fluorescence to media pH at each of the last three solutions. The average pH value during perfusion with each solution was then calculated (reported adjacent to each curve, Fig. 3.6C-D). The initial pH 7.00 perfusion data were not used to produce the standard curve (pH versus fluorescence), so the ability of mNect to

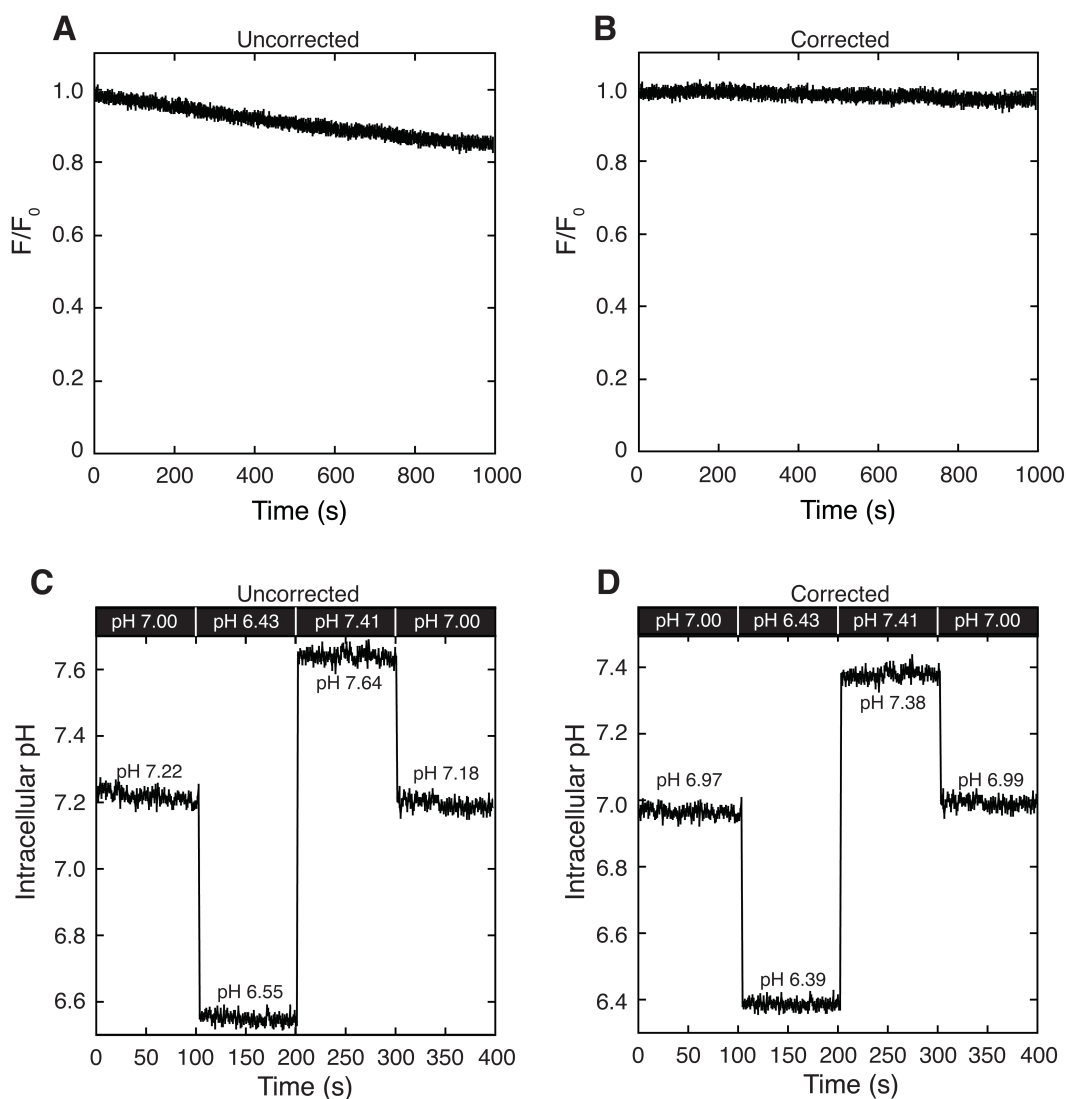


Figure 3.6. **Correction for mNectarine photobleaching.** HEK293 cells were transiently transfected with free cytosolic mNect cDNA, and fluorescence was monitored ($\lambda_{\text{ex}} = 550 \text{ nm}$ and $\lambda_{\text{em}} = 573 \text{ nm}$). (A, B) Cells were perfused with nigericin/high potassium solution, pH 7.0 to clamp intracellular pH. (A) Raw mNectarine fluorescence at pH 7.0, declining as a result of photobleaching. (B) mNectarine fluorescence at pH 7.0. Data from panel A has been corrected for photobleaching, using the approach described in methods. (C, D) HEK293 cells transfected with mNect cDNA were perfused consecutively with nigericin/high potassium solutions at pHs indicated in the black bars above curves. To minimize the period of sample illumination, samples were perfused without illumination for 480 s in each solution prior to collecting fluorescence data. Above or below each trace are the average pH values for each perfusion interval, calculated from the fluorescence data. (C) Data not corrected for photobleaching. (D) Data from panel C corrected for photobleaching, using the approach described in methods.

report pH during this perfusion reveals the reliability of mNect during a typical experiment. Without photobleaching correction there are significant differences between the pH reported by mNect and the medium pH (Fig. 3.6C). In particular, during the initial perfusion with pH 7.00 medium, the data fitted a pH value of 7.22 (Fig. 3.6C). By contrast, the photobleaching correction greatly improved the concordance between medium pH and pH reported by mNect. Indeed, mNect reported a pH of 6.97 during the initial pH 7.00 perfusion (Fig. 3.6D). Together these data reveal that after correction for photobleaching, mNect, calibrated by sequential perfusion with nigericin/high potassium media in the pH 6.5-7.5 range is able to report accurately on cytosolic pH.

3.2.6 Measurement of cytosolic pH by mNect, mNect.hCNT3 and BCECF

To test the reliability of mNect and mNect.hCNT3 as reporters of cytosolic pH, we compared their ability to report cytosolic pH to data collected using the well-established pH-sensitive dye, BCECF (Fig. 3.7). HEK293 cells were transiently co-transfected with cytosolic mNectarine and hCNT3 cDNA, or mNect.hCNT3 or with hCNT3 alone. These latter cells were loaded with BCECF, by incubation with BCECF-AM. Cells were perfused with nigericin/high potassium solutions near pH 7.5, 6.5 and 7.0. mNect and mNect.hCNT3 fluorescence was corrected for photobleaching. As described above, the average fluorescence values at each medium pH were then used to

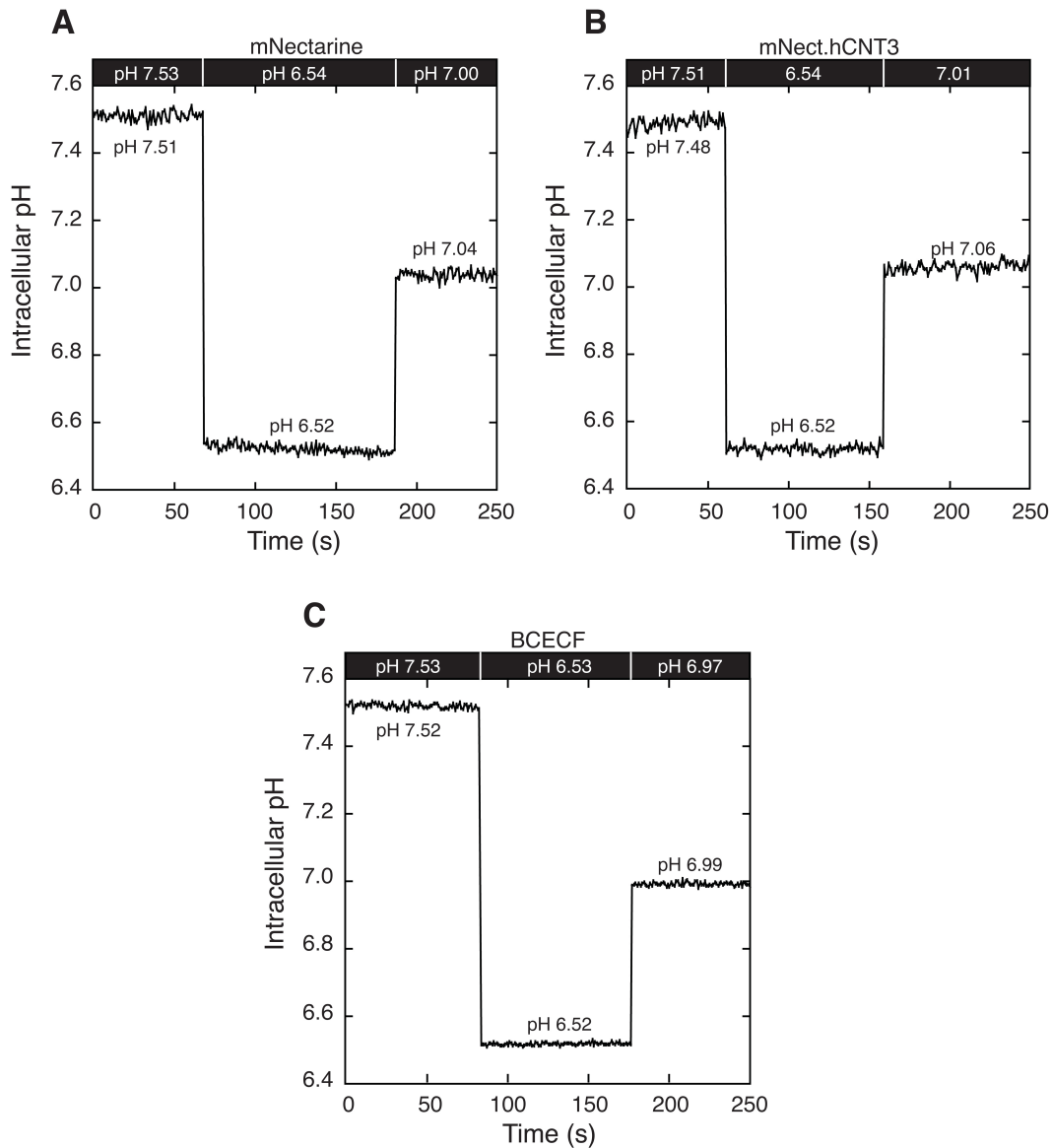


Figure 3.7. **Measurement of intracellular pH, using cytosolic mNectarine, mNect.hCNT3 and BCECF.** HEK293 cells were transiently co-transfected with cytosolic mNectarine and hCNT3 cDNA (A) or mNect.hCNT3 cDNA (B) or hCNT3 cDNA (C). hCNT3 transfected cells were incubated with the pH-sensitive dye BCECF-AM (C). Cells were perfused with nigericin/high potassium calibration solutions at pHs indicated in the black bars above curves to calibrate fluorescence to pH. To minimize the period of sample illumination, samples were perfused without illumination for 480 s in each solution prior to collecting fluorescence data. Average pH values for each perfusion interval (calculated from the fluorescence data) is indicated above or below the trace. (A, B) mNect fluorescence ($\lambda_{\text{ex}} = 550 \text{ nm}$ and $\lambda_{\text{em}} = 573 \text{ nm}$) was corrected for photobleaching. (C) BCECF fluorescence was monitored at $\lambda_{\text{ex}} = 440 \text{ nm}$ and 502.5 nm and $\lambda_{\text{em}} = 528.7 \text{ nm}$.

construct a standard curve, which was then applied to the fluorescence data, to transform it to intracellular pH (Fig. 3.7). Comparison between the pH of perfusion medium to reported cytosolic pH determined from fluorescence, reveals that mNect, mNect.hCNT3 and BCECF are similar in their ability to report cytosolic pH. We then measured the absolute difference in pH between the medium pH and the pH reported by BCECF and mNect.hCNT3 to provide a quantitative comparison of the reliability of the two fluorescent pH reporters. For BCECF the mean absolute difference was 0.013 ± 0.003 pH units ($n = 12$) and for mNect.hCNT3 the mean absolute difference was 0.038 ± 0.005 pH units ($n = 24$). We conclude that BCECF reports on cytosolic pH more accurately than mNect.hCNT3, but that mNect.hCNT3 can be expected to report on cytosolic pH within 0.04 pH units of the “true” cytosolic pH over the pH 6.5-7.5 range.

3.2.7 H⁺/uridine co-transport

We next examined the ability of the mNectarine.hCNT3 fusion proteins to report on changes in intracellular pH upon stimulation of H⁺/nucleoside co-transport. We used uridine as the nucleoside of choice because uridine elicits the largest nucleoside-induced inward currents under Na⁺-free, pH 5.5 conditions, which were previously found necessary for robust H⁺/uridine co-transport [10]. HEK293 cells were transiently transfected with cDNAs encoding mNect.hCNT3 or mNect.hCNT3-F563C (Fig. 3.8). Cells were perfused consecutively with Na⁺-free MBSS buffer, in which ChCl was substituted for NaCl, at pH 7.5, Na⁺-free MBSS buffer, pH 5.5 and Na⁺-free MBSS buffer, pH 5.5 containing 0.5 mM

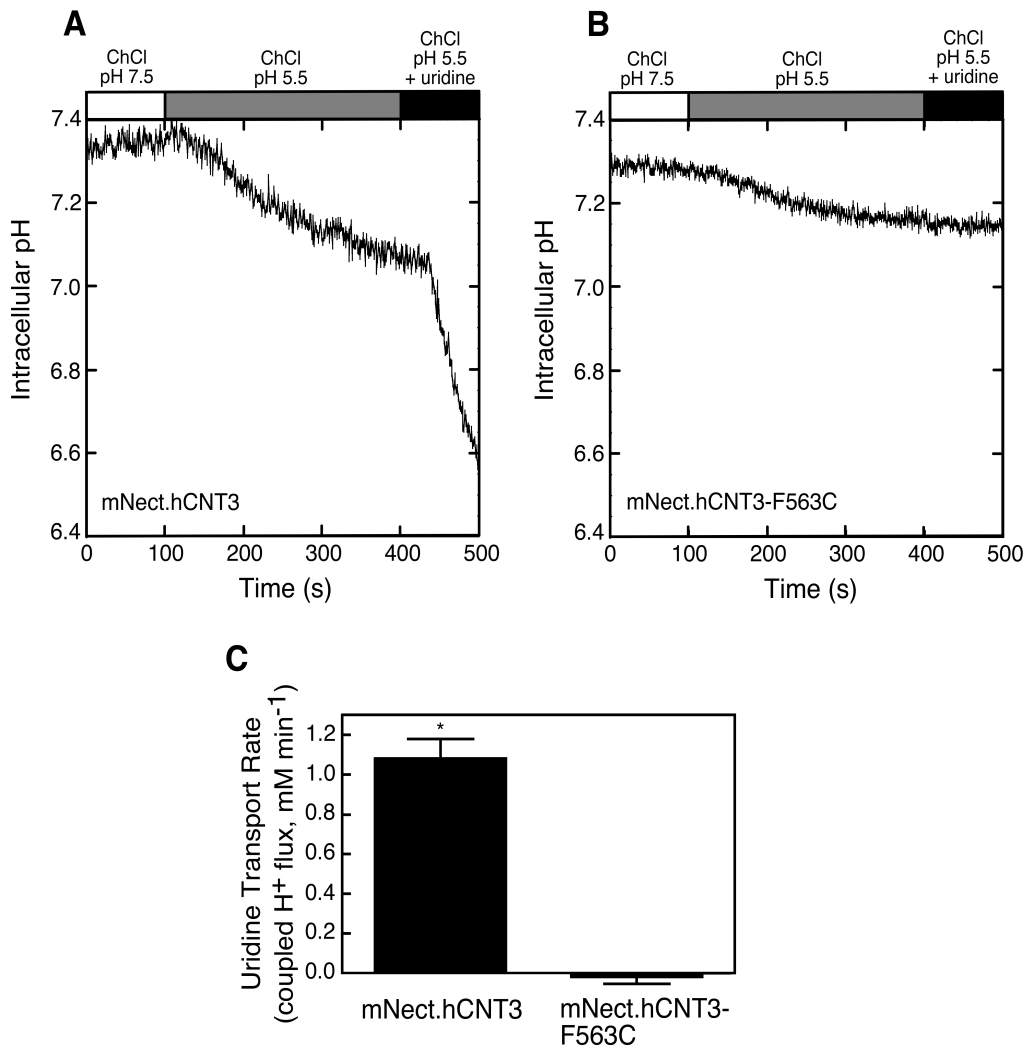


Figure 3.8. **hCNT3 mediated H⁺/uridine co-transport measured by mNectarine-hCNT3.** HEK293 cells were transiently transfected with mNect.hCNT3 cDNA (A) or with mNect.hCNT3-F563C cDNA (B). mNect.hCNT3 fluorescence was monitored at $\lambda_{\text{ex}} = 550$ nm and $\lambda_{\text{em}} = 573$ nm. Cells were perfused consecutively with Na⁺-free MBSS buffer, pH 7.5 (open bar), in which NaCl is replaced by choline chloride, Na⁺-free MBSS buffer, pH 5.5 (grey bar) and Na⁺-free MBSS buffer with 0.5 mM uridine, pH 5.5 (black bar). At the end of each experiment photobleaching-corrected fluorescence values were calibrated to pH via the nigericin/high potassium technique (not shown in figure) [36]. A. pH_i transients observed for mNect.hCNT3 transfected cells. B. pH_i transients observed for mNect.hCNT3-F563C transfected cells. C. Quantification of the change in rate of acidification (proton flux in units of mM·min⁻¹) upon switching to uridine-containing medium. Error bars represent standard error (n = 5). Asterisk indicates significant difference (P < 0.0001).

uridine. Each experiment was then calibrated for pH using the nigericin/high potassium method [36]. Co-transport of uridine with H^+ , which was initiated by the addition of uridine, was monitored by measuring intracellular pH (pH_i). Fluorescence data were corrected for photobleaching, and corrected fluorescence data was converted to pH_i . Transport rates were determined by linear regression of the initial acidification rate from the first 20 seconds after addition of uridine minus the rate before addition of uridine.

pH 5.5 Na^+ -free MBSS medium induced a slow acidification of mNect.hCNT3 and mNect.hCNT3-F563C transfected cells (Fig. 3.8A-B), which is addressed below. The rate of acidification increased significantly upon addition of 0.5 mM uridine, only in mNect.hCNT3-expressing cells (Fig. 3.8A-B), consistent with hCNT3-mediated H^+ -coupled uridine transport. Quantification of the change in the rate of acidification (proton flux in units of $mM \cdot min^{-1}$) upon switching to uridine-containing medium revealed that cells transfected with mNect.hCNT3 had a proton flux of $1.08 \pm 0.10 mM \cdot min^{-1}$ while cells transfected with the inactive hCNT3 mutant fusion protein, mNect.hCNT3-F563C, had a proton flux of $-0.02 \pm 0.1 mM \cdot min^{-1}$ (Fig. 3.8C). Assuming a H^+ :nucleoside coupling stoichiometry of 1:1, as found for hCNT3 uridine transport when expressed in *X. laevis* oocytes [9, 10], these data imply that the rate of change of cytosolic concentration of uridine is the same as the rate of change of $[H^+]$, found using mNect.hCNT3. Together these results demonstrate that the mNect.hCNT3 fusion protein reports on H^+ /uridine co-transport by sensing changes in pH_i associated with coupled H^+ /uridine influx.

One caveat, however, relates to the calculation of proton flux, using the established buffer capacity of the bulk cytosol of HEK293 cells. We measured intracellular pH using mNect.hCNT3, anchored at the surface of the plasma membrane. If the buffer capacity at the membrane surface, in the vicinity of mNect.hCNT3, differs from bulk cytosol, it would affect the conversion of dpH_i/dt values to H^+ flux. That said, the buffer capacity at the membrane surface is a constant; transport rates can therefore be reliably compared between different cell samples, as the buffer capacity would be the same between them. Further, it is unlikely that the buffer capacity at the plasma membrane surface differs dramatically from bulk cytosol.

Since point mutations can sometimes impair trafficking of membrane proteins, we assessed the plasma membrane localization of mNect.hCNT3 compared to mNect.hCNT3-F563C. HEK293 cells transfected with either mNect.hCNT3 or mNect.hCNT3-F563C cDNA had similar degrees of plasma membrane localization on the basis of imaging mNectarine fluorescence by confocal microscopy (Fig. 3.9).

To assess the reliability of the mNect.hCNT3 fusion as an assay for H^+ /nucleoside co-transport, we measured the K_m of mNect.hCNT3 for uridine. HEK293 cells were transiently transfected with mNect.hCNT3 cDNA, and were consecutively perfused with Na^+ -free MBSS buffer at pH 7.5, Na^+ -free MBSS buffer, pH 5.5 and Na^+ -free MBSS buffer, pH 5.5 containing varying amounts of uridine, from 0 to 960 μM . The change in the rate of acidification (proton flux in units of $mM \cdot min^{-1}$) was quantified upon switching to uridine-containing medium

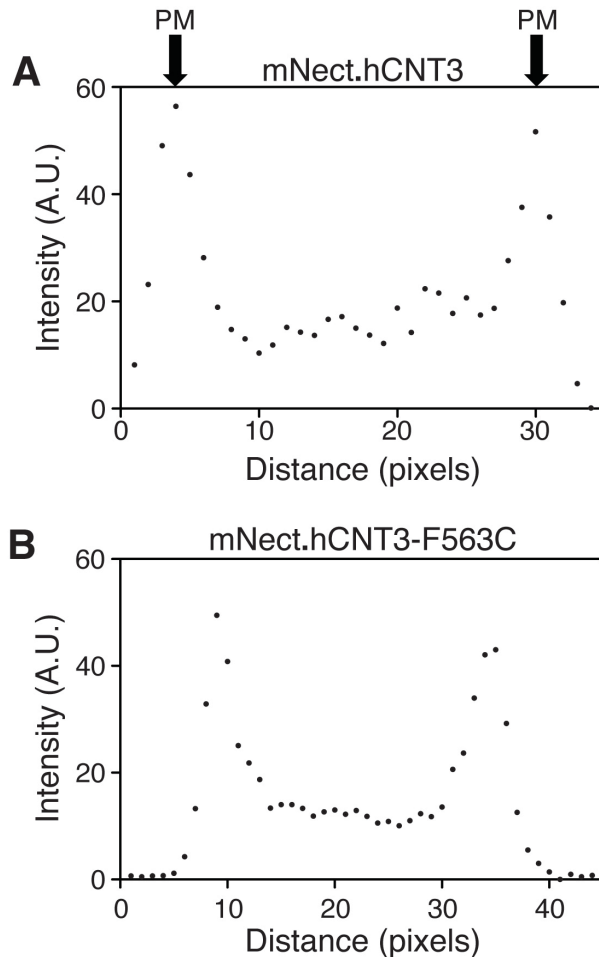


Figure 3.9. **Plasma membrane localization of mNect.hCNT3 and mNect.hCNT3-F563C.** HEK293 cells transfected with mNect.hCNT3 or mNect.hCNT3-F563 cDNA were imaged by confocal microscopy. The level of FP abundance across the entire cell (plasma membrane, cytosol, and plasma membrane) was analyzed with ImageJ software. Plasma membrane (PM) is indicated by black arrow. Pixel intensity versus distance was plotted, and the area under the curve was analyzed with PRISM software.

at each concentration of uridine. Figure 3.10 shows a representative example of three separate experiments used to calculate the K_m for uridine transport in HEK293 cells, as measured with mNect.hCNT3. The K_m determined was $72 \pm 24 \mu\text{M}$ ($n = 3$), which lies between the two previously published values of $110 \pm 10 \mu\text{M}$ and $62.4 \pm 5.4 \mu\text{M}$ found in oocytes [10, 12]. We conclude that measurement of uridine flux by following H^+ movement with mNect.hCNT3 is an accurate assay of H^+ /nucleoside co-transport.

Radiolabelled substrate uptake studies in oocytes found that uridine is transported to a similar extent in both acidic Na^+ -free and acidic Na^+ -containing conditions [10, 12]. Charge/uptake experiments suggested that in Na^+ -containing buffer, pH 5.5, both Na^+ and H^+ contribute to the driving force, and that one of the two Na^+ binding sites is shared by H^+ [10]. To determine whether a H^+ is co-transported with uridine in acidic Na^+ -containing medium, HEK293 cells were transiently transfected with mNect.hCNT3 or mNect.hCNT3-F563C cDNA. Cells were perfused with Na^+ -free MBSS buffer, pH 5.5, in which NaCl was replaced by ChCl, Na^+ -containing MBSS buffer, pH 5.5 and Na^+ -containing MBSS buffer, pH 5.5, containing 0.5 mM uridine. The Na^+/H^+ exchange inhibitor, EIPA (5 μM), was present in all perfusion buffers. The data was collected and analyzed as described above.

Addition of uridine induced acidification in both Na^+ -free (Fig. 3.11B) and Na^+ -containing medium (Fig. 3.11A) in mNect.hCNT3 transfected cells. Cells expressing catalytically-inactive mNect.hCNT3-F563C had no increase in acidification rate upon addition of uridine to the medium (Fig. 3.11C).

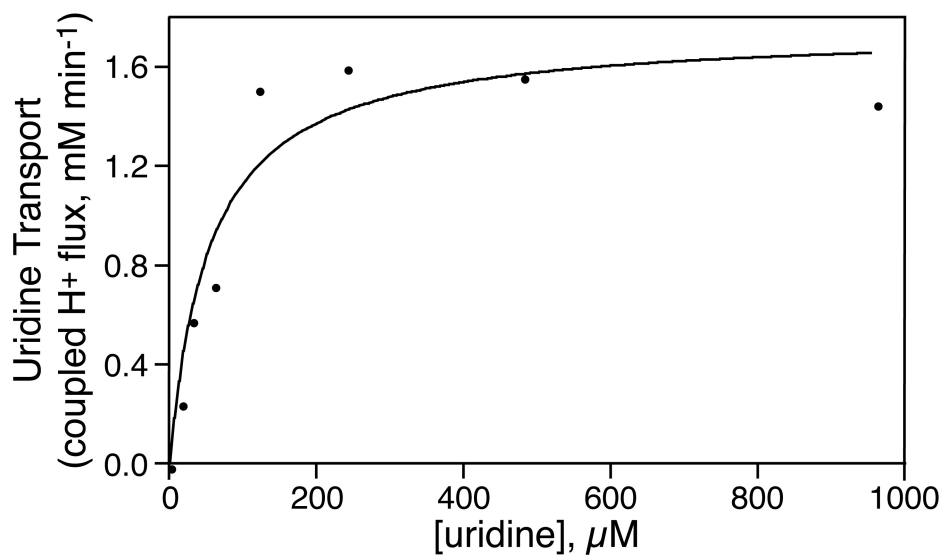


Figure 3.10. **Kinetics of H^+ /uridine co-transport in HEK293 cells.** HEK293 cells were transiently transfected with mNect.hCNT3 cDNA. mNect.hCNT3 fluorescence was monitored at $\lambda_{\text{ex}} = 550 \text{ nm}$ and $\lambda_{\text{em}} = 573 \text{ nm}$. Cells were perfused consecutively with Na^+ -free MBSS buffer, pH 7.5, in which NaCl is replaced by choline chloride, Na^+ -free MBSS buffer, pH 5.5 and Na^+ -free MBSS buffer, pH 5.5, containing varying concentrations of uridine from 0-960 μM . At the end of each experiment pH was calibrated via the nigericin/high potassium technique and fluorescence values were calibrated to pH. The change in the rate of acidification (proton flux in units of $\text{mM}\cdot\text{min}^{-1}$) was quantified upon switching to uridine-containing medium at each concentration of uridine. This graph is a representative example of three separate experiments used to calculate the K_m of mNect.hCNT3 for uridine.

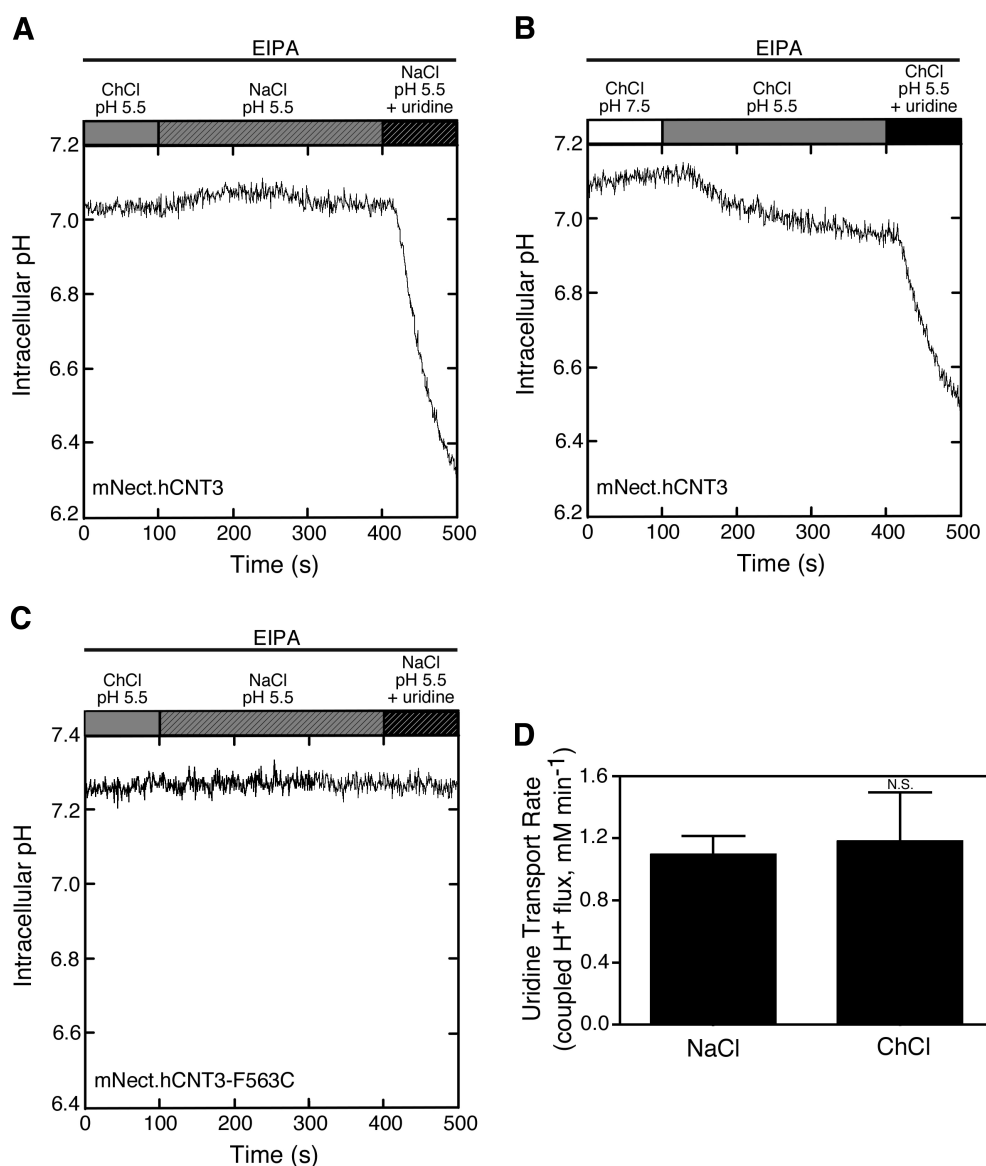


Figure 3.11. **Effect of Na⁺ on H⁺/uridine co-transport.** HEK293 cells were transiently transfected with mNect.hCNT3 cDNA (A, B) or with mNect.hCNT3-F563C cDNA (C). mNect.hCNT3 fluorescence was monitored at $\lambda_{\text{ex}} = 550 \text{ nm}$ and $\lambda_{\text{em}} = 573 \text{ nm}$. Cells were perfused with MBSS buffer, pH 5.5 (grey bars) or MBSS buffer, pH 5.5, containing 0.5 mM uridine (black bars). Perfusion with Na⁺-containing MBSS buffer is indicated by hatched bars, and perfusion with Na⁺-free MBSS buffer, in which NaCl is replaced by choline chloride (ChCl), is indicated by un-hatched bars. Open bar indicates perfusion with Na⁺-free MBSS, pH 7.5. All buffers contained 5 μM EIPA. (D) Quantification of the change in rate of acidification (proton flux in units of $\text{mM}\cdot\text{min}^{-1}$) upon switching to uridine-containing medium. Error bars represent standard error ($n = 3$). N.S. indicates non-significant difference ($P = 0.81$).

Quantification of the increase in acidification rate following addition of uridine (Fig. 3.11D) revealed that Na^+ had no effect on the acidification rate (1.09 ± 0.11 or $1.18 \pm 0.32 \text{ mM min}^{-1}$, in the absence or presence of Na^+ , respectively). This provides support for the proposed mechanism that in acidic Na^+ -containing conditions, 1 Na^+ and 1 H^+ are transported per uridine molecule, while in acidic Na^+ -free conditions, 1 H^+ alone is transported per uridine molecule [9-12].

Prior to the addition of uridine, the mNect.hCNT3-F563C transfected cells acidified to a lesser extent than the mNect.hCNT3 transfected cells (Fig. 3.8), but this difference was found to be not statistically significant, based on analysis of pH_i immediately prior to addition of uridine (pH_i s of 6.9 ± 0.05 and 7.1 ± 0.05 , for mNect.hCNT3 and mNect.hCNT3-F563C, respectively) (Fig. 3.12). We reasoned that Na^+ -free medium might cause the plasma membrane Na^+/H^+ exchanger (NHE) to act in reverse mode, exporting Na^+ and importing H^+ , resulting in acidification upon switching from Na^+ -containing to Na^+ free medium. Indeed, cytosolic acidification was found in Na^+ -free medium, but only at pH 5.5, not at pH 7.5 (Fig. 3.8A-B). Since acidification rates were similar in cells expressing functional and catalytically inactive hCNT3 (Fig. 3.8A-B, Fig. 3.12), the acidification mechanism is inherent to the HEK293 cells. To assess the possible role of NHE in cytosolic acidification 5 μM EIPA, a Na^+/H^+ exchange inhibitor [37], was added to media (Fig. 3.11). EIPA was unable to suppress the acidification rate in Na^+ free medium (Fig. 3.11B). Together these data suggest that there is a H^+ leak into HEK293 cells in acidic Na^+ -free medium that is independent of NHE and hCNT3. The identity of the pathway is unknown, but

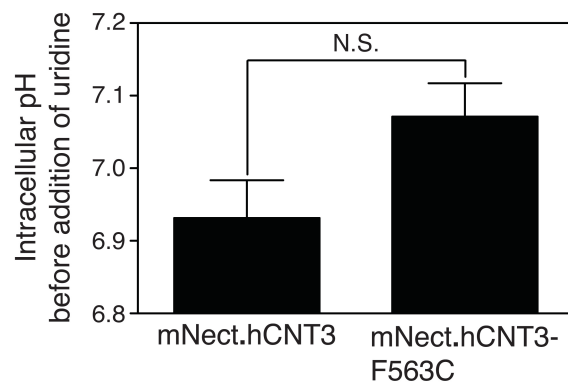


Figure 3.12. **Intracellular pH immediately prior to addition of uridine in mNect.hCNT3 and mNect.hCNT3-F563C expressing cells.** HEK293 cells were transiently transfected with mNect.hCNT3 or mNect.hCNT3-F563C cDNA and subjected to H⁺/uridine co-transport assay, photobleaching correction and calibration (same as in Fig. 3.8). The mean pH for the 20 s immediately prior to the addition of uridine was determined for both mNect.hCNT3 and mNect.hCNT3-F563C expressing cells. Error bars represent standard error (n = 5). N.S. indicates non-significant difference (P = 0.07).

H⁺ leak through cation channels has been reported [38, 39]. The background H⁺ leak can be avoided by conducting mNect.hCNT3 assays of H⁺/uridine co-transport in the presence of Na⁺, since no acidification was found at pH 5.5 until uridine was added to mNect.hCNT3 expressing cells (Fig. 3.11A,C).

3.3 Discussion

We utilized hCNT3's H⁺ coupling characteristics to develop a new method to assay nucleoside transport in cultured mammalian cells. This assay was made possible by engineering a new pH-sensitive red fluorescent protein, mNectarine. mNectarine, fused to the N-terminus of hCNT3, was able to reliably report on changes in pH at the intracellular surface of hCNT3 in real time. Addition of uridine to mNect.hCNT3 expressing cells, in both Na⁺-free and Na⁺-containing conditions elicited an increase in the rate of acidification that was not seen in the negative control (mNect.hCNT3-F563C expressing cells). Our data are consistent with hCNT3-mediated Na⁺/H⁺/nucleoside co-transport under acid conditions.

Using mNect.hCNT3 to measure uridine flux by monitoring H⁺ co-transport is advantageous since it enables direct measurement of changes in intracellular H⁺ concentration, which, up until now, had only been inferred from H⁺ activation of ¹⁴C-uridine influx and pH-dependent uridine-evoked currents in oocytes [8, 9, 32]. The present experiments therefore provide the first direct evidence that hCNT3 transports H⁺. Since we did not directly measure uridine flux in these experiments, it is formally possible that the mNect.hCNT3 assay

measures an hCNT3-mediated H^+ flux unrelated to uridine transport. We consider this unlikely since under similar extracellular acid medium conditions uptake of radioactive nucleoside was observed in oocytes [9, 10].

We assessed the reliability of mNect.hCNT3 as a reporter for hCNT3 H^+ /nucleoside co-transport, by measuring the K_m of mNect.hCNT3 for uridine. The K_m determined here ($72 \pm 24 \mu M$) was between two previously published values for hCNT3 expressed in oocytes (110 ± 10 and $62 \pm 5 \mu M$) [10, 12], indicating that mNect.hCNT3 provides an accurate method to measure hCNT3 kinetics.

This study illuminates the mechanism of nucleoside transport under conditions of extracellular acid and Na^+ . Previous investigations in *X. laevis* oocytes demonstrated that uridine was transported with high efficiency in both Na^+ -containing medium at pH 5.5, and Na^+ -free medium at pH 5.5, although to a somewhat lesser extent under Na^+ -free conditions [10, 12]. hCNT3 co-transport of nucleoside with Na^+ has been verified outside oocytes, using yeast and mammalian cells [34, 40, 41]. In the current study, there was H^+ movement in both acidic Na^+ -containing and acidic Na^+ -free medium, with no significant difference in transport rate between the two conditions. This result indicates that H^+ is co-transported with uridine in acidic Na^+ -containing buffer. Charge/flux ratio experiments in oocytes revealed that hCNT3 functions with 2:1 cation:uridine stoichiometry in both acidic and alkaline Na^+ -containing medium, compared to a 1:1 cation:uridine stoichiometry in acidic Na^+ -free medium [10, 12]. Since we find similar rates of H^+ movement in the presence and absence of

Na^+ , the present data support a model in which 1 H^+ and 1 Na^+ are transported per uridine molecule in acidic Na^+ -containing medium, compared to 1 H^+ per uridine molecule in the absence of Na^+ , and 2 Na^+ per uridine molecule in alkaline conditions.

mNect.hCNT3 can be used to measure the transport rate for any nucleoside or nucleoside drug that is co-transported with H^+ , so any range of substrates can be assayed for transport, even if a radioactive analogue is unavailable. This characteristic, along with utilizing a pH-sensitive fluorescent reporter, opens up the possibility of high-throughput assays in which a wide range of possible substrates could be added to mNect.hCNT3 transfected cells grown in multi-well plates while monitoring fluorescence changes over time with a multi-well plate fluorimeter. mNect.hCNT3 also provides the possibility of high-throughput screening for inhibitors, as no high-affinity CNT inhibitors have yet been identified. In contrast to hCNT3 assays performed using *Xenopus laevis* oocytes [9, 10, 32], the mNect.hCNT3 assay enables studies of hCNT3 regulation in a physiologically relevant mammalian cell context.

Interestingly, hCNT3 exhibits markedly different selectivity characteristics for symport of physiological nucleosides and therapeutic nucleoside drugs in acidic Na^+ -free or alkaline Na^+ -containing conditions [10]. For example, in acidic Na^+ -free conditions, transport of guanosine, AZT (3'-azido-3'-deoxythymidine) and ddC (2',3'-dideoxycytidine) are almost completely abolished [10, 32]. This suggests that binding of Na^+ or H^+ induces cation-specific conformational changes in hCNT3 [10]. Differential H^+ or Na^+ binding

to the SGLT1 Na⁺/glucose transporter also leads to cation-specific conformational changes [42]. Using mNect.hCNT3, it will be possible to measure transport of nucleosides and nucleoside drugs in acidic Na⁺-containing conditions. In conjunction with corresponding electrophysiological recordings in hCNT3-expressing oocytes [9, 10, 12, 32], it may be possible to discern an intermediate conformation where both Na⁺ and H⁺ are bound.

The concentrative nucleoside transporters are primarily expressed in epithelial cells where they are involved in absorption, secretion, distribution and elimination of nucleosides and nucleoside analogs [2, 3, 11]. hCNT3 is especially abundant in the kidney, and may be the key CNT at the apical surface of the proximal tubule [3, 11]. The ability of hCNT3 to couple nucleoside movement to either a Na⁺ and/or H⁺ gradient may be advantageous in the kidney, as the lumen of the proximal tubule is acidic, and hCNT3 could take advantage of the H⁺ gradient to maximize its transport rate in these conditions. Both hCNT3 and SGLT1, which have similar transport kinetics, are present in the intestine, which also has an acidic luminal environment, particularly in the more proximal regions [43]. Thus, hCNT3's H⁺-coupling characteristic may be physiologically and pharmacologically important [3, 9].

The use of pH-sensitive fluorescent protein fusions as an assay of transport activity extends beyond hCNT3. mNectarine could be fused to any transporter that induces a change in intracellular pH. Such transporters could include the H⁺-coupled PepT1/2 peptide transporters [44, 45], SGLT1 [43] and the MCT1 monocarboxylate transporter [46], or any of the transport proteins

involved in the regulation of pH_i , including $\text{Cl}^-/\text{HCO}_3^-$ exchangers (AEs) [47], sodium proton exchangers (NHEs) [48], or sodium bicarbonate co-transporters (NBCs) [49]. PepT1 [50], MCT1 [51], NHE1 [48], and the SLC4 family members (including AEs, and NBCs) [49], all have at least one intracellular terminus, so an mNectarine fusion could be constructed. SGLT1 does not have intracellular N or C termini, but FP fusions could possibly be made in the large cytosolic loop [52]. Fusion of mNectarine to these proteins would report on changes in pH local to the transporter, and would be more specific than simply measuring pH changes in the bulk cytosol with a pH-sensitive intracellular dye. Moreover, the self-referencing nature of an mNect.transporter fusion ensures that transport activity is measured only in the cells expressing the transport protein. This would be particularly beneficial in studying pH microdomains or metabolons [46, 53].

Furthermore, mNectarine's spectral characteristics make it ideal for use as a partner with other fluorescent reporters. Even more tantalizing, is the prospect of pairing one mNectarine fusion protein with another pH-sensitive fluorescent protein fusion. This would allow simultaneous measurement of pH in two different regions of a cell. For example, mNectarine can be paired with the green fluorescent protein deGFP4 [15, 54], as they exhibit spectrally distinct wavelengths, which do not exhibit crosstalk (see chapter 4). Indeed, chapter 4 investigates the phenomenon of differential pH surrounding pH regulatory transport proteins.

In conclusion, we have developed a method to measure H⁺/uridine co-transport in mammalian cells by fusing the pH-sensitive fluorescent protein, mNectarine, to the N-terminus of hCNT3. mNectarine is a bright, pH-sensitive mRFP with a pK_a well-suited to measurement of physiological pH changes. Fusion to hCNT3 created a self-reporting probe of nucleoside transport that can be expressed in mammalian cells. Furthermore, mNect.hCNT3 reports on nucleoside transport in real time, and enables measurement of the transportability of any substrate that is coupled to H⁺ flux. Fusion to the pH-reporting mNectarine is an approach that could be extended to high-throughput assays, and could be used to report on the transport activity of any pH transporter. Taken together, our findings demonstrate that mNect.hCNT3 is a valid reporter of H⁺/nucleoside co-transport, and support a transport mechanism where 1 H⁺ and 1 Na⁺ are co-transported with uridine in acidic Na⁺-containing conditions.

Bibliography

1. Griffith DA & Jarvis SM (1996) Nucleoside and nucleobase transport systems of mammalian cells. *Biochim Biophys Acta* **1286**, 153-181.
2. Young JD, Cheeseman, C.I., Mackey, J.R., Cass, C.E. and Baldwin, S.A. (2000) Molecular Mechanisms of Nucleoside and Nucleoside Drug Transport. In *Gastrointestinal Transport (Current Topics in Membranes)* (Barrett KE, and Donowitz, M., ed, pp. 329-378. Academic Press, San Diego.
3. Elwi AN, Damaraju VL, Baldwin SA, Young JD, Sawyer MB & Cass CE (2006) Renal nucleoside transporters: physiological and clinical implications. *Biochem Cell Biol* **84**, 844-858.
4. King AE, Ackley MA, Cass CE, Young JD & Baldwin SA (2006) Nucleoside transporters: from scavengers to novel therapeutic targets. *Trends Pharmacol Sci* **27**, 416-425.
5. Zhang J, Visser F, King KM, Baldwin SA, Young JD & Cass CE (2007) The role of nucleoside transporters in cancer chemotherapy with nucleoside drugs. *Cancer Metastasis Rev* **26**, 85-110.
6. Ritzel MW, Yao SY, Huang MY, Elliott JF, Cass CE & Young JD (1997) Molecular cloning and functional expression of cDNAs encoding a human Na⁺-nucleoside cotransporter (hCNT1). *Am J Physiol* **272**, C707-714.
7. Ritzel MW, Yao SY, Ng AM, Mackey JR, Cass CE & Young JD (1998) Molecular cloning, functional expression and chromosomal localization of a cDNA encoding a human Na⁺/nucleoside cotransporter (hCNT2) selective for purine nucleosides and uridine. *Mol Membr Biol* **15**, 203-211.
8. Ritzel MW, Ng AM, Yao SY, Graham K, Loewen SK, Smith KM, Ritzel RG, Mowles DA, Carpenter P, Chen XZ, et al. (2001) Molecular identification and characterization of novel human and mouse concentrative Na⁺-nucleoside cotransporter proteins (hCNT3 and mCNT3) broadly selective for purine and pyrimidine nucleosides (system cib). *J Biol Chem* **276**, 2914-2927.
9. Smith KM, Slugoski MD, Cass CE, Baldwin SA, Karpinski E & Young JD (2007) Cation coupling properties of human concentrative nucleoside transporters hCNT1, hCNT2 and hCNT3. *Mol Membr Biol* **24**, 53-64.
10. Smith KM, Slugoski MD, Loewen SK, Ng AM, Yao SY, Chen XZ, Karpinski E, Cass CE, Baldwin SA & Young JD (2005) The broadly selective

- human Na⁺/nucleoside cotransporter (hCNT3) exhibits novel cation-coupled nucleoside transport characteristics. *J Biol Chem* **280**, 25436-25449.
11. Damaraju VL, Elwi AN, Hunter C, Carpenter P, Santos C, Barron GM, Sun X, Baldwin SA, Young JD, Mackey JR, et al. (2007) Localization of broadly selective equilibrative and concentrative nucleoside transporters, hENT1 and hCNT3, in human kidney. *Am J Physiol Renal Physiol* **293**, F200-211.
 12. Slugoski MD, Smith KM, Mulinta R, Ng AM, Yao SY, Morrison EL, Lee QO, Zhang J, Karpinski E, Cass CE, et al. (2008) A conformationally mobile cysteine residue (Cys-561) modulates Na⁺ and H⁺ activation of human CNT3. *J Biol Chem* **283**, 24922-24934.
 13. Giepmans BN, Adams SR, Ellisman MH & Tsien RY (2006) The fluorescent toolbox for assessing protein location and function. *Science* **312**, 217-224.
 14. Miesenböck G, De Angelis DA & Rothman JE (1998) Visualizing secretion and synaptic transmission with pH-sensitive green fluorescent proteins. *Nature* **394**, 192-195.
 15. Hanson GT, McAnaney TB, Park ES, Rendell ME, Yarbrough DK, Chu S, Xi L, Boxer SG, Montrose MH & Remington SJ (2002) Green fluorescent protein variants as ratiometric dual emission pH sensors. 1. Structural characterization and preliminary application. *Biochemistry* **41**, 15477-15488.
 16. Bizzarri R, Arcangeli C, Arosio D, Ricci F, Faraci P, Cardarelli F & Beltram F (2006) Development of a novel GFP-based ratiometric excitation and emission pH indicator for intracellular studies. *Biophys J* **90**, 3300-3314.
 17. Ai HW, Shaner NC, Cheng Z, Tsien RY & Campbell RE (2007) Exploration of new chromophore structures leads to the identification of improved blue fluorescent proteins. *Biochemistry* **46**, 5904-5910.
 18. Subach OM, Gundorov IS, Yoshimura M, Subach FV, Zhang J, Gruenwald D, Souslova EA, Chudakov DM & Verkhusha VV (2008) Conversion of red fluorescent protein into a bright blue probe. *Chem Biol* **15**, 1116-1124.
 19. Abad MF, Di Benedetto G, Magalhaes PJ, Filippin L & Pozzan T (2004) Mitochondrial pH monitored by a new engineered green fluorescent protein mutant. *J Biol Chem* **279**, 11521-11529.
 20. Llopis J, McCaffery JM, Miyawaki A, Farquhar MG & Tsien RY (1998) Measurement of cytosolic, mitochondrial, and Golgi pH in single living cells with green fluorescent proteins. *Proc Natl Acad Sci U S A* **95**, 6803-6808.

21. Matz MV, Fradkov AF, Labas YA, Savitsky AP, Zaraisky AG, Markelov ML & Lukyanov SA (1999) Fluorescent proteins from nonbioluminescent Anthozoa species. *Nat Biotechnol* **17**, 969-973.
22. Shaner NC, Campbell RE, Steinbach PA, Giepmans BN, Palmer AE & Tsien RY (2004) Improved monomeric red, orange and yellow fluorescent proteins derived from *Discosoma* sp. red fluorescent protein. *Nat Biotechnol* **22**, 1567-1572.
23. Campbell RE, Tour O, Palmer AE, Steinbach PA, Baird GS, Zacharias DA & Tsien RY (2002) A monomeric red fluorescent protein. *Proc Natl Acad Sci U S A* **99**, 7877-7882.
24. Griesbeck O, Baird GS, Campbell RE, Zacharias DA & Tsien RY (2001) Reducing the environmental sensitivity of yellow fluorescent protein. Mechanism and applications. *J Biol Chem* **276**, 29188-29194.
25. Shaner NC, Lin MZ, McKeown MR, Steinbach PA, Hazelwood KL, Davidson MW & Tsien RY (2008) Improving the photostability of bright monomeric orange and red fluorescent proteins. *Nat Methods* **5**, 545-551.
26. Jach G, Pesch M, Richter K, Frings S & Uhrig JF (2006) An improved mRFP1 adds red to bimolecular fluorescence complementation. *Nat Methods* **3**, 597-600.
27. Ai HW, Henderson JN, Remington SJ & Campbell RE (2006) Directed evolution of a monomeric, bright and photostable version of *Clavularia* cyan fluorescent protein: structural characterization and applications in fluorescence imaging. *Biochem J* **400**, 531-540.
28. Ai HW, Olenych SG, Wong P, Davidson MW & Campbell RE (2008) Hue-shifted monomeric variants of *Clavularia* cyan fluorescent protein: I identification of the molecular determinants of color and applications in fluorescence imaging. *BMC Biol* **6**, 13.
29. Shu X, Shaner NC, Yarbrough CA, Tsien RY & Remington SJ (2006) Novel chromophores and buried charges control color in mFruits. *Biochemistry* **45**, 9639-9647.
30. Hu H, Endres CJ, Chang C, Umaphathy NS, Lee EW, Fei YJ, Itagaki S, Swaan PW, Ganapathy V & Unadkat JD (2006) Electrophysiological characterization and modeling of the structure activity relationship of the human concentrative nucleoside transporter 3 (hCNT3). *Mol Pharmacol* **69**, 1542-1553.
31. Slugoski MD, Ng AM, Yao SY, Smith KM, Lin CC, Zhang J, Karpinski E, Cass CE, Baldwin SA & Young JD (2008) A proton-mediated conformational shift identifies a mobile pore-lining cysteine residue (Cys-

- 561) in human concentrative nucleoside transporter 3. *J Biol Chem* **283**, 8496-8507.
32. Plummer TH, Jr. & Tarentino AL (1991) Purification of the oligosaccharide-cleaving enzymes of *Flavobacterium meningosepticum*. *Glycobiology* **1**, 257-263.
 33. Toan SV, To KK, Leung GP, de Souza MO, Ward JL & Tse CM (2003) Genomic organization and functional characterization of the human concentrative nucleoside transporter-3 isoform (hCNT3) expressed in mammalian cells. *Pflugers Arch* **447**, 195-204.
 34. Hamilton SR, Yao SY, Ingram JC, Hadden DA, Ritzel MW, Gallagher MP, Henderson PJ, Cass CE, Young JD & Baldwin SA (2001) Subcellular distribution and membrane topology of the mammalian concentrative Na⁺-nucleoside cotransporter rCNT1. *J Biol Chem* **276**, 27981-27988.
 35. Thomas JA, Buchsbaum RN, Zimniak A & Racker E (1979) Intracellular pH measurements in Ehrlich ascites tumor cells utilizing spectroscopic probes generated in situ. *Biochemistry* **18**, 2210-2218.
 36. Alexander RT, Furuya W, Szaszi K, Orłowski J & Grinstein S (2005) Rho GTPases dictate the mobility of the Na/H exchanger NHE3 in epithelia: role in apical retention and targeting. *Proc Natl Acad Sci U S A* **102**, 12253-12258.
 37. Zhang J, Tackaberry T, Ritzel MW, Raborn T, Barron G, Baldwin SA, Young JD & Cass CE (2006) Cysteine-accessibility analysis of transmembrane domains 11-13 of human concentrative nucleoside transporter 3. *Biochem J* **394**, 389-398.
 38. Errasti-Murugarren E, Pastor-Anglada M & Casado FJ (2007) Role of CNT3 in the transepithelial flux of nucleosides and nucleoside-derived drugs. *J Physiol* **582**, 1249-1260.
 39. Hirayama BA, Loo DD & Wright EM (1997) Cation effects on protein conformation and transport in the Na⁺/glucose cotransporter. *J Biol Chem* **272**, 2110-2115.
 40. Hirayama BA, Loo DD & Wright EM (1994) Protons drive sugar transport through the Na⁺/glucose cotransporter (SGLT1). *J Biol Chem* **269**, 21407-21410.
 41. Mackenzie B, Loo DD, Fei Y, Liu WJ, Ganapathy V, Leibach FH & Wright EM (1996) Mechanisms of the human intestinal H⁺-coupled oligopeptide transporter hPEPT1. *J Biol Chem* **271**, 5430-5437.

42. Chen XZ, Zhu T, Smith DE & Hediger MA (1999) Stoichiometry and kinetics of the high-affinity H⁺-coupled peptide transporter PepT2. *J Biol Chem* **274**, 2773-2779.
43. Becker HM & Deitmer JW (2008) Nonenzymatic proton handling by carbonic anhydrase II during H⁺-lactate cotransport via monocarboxylate transporter 1. *J Biol Chem* **283**, 21655-21667.
44. McMurtrie HL, Cleary HJ, Alvarez BV, Loisel FB, Sterling D, Morgan PE, Johnson DE & Casey JR (2004) The bicarbonate transport metabolon. *J Enzyme Inhib Med Chem* **19**, 231-236.
45. Slepko ER, Rainey JK, Sykes BD & Fliegel L (2007) Structural and functional analysis of the Na⁺/H⁺ exchanger. *Biochem J* **401**, 623-633.
46. Romero MF (2005) Molecular pathophysiology of SLC4 bicarbonate transporters. *Curr Opin Nephrol Hypertens* **14**, 495-501.
47. Daniel H & Kottra G (2004) The proton oligopeptide cotransporter family SLC15 in physiology and pharmacology. *Pflugers Arch* **447**, 610-618.
48. Poole RC, Sansom CE & Halestrap AP (1996) Studies of the membrane topology of the rat erythrocyte H⁺/lactate cotransporter (MCT1). *Biochem J* **320 (Pt 3)**, 817-824.
49. Wright EM & Turk E (2004) The sodium/glucose cotransport family SLC5. *Pflugers Arch* **447**, 510-518.
50. Sterling D, Reithmeier RA & Casey JR (2001) A transport metabolon. Functional interaction of carbonic anhydrase II and chloride/bicarbonate exchangers. *J Biol Chem* **276**, 47886-47894.
51. Johnson DE & Casey JR (2008) pH Micro-Environments Associated with Transport Activity of the Erythrocyte Membrane Cl⁻/HCO₃⁻ Exchanger, AE1. *FASEB J* **22**, 759.710.

Chapter 4: Cytosolic H⁺ Microdomain Developed During Ion Transport

A version of this chapter has been **submitted**: Johnson, D.E., and J.R. Casey. 2011. Cytosolic H⁺ Microdomain Developed During Ion Transport. *J. Physiol.* **Submitted.**

4.1 Introduction

A cell's ability to convert environmental stimuli into a specific cellular response arises in part from locally restricted signalling, enhanced by organellar barriers and cytosolic heterogeneity of solute concentration. Solute microdomains, such as Ca^{++} and cAMP, are the product of precise regulation of the concentration of solute in space, time and amplitude. Cells carefully control cytosolic pH through the activity of pH-regulatory transport proteins [1, 2]. Whether H^+ microdomains develop near the cytosolic surface of such transporters has not been established, but is of particular interest given the breadth of cellular processes regulated by pH changes [3].

AE1, a plasma membrane $\text{Cl}^-/\text{HCO}_3^-$ exchanger, is the predominant protein of the erythrocyte plasma membrane [4, 5]. α -intercalated cells of the distal renal tubule express an N-terminally truncated AE1 variant (kAE1) [6]. Erythrocyte AE1 has an intracellular amino-terminal domain that interacts with cytoskeletal proteins and glycolytic enzymes [7], a membrane-spanning domain responsible for $\text{Cl}^-/\text{HCO}_3^-$ exchange activity [5, 8], and a short cytosolic C-terminus containing an acidic motif (LDADD) that binds cytosolic carbonic anhydrase isoform II (CAII) [9, 10]. CAs catalyze the hydration of CO_2 to form HCO_3^- and H^+ . CAII interacts physically and functionally with AE1 to form a bicarbonate transport metabolon [9, 11], a physical complex of enzymes in a linked metabolic pathway that functions to maximize flux of substrate through the pathway by limiting its loss through diffusion [12]. In the presence of CAII AE1

has a high turnover rate of $5 \times 10^4 \text{ s}^{-1}$, which is among the fastest rates for a membrane transport protein [13].

H^+ diffusion rates have been studied in cardiomyocytes by creation of local pH_i disturbances, using acid-filled patch-pipettes [14-16], local microperfusion of extracellular membrane-permeant acids or bases [17], and flash photolysis-induced release of caged H^+ [18]. Cytosolic H^+ gradients as large as 1 pH unit were established, which persisted for minutes [14]. Diffusion of H^+ in the cytosol is two orders of magnitude slower than in water; a H^+ gradient requires 1 minute to diffuse 100 μm along the length of a cardiomyocyte [15, 17]. Cytosolic diffusion rates are slowed by interaction of H^+ with buffering groups on slowly-moving macromolecules [19]. The addition of a mobile buffer ($\text{CO}_2/\text{HCO}_3^-$) increases the rate of H^+ diffusion, thus decreasing the longitudinal pH gradient in cells [16, 17], although the magnitude of the effect depends on the rate of H^+ loading [16, 17].

Cytosolic H^+ gradients have been found in other cells. H^+ discontinuities in isolated mouse intestinal enterocytes result from the activity of proton-coupled dipeptide transporters [20]. H^+ gradients are generated in oligodendrocytes by differential subcellular distribution of Na^+/H^+ exchangers (NHEs), $\text{Na}^+/\text{HCO}_3^-$ co-transporters and CAII [21]. Acidification of the leading edge of tumor cells is associated with polarized expression of pH-regulatory proteins, including AEs [22], NHEs [23], CAs [24], monocarboxylate transporters [25], and H^+ -ATPases [26]. A similar phenomenon is also seen in microvascular endothelial cells [27].

Do H^+ microdomains form around pH-regulatory transport proteins, like AE1? Rapid AE1-mediated HCO_3^- transport, combined with a low rate of H^+ diffusion in the cytosol suggest that H^+ microdomains develop around AE1 during Cl^-/HCO_3^- exchange. Proteins in close proximity to AE1 would thus be subjected to a different pH than those more distant from AE1. To examine the presence of a H^+ microdomain around the surface of AE1, the pH-sensitive fluorescent proteins (FPs) deGFP4, a dual emission green FP [28] and monomeric Nectarine (mNect), an RFP variant [29] were fused respectively to AE1, and the inactive control plasma membrane protein hCNT3-F563C. pH_i changes during AE1-mediated Cl^-/HCO_3^- exchange were measured concomitantly at the surface of plasma membrane deGFP4.AE1 and mNect.hCNT3-F563C. To measure the spatial dimensions of the H^+ microdomain around AE1, deGFP4.AE1 and mNect.hCNT3-F563C were expressed at different ratios in HEK293 cells, and the average distance between the two proteins at the plasma membrane was determined.

4.2 Results

4.2.1 Construction and characterization of pH-reporter fusion proteins

Our aim was to determine whether a H^+ microdomain develops around AE1 as it exchanges Cl^- for HCO_3^- , which requires a pH probe with high spatial and temporal resolution. We used pH-sensitive fluorescent proteins (FPs) with

pK_a values in the physiological range [28, 29] that localize to distinct regions. deGFP4 [28] was fused to the N-terminal cytoplasmic domain of AE1 to construct deGFP4.AE1, which reported pH at the surface of AE1 (Fig. 4.1A). We avoided fusion to the cytosolic C-terminal tail of AE1 out of concern that deGFP4 might interfere with plasma membrane trafficking and CAII binding, both of which require the C-terminal AE1 tail [9, 30]. To measure pH simultaneously at a plasma membrane region physically distant from AE1, we fused mNectarine (mNect, an RFP variant) to the intracellular N-terminus of an inactive isoform of the human Na^+ -coupled nucleoside co-transporter, hCNT3-F563C, generating mNect.hCNT3-F563 (Fig. 4.1B) [29]. While wildtype hCNT3 can transport H^+ along with nucleoside exclusively under acid conditions, the mutant hCNT3-F563C cannot transport H^+ [29]. mNect.hCNT3-F563C thus acts as a plasma membrane-localized protein, not involved in H^+ translocation. To ensure that we could accurately measure pH near and away from AE1, we completed control experiments.

The optimal λ_{ex} and λ_{em} wavelengths to detect [H^+] were determined by wavelength scans on solubilised and intact HEK293 cells transfected with deGFP4 cDNA (Fig. 4.2). In solubilized cells, the peak $\lambda_{ex} = 396$ nm and the peak $\lambda_{em} = 512$ nm (Fig. 4.2A), which were close to the peaks obtained with purified deGFP4 [28]. Fluorescence excitation spectra were collected for intact deGFP4-transfected HEK293 cells, or vector-alone transfected cells clamped at pHs 7.5, 7.0, and 6.5 with nigericin/high potassium (Fig. 4.2B). deGFP4 fluorescence decreased with decreasing pH, in a manner similar to that seen with

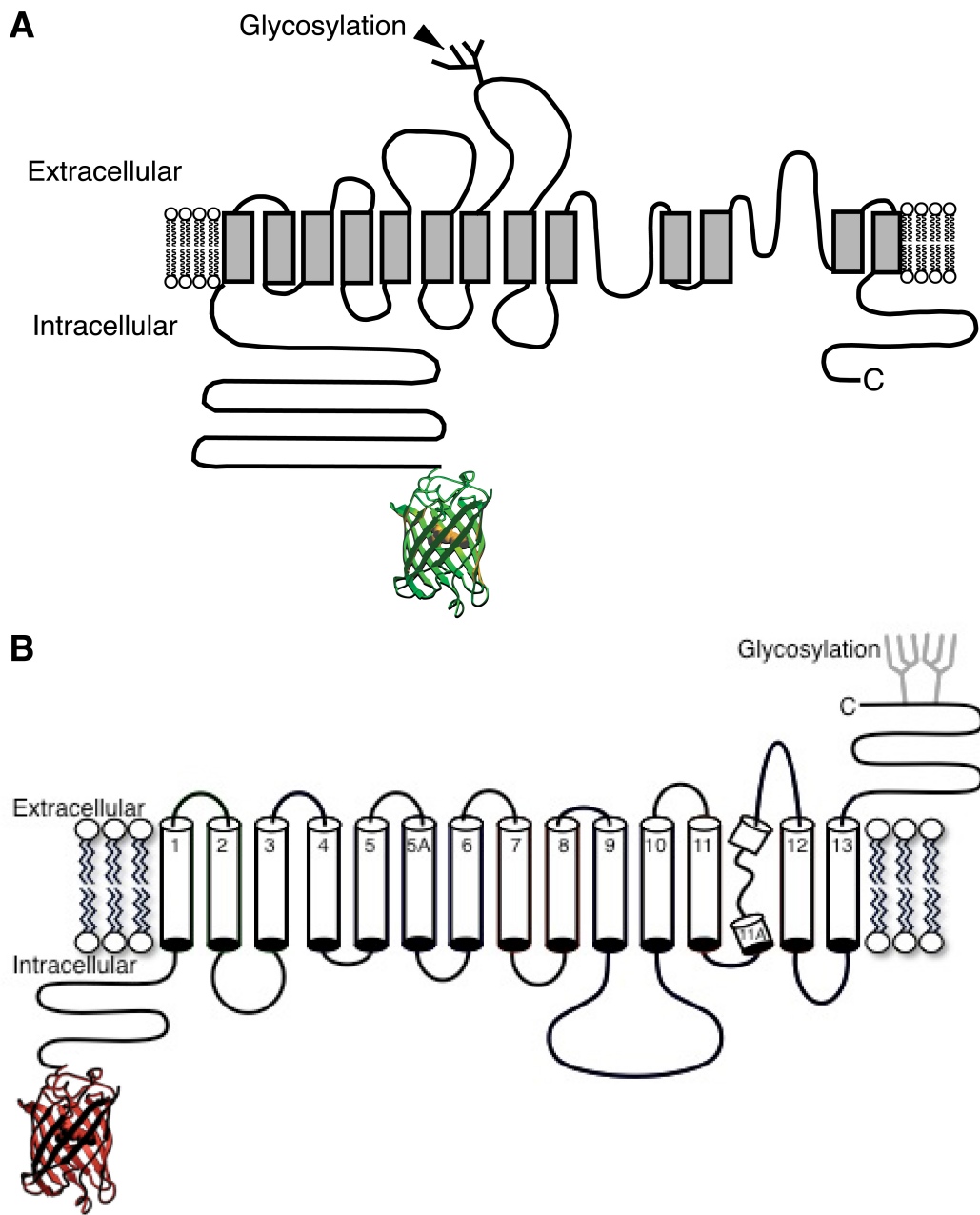


Figure 4.1. **deGFP4.AE1 and mNect.hCNT3 topology model.** Topology models of deGFP4.AE1 (A) and mNect.hCNT3 (B), drawn to approximate scale.

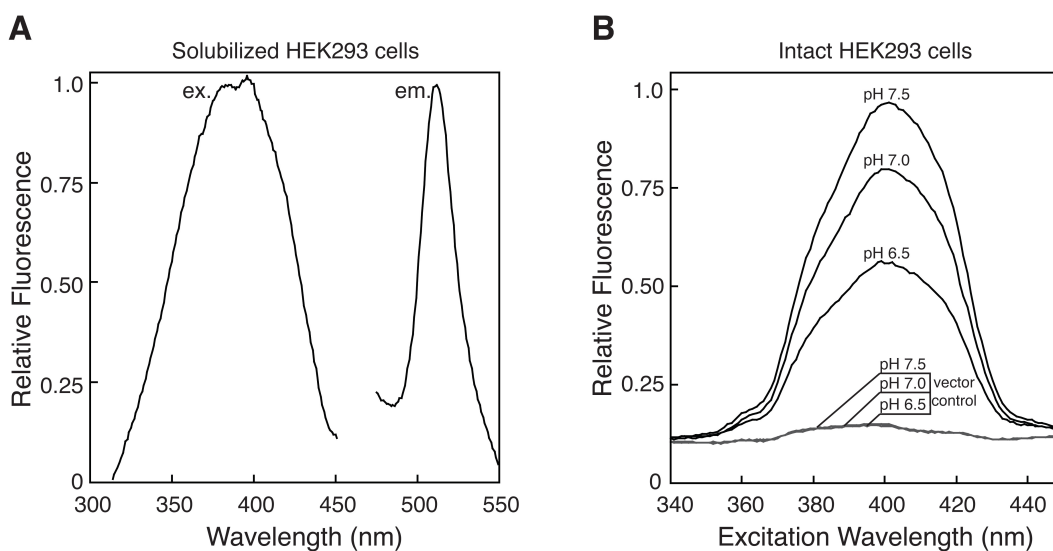


Figure 4.2. Spectral characterization of deGFP4 expressed in HEK293 cells. HEK293 cells were transfected with deGFP4 cDNA. (A) Cell lysates were prepared from the cells and excitation (ex.) and emission (em.) scans were collected at respective fixed emission and excitation wavelengths 510 and 400 nm. (B) Fluorescence excitation spectra ($\lambda_{em} = 510$ nm) of intact deGFP4 and vector alone transfected HEK293 cells clamped at pH 7.5, 7.0, and 6.5 with nigericin/high solutions. Upper three traces are for cells expressing deGFP4, clamped at indicated pH values. The lower, overlapping traces are for vector-alone transfected cells, clamped at indicated pH values.

purified deGFP4 [28]. In intact HEK293 cells the peak excitation wavelength was 399 nm at pH 6.5 and 7.0, and 401 nm at pH 7.5 (Fig. 4.2B). The observed fluorescence of deGFP4-transfected cells can be attributed to deGFP4 fluorescence, as little fluorescence was observed when similar numbers of vector-alone transfected HEK293 cells were subjected to fluorescence excitation scans (Fig. 4.2B, lower curves). Similar experiments were previously conducted on mNectarine-transfected HEK293 cells [29].

We characterized the functional activity of deGFP4.AE1 in comparison to AE1 alone and found that fusion of the FP did not affect AE1 transport activity (Fig. 4.3). HEK293 cells grown on glass coverslips were transfected with either AE1 or deGFP4-Y66L.AE1, a non-fluorescent deGFP4 fused to N-terminus of AE1 [31]. The non-fluorescent deGFP4-Y66L was used so that deGFP4 fluorescence would not interfere with measurements of pH made in these experiments using the pH-sensitive fluorescent dye, BCECF-AM. Transfected cells were incubated with BCECF-AM, placed on the stage of an inverted microscope attached to a photometer, and perfused alternately with Cl⁻-containing and Cl⁻-free Ringer's buffers, followed by calibration to pH (Fig. 4.3A-B). The change in the transmembrane Cl⁻ gradient upon switching to Cl⁻-free Ringer's buffer drives AE1-mediated Cl⁻ efflux from the cell in exchange for HCO₃⁻, causing an intracellular alkalization detected by the pH-sensitive probe as an increase in fluorescence. Cl⁻/HCO₃⁻ exchange rates were determined by linear regression of the initial rate of pH_i change upon switching to Cl⁻-free Ringer's buffer. Flux of H⁺-equivalents (mM·min⁻¹) was calculated as $dpH_i/dt \cdot \beta_{total}$, where

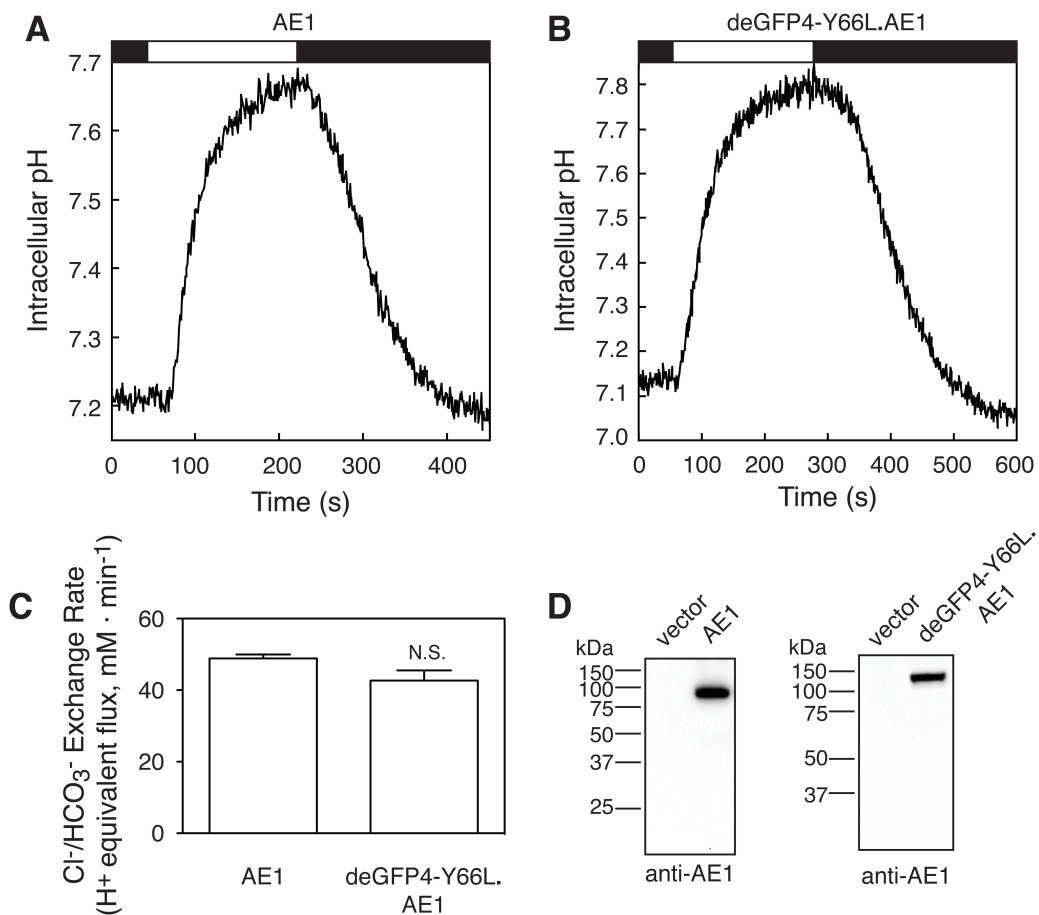


Figure 4.3. Cl⁻/HCO₃⁻ exchange activity of AE1 and deGFP4.AE1. HEK293 cells grown on glass coverslips were transiently co-transfected with AE1 cDNA (A) or deGFP4-Y66L.AE1 cDNA, a non-fluorescent deGFP4 fused to the N-terminus of AE1 (B), and incubated with the pH-sensitive dye BCECF-AM. Coverslips were placed on the stage of an inverted microscope attached to a photometer, and perfused alternately with Cl⁻-containing Ringer's buffer (black bar) and Cl⁻-free Ringer's buffer (white bar), at 24 °C. At the end of each experiment pH was calibrated via the nigericin/high potassium technique (not shown). (C) Quantification of the initial Cl⁻/HCO₃⁻ exchange rate upon switching to Cl⁻-free Ringer's buffer, corrected for activity of vector-transfected cells. Error bars represent standard error (n = 3). N.S. indicates non-significant difference (P = 0.1), compared to AE1. (D) HEK293 cells transiently transfected with AE1, deGFP4-Y66L.AE1, or vector alone cDNA were separated by SDS-PAGE, immunoblotted, and probed with an anti-AE1 (IVF12) antibody.

$\beta_{\text{total}} = \beta_i + \beta_{\text{CO}_2}$, and where β_i was experimentally determined (Fig. 4.4), and $\beta_{\text{CO}_2} = 2.3 \times [\text{HCO}_3^-]$ [32]. Data was corrected for activity of vector-transfected cells. Data revealed that there were no significant differences in the H^+ fluxes reported between the AE1 and deGFP4-Y66L.AE1 transfected cells (49 ± 1 and 43 ± 3 mM min^{-1} , respectively) (Fig. 4.3C). Expression of WT AE1 and deGFP4-Y66L.AE1 was confirmed on immunoblots (Fig. 4.3D). Together these data suggest that fusion of deGFP4 to AE1 does not significantly impair the $\text{Cl}^-/\text{HCO}_3^-$ exchange activity of AE1, which is consistent with results found previously [34].

Although deGFP4 and mNect exhibit spectrally distinct λ_{ex} and λ_{em} , it was necessary to determine if there was crosstalk between the two FPs in our experimental set-up. HEK293 cells grown on glass coverslips were co-transfected with AE1, and *either* cytosolic deGFP4 *or* cytosolic mNect. Fluorescence changes associated with AE1 activity were monitored in both the red and green channels (Fig. 4.5). Fluorescence data were not corrected for photobleaching or calibrated to pH, but were plotted as raw fluorescence counts. Spurious spill-over was quantified as red fluorescence measured in deGFP4 transfected cells and green fluorescence measured in mNect transfected cells, and expressed as a % of counts in the appropriate channel, with values of 0.14% and 3.6%, respectively. The higher value found for the background deGFP4 channel is likely due to higher autofluorescence at the lower λ_{ex} . The “spill-over” recordings did not detect a change of pH concurrent with AE1 activity (Fig. 4.5A,B, lower panels). We conclude that deGFP4 and mNect do not exhibit fluorescence crosstalk.

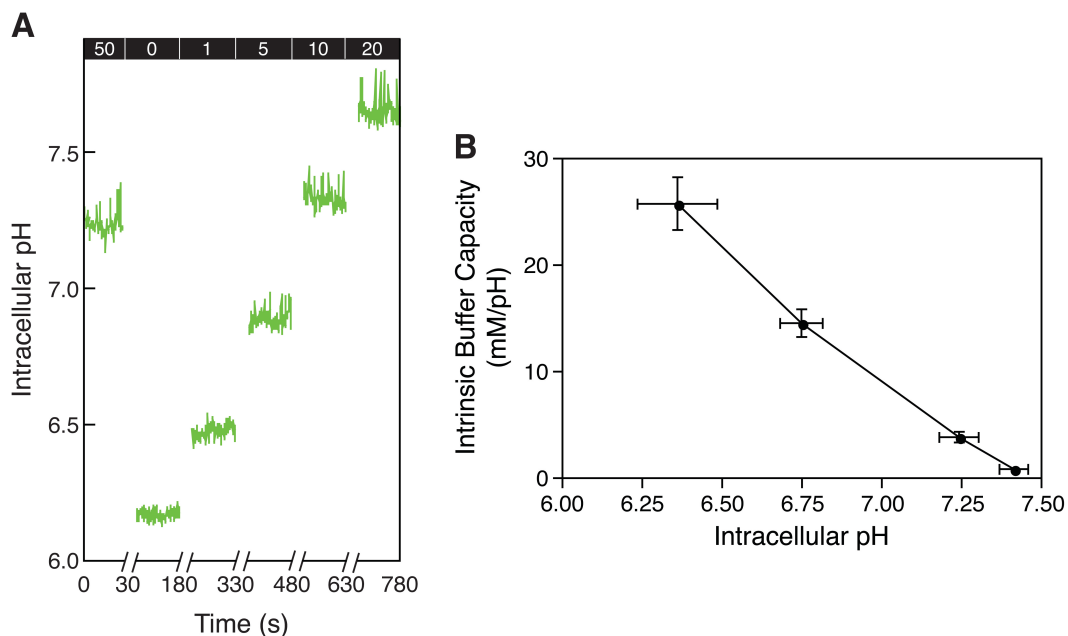


Figure 4.4. **Intracellular buffer capacity.** (A) HEK293 cells grown on glass coverslips and transiently transfected with deGFP4.AE1 cDNA were mounted on the confocal microscope stage and perfused consecutively with HCO₃⁻-free Ringer's buffer at 37 °C, containing 50, 0, 1, 5, 10, and 20 mM NH₄Cl, as indicated in bars at top. At the end of each experiment pH was calibrated via the nigericin/high potassium technique (not shown). deGFP4 fluorescence in PM ROIs was corrected for photobleaching and converted to pH_i. Breaks in the X-axis represent time (120 s) during which illumination was paused to minimize photobleaching. (B) The intracellular NH₄Cl concentration ([NH₄Cl]_i) was calculated using the Henderson-Hasselbalch equation, and the intrinsic buffer capacity (β_i) was calculated as Δ[NH₄Cl]_i/ΔpH_i (mM/pH) [33]. Error bars represent standard error (n = 3).

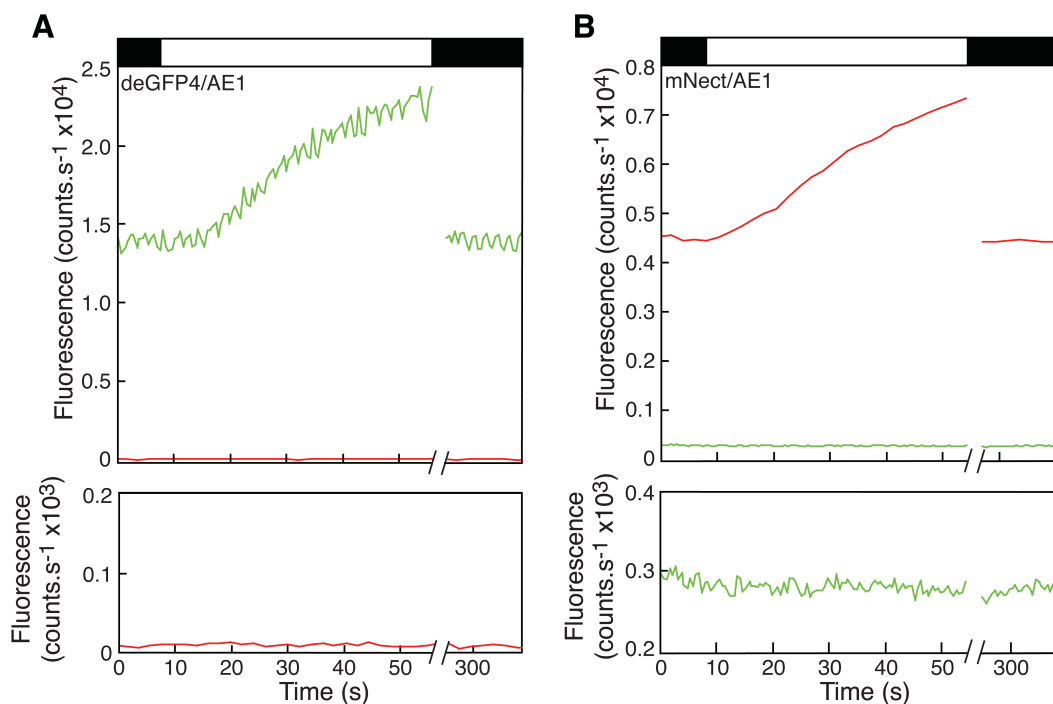


Figure 4.5. **Assessment of crosstalk during simultaneous measurement of deGFP4 and mNectarine fluorescence.** HEK293 cells grown on glass coverslips were transiently co-transfected with either deGFP4 and AE1 cDNAs (A), or mNect and AE1 cDNAs (B). Coverslips were placed on the stage of a confocal microscope, and perfused alternately with Cl⁻-containing Ringer's buffer (black bars) and Cl⁻-free Ringer's buffer (white bar), at 24 °C. Breaks in the x-axis represent time (240 s) during which illumination was paused. (A) Fluorescence of deGFP4/AE1 co-transfected cells. Green trace represents deGFP4 fluorescence and red trace represents mNect fluorescence wavelength. Lower panel is a magnification of red trace from upper panel. (B) Fluorescence of mNect/AE1 co-transfected cells. Red trace represents mNect fluorescence and green trace represents deGFP4 fluorescence wavelength. Lower panel is a magnification of green trace from upper panel.

We did not expect to observe fluorescence resonance energy transfer (FRET) between deGFP4 and mNect since FRET requires molecules to be within 0.01 μm of each other [35], and our analysis shows that at closest deGFP4.AE1 and mNect.hCNT3-F563C are $\sim 0.03 \mu\text{m}$ apart. Furthermore, the emission spectrum of deGFP4 does not overlap with the excitation spectrum of mNect (Figs. 3.5 and 4.2, and [28, 29]). As an experimental test, however, we examined cells co-transfected with deGFP4.AE1 and a varied amount of mNect.hCNT3-F563C (similarly to Figs. 4.16, 4.18, 4.19). FRET is most readily assessed by the diminution of fluorescent emission of the donor, as its energy is transferred to the fluorescence acceptor. The fluorescence emission intensity of deGFP4.AE1 (possible fluorescence donor) did not change as the amount of mNect.hCNT3-F563C increased (Fig. 4.6). There is no FRET between deGFP4.AE1 and mNect.hCNT3-F563C under the conditions used to measure the H^+ microdomain.

4.2.2 Halide sensitivity of FP fluorescence

Many fluorescent proteins are pH-sensitive [36], but the fluorescence of some is additionally quenched by halides [37]. This was an issue since AE1 exchanges Cl^- for HCO_3^- thus affecting $[\text{Cl}^-]$ and $[\text{H}^+]$ concurrently. The degree to which deGFP4 and mNect fluorescence were quenched by H^+ and Cl^- was quantified by measuring Stern-Volmer constants (Fig. 4.7). The two FPs are quenched 10^8 -fold more strongly by H^+ than Cl^- on a molar basis. Moreover, the two FPs will respond to a shift from 0 to 100 mM Cl^- by a decrease in

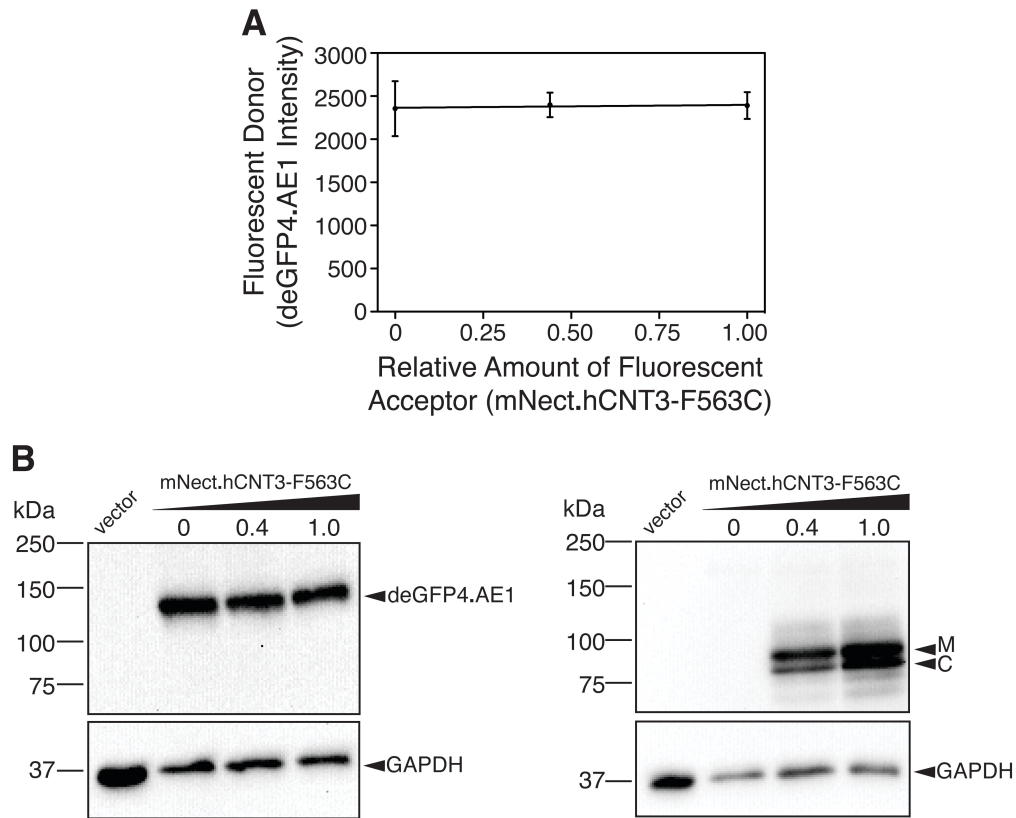


Figure 4.6. Assessment of fluorescence resonance energy transfer (FRET) between deGFP4 and mNectarine. HEK293 cells grown on glass coverslips were transiently co-transfected with deGFP4.AE1 and increasing amounts of mNect.hCNT3-F563C cDNA, or empty vector cDNA. (A) Coverslips were placed on the stage of a confocal microscope, and perfused with nigericin/high potassium solution, pH 7.0 (24 °C), to clamp cytosolic pH. Fluorescence of deGFP4.AE1 was monitored for 30 s. Fluorescence data were fitted by linear regression, and the slope of the line is not significantly different than zero ($P = 0.4$, $R^2 = 0.8$, $n = 3$). (B) Expression of deGFP4.AE1 and mNect.hCNT3-F563C. Transfected HEK293 cells were separated by SDS-PAGE, immunoblotted, and probed with anti-AE1 (IVF12) (top left), anti-RFP (top right) or anti-GAPDH (bottom) antibodies. Numbers above immunoblot indicate relative amount of mNect.hCNT3-F563C. M indicates mature glycosylated and C indicates core glycosylated.

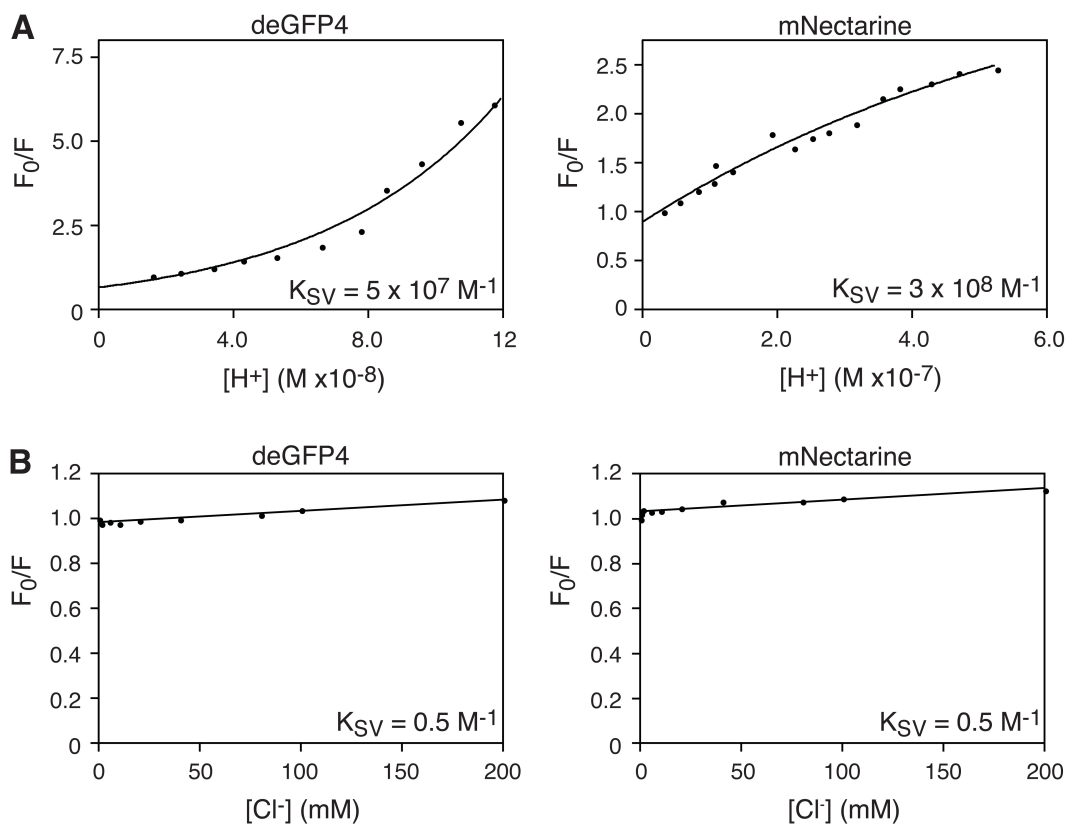


Figure 4.7. **Fluorescence quenching of deGFP4 and mNectarine by H^+ and Cl^- .** HEK293 cells were transiently transfected with deGFP4 or mNect cDNA. Cells were solubilized with 5% Triton X-100, 50 mM phosphate, pH 7.6, and titrated with (A) 50 mM phosphate, pH 4.0 or (B) 400 mM or 4.0 M NaCl. F_0 is the initial fluorescence intensity (at pH 7.8 for deGFP4 and pH 7.5 for mNect, or 0 mM Cl^-) and F is the fluorescence intensity at each $[H^+]$ or $[Cl^-]$. Calculated Stern-Volmer constants (K_{SV}) for either H^+ (A) or Cl^- (B) are indicated as inset values in each panel.

fluorescence of no more than 5%, indicating that both proteins are suitable to measure pH during $\text{Cl}^-/\text{HCO}_3^-$ exchange.

4.2.3 Correction for FP photobleaching

Extended periods of illumination of deGFP4 and mNect, under pH-clamped conditions, resulted in a continuous decrease of fluorescence, indicative of photobleaching (Fig. 4.8A). We corrected for photobleaching by fitting fluorescence data from pH 7.0-clamped deGFP4 and mNect co-transfected HEK293 cells (Fig. 4.8A) with an exponential decay equation, and applying an exponential correction [29] (Fig. 4.8B). To limit the effects of photobleaching, FP illumination was paused during experiments when possible.

The ability of cytosolic deGFP4 and mNect to report HEK293 cell cytosolic pH accurately following photobleaching correction was assessed by sequentially clamping cytosolic pH to medium pH, using the H^+ ionophore nigericin (Fig. 4.8C). Data was corrected for photobleaching, and fluorescence was calibrated to cytosolic pH by generation of a standard curve, relating average fluorescence to medium pH at standard pH values. Average pH values during perfusion with each solution were then calculated (Fig. 4.8C). The absolute difference in pH reported by deGFP4 and mNect was 0.02 ± 0.01 pH units, and the absolute difference between medium pH and FP-reported pH was 0.03 ± 0.01 and 0.02 ± 0.01 for deGFP4 and mNect, respectively. The magnitude of these errors in measurement of cytosolic pH are close to the 0.01 pH unit error found previously for the well-established pH-sensor, BCECF-AM [29]. There was a

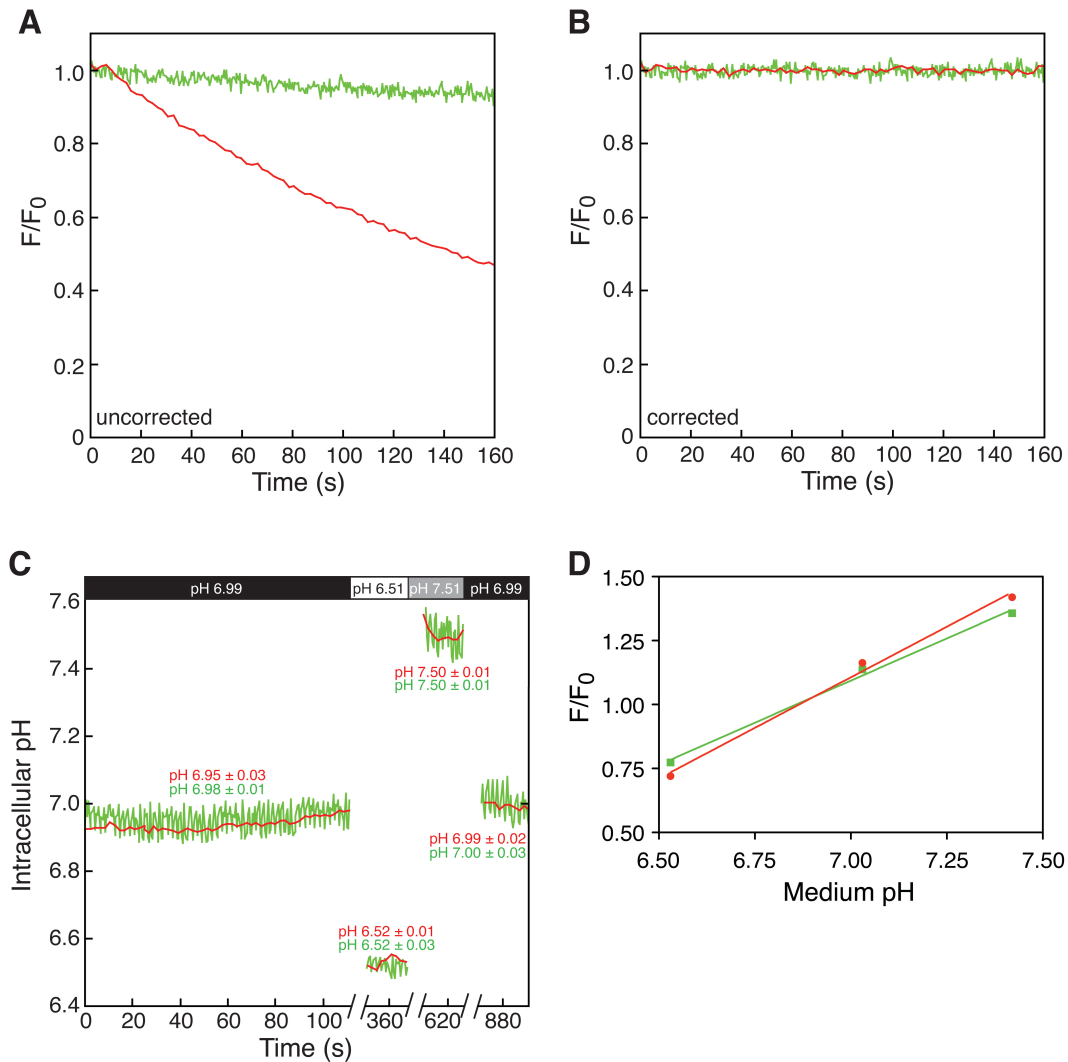


Figure 4.8. **Photobleaching correction for deGFP4 and mNectarine.** HEK293 cells grown on glass coverslips were transiently co-transfected with deGFP4 and mNect cDNAs and placed on the stage of a confocal microscope. (A,B) Cells were perfused with nigericin/high potassium solution, pH 7.0 (24 °C), to clamp cytosolic pH. deGFP4 (green) and mNect (red) fluorescence were monitored. F_0 is the initial fluorescence intensity and F is the fluorescence intensity at each time point. (B) Data from *panel A* has been corrected for photobleaching, using the approach described in methods. (C) Cells were perfused consecutively with nigericin/high potassium medium, at the pHs indicated in bars at top. Fluorescence values were corrected for photobleaching, and transformed to pH_i . Coloured numbers above and below the traces indicate average pH reported by each deGFP4 ($n = 5$) and mNect ($n = 5$). Breaks in the X-axis represent time (240 s) during which illumination was paused to minimize photobleaching. (D) Plot of F/F_0 versus medium pH derived from pH clamping experiment similar to that shown in *panel C*. Note that Y error bars are plotted, but are smaller than data points.

linear relationship between medium pH and fluorescence of deGFP4 and mNect in co-transfected cells (Fig. 4.8D). We conclude that after correction for photobleaching and appropriate calibration, deGFP4 and mNect accurately report cytosolic pH.

The accuracy of changes in pH_i reported by cytosolic deGFP4 and mNect during AE1-mediated $\text{Cl}^-/\text{HCO}_3^-$ exchange was examined next. HEK293 cells grown on glass coverslips were transiently co-transfected with cytosolic deGFP4, cytosolic mNect, and either AE1 or AE1-P652C, a functionally inactive mutant of AE1 [38]. Coverslips were placed on the stage of a confocal microscope, and perfused alternately with Cl^- -containing Ringer's buffer and Cl^- -free Ringer's buffer. HCO_3^- transport rates were determined by linear regression of the initial rate of pH_i change upon switching to Cl^- -free Ringer's buffer, and flux of H^+ -equivalents calculated. A rise in pH_i in response to switching to Cl^- -free Ringer's buffer was observed for deGFP4/mNect/AE1 co-transfected cells (Fig. 4.9A), but not for cells co-transfected with inactive AE1-P652C (Fig. 4.9B). The H^+ -equivalent fluxes reported by deGFP4 and mNect in AE1 co-transfected cells did not differ significantly from each other (Fig. 4.9C). Background H^+ -equivalent flux reported by deGFP4 and mNect in AE1-P652C co-transfected cells also did not differ significantly from each other (Fig. 4.9C). The slight acidification observed suggests that there may be a slight increase in the CO_2 concentration in the Cl^- -free Ringer's solution, which would slightly decrease the rate of measured alkalization observed in AE1-transfected cells (Fig. 4.9A). Together, these data reveal that deGFP4 and mNect report indistinguishable pH values during AE1-

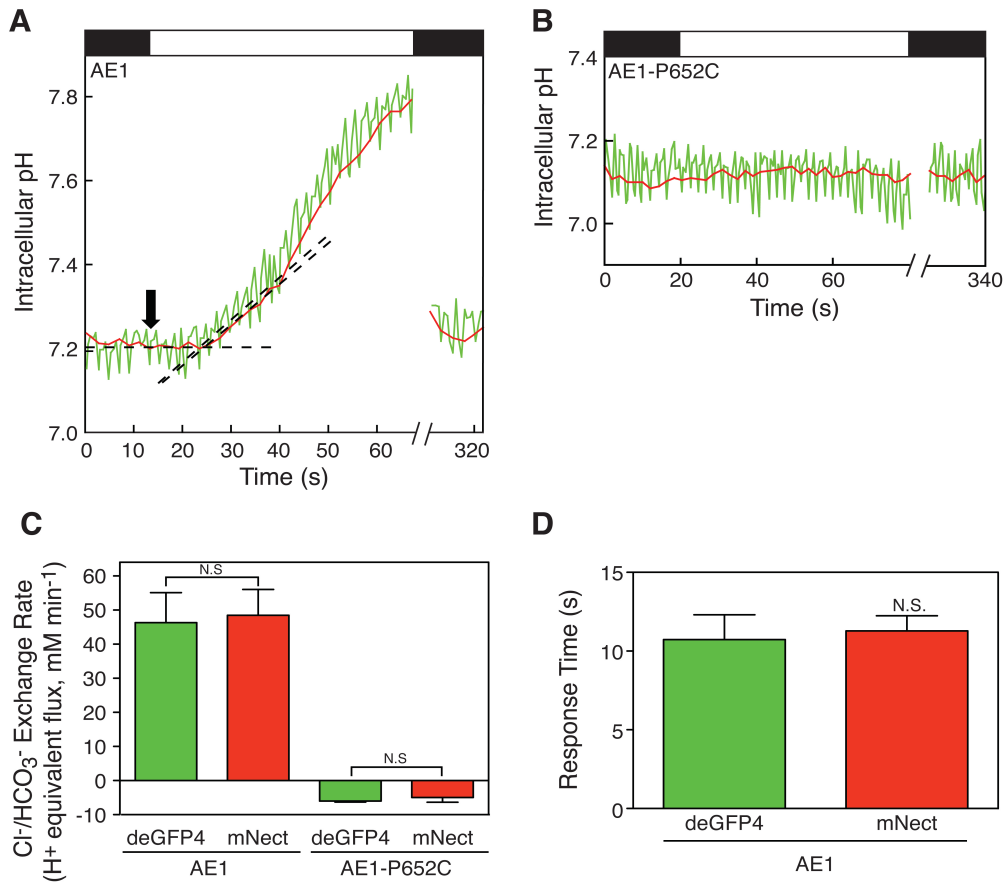


Figure 4.9. pH and response time measured using cytosolic deGFP4 and mNectarine during AE1-mediated Cl⁻/HCO₃⁻ exchange. HEK293 cells grown on glass coverslips were transiently co-transfected with deGFP4 and mNect cDNAs and AE1-WT cDNA (A) or AE1-P652C cDNA, a functionally inactive mutant of AE1 (B). Coverslips were placed on the stage of a confocal microscope, and perfused alternately with Cl⁻-containing Ringer's buffer (black bars) and Cl⁻-free Ringer's buffer (white bar), at 24 °C. At the end of each experiment pH was calibrated via the nigericin/high potassium technique (not shown). Green and red traces represent deGFP4 and mNect fluorescence, respectively. Fluorescence values were corrected for photobleaching, and transformed to pH. Breaks in the X-axis represent time (240 s) during which illumination was paused to minimize photobleaching. Dashed lines represent linear regression of baseline pH_i and initial rate of pH_i change resulting from Cl⁻/HCO₃⁻ exchange. Black arrow indicates the time point when perfusion was switched to Cl⁻-free Ringer's buffer. (C) Quantification of the initial Cl⁻/HCO₃⁻ exchange rate upon switching to Cl⁻-free Ringer's buffer. Error bars represent standard error (n = 3 or 4). N.S. indicates non-significant difference (P = 0.9 and P = 0.5, respectively). (D) In Cl⁻/HCO₃⁻ exchange assays of cells transfected with AE1-WT, response time represents the elapsed time between perfusion switch to Cl⁻-free Ringer's buffer (indicated by black arrow in A) and the start pH_i of rise reported by cytosolic deGFP4 and cytosolic mNect. Error bars represent standard error (n = 4). N.S. indicates non-significant difference (P = 0.8).

mediated $\text{Cl}^-/\text{HCO}_3^-$ exchange, and that the alkalinization observed in AE1-transfected cells arises from the change in the Cl^- gradient, and not a decrease in CO_2 concentration between the two solutions.

In each $\text{Cl}^-/\text{HCO}_3^-$ exchange assay cells were perfused with Ringer's buffer, followed by Ringer's buffer without Cl^- , to induce AE1-mediated $\text{Cl}^-/\text{HCO}_3^-$ exchange and associated alkalinization. Illumination was then consistently paused for 240 s to minimize photobleaching and perfusion was concomitantly switched back to Cl^- -containing Ringer's buffer. Following this 240 s interval without illumination (see broken X-axis Fig. 4.9A, B), samples were again illuminated in order to record the return to baseline pH. The data following the pause in illumination show the return to baseline pH, indicating that correction for photobleaching was effective.

To examine the temporal response of free cytosolic deGFP4 and mNect to changes of pH_i we measured the time between the removal of extracellular Cl^- and the FP's detection of a change in pH_i during AE1-mediated $\text{Cl}^-/\text{HCO}_3^-$ exchange (Fig. 4.9A). dpH_i/dt was determined by linear regression of the initial rate of pH_i change upon switching to Cl^- -free Ringer's buffer. Baseline pH_i was also fitted by linear regression. The intersection of these two lines represents the time when each FP began to detect a change in pH_i (Fig. 4.9A). The time at which the medium was switched to Cl^- -free Ringer's buffer was subtracted from this value to obtain the response time to detect the pH_i change. Measured in this way response time integrates the time taken to exchange media, the rate of pH_i change induced by AE1, the rate of H^+ diffusion and the time taken for the FP to change

fluorescence upon pH variation. All of these factors but the last are the same for deGFP4 and mNect in the experimental design used here, so any difference in response time is attributable to a difference in temporal response of the two FPs. There was no significant difference in response time during $\text{Cl}^-/\text{HCO}_3^-$ exchange between cytosolic deGFP4 and mNect (10.7 ± 1.6 s and 11.3 ± 1.0 s, respectively). To assess the temporal responsiveness of deGFP4 and mNect independently of $\text{Cl}^-/\text{HCO}_3^-$ exchange, we also measured deGFP4 and mNect response time after an NH_4Cl pre-pulse (Fig. 4.10). There was no significant difference in cytosolic deGFP4 and mNect response time (7.9 ± 0.1 s and 7.9 ± 0.3 s, respectively) (Fig. 4.10). To further examine the nature of the time delay, we measured the time taken to detect the fluorescence of BCECF upon switching from media alone to media containing the fluorophore BCECF. BCECF was initially detected at 5.4 ± 1.0 s, with complete media exchange occurring at 10.4 ± 2.4 s (data not shown). Thus of the 7.9 s response time for deGFP4 and mNect to detect NH_4Cl -associated acidification, 5.4 s arises from the time to exchange solutions in the perfusion chamber. Together, these data reveal that the temporal responses of deGFP4 and mNect to changes of pH are indistinguishable, and that a significant component of the time delay is the time taken to exchange solution (Figs. 4.9, 4.10).

4.2.4 Discrimination of ER and plasma membrane fluorescence

As is common with membrane proteins expressed in transfected cells, AE1 does not process fully to the plasma membrane (PM) in HEK293 cells [9].

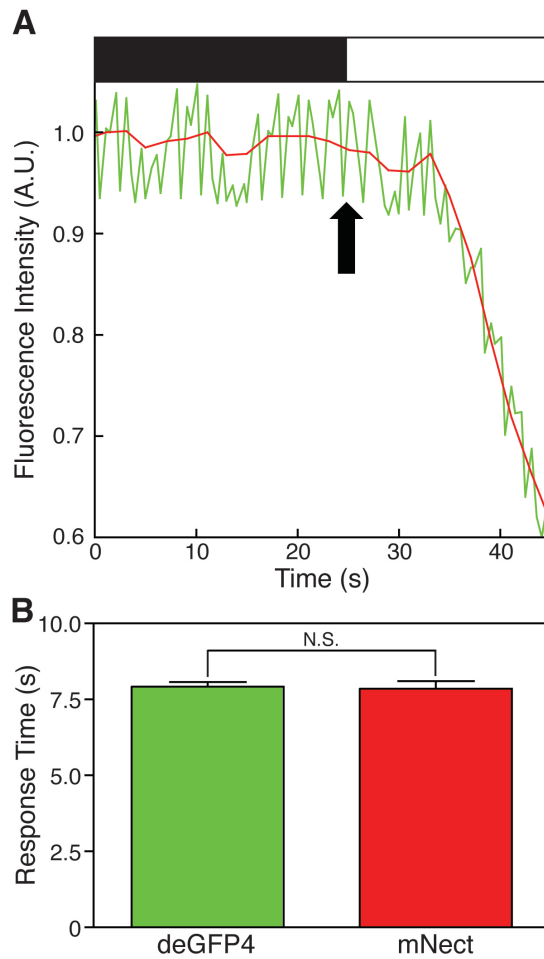


Figure 4.10. **Cytosolic deGFP4 and mNectarine temporal responsiveness to pH changes induced by NH₄Cl.** (A) HEK293 cells grown on glass coverslips and transiently co-transfected with deGFP4 and mNect were mounted on the confocal microscope stage and perfused with HCO₃⁻-free Ringer's buffer, containing 50 mM NH₄Cl (black bar) or 0 mM NH₄Cl (white bar), at 37 °C. (B) Response time represents the elapsed time between perfusion switch to 0 mM NH₄Cl (indicated as black arrow in A) and the start of pH_i reduction reported by cytosolic deGFP4 and cytosolic mNect. Error bars represent standard error (n = 4). N.S. indicates non-significant difference (P = 0.8).

The presence of endoplasmic reticulum (ER)-retained deGFP4.AE1 leads to the possibility that fluorescence measurements report not only on plasma membrane deGFP4.AE1, but also ER-associated deGFP4.AE1 not experiencing a transmembrane Cl^- gradient and therefore not active in $\text{Cl}^-/\text{HCO}_3^-$ exchange. As the ER forms a reticular network and comes into very close proximity to the PM [39], fluorescence measured from a PM region of interest (ROI) might also include ER-associated fluorescence. To quantify the ER-associated fluorescence in the PM ROIs, mNect was fused to the cytoplasmic C-terminus of the ER-marker, calnexin (CNX) [40, 41]. Cells were co-transfected with deGFP4.AE1 and CNX.mNect cDNAs, or deGFP4.AE1 and mNect.hCNT3-F563C cDNAs, and the deGFP4 and mNect fluorescence was determined in PM ROIs of each cell type. To normalize for differences in protein expression and size of ROI, mNect fluorescence was normalized to set deGFP4 fluorescence to the same level in each ROI. Assuming that the intensity of ER-associated mNect fluorescence was the same in cells expressing mNect.hCNT3-F563C, or CNX.mNect, we determined the amount of mNect fluorescence in the PM ROI arising from ER-associated mNect. Approximately 17% of the PM mNect signal arose from ER-associated mNect (Table 4.1), which needs to be considered when interpreting later results.

4.2.5 Measurement of the rate of H^+ diffusion from plasma membrane to cytosolic surface of ER

To measure the H^+ diffusion rate from the plasma membrane to the ER surface, $\text{Cl}^-/\text{HCO}_3^-$ exchange was carried out in cells co-expressing deGFP4.AE1

Table 4.1. **Quantification of ER-associated fluorescence in PM ROI.** The mean fluorescence intensity (in pixels) of PM ROIs used in the calculation of quantification of ER-associated fluorescence in PM ROI, as described in section 2.2.18.

mNect.hCNT3-F563C/deGFP4.AE1 co-transfected cells

| Probe | Localization | ROI | Fluorescence Intensity (pixels) |
|-------------------|---------------------|------------|--|
| mNect.hCNT3-F563C | ER, PM | PM | 4291 |
| deGFP4.AE1 | ER, PM | PM | 1692 |

CNX.mNect/deGFP4.AE1 co-transfected cells

| Probe | Localization | ROI | Fluorescence Intensity (pixels) |
|--------------|---------------------|------------|--|
| CNX.mNect | ER | PM | 637 |
| deGFP4.AE1 | ER, PM | PM | 1453 |

and CNX.mNect. PM and ER ROIs were selected (Fig. 4.11A), and fluorescence intensities determined. Following removal of extracellular Cl^- , the lag time to detect the rise of pH at CNX.mNect was significantly longer (23.2 ± 1.8 s) than at deGFP4.AE1 (16.1 ± 1.4 s) (Fig. 4.11B-C). It took approximately 7 s longer for CNX.mNect to detect a change in pH_i initiated by AE1 at a distance of 4 μm from AE1 (the distance between the PM and centre of ER ROIs), which corresponds to a H^+ diffusion rate of 0.6 $\mu\text{m}/\text{s}$. The lag time does not arise from the rate at which each FP is able to report pH, since the two free cytosolic FPs have the same temporal responsiveness (Figs. 4.9D, 4.10).

4.2.6 Measurement of the rate of H^+ diffusion along the cytosolic surface of the plasma membrane

The central question we wanted to answer is: does the pH in the immediate environment of AE1 differ from other sites at the plasma membrane? To answer this question we measured pH_i changes and differences in time of pH rise (ΔT) at varied deGFP4.AE1:mNect.hCNT3-F563C co-transfection ratios during AE1-mediated $\text{Cl}^-/\text{HCO}_3^-$ exchange. Varying the amount of mNect.hCNT3-F563C cDNA at constant levels of deGFP4.AE1 cDNA will produce cells with differing amounts of mNect.hCNT3-F563C at the plasma membrane. Correspondingly, there will be a range of average distances between deGFP4.AE1 and mNect.hCNT3-F563C.

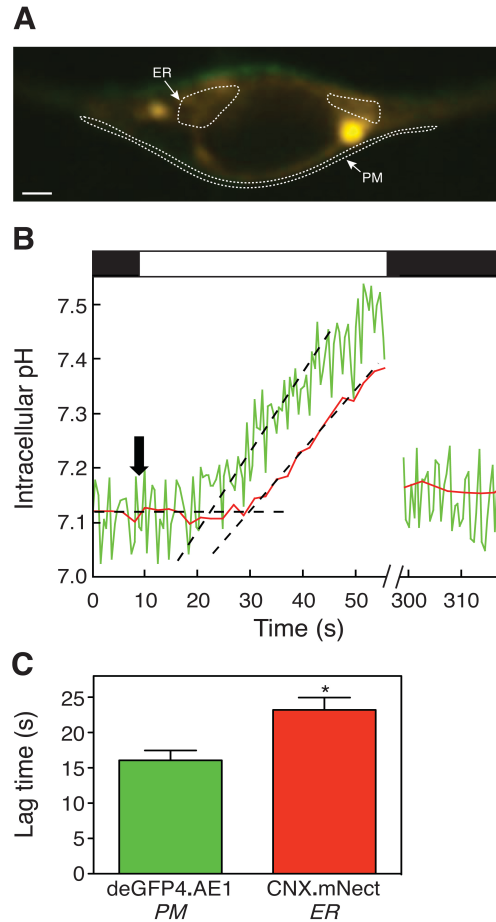


Figure 4.11. Lag time associated with $\text{Cl}^-/\text{HCO}_3^-$ exchange: measurement at plasma membrane and endoplasmic reticulum. (A) Live cell fluorescence confocal image of an HEK293 cell, transiently co-transfected with deGFP4.AE1 and CNX.mNect cDNAs. White dashed lines illustrate the regions of interest (ROIs) whose fluorescence was quantified as a function of time, using the approach described in methods. PM and ER indicate plasma membrane ROI and ER ROI, respectively. White bar represents $4\ \mu\text{m}$. (B) HEK293 cells grown on glass coverslips were co-transfected with deGFP4.AE1 and CNX.mNect cDNAs. Coverslips were placed on the stage of a confocal microscope, and perfused alternately with Cl^- -containing Ringer's buffer (black bars) and Cl^- -free Ringer's buffer (white bar), at $24\ ^\circ\text{C}$. At the end of each experiment pH was calibrated via the nigericin/high potassium technique (not shown). Green and red traces represent deGFP4.AE1 and CNX.mNect fluorescence, respectively. Fluorescence values were corrected for photobleaching, and converted to pH. Breaks in the X-axis represent time ($240\ \text{s}$) during which illumination was paused to minimize photobleaching. Black dashed lines represent linear regression of baseline pH_i and initial rate of pH_i change resulting from $\text{Cl}^-/\text{HCO}_3^-$ exchange. Black arrow indicates the time point when perfusion switched to Cl^- -free Ringer's buffer. (C) Lag time between changing to Cl^- -free buffer and start of rise in pH_i for plasma membrane deGFP4.AE1 and ER-resident CNX.mNect. Error bars represent standard error ($n = 3$). Asterisk indicates significant difference ($P = 0.03$).

The mean deGFP4.AE1-mNect.hCNT3-F563C distance was calculated on the basis of the amount of deGFP4.AE1 and mNect.hCNT3-F563C present in each cell (Fig. 4.12), and fraction of protein at the cell surface (Fig. 4.13). To determine the spatial distribution of molecules at the cell surface, we need to know if AE1 and hCNT3 associate into dimers or higher molecular weight oligomers. The functional unit of AE1 is established as a dimer [42-44], but the oligomeric state of hCNT3 has yet to be determined. SDS-PAGE is unsuitable to assay native quaternary structure, as SDS is a denaturing detergent that disrupts oligomeric assemblies. We therefore performed perfluorooctanoic acid polyacrylamide gel electrophoresis (PFO-PAGE) [45-47], which preserves native quaternary structure. HEK293 cells transiently transfected with mNect.hCNT3-F563C or AE1 were lysed, and proteins were separated by either PFO-PAGE or SDS-PAGE. Disulphide bridges might form between cysteine residues in the extracellular C-terminal tail of hCNT3 [48], causing possible hCNT3 dimerization, so we conducted the mNect.hCNT3-F563C PFO experiment in the presence and absence of the reducing agent, dithiothreitol (DTT). mNect.hCNT3-F563C is detected as multiple bands around 100 kDa, representing core and mature glycosylated forms of the protein [29]. These bands are detected in both the PFO-PAGE (Fig. 4.14A) and the SDS-PAGE (Fig. 4.14B) immunoblots, at the same molecular weight. The absence of bands around 200 kDa on the PFO-PAGE immunoblot indicates that hCNT3 does not form dimers in the presence or absence of DTT (Fig. 4.14A). As a positive control, we also assayed the

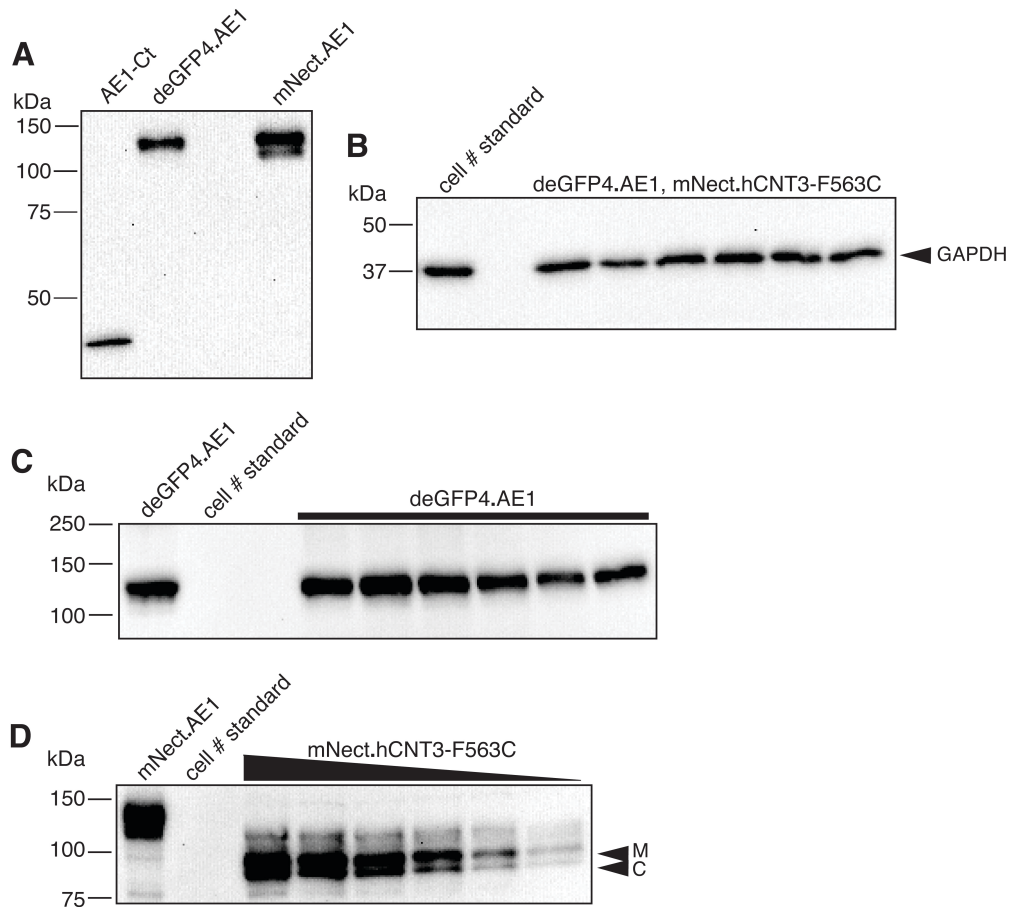


Figure 4.12. Quantification of deGFP4.AE1, mNect.AE1 and cell number standards. (A) Cell lysates from HEK293 cells transfected with deGFP4.AE1 or mNect.AE1 were resolved on SDS-PAGE along with 40 ng of AE1-Ct standard. Immunoblot was probed with an anti-AE1 (IVF12) antibody. Bands were quantified by densitometry, and the amount (in moles/10 μ l) of deGFP4.AE1 and mNect.AE1 was determined. These samples were used as standards in subsequent immunoblots. (B) HEK293 cells were harvested, counted and corresponding detergent lysates were used as a cell number standard on all immunoblots. Representative immunoblot of cell number standard, along with deGFP4.AE1/mNect.hCNT3-F563C experimental samples (described below) probed with an anti-GAPDH antibody. (C,D) HEK293 cells were transiently co-transfected with cDNA encoding a constant amount of deGFP4.AE1 cDNA, a decreasing amount mNect.hCNT3-F563C cDNA, and untagged hCNT3. Cell lysates, deGFP4.AE1 or mNect.AE1 standards, and cell number standard were separated by SDS-PAGE. Immunoblots were probed with anti-AE1 antibody (IVF12) (C), or anti-RFP antibody (D). Bands were quantified by densitometry and the amount of deGFP4.AE1 and mNect.hCNT3-F563C (in molecules/cell) was used in further analysis. M indicates mature glycosylated and C indicates core glycosylated.

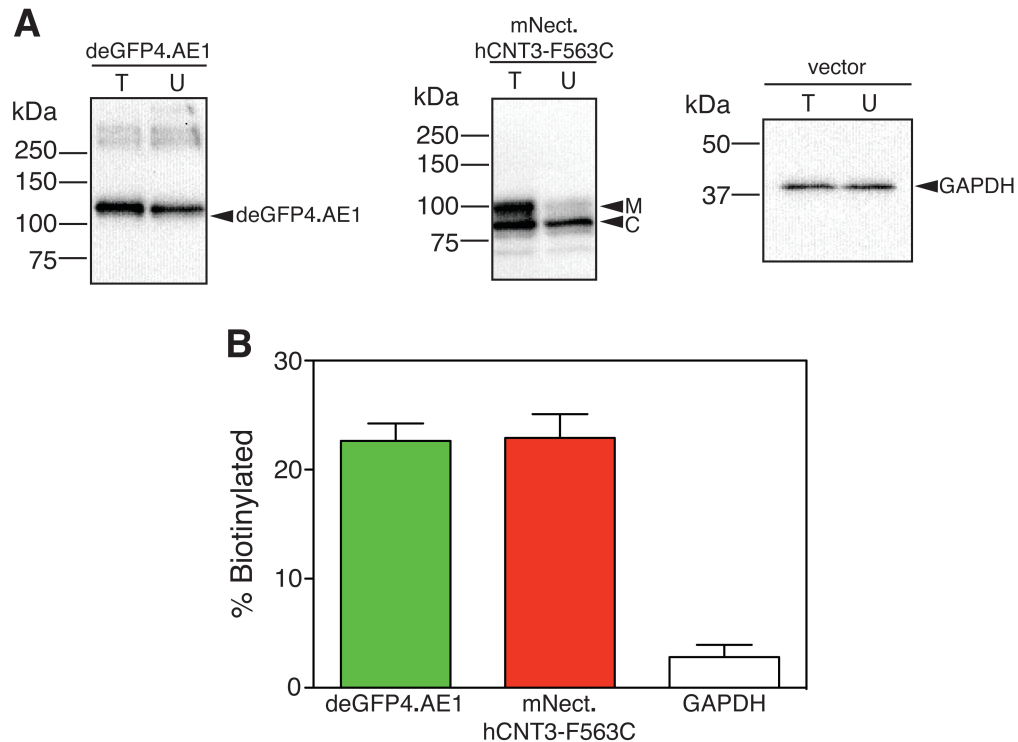


Figure 4.13. Cell surface processing of deGFP4.AE1 and mNect.hCNT3-F563C. HEK293 cells were transiently co-transfected with varying deGFP4.AE1:mNect.hCNT3-F563C cDNA ratios, or with empty vector. The amount of deGFP4.AE1 cDNA remained constant, while the amount of mNect.hCNT3-F563C cDNA decreased over six different ratios. hCNT3 alone was added to ensure an equal amount of membrane protein was expressed. Cells were labeled with Sulfo-NHS-SS-Biotin and lysed. Half of the total (T) lysate was removed for SDS-PAGE analysis, and half was incubated with streptavidin resin. Biotinylated proteins (at the cell surface) were bound to streptavidin resin, while unbiotinylated proteins (intracellular) remained in the unbound fraction (U). (A) Equal amounts of total lysate (T) and unbound supernatant (U) were separated by SDS-PAGE. Immunoblots were probed with anti-AE1 (IVF12), anti-RFP or anti-GAPDH antibodies. M indicates mature glycosylated and C indicates core glycosylated. (B) Fraction of protein labeled by the membrane-impermeant biotinylation reagent (representing protein at the cell surface) as calculated by densitometry, averaged for all deGFP4.AE1:mNect.hCNT3-F563C cDNA ratios. Error bars represent standard error (n = 50 to 56).

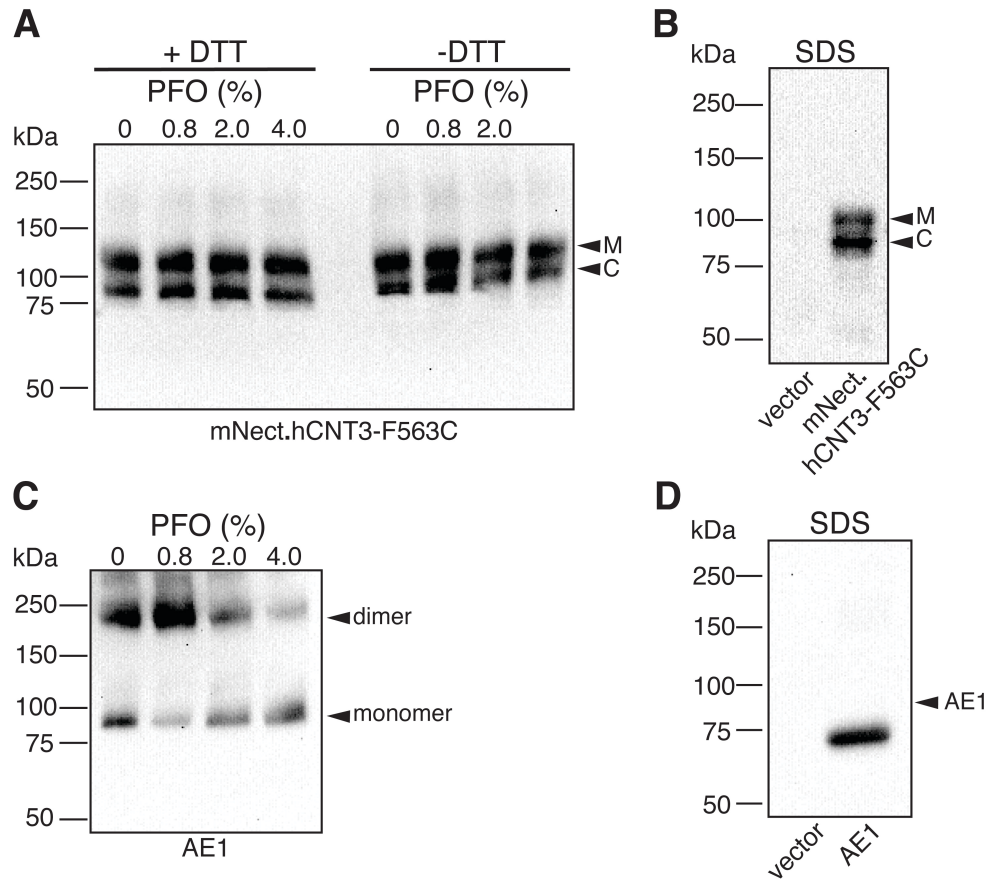


Figure 4.14. **Oligomeric state of mNect.hCNT3-F563C and AE1 assessed by PFO-PAGE.** HEK293 cells were transiently transfected with mNect.hCNT3-F563C (A,B), AE1 (C,D), or empty vector (B,D) cDNAs. (A,C) Cell lysates were mixed with PFO sample buffer containing 0, 0.8, 2.0 or 4.0% PFO, with (+) or without (-) DTT and separated by PFO-PAGE. At low concentrations PFO is non-denaturing, but higher concentrations will disrupt protein-protein interactions. (B,D) Cell lysates were separated by SDS-PAGE. Immunoblots were probed with anti-RFP (A,B) or anti-AE1 (IVF12) (C,D) antibody. M indicates mature glycosylated and C indicates core glycosylated.

oligomeric state of AE1 (Fig. 4.14C). We were able to detect both AE1 monomer and dimer, with more dimer present at lower concentrations of PFO (Fig. 4.14C). AE1 migrated as a single band at approximately 100 kDa in the SDS-PAGE gel, which represents fully dissociated monomer (Fig. 4.14D). We conclude that deGFP4.AE1 is a dimer and mNect.hCNT3-F563C is a monomer under native conditions, in the plasma membrane of HEK293 cells. This was used in calculations of protein distribution. Given the detection limits of deGFP4 and mNect we were unable to make measurements over a broader range of deGFP4.AE1:mNect.hCNT3-F563C expression ratios.

These calculations assume a random distribution of proteins at the plasma membrane. To investigate the distribution of the FPs at the plasma membrane, HEK293 cells co-transfected with deGFP4.AE1 and mNect.hCNT3-F563C cDNA were analyzed by confocal microscopy. Less than 4% of pixels at the plasma membrane could be detected as peaks whose intensities were more than 10% of the maximum intensity (Fig. 4.15). We conclude that deGFP4.AE1 and mNect.hCNT3-F563C are expressed randomly at the plasma membrane of HEK293 cells, at least at the resolution of the light microscope.

Two parameters were assessed as measures of H⁺ microdomain formation at the plasma membrane during Cl⁻/HCO₃⁻ exchange by AE1: **1. ΔT :** If a H⁺ microdomain forms there should be a time difference between when deGFP4.AE1 and a protein distant from AE1 (mNect.hCNT3-F563C) sense the pH_i change. **2. *Rate of pH change.*** During HCO₃⁻ influx the pH will rise as a result of base entry. We expect that the rate of pH change detected by deGFP4.AE1 will be faster than

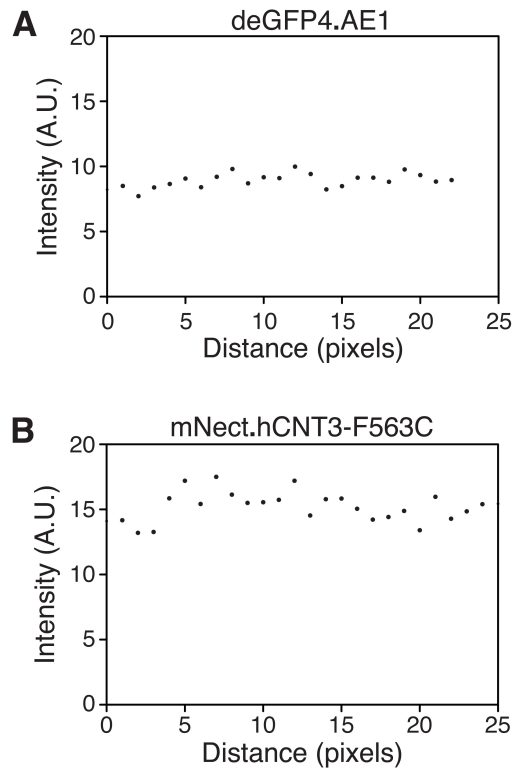


Figure 4.15. **Distribution of deGFP4.AE1 and mNect.hCNT3-F563C at the plasma membrane.** HEK293 cells transiently co-transfected with deGFP4.AE1 and mNect.hCNT3-F563C cDNAs were analyzed by confocal microscopy. The level of FP abundance along portions of the plasma membrane was analyzed and pixel intensity versus distance was plotted.

the rate detected by a distant protein, as the pH gradient would be highest at the centre of the H⁺ microdomain.

Cl⁻/HCO₃⁻ exchange assays were conducted on HEK293 cells co-expressing deGFP4.AE1 and mNect.hCNT3-F563C (Fig. 4.16) over the range of distances described above. Time differences and rates of pH_i change were determined in PM ROIs (as seen in Fig. 4.11A).

Time differences (ΔT) were measured as the difference between the extrapolated time when each of the two pH-reporter FPs initially detected a rise in pH_i during Cl⁻/HCO₃⁻ exchange (Fig. 4.16A). Plots of ΔT versus average deGFP4.AE1-mNect.hCNT3-F563C distance revealed that ΔT increased with increasing distance (Fig. 4.16B), and that the slope of the linear regression fit was significantly different than zero ($P = 0.04$). The slope of the linear fit is 175 s/ μm , which corresponds to a H⁺ diffusion rate along the plasma membrane of 0.01 $\mu\text{m}/\text{s}$. The time difference between when pH_i changes were detected at the surface of deGFP4.AE1 and mNect.hCNT3-F563C is consistent with a H⁺ microdomain originating at the surface of AE1 during HCO₃⁻ transport.

4.2.7 Estimation of the size of the H⁺ microdomain

The dataset was analysed in a second way. The initial rate of pH_i change initiated by AE1-mediated Cl⁻/HCO₃⁻ exchange reported by mNect.hCNT3-F563C was normalized to the rate reported by deGFP4.AE1 and plotted as a function of distance between the two proteins (Fig. 4.16C). The slope of the linear regression fit was significantly different than zero ($P = 0.03$), indicating

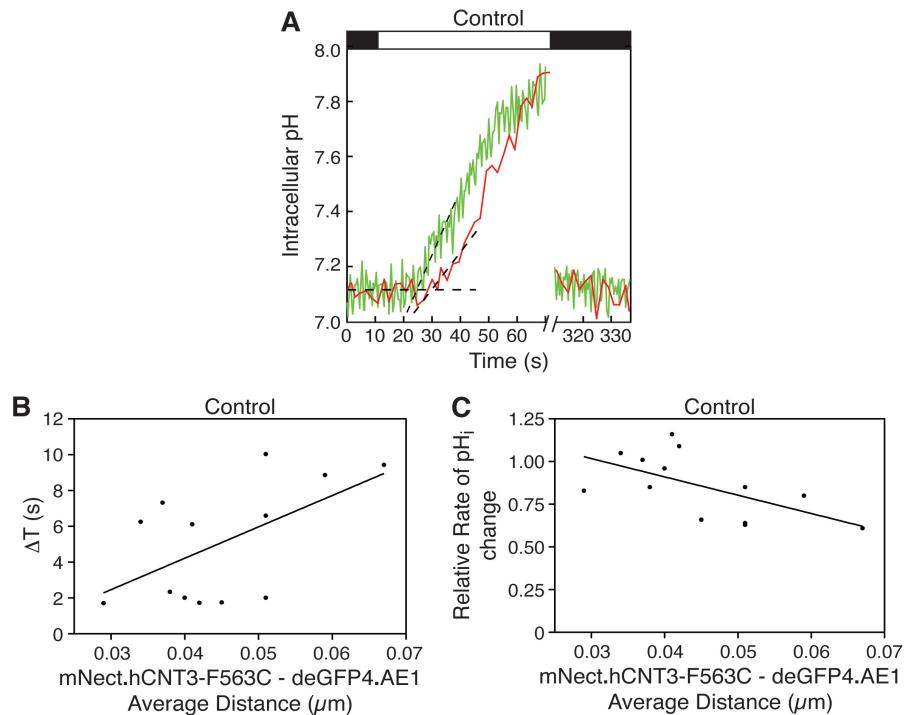


Figure 4.16. Evidence for a H^+ microdomain around AE1. HEK293 cells grown on glass coverslips were transiently co-transfected with cDNA encoding deGFP4.AE1, mNect.hCNT3-F563C, and untagged hCNT3. The amount of deGFP4.AE1 cDNA remained constant, and the amount of mNect.hCNT3-F563C decreased, compensated by increasing amounts of hCNT3 cDNA alone, to maintain a constant combined amount of mNect.hCNT3-F563C and hCNT3 cDNA. With appropriate calibration this enabled determination of average distance between mNect.hCNT3-F563C and deGFP4.AE1. Coverslips were placed on the stage of a confocal microscope, and perfused alternately with Cl^- -containing Ringer's buffer (black bars) and Cl^- -free Ringer's buffer (white bar), containing DMSO (control), at 37 °C. In three to four separate replicates, cells were transfected with one of four deGFP4.AE1:mNect.hCNT3 cDNA ratios (8:1, 4:1, 3:1 or 2:1). pH_i changes were determined for three to five cells per replicate. For each cell sample, the average distance separating deGFP4.AE1 and mNect.hCNT3-F563C was determined as described in section 2.2.22. (A) pH transient observed for deGFP4.AE1 (green) and mNect.hCNT3 (red) molecules at a distance of $\sim 0.07 \mu\text{m}$ apart. Breaks in the X-axis represent time (240 s) during which illumination was paused to minimize photobleaching. Black dashed lines represent linear regression of baseline pH_i and initial rate of pH_i change resulting from $\text{Cl}^-/\text{HCO}_3^-$ exchange. The difference between the time when a pH_i rise was detected at deGFP4.AE1 and at mNect.hCNT3-F563C was calculated as time delay (ΔT) (B). The data was fitted by linear regression, and the slope of the line is significantly different than zero ($P = 0.04$, $R^2 = 0.6$). (C) The rate of pH_i change at the surface of deGFP4.AE1 and mNect.hCNT3-F563C was measured during $\text{Cl}^-/\text{HCO}_3^-$ exchange and relative rate of pH_i change = hCNT3-F563C rate/AE1 rate. The data was fitted with linear regression, and the slope of the line is significantly different than zero ($P = 0.03$, $R^2 = 0.6$).

that distant mNect.hCNT3-F563C detects a lower rate of pH_i change than detected at the surface of AE1. We measured differences in pH_i that extended $\sim 0.07 \mu\text{m}$ from AE1. Thus, our calculations of average distances have allowed us to estimate the size of the H^+ microdomain at a resolution smaller than the limit of light microscopy. Extrapolation of the linear fit to the relative rate of pH_i change limit of 0 revealed a distance of $0.13 \mu\text{m}$, which represents the limit over which the environment around AE1 differs. In other words, this provides an estimate of the radius of the H^+ microdomain, assuming the data (Fig. 4.16C) can be fit by a straight line. We could not justifiably fit the data with another function, so $0.13 \mu\text{m}$ is the best estimate of the radius ($0.3 \mu\text{m}$ diameter) of the H^+ microdomain surrounding AE1. We conclude that plasma membrane proteins distant from AE1 experience a slower rise in pH during AE1-mediated HCO_3^- influx, over a narrow distance range, consistent with a H^+ microdomain around AE1. We further analysed the plateau pH reached upon achieving equilibrium in Cl^- free medium (Fig. 4.17). There was no significant difference between the plateau pH detected by deGFP4.AE1 and mNect.hCNT3-F563C, when the proteins were separated by either $0.03 \mu\text{m}$ or $0.07 \mu\text{m}$ (Fig. 4.17). This indicates that the H^+ microdomain diminishes within the approximately 50 s taken to reach the new equilibrium pH.

4.2.8 Role of carbonic anhydrase in H^+ microdomain formation

Carbonic anhydrase has two opposing roles in the generation of a H^+ microdomain around AE1. CAII maximizes the $\text{Cl}^-/\text{HCO}_3^-$ exchange rate of AE1 [13] (increasing the potential to develop a H^+ microdomain), but CA also

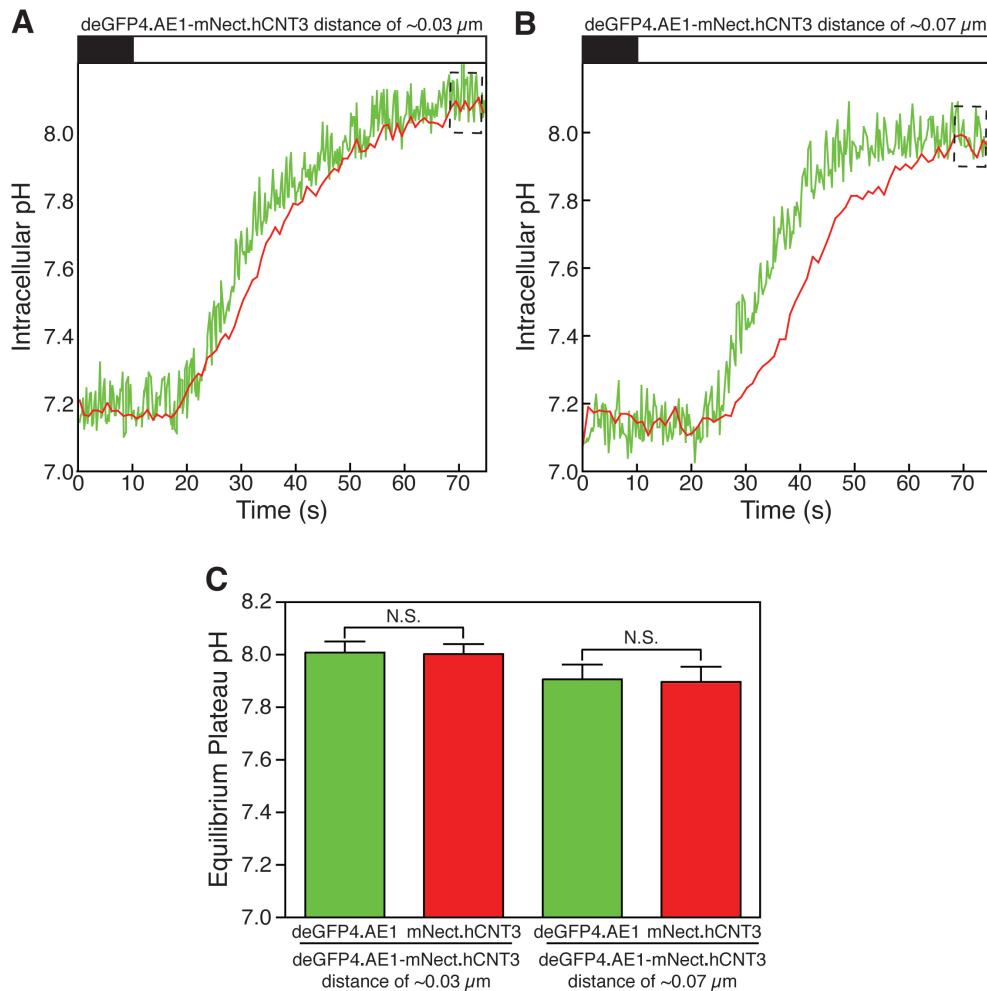


Figure 4.17. Equilibrium plateau pH after Cl/HCO_3^- exchange reported by deGFP4.AE1 and mNect.hCNT3. HEK293 cells grown on glass coverslips were transiently co-transfected with cDNA encoding deGFP4.AE1, mNect.hCNT3, and untagged hCNT3, at two different cDNA ratios, which resulted in average separation distances between deGFP4.AE1 and mNect.hCNT3 of 0.03 and 0.07 μm , as shown. The amount of deGFP4.AE1 cDNA remained constant, and the amount of mNect.hCNT3 decreased, compensated by increasing amounts of hCNT3 cDNA alone, to maintain a constant combined amount of mNect.hCNT3 and hCNT3 cDNA. Coverslips were placed on the stage of a confocal microscope, and perfused consecutively with Cl^- -containing Ringer's buffer (black bar) and Cl^- -free Ringer's buffer (white bar), at 37 $^\circ\text{C}$. At the end of each experiment pH was calibrated via the nigericin/high potassium technique (data not shown). (A) pH transient observed for deGFP4.AE1 (green) and mNect.hCNT3 (red) molecules at a distance of $\sim 0.03 \mu\text{m}$ apart. The equilibrium plateau pH is indicated by dashed box. (B) pH transient observed for deGFP4.AE1 (green) and mNect.hCNT3 (red) molecules at a distance of $\sim 0.07 \mu\text{m}$ apart. (C) The mean equilibrium plateau pH of each trace was measured. Error bars represent standard error ($n = 3$). N.S. indicates non-significant difference ($P = 0.9$).

accelerates H^+ diffusion [16] (dissipating a H^+ microdomain). In AE1-transfected cells endogenous CAII expression levels are approximately stoichiometric with AE1 [13] and no other cytosolic CA isoform is known to be expressed in HEK293 cell. To examine the role that CAII has in the development of the H^+ microdomain around AE1, Cl^-/HCO_3^- exchange assays were conducted in HEK293 cells co-transfected with different expression ratios of deGFP4.AE1 and mNect.hCNT3-F563C in the presence of the carbonic anhydrase inhibitor, ethoxzolamide (Fig. 4.18A). CA inhibition decreased the rate of Cl^-/HCO_3^- exchange by 66%, and suppressed H^+ microdomain formation as indicated by the lack of effect of changing deGFP4.AE1-mNect.hCNT3-F563C distance on either ΔT (Fig. 4.18B) or rate of pH_i change (Fig. 4.18C). This contrasts with the data collected using coverslips from the same dish of transfected cells, in the absence of ethoxzolamide, where a H^+ microdomain was observed (Fig. 4.16B,C).

The experiments of Figs. 4.16 and 4.18 were performed at physiological temperature, 37 °C. To determine the effect of temperature on H^+ microdomain development, we performed the same analysis at 24 °C (Fig. 4.19). These experiments confirmed the presence of a H^+ microdomain around AE1. At 24 °C the estimated size of the H^+ microdomain was slightly larger, 0.17 μm , than that found at 37 °C, consistent with a slowed diffusion rate at lower temperature. Measurement of the H^+ diffusion rate on the basis of ΔT , however, indicated a slope of 99 s/ μm (0.01 $\mu m/s$), which does not differ from the rate of H^+ movement at 37 °C.

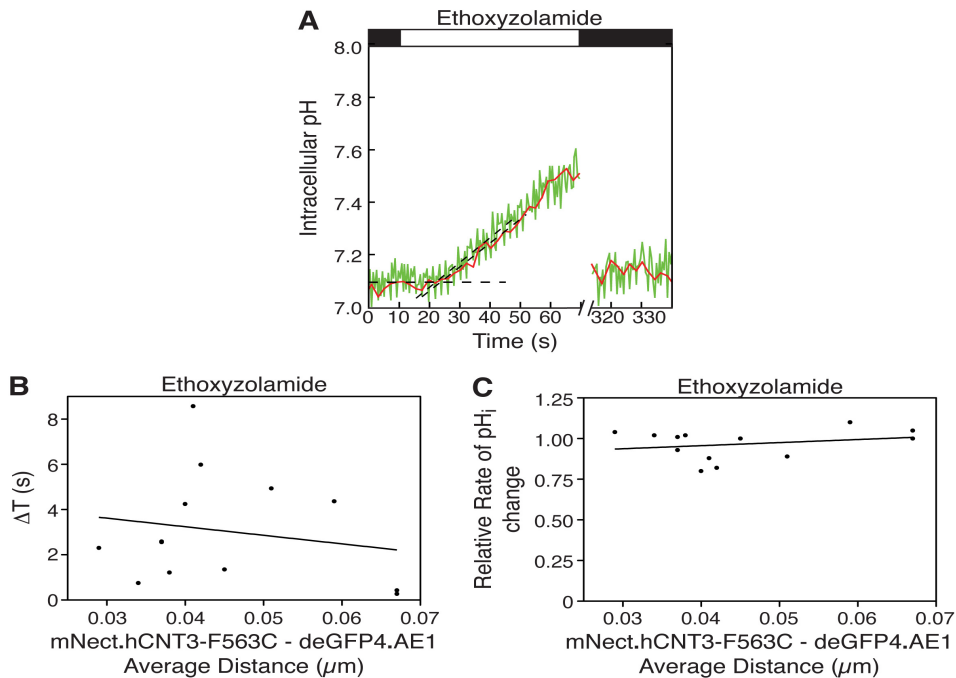


Figure 4.18. Role of CAII in H^+ microdomain formation around AE1. HEK293 cells grown on glass coverslips were transiently co-transfected with cDNA encoding deGFP4.AE1, mNect.hCNT3-F563C, and untagged hCNT3. The amount of deGFP4.AE1 cDNA remained constant, and the amount of mNect.hCNT3-F563C decreased, compensated by increasing amounts of hCNT3 cDNA alone, to maintain a constant combined amount of mNect.hCNT3-F563C and hCNT3 cDNA. With appropriate calibration this enabled determination of average distance between mNect.hCNT3-F563C and deGFP4.AE1. Coverslips were placed on the stage of a confocal microscope, and perfused alternately with Cl^- -containing Ringer's buffer (black bars) and Cl^- -free Ringer's buffer (white bar), containing $100 \mu\text{M}$ ethoxyzolamide, at 37°C . In three to four separate replicates, cells were transfected with one of four deGFP4.AE1:mNect.hCNT3 cDNA ratios (8:1, 4:1, 3:1 or 2:1). pH_i changes were determined for three to five cells per replicate. For each cell sample, the average distance separating deGFP4.AE1 and mNect.hCNT3-F563C was determined as described in section 2.2.22. (A) pH transient observed for deGFP4.AE1 (green) and mNect.hCNT3 (red) molecules at a distance of $\sim 0.07 \mu\text{m}$ apart. Breaks in the X-axis represent time (240 s) during which illumination was paused to minimize photobleaching. Black dashed lines represent linear regression of baseline pH_i and initial rate of pH_i change resulting from $\text{Cl}^-/\text{HCO}_3^-$ exchange. The difference between the time when a pH_i rise was detected at deGFP4.AE1 and at mNect.hCNT3-F563C was calculated as time delay (ΔT) (B). The data was fitted by linear regression, and the slope of the line is not significantly different than zero ($P = 0.5$, $R^2 = 0.2$). (C) The rate of pH_i change at the surface of deGFP4.AE1 and mNect.hCNT3-F563C was measured during $\text{Cl}^-/\text{HCO}_3^-$ exchange and relative rate of pH_i change = hCNT3-F563C rate/ AE1 rate. The data was fitted with linear regression, and the slope of the line is not significantly different than zero ($P = 0.4$, $R^2 = 0.3$).

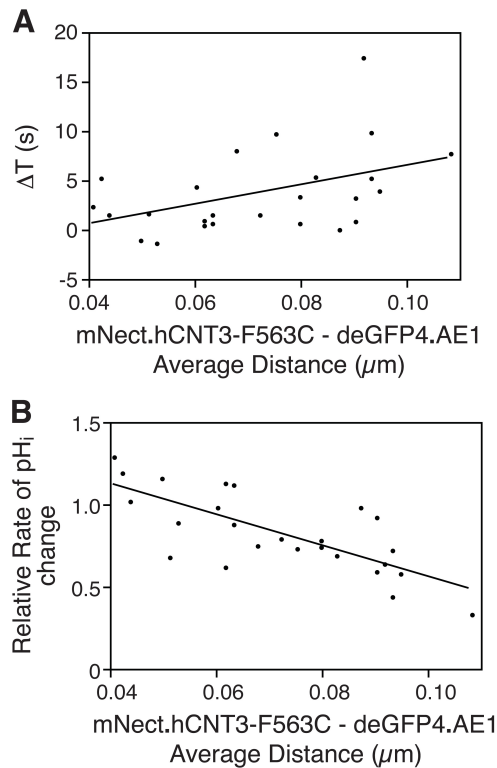


Figure 4.19. Effect of temperature on the H^+ microdomain around AE1. HEK293 cells grown on glass coverslips were transiently co-transfected with cDNA encoding deGFP4.AE1, mNect.hCNT3-F563C, and untagged hCNT3. The amount of deGFP4.AE1 cDNA remained constant, and the amount of mNect.hCNT3-F563C decreased, compensated by increasing amounts of hCNT3 cDNA alone, to maintain a constant combined amount of mNect.hCNT3-F563C and hCNT3 cDNA. Coverslips were placed on the stage of a confocal microscope, and perfused alternately with Cl^- -containing Ringer's buffer and Cl^- -free Ringer's buffer, at 24 °C. At the end of each experiment pH was calibrated via the nigericin/high potassium technique. In three to four separate replicates, cells were transfected with one of six deGFP4.AE1:mNect.hCNT3 cDNA ratios (8:1, 4:1, 2:1, 1.3:1, 1:1, 0.7:1). pH_i changes were determined for three to five cells per replicate. For each cell sample, the average distance separating deGFP4.AE1 and mNect.hCNT3-F563C was determined as described in section 2.2.22. (A) The difference between the time when a pH_i rise was detected at deGFP4.AE1 and at mNect.hCNT3-F563C was calculated as time delay (ΔT). The data was fitted by linear regression, and the slope of the line is significantly different than zero ($P = 0.03$, $R^2 = 0.4$). (B) The rate of pH_i change at the surface of deGFP4.AE1 and mNect.hCNT3-F563C was measured during $\text{Cl}^-/\text{HCO}_3^-$ exchange. The figure plots the rate of pH_i change at the surface of hCNT3-F563C/rate at surface of AE1. The data was fitted by linear regression, and the slope of the line is significantly different than zero ($P < 0.0001$, $R^2 = 0.7$).

4.3 Discussion

In this work we addressed the question of whether a H^+ microdomain forms around the pH-regulatory transporter, AE1. Rapid AE1-mediated HCO_3^- transport, combined with a low rate of H^+ diffusion in the cytosol could cause discontinuities in pH (a H^+ microdomain) immediately surrounding AE1. To measure the H^+ microdomain around AE1, the pH-sensitive fluorescent proteins, deGFP4 and mNect were respectively fused to AE1 and the inactive control plasma membrane protein hCNT3. As the distance between deGFP4.AE1 and mNect.hCNT3 increased, there was a time delay in the detection of pH_i change and a reduction in the rate of pH_i change at hCNT3, corresponding to a H^+ microdomain spanning 0.3 μm in diameter (Fig. 4.20). Carbonic anhydrase enzymes have a central role in the development of the H^+ microdomain around AE1 as pharmacological inhibition of carbonic anhydrase activity abolished the H^+ microdomain. Under physiologically-significant conditions (pH changes developed by the activity of membrane transport proteins initiated only by ion gradients) there is a time delay between when the pH change occurs at the plasma membrane and when it reaches intracellular organelles, representing the rate of H^+ movement across the cytosol. H^+ microdomains may be associated with other pH-regulatory transporters, which has broad implications for cellular functions.

4.3.1 Size of the H^+ microdomain

A H^+ microdomain is defined as a discrete region ($\sim 1 \mu m$ in diameter) with a pH value that differs from the surrounding cytoplasm by >0.1 pH unit [21].

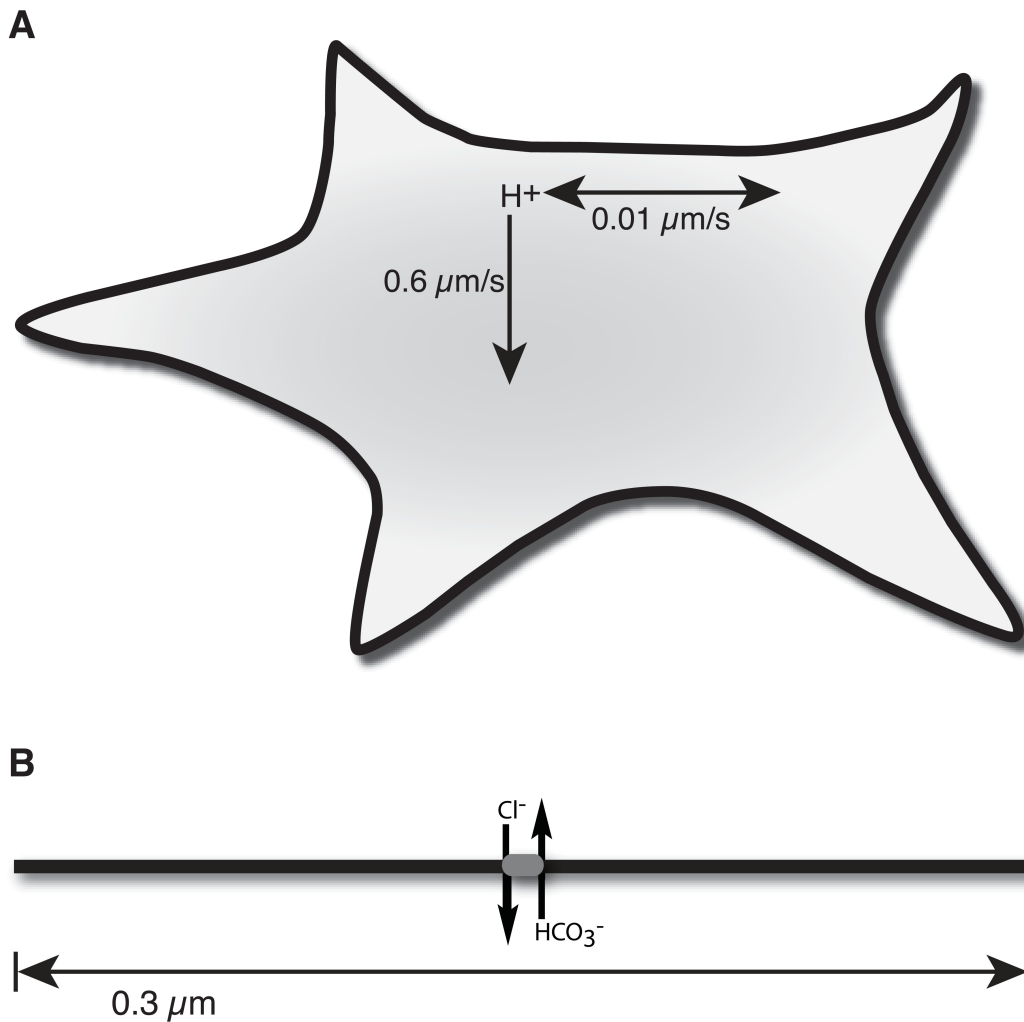


Figure 4.20. **Model for H⁺ diffusion and H⁺ microdomain around AE1.** (A) In HEK293 cells two different H⁺ diffusion rates were observed, 0.6 μm/s moving outwards from the plasma membrane and 0.01 μm/s horizontally along the plasma membrane. (B) Cartoon depicts a region of the plasma membrane (thick black line), which is approximately 40 Å thick in mammals. AE1 (grey oval), facilitating transmembrane Cl⁻/HCO₃⁻ exchange, is 120 Å long [43]. The H⁺ microdomain around AE1 was estimated as 0.3 μm in diameter.

We found that pH around AE1 differs from pH at other locations on the plasma membrane, in a region extending 0.13-0.17 μm from AE1, corresponding to a H^+ microdomain of 0.3 μm diameter (Fig. 4.20). There may be an error in our estimation of AE1-hCNT3 distance. As mentioned, we may under-represent the microdomain measured, since 17% of the fluorescence measured arises from ER-associated proteins. There is some uncertainty of the actual surface area of an HEK293 cell, and errors in our estimate would alter the calculated size of the microdomain. Further, it is difficult to gauge how much error is associated with the immunoblot analysis used to calculate protein density in the plasma membrane. In the end, while there is some uncertainty in the exact distance over which a H^+ microdomain was observed surrounding AE1, the data is compelling that as distances extend away from AE1, the remote location detects a slower rate of pH_i change relative to AE1, with a delay in the detection of the change in pH. This conclusion is not likely confounded by other interpretations since results of control experiments rule these possibilities out. Cytosolic deGFP4 and mNect report pH_i indistinguishably, with respect to their response time and the rate of pH_i rise they detect, so the differences we report here do not arise from the different fluorescent reporters fused to AE1 and hCNT3. deGFP4 and mNect fluorescence were discretely measured, with no interference from one FP into the wavelength range used to measure the other FP. There was no FRET between deGFP4 and mNect, so differences observed over the range of deGFP4:AE1:mNect:hCNT3 expression ratios were not confounded by this phenomenon.

How does the scale of the observed H^+ microdomain compare to that of other cellular structures? Ca^{++} and cAMP microdomains of 0.4-2 μm occur in cardiomyocytes [49-51], so the 0.3 μm H^+ microdomain is potentially smaller. Solute microdomain size varies with solute transport rate, diffusion rate, and cytosolic concentration of substance [52], so it is not surprising that a H^+ microdomain differs from other solute microdomains. Ca^{++} channels localize to plasma membrane lipid rafts and caveolae, which are respectively 0.01-0.2 μm and 0.05-0.1 μm in diameter [53]. The 0.3 μm H^+ microdomain around AE1 is therefore larger than lipid rafts and caveolae, which act as organizing centres for cell signalling. Cardiomyocyte transverse tubules occur at intervals of $\sim 2 \mu m$ along the longitudinal axis of myocytes, and as such, no part of the cytoplasm is more than $\sim 1 \mu m$ from the nearest T-tubule [54], suggesting that H^+ microdomains of less than 1 μm may form. Interestingly, Cl^-/HCO_3^- exchangers, AE3 and SLC26A6, localize to transverse tubules and sarcoplasmic reticulum of cardiomyocytes, where they have been suggested to function in localized pH regulation [55].

4.3.2 Role of carbonic anhydrase in H^+ microdomain formation

The data here indicate that carbonic anhydrase activity is required for the H^+ microdomain to form. The carbonic anhydrase inhibitor, ethoxzolamide, suppressed H^+ microdomain formation. CA may play multiple roles in H^+ microdomain formation. First, we found that the rate of Cl^-/HCO_3^- exchange decreases by 66% upon CA inhibition, consistent with previous data [9]. The

reduced rate of HCO_3^- transport will reduce the driving force for H^+ microdomain formation, allowing H^+ diffusion to overcome H^+ accumulation. Indeed, the ability of CA activity (in conjunction with $\text{CO}_2/\text{HCO}_3^-$ buffer) to diminish a H^+ microdomain (by increasing H^+ diffusion) depends on the magnitude of acid-equivalent flux [17]. CA activity had virtually no effect on H^+ mobility when rapid acid-equivalent fluxes were induced in cardiomyocytes [17, 18], while CAII had a dramatic effect on H^+ diffusion away from the slower transporting MCT1 [56] and PepT1 [20]. Second, considerable evidence supports the existence of a HCO_3^- transport metabolon, the physical complex of AE1 with cytosolic CAII [12]. Since CAII localizes to the cytosolic C-terminus of AE1, the site of H^+ production or consumption is also localized to the surface of AE1, promoting H^+ microdomain formation. Inhibition of CA function leaves $\text{CO}_2 \rightleftharpoons \text{HCO}_3^- + \text{H}^+$ interconversion to occur uncatalyzed and at random locations in the cytosol, which is counter to H^+ microdomain formation.

4.3.3 Rates of H^+ diffusion

H^+ diffusion from AE1 at the plasma membrane, to ER-localized CNX.mNect occurred at $0.6 \mu\text{m/s}$ (Fig. 4.20) while, $\sim 1.5 \mu\text{m/s}$ was reported for H^+ diffusion in cardiomyocytes [15, 17]. Great care needs to be taken in comparing our value for H^+ diffusion to that reported in cardiomyocytes, given the difference in experimental conditions. In the cardiomyocyte experiments acid was microinjected into the cells, resulting in a faster rise in $[\text{H}^+]$. Moreover, a much larger $[\text{H}^+]$ gradient was present in the cardiomyocyte experiments than in

ours. Acid was microinjected at pH 3 (1 mM H⁺), diffusing into cytosolic pH around pH 7.2 (6.3 x 10⁻⁸ M H⁺), giving a concentration gradient of 16 000 fold. In our experiments, pH rose to only 7.8 (1.6 x 10⁻⁸ M H⁺) from baseline of pH 7.2 (6.3 x 10⁻⁸ M H⁺), corresponding to a [H⁺] gradient of only four-fold. Since the concentration gradient provides the driving force for H⁺ diffusion, we would expect a lower rate of H⁺ diffusion when pH changes were driven by physiological Cl⁻/HCO₃⁻ exchange, than when driven by non-physiological, large concentration gradients. Cardiomyocytes may also differ in cytosolic structure/composition compared to HEK293 cells, and are rod-shaped, which may also contribute to the observed differences in diffusion rates.

Experiments in cardiomyocytes [15, 17] were performed with great care, and with an experimental design that enabled greater precision and modelling than was possible for our experiments. In cardiomyocytes it was possible to determine H⁺ diffusion coefficients, but this was not possible in the present experimental design, unfortunately. Use of diffusion coefficients allows for a better prediction of diffusion rates; rate will vary with distance since diffusion coefficients have units of cm².s⁻¹. Our measurement of a diffusion rate of 0.6 μm.s⁻¹ was measured over a distance of 4 μm, but will not be accurate over other scales. That said, the value does provide some notion of the time scale for H⁺ diffusion through cytosol associated with membrane transport of H⁺ equivalents.

The H⁺ diffusion rate from AE1 to hCNT3 (0.01 μm/s), along the plasma membrane, is 60 fold slower than the rate from AE1 to the ER surface, across the cytosol (Fig. 4.20). As discussed above the diffusion rate applies to only a single

distance and the caveats discussed above apply equally here. Because of the small distance scale over which these measurements were made, the slow rate of diffusion implies a dramatically low diffusion coefficient for H^+ along the cytosolic surface of the plasma membrane. In these experiments great care was taken to control for confounding factors that might have influenced the results. Nonetheless given the surprisingly slow rate of H^+ diffusion that we have observed along the membrane surface, it is possible that some methodological artefact is present in the experiment. Arguing against this, however, the time when pH changes were detected and the rate of pH change both varied with distance from AE1, in repeated experiments performed at two different temperatures (Figs. 4.16, 4.19). The possibility of a methodological problem is also reduced by the observation that inhibition of carbonic anhydrase suppressed the distance dependence of the time and rate of pH change (Fig. 4.18).

We can only speculate about the cause for the surprisingly slow H^+ diffusion rate along the plasma membrane. Restriction of diffusion by the plasma membrane barrier may contribute to the slow rate. Negative surface charge associated with the inner leaflet of the plasma membrane, attracts cationic molecules [57], which could also slow H^+ movement along the plasma membrane surface. Many fixed or slowly diffusing ionizable groups reside close to AE1 since protein diffusion is slow in the plane of the bilayer and many membrane proteins are further constrained by cytoskeletal interactions. Association of H^+ with physically-restricted proteins will slow their diffusion. Our measurements may not have considered plasma membrane surface features that would increase

the surface area, which would serve to under-report the rate of H^+ movement. Together these data provide a first measurement of the diffusion of H^+ from point sources along the plasma membrane.

H^+ buffering also is a consideration in this work, as deGFP4 and mNect (fused to AE1 and hCNT3) contain protonatable amino acid side-chains. We note that each AE1 transports up to 5×10^4 ions. s^{-1} , while each AE1 has one deGFP4 associated with it. The only residues likely to contribute to pH buffering in the physiological range are histidine (pK_a 6.1) and lysine (pK_a 10.5), of which 8 and 20 are found in deGFP4, respectively. The maximum buffering that deGFP4 could provide is thus miniscule on the scale of the H^+ -equivalent flux carried by AE1. Furthermore, while we have fixed deGFP4 onto the cytoplasmic domain of AE1, potentially adding to local buffering, we note that AE1 in erythrocytes and in kidney is part of a large fixed “macrocomplex” composed of cytoskeletal proteins and integral membrane proteins [58-60]. Thus the physiological environment of AE1 contains a high level of fixed proteins, which would contribute more strongly to localized buffering than would deGFP4.

4.3.4 Potential physiological significance of H^+ microdomains and observed low rates of H^+ diffusion

What significance does the AE1-associated H^+ microdomain have on erythrocyte function? Erythrocyte pH has a profound effect on hemoglobin (Hb) function, as an increase in the concentration of H^+ or CO_2 reduces the O_2 affinity of Hb, known as the Bohr effect, which is key to O_2 release into the tissues [61].

AE1 carries out its $\text{Cl}^-/\text{HCO}_3^-$ function in the brief (0.2 to 1 s) periods when the erythrocyte transits peripheral and pulmonary capillaries [62]. In the 0.2-1 s capillary transit time, a H^+ gradient generated by AE1 activity will move laterally along the erythrocyte membrane 0.002-0.01 μm , and move radially into the cell 0.1-0.6 μm . Since erythrocyte diameter is $\sim 8 \mu\text{m}$ [63], H^+ diffuse throughout only a small fraction of the entire erythrocyte. The hemoglobin-dense erythrocyte cytosol has an especially high buffer capacity [64] which may slow H^+ diffusion because of restricted hemoglobin mobility. This slow rate of H^+ diffusion may in part explain the requirement for the exceptionally high density of AE1 in the erythrocyte, where it constitutes 50% of integral membrane protein [4].

Do these data suggest that H^+ microdomains form around other pH-regulatory transporters? The ubiquitous and arguably most important pH-regulatory transporter is the alkalinizing Na^+/H^+ exchanger, NHE1 [65]. Since AE1 is dimeric [42], a larger H^+ microdomain would be expected to form than would if AE1 were monomeric. NHE1 is also dimeric [66], and has a relatively rapid turnover rate of $\sim 700\text{-}2000 \text{ s}^{-1}$ [67, 68]. While this rate is lower than AE1 (up to $5 \times 10^4 \text{ s}^{-1}$), a H^+ microdomain smaller than AE1's may still form around NHE1. The turnover rates of other pH-altering transporters are much slower: the proton-dependent oligopeptide transporter isoform 1 has a turnover rate of 100 s^{-1} [69], and the monocarboxylate transporter isoform 1 has a turnover rate of 12 s^{-1} [70], thereby decreasing the magnitude of a possible H^+ microdomain around them.

The localized pH_i changes we have measured could lead to a localized

regulation of function of nearby proteins. Indeed, Ca^{++} -sensitive adenylyl cyclase activity is influenced by pH changes driven by NHE1 activity, both of which localize to lipid rafts and caveolae [71]. An AE1-generated H^+ microdomain would also affect the function of nearby proteins. For example, gating of K^+ channel, Kir1.1, is sensitive to pH changes as small as 0.2 pH units [72]. As well, phosphofructokinase exhibits striking changes in activity over a few tenths of a pH unit [73], and binds the N-terminus of AE1, along with other glycolytic enzymes [74], suggesting that the enzymes may localize to the AE1 surface in order to be subject to pH regulation by AE1's H^+ microdomain. Further, kAE1 activity has been suggested to establish H^+ microdomains in glomerular podocytes to modulate nearby pH-sensitive TRPC (transient receptor potential superfamily of non-selective cation channels) [59]. Broader effects of plasma membrane pH are suggested by observations that cationic peptides, like K-Ras, associate with negative charges on plasma membrane phosphoinositides and phosphatidylserine [57]. The slow rates of H^+ diffusion that we observed along the plasma membrane surface suggest that pH-regulatory transporters may have especially strong pH-modulatory effects on the plasma membrane environment. Acid accumulated in the H^+ microdomain around a transporter could affect the ability of cationic signalling peptides to associate with the plasma membrane, thus influencing the signalling cascades in the vicinity of the transporter.

Using pH-sensitive fluorescent fusion proteins we measured a H^+ microdomain around AE1 of 0.3 μm in diameter generated by its $\text{Cl}^-/\text{HCO}_3^-$ exchange activity. H^+ microdomain formation was dependent on carbonic

anhydrase activity. We also found that the rate of H^+ diffusion along the plasma membrane is 60-fold slower than from the plasma membrane to the ER surface. This is the first evidence for a H^+ microdomain detected at this scale driven by physiological ion transport activity. H^+ microdomains may be a widespread phenomenon with extensive physiological implications.

Bibliography

1. Laude AJ & Simpson AW (2009) Compartmentalized signalling: Ca²⁺ compartments, microdomains and the many facets of Ca²⁺ signalling. *FEBS J* **276**, 1800-1816.
2. Neves SR & Iyengar R (2009) Models of spatially restricted biochemical reaction systems. *J Biol Chem* **284**, 5445-5449.
3. Casey JR, Grinstein S & Orłowski J (2010) Sensors and regulators of intracellular pH. *Nat Rev Mol Cell Biol* **11**, 50-61.
4. Fairbanks G, Steck TL & Wallach DFH (1971) Electrophoretic analysis of the major polypeptides of the human erythrocyte membrane. *Biochemistry* **10**, -2617.
5. Cordat E & Casey JR (2009) Bicarbonate transport in cell physiology and disease. *Biochem J* **417**, 423-439.
6. Alper SL, Chernova MN & Stewart AK (2001) Regulation of Na⁺-independent Cl⁻/HCO₃⁻ exchangers by pH. *Jop* **2**, 171-175.
7. Low PS (1986) Structure and function of the cytoplasmic domain of band 3: center of erythrocyte membrane-peripheral protein interactions. *Biochim Biophys Acta* **864**, 145-167.
8. Grinstein S, Ship S & Rothstein A (1978) Anion transport in relation to proteolytic dissection of band 3 protein. *Biochim Biophys Acta* **507**, 294-304.
9. Sterling D, Reithmeier RA & Casey JR (2001) A transport metabolon. Functional interaction of carbonic anhydrase II and chloride/bicarbonate exchangers. *J Biol Chem* **276**, 47886-47894.
10. Vince JW, Carlsson U & Reithmeier RA (2000) Localization of the Cl⁻/HCO₃⁻ anion exchanger binding site to the amino-terminal region of carbonic anhydrase II. *Biochemistry* **39**, 13344-13349.
11. Reithmeier RA (2001) A membrane metabolon linking carbonic anhydrase with chloride/bicarbonate anion exchangers. *Blood Cells Mol Dis* **27**, 85-89.
12. Johnson DE & Casey JR (2009) Bicarbonate Transport Metabolons. In *Drug Design of Zinc-Enzyme Inhibitors: Functional, Structural and Disease Applications*, Supuran CT and J. Winum, J. Eds, Wiley Chapter 20, p.p. 415-437.

13. Sterling D & Casey JR (2002) Bicarbonate transport proteins. *Biochem Cell Biol* **80**, 483-497.
14. Spitzer KW, Ershler PR, Skolnick RL & Vaughan-Jones RD (2000) Generation of intracellular pH gradients in single cardiac myocytes with a microperfusion system. *Am J Physiol Heart Circ Physiol* **278**, H1371-1382.
15. Vaughan-Jones RD, Peercy BE, Keener JP & Spitzer KW (2002) Intrinsic H⁺ ion mobility in the rabbit ventricular myocyte. *J Physiol* **541**, 139-158.
16. Spitzer KW, Skolnick RL, Peercy BE, Keener JP & Vaughan-Jones RD (2002) Facilitation of intracellular H⁺ ion mobility by CO₂/HCO₃⁻ in rabbit ventricular myocytes is regulated by carbonic anhydrase. *J Physiol* **541**, 159-167.
17. Swietach P, Leem CH, Spitzer KW & Vaughan-Jones RD (2005) Experimental generation and computational modeling of intracellular pH gradients in cardiac myocytes. *Biophys J* **88**, 3018-3037.
18. Swietach P, Spitzer KW & Vaughan-Jones RD (2007) pH-Dependence of extrinsic and intrinsic H⁺-ion mobility in the rat ventricular myocyte, investigated using flash photolysis of a caged-H⁺ compound. *Biophys J* **92**, 641-653.
19. Vaughan-Jones RD, Spitzer KW & Swietach P (2006) Spatial aspects of intracellular pH regulation in heart muscle. *Prog Biophys Mol Biol* **90**, 207-224.
20. Stewart AK, Boyd CA & Vaughan-Jones RD (1999) A novel role for carbonic anhydrase: cytoplasmic pH gradient dissipation in mouse small intestinal enterocytes. *J Physiol* **516** (Pt 1), 209-217.
21. Ro HA & Carson JH (2004) pH microdomains in oligodendrocytes. *J Biol Chem* **279**, 37115-37123.
22. Klein M, Seeger P, Schuricht B, Alper SL & Schwab A (2000) Polarization of Na⁺/H⁺ and Cl⁻/HCO₃⁻ exchangers in migrating renal epithelial cells. *J Gen Physiol* **115**, 599-608.
23. Stuwe L, Muller M, Fabian A, Waning J, Mally S, Noel J, Schwab A & Stock C (2007) pH dependence of melanoma cell migration: protons extruded by NHE1 dominate protons of the bulk solution. *J Physiol* **585**, 351-360.
24. Swietach P, Wigfield S, Cobden P, Supuran CT, Harris AL & Vaughan-Jones RD (2008) Tumor-associated carbonic anhydrase 9 spatially coordinates intracellular pH in three-dimensional multicellular growths. *J Biol Chem* **283**, 20473-20483.

25. Halestrap AP & Meredith D (2004) The SLC16 gene family-from monocarboxylate transporters (MCTs) to aromatic amino acid transporters and beyond. *Pflugers Arch* **447**, 619-628.
26. Martinez-Zaguilan R, Raghunand N, Lynch RM, Bellamy W, Martinez GM, Rojas B, Smith D, Dalton WS & Gillies RJ (1999) pH and drug resistance. I. Functional expression of plasmalemmal V-type H⁺-ATPase in drug-resistant human breast carcinoma cell lines. *Biochem Pharmacol* **57**, 1037-1046.
27. Rojas JD, Sennoune SR, Maiti D, Bakunts K, Reuveni M, Sanka SC, Martinez GM, Seftor EA, Meininger CJ, Wu G, et al. (2006) Vacuolar-type H⁺-ATPases at the plasma membrane regulate pH and cell migration in microvascular endothelial cells. *Am J Physiol Heart Circ Physiol* **291**, H1147-1157.
28. Hanson GT, McAnaney TB, Park ES, Rendell ME, Yarbrough DK, Chu S, Xi L, Boxer SG, Montrose MH & Remington SJ (2002) Green fluorescent protein variants as ratiometric dual emission pH sensors. 1. Structural characterization and preliminary application. *Biochemistry* **41**, 15477-15488.
29. Johnson DE, Ai HW, Wong P, Young JD, Campbell RE & Casey JR (2009) Red Fluorescent Protein pH Biosensor to Detect Concentrative Nucleoside Transport. *J Biol Chem* **284**, 20499-20511.
30. Chernova MN, Humphreys BD, Robinson DH, Stuart-Tilley AK, Garcia AM, Brosius FC & Alper SL (1997) Functional consequences of mutations in the transmembrane domain and the carboxy-terminus of the murine AE1 anion exchanger. *Biochim Biophys Acta* **1329**, 111-123.
31. Rosenow MA, Huffman HA, Phail ME & Wachter RM (2004) The crystal structure of the Y66L variant of green fluorescent protein supports a cyclization-oxidation-dehydration mechanism for chromophore maturation. *Biochemistry* **43**, 4464-4472.
32. Sterling D & Casey JR (1999) Transport activity of AE3 chloride/bicarbonate anion-exchange proteins and their regulation by intracellular pH. *Biochem J* **344 Pt 1**, 221-229.
33. Loisel FB & Casey JR (2010) Measurement of Intracellular pH. *Methods Mol Biol* **637**, 311-331.
34. Beckmann R, Toyne AM, Smythe JS, Anstee DJ & Tanner MJ (2002) An N-terminal GFP tag does not alter the functional expression to the plasma membrane of red cell and kidney anion exchanger (AE1) in mammalian cells. *Mol Biol* **19**, 187-200.

35. Sekar RB & Periasamy A (2003) Fluorescence resonance energy transfer (FRET) microscopy imaging of live cell protein localizations. *J Cell Biol* **160**, 629-633.
36. Miesenböck G, De Angelis DA & Rothman JE (1998) Visualizing secretion and synaptic transmission with pH-sensitive green fluorescent proteins. *Nature* **394**, 192-195.
37. Wachter RM & Remington SJ (1999) Sensitivity of the yellow variant of green fluorescent protein to halides and nitrate. *Curr Biol* **9**, R628-629.
38. Tang XB, Fujinaga J, Kopito R & Casey JR (1998) Topology of the region surrounding Glu681 of human AE1 protein, the erythrocyte anion exchanger. *J Biol Chem* **273**, 22545-22553.
39. Bola B & Allan V (2009) How and why does the endoplasmic reticulum move? *Biochem Soc Trans* **37**, 961-965.
40. Rajagopalan S, Xu Y & Brenner MB (1994) Retention of unassembled components of integral membrane proteins by calnexin. *Science* **263**, 387-390.
41. Michalak M, Groenendyk J, Szabo E, Gold LI & Opas M (2009) Calreticulin, a multi-process calcium-buffering chaperone of the endoplasmic reticulum. *Biochem J* **417**, 651-666.
42. Casey JR & Reithmeier RA (1991) Analysis of the oligomeric state of Band 3, the anion transport protein of the human erythrocyte membrane, by size exclusion high performance liquid chromatography. Oligomeric stability and origin of heterogeneity. *J Biol Chem* **266**, 15726-15737.
43. Wang DN, Kuhlbrandt W, Sarabia VE & Reithmeier RA (1993) Two-dimensional structure of the membrane domain of human band 3, the anion transport protein of the erythrocyte membrane. *EMBO J* **12**, 2233-2239.
44. Wang DN, Sarabia VE, Reithmeier RA & Kuhlbrandt W (1994) Three-dimensional map of the dimeric membrane domain of the human erythrocyte anion exchanger, Band 3. *EMBO J* **13**, 3230-3235.
45. Ramjeesingh M, Huan LJ, Garami E & Bear CE (1999) Novel method for evaluation of the oligomeric structure of membrane proteins. *Biochem J* **342 (Pt 1)**, 119-123.
46. Penna A, Demuro A, Yeromin AV, Zhang SL, Safrina O, Parker I & Cahalan MD (2008) The CRAC channel consists of a tetramer formed by Stim-induced dimerization of Orai dimers. *Nature* **456**, 116-120.

47. Kedei N, Szabo T, Lile JD, Treanor JJ, Olah Z, Iadarola MJ & Blumberg PM (2001) Analysis of the native quaternary structure of vanilloid receptor 1. *J Biol Chem* **276**, 28613-28619.
48. Zhang J, Tackaberry T, Ritzel MW, Raborn T, Barron G, Baldwin SA, Young JD & Cass CE (2006) Cysteine-accessibility analysis of transmembrane domains 11-13 of human concentrative nucleoside transporter 3. *Biochem J* **394**, 389-398.
49. Tian J & Xie ZJ (2008) The Na-K-ATPase and calcium-signaling microdomains. *Physiology (Bethesda)* **23**, 205-211.
50. Sugimori M, Lang EJ, Silver RB & Llinas R (1994) High-resolution measurement of the time course of calcium-concentration microdomains at squid presynaptic terminals. *Biol Bull* **187**, 300-303.
51. Zaccolo M & Pozzan T (2002) Discrete microdomains with high concentration of cAMP in stimulated rat neonatal cardiac myocytes. *Science* **295**, 1711-1715.
52. Barros LF & Martinez C (2007) An enquiry into metabolite domains. *Biophys J* **92**, 3878-3884.
53. Pani B & Singh BB (2009) Lipid rafts/caveolae as microdomains of calcium signaling. *Cell Calcium* **45**, 625-633.
54. Orchard C & Brette F (2008) t-Tubules and sarcoplasmic reticulum function in cardiac ventricular myocytes. *Cardiovasc Res* **77**, 237-244.
55. Alvarez BV, Kieller DM, Quon AL, Robertson M & Casey JR (2007) Cardiac hypertrophy in anion exchanger 1-null mutant mice with severe hemolytic anemia. *Am J Physiol Heart Circ Physiol* **292**, H1301-1312.
56. Becker HM & Deitmer JW (2008) Nonenzymatic proton handling by carbonic anhydrase II during H⁺-lactate cotransport via monocarboxylate transporter 1. *J Biol Chem* **283**, 21655-21667.
57. Yeung T, Gilbert GE, Shi J, Silvius J, Kapus A & Grinstein S (2008) Membrane phosphatidylserine regulates surface charge and protein localization. *Science* **319**, 210-213.
58. Bruce LJ, Beckmann R, Ribeiro ML, Peters LL, Chasis JA, Delaunay J, Mohandas N, Anstee DJ & Tanner MJ (2003) A band 3-based macrocomplex of integral and peripheral proteins in the RBC membrane. *Blood* **101**, 4180-4188.

59. Wu F, Saleem MA, Kampik NB, Satchwell TJ, Williamson RC, Blattner SM, Ni L, Toth T, White G, Young MT, et al. (2010) Anion exchanger 1 interacts with nephrin in podocytes. *J Am Soc Nephrol* **21**, 1456-1467.
60. Keskanokwong T, Shandro HJ, Johnson DE, Kittanakom S, Vilas GL, Thorner P, Reithmeier RA, Akkarapatumwong V, Yenchitsomanus PT & Casey JR (2007) Interaction of integrin-linked kinase with the kidney chloride/bicarbonate exchanger, kAE1. *J Biol Chem* **282**, 23205-23218.
61. Jensen FB (2004) Red blood cell pH, the Bohr effect, and other oxygenation-linked phenomena in blood O₂ and CO₂ transport. *Acta Physiol Scand* **182**, 215-227.
62. Kayar SR, Hoppeler H, Armstrong RB, Laughlin MH, Lindstedt SL, Jones JH, Conley KR & Taylor CR (1992) Estimating transit time for capillary blood in selected muscles of exercising animals. *Pflugers Arch* **421**, 578-584.
63. Jay AW (1975) Geometry of the human erythrocyte. I. Effect of albumin on cell geometry. *Biophys J* **15**, 205-222.
64. Swietach P, Tiffert T, Mauritz JM, Seear R, Esposito A, Kaminski C, Lew VL & Vaughan-Jones RD (2010) Hydrogen ion dynamics in human red blood cells. *J Physiol*, **In Press**.
65. Malo ME & Fliegel L (2006) Physiological role and regulation of the Na⁺/H⁺ exchanger. *Can J Physiol Pharmacol* **84**, 1081-1095.
66. Moncoq K, Kemp G, Li X, Fliegel L & Young HS (2008) Dimeric structure of human Na⁺/H⁺ exchanger isoform 1 overproduced in *Saccharomyces cerevisiae*. *J Biol Chem* **283**, 4145-4154.
67. Cavet ME, Akhter S, de Medina FS, Donowitz M & Tse CM (1999) Na⁺/H⁺ exchangers (NHE1-3) have similar turnover numbers but different percentages on the cell surface. *Am J Physiol* **277**, C1111-1121.
68. Dixon SJ, Cohen S, Cragoe EJ, Jr. & Grinstein S (1987) Estimation of the number and turnover rate of Na⁺/H⁺ exchangers in lymphocytes. Effect of phorbol ester and osmotic shrinking. *J Biol Chem* **262**, 3626-3632.
69. Mackenzie B, Loo DD, Fei Y, Liu WJ, Ganapathy V, Leibach FH & Wright EM (1996) Mechanisms of the human intestinal H⁺-coupled oligopeptide transporter hPEPT1. *J Biol Chem* **271**, 5430-5437.
70. Ovens MJ, Davies AJ, Wilson MC, Murray CM & Halestrap AP (2010) AR-C155858 is a potent inhibitor of monocarboxylate transporters MCT1 and

MCT2 that binds to an intracellular site involving transmembrane helices 7-10. *Biochem J* **425**, 523-530.

71. Willoughby D, Masada N, Crossthwaite AJ, Ciruela A & Cooper DM (2005) Localized Na⁺/H⁺ exchanger 1 expression protects Ca²⁺-regulated adenylyl cyclases from changes in intracellular pH. *J Biol Chem* **280**, 30864-30872.
72. Schulte U & Fakler B (2000) Gating of inward-rectifier K⁺ channels by intracellular pH. *Eur J Biochem* **267**, 5837-5841.
73. Trivedi B & Danforth WH (1966) Effect of pH on the kinetics of frog muscle phosphofructokinase. *J Biol Chem* **241**, 4110-4112.
74. Campanella ME, Chu H & Low PS (2005) Assembly and regulation of a glycolytic enzyme complex on the human erythrocyte membrane. *Proc Natl Acad Sci U S A* **102**, 2402-2407.

Chapter 5: Summary and Future Directions

5.1 Summary

The objective of this thesis was to examine local pH changes at the intracellular surface of membrane transport proteins during AE1-mediated $\text{Cl}^-/\text{HCO}_3^-$ exchange or hCNT3-mediated Na^+/H^+ /nucleoside co-transport. Plasma membrane pH was monitored with the pH-sensitive fluorescent proteins deGFP4 fused to the N-terminus of AE1 (deGFP4.AE1) and mNectarine fused to the N-terminus of hCNT3 (mNect.hCNT3) or an inactive hCNT3 mutant (mNect.hCNT3-F563C). Ultimately, we wanted to answer the question of whether a H^+ microdomain (a region of discontinuous cytosolic H^+ concentration) forms around AE1 as it exchanges Cl^- for HCO_3^- .

5.1.1 Red Fluorescent Protein Biosensor to Detect Concentrative Nucleoside Transport

Human concentrative nucleoside transporter, hCNT3, can couple the inward movement of nucleosides to either the Na^+ electrochemical gradient (2 Na^+ : 1 nucleoside) or a H^+ gradient (1 H^+ : 1 nucleoside) in the absence of Na^+ [1, 2]. At pH 5.5, hCNT3 also transports uridine in the presence of Na^+ with a 2 cation: 1 nucleoside stoichiometry, which raises the possibility that 1 H^+ and 1 Na^+ may be transported per nucleoside molecule in these conditions [1-4]. Prior to the work described in this thesis, however, H^+ co-transport had only been inferred from acid activation of ^{14}C -uridine influx and pH-dependent uridine-

evoked currents in oocytes [1, 5, 6]. There had been no direct demonstration that hCNT3 can transport H^+ .

In this thesis (chapter 3) we describe a new approach to directly monitor H^+ /uridine co-transport in HEK293 cells. We report the development of a new pH sensitive monomeric red fluorescent protein, mNectarine (mNect) [7]. mNect has a pK_a of 6.9, making it ideally suited to monitor dynamic pH changes in mammalian cytosol (pH \sim 7.3 [8]). pH changes at the intracellular surface of hCNT3 were monitored by fusing mNect to the N-terminus of hCNT3 (mNect.hCNT3) or an inactive hCNT3 mutant (mNect.hCNT3-F563C). We demonstrate that after photobleaching correction and calibration to pH, mNect and mNect fusion proteins report pH comparably to the well-established pH-sensitive dye, BCECF-AM. We further demonstrate that mNect.hCNT3 accurately measures hCNT3 kinetics, based on the determination that the K_m of mNect.hCNT3 for uridine was between two previously published values for hCNT3 expressed in oocytes [2, 4].

HEK293 cells, transiently transfected with mNect.hCNT3 or mNect.hCNT3-F563C, were incubated at the permissive pH for H^+ -coupled nucleoside transport, pH 5.5, under both Na^+ -free and Na^+ -containing conditions. In mNect.hCNT3-expressing cells (but not under negative control conditions) the rate of acidification increased in media containing 0.5 mM uridine, providing the first direct evidence for H^+ -coupled uridine transport. At pH 5.5, there was no significant difference in uridine transport rates (coupled H^+ flux) in the presence or absence of Na^+ . Charge/flux ratio experiments in *Xenopus laevis* oocytes

indicate that hCNT3 functions with a 2 cation: 1 uridine stoichiometry in both acidic and alkaline Na^+ -containing medium, compared to a 1 cation: 1 uridine stoichiometry in acidic Na^+ -free medium [2, 4]. Our results, in conjunction with oocyte data, provides support for the proposed mechanism that in acidic Na^+ -containing conditions, 1 Na^+ and 1 H^+ are transported per uridine molecule, while in acidic Na^+ -free conditions, 1 H^+ alone is transported per uridine molecule [1-4].

In acid environments, including renal proximal tubule and intestine, H^+ /nucleoside co-transport may drive both physiological nucleoside and nucleoside-analogue accumulation by hCNT3.

5.1.2 Cytosolic H^+ Microdomain Developed During Ion Transport

Solute microdomains are regions of discontinuous cytosolic solute concentration that develop from the activity of ion channels or transporters. Microdomain formation is enhanced by rapid solute transport and slow diffusion rates [9]. Ca^{++} and cAMP microdomains of 0.4-2 μm occur in cardiomyocytes and endothelial cells, and contribute to spatially restricted signaling [10-13]. While pH discontinuities have been observed in cardiomyocytes [14, 15], intestinal enterocytes [16], oligodendrocytes [17], and tumor cells [18], whether or not H^+ microdomains develop near the cytosolic face of pH-regulatory transporters had not been conclusively established, prior to the work presented in this thesis. Understanding physiological local changes in pH is critical to understanding cellular pH regulation, given the breadth of cellular process regulated by pH changes [19].

In this thesis (chapter 4) we address the question of whether a H^+ microdomain forms around the pH-regulatory transporter, AE1. AE1 interacts physically and functionally with CAII to form a bicarbonate transport metabolon, which functions to maximize HCO_3^- flux through the transporter [20, 21]. In the presence of CAII AE1 has a high turnover rate of $5 \times 10^4 \text{ s}^{-1}$, which is among the fastest rate for a membrane transporter [22]. Rapid AE1-mediated HCO_3^- transport, combined with a low rate of H^+ diffusion in the cytosol, suggested that H^+ microdomains develop around AE1 during Cl^-/HCO_3^- exchange.

Generation of a H^+ microdomain around AE1 would result in proteins in close proximity to AE1 being subject to a different pH than those more distant from AE1. To measure the magnitude of the H^+ microdomain around AE1, we monitored spatial differences in pH, near and remote from AE1 using pH-sensitive fluorescent protein fusions. Plasma membrane pH was monitored by deGFP4 fused to the N-terminus of AE1 (deGFP4.AE1) and mNect fused to the N-terminus of an inactive mutant of the Na^+ -coupled nucleoside co-transporter, hCNT3 (mNect.hCNT3-F563C). pH at the cytoplasmic surface of the ER was monitored by mNect fused to cytosolic face of ER-resident calnexin (CNX.mNect).

To ensure that we could accurately measure pH near and away from AE1, we completed control experiments. We characterized the functional activity of deGFP4.AE1 in comparison to AE1 alone and found that fusion of the FP did not affect AE1 transport activity. We determined that deGFP4 and mNect fluorescence could be measured concurrently without interference from each

other. That is, there was no crosstalk between deGFP4 and mNect. Similarly, there was no fluorescence resonance energy transfer (FRET) between deGFP4 and mNect. Further, deGFP4 and mNect fluorescence are pH-sensitive and Cl^- insensitive. After photobleaching correction and calibration to pH, deGFP4 and mNect report pH indistinguishably (rate of pH_i change and response time), whether in pH-clamped conditions, during $\text{Cl}^-/\text{HCO}_3^-$ exchange, or after an NH_4Cl pre-pulse. We conclude that deGFP4 and mNect are suitable to simultaneously measure $\text{Cl}^-/\text{HCO}_3^-$ exchange when co-expressed in HEK293 cells.

The magnitude of the H^+ microdomain around AE1 at the plasma membrane was monitored by varying the deGFP4.AE1 to mNect.hCNT3-F563C distance (varied by co-transfecting HEK293 cells with different amounts of deGFP4.AE1 and mNect.hCNT3-F563C cDNA). As the deGFP4.AE1-mNect.hCNT3-F563C distance increased, mNect.hCNT3-F563C detected the cytosolic pH change with a time delay and a reduced rate of pH change, compared to deGFP4.AE1. This indicates the formation of a H^+ microdomain around deGFP4.AE1. The calculated H^+ diffusion rate along the plasma membrane was $0.01 \mu\text{m/s}$, and the diameter of the H^+ microdomain was $0.3 \mu\text{m}$. In contrast, the H^+ diffusion rate from deGFP4.AE1 to the cytosolic ER-surface was $0.6 \mu\text{m/s}$, 60-fold faster.

CAII has two opposing roles in H^+ microdomain formation. CAII maximizes the AE1-mediated $\text{Cl}^-/\text{HCO}_3^-$ exchange rate [20, 21] (increasing potential to develop a H^+ microdomain) but CAII also accelerates H^+ diffusion [16, 23] (dissipating a H^+ microdomain). Carbonic anhydrase activity was

essential for the H^+ microdomain around AE1 to form, as CA inhibition by ethoxzolamide suppressed H^+ microdomain formation. We reasoned that the reduced rate of HCO_3^- transport will reduce the driving force for H^+ microdomain formation, allowing H^+ diffusion to overcome H^+ accumulation.

In summary, under physiologically-significant conditions (pH changes developed by the activity of membrane transport proteins initiated only by ion gradients) there is a time delay between when the pH change occurs at the plasma membrane and when it reaches nearby proteins or intracellular organelles. We measured a H^+ microdomain around AE1 of 0.3 μm in diameter generated by its Cl^-/HCO_3^- exchange activity. This is the first evidence for a H^+ microdomain detected at this scale driven by physiological ion transport activity. The AE1-associated H^+ microdomain may be especially critical in erythrocyte function, and the slow rate of H^+ diffusion may in part explain the requirement for the exceptionally high density of AE1 in the erythrocyte, where it constitutes 50% of integral membrane protein [24]. H^+ microdomains may be associated with other pH-regulatory transporters, which has broad implications for cellular functions, as virtually every cellular process is sensitive to pH [19].

5.2 Future Directions

As discussed in chapter 3, mNect.hCNT3 can be used to measure the transport rate of any nucleoside or nucleoside drug that is co-transported with H^+ , so any range of substrates can be assayed for transport, even if a radioactive analogue is unavailable. This opens up the possibility of high-throughput assays

in which a wide range of possible substrates could be added to mNect.hCNT3-transfected cells grown in multi-well plates while monitoring fluorescence changes over time with a multi-well plate fluorimeter. mNect.hCNT3 also provides the possibility of high-throughput screening for additional hCNT3 activators and inhibitors [25-27]. Interestingly, hCNT3 exhibits markedly different selectivity characteristics for symport of physiological nucleosides and therapeutic nucleoside drugs in acidic Na^+ -free or alkaline Na^+ -containing conditions [2]. This suggests that binding of Na^+ or H^+ induces cation-specific conformational changes in hCNT3 [2]. Using mNect.hCNT3, it will be possible to measure transport of nucleosides and nucleoside drugs in acidic Na^+ -containing conditions. In conjunction with corresponding electrophysiological recordings in hCNT3-expressing oocytes [1, 2, 4, 6], it may be possible to discern an intermediate conformation where both Na^+ and H^+ are bound.

In our experiments (chapters 3 and 4), we used a non-polarized cell line (HEK293) transiently transfected with cDNA encoding fluorescent protein fusions. For future experiments, it would be ideal to have stably-transfected cell lines expressing all of our constructs, individually or together. While we attempted to control for differences in protein expression between experiments (e.g. individual photobleaching corrections and pH calibrations) stable-expression would further minimize expression differences. Further, stable-expression would likely result in higher plasma membrane targeting, minimizing the percentage of fluorescent signal spill-over from the ER. Unfortunately, stable-expression may also lower overall expression, making it more difficult to detect fusion protein

fluorescence. It would also be interesting to look at H^+ microdomain formation and H^+ diffusion rates in a polarized epithelial cell line, such as Madin-Darby Canine Kidney Cells (MDCK cells), where ion gradients would be generated from either the apical or basolateral surface.

On a related note, we compare the H^+ diffusion rate from deGFP4.AE1 to the cytosolic ER-surface ($0.6 \mu\text{m/s}$) to H^+ diffusion rates measured in cardiomyocytes ($1\text{-}2 \mu\text{m/s}$) [28]. To make a more direct comparison of H^+ diffusion rates we could express deGFP4 and mNect fusion proteins in cardiomyocytes, using adenoviral transduction [29]. In fact, deGFP4.AE1 and mNect.hCNT3 adenoviral constructs have already been generated in the lab. Specifically, we could monitor pH changes and H^+ diffusion rates detected by deGFP4.AE1 and mNect.hCNT3 during AE-mediated $\text{Cl}^-/\text{HCO}_3^-$ exchange, in the presence and absence of a CA inhibitor. As an additional control, we could inject acid at one pole of the cardiomyocyte to compare our experimental technique to that of Vaughan-Jones and colleagues [28].

The resolution of conventional confocal microscopy is limited laterally to $\sim 200 \text{ nm}$ and axially to $\sim 500 \text{ nm}$ [30]. In other words, two objects cannot be separated at distances lower than 200 nm . Using confocal microscopy, we concluded that deGFP4.AE1 and mNect.hCNT3-F563C are distributed randomly at the plasma membrane of HEK293 cells. Superresolution microscopy, however, has revealed that many proteins cluster at the plasma membrane [30]. For example, Ras proteins concentrate in plasma membrane microdomains called nanoclusters [31]. Using immunoblot analysis, we have calculated deGFP4.AE1

to mNect.hCNT3-F563C distances of ~30-70 nm, which is below the resolution limit of light microscopy. Superresolution microscopy would allow us to more precisely investigate deGFP4.AE1 and mNect.hCNT3-F563C distribution and intermolecular distance at the plasma membrane, which would provide a better estimate of the size of the H⁺ microdomain around AE1. In HeLa cells, hCNT3-WT is localized to both lipid raft and nonlipid raft domains [25]. It is possible that hCNT3 exhibits similar localization in HEK293 cells. This finding is not likely to alter our interpretation of a H⁺ microdomain around AE1 because pH_i changes were monitored around the entire plasma membrane, thereby reporting on average hCNT3 distribution, which would include both lipid raft and nonlipid raft localized hCNT3.

CA activity is essential for the formation of the H⁺ microdomain around AE1. These experiments were conducted by inhibiting CA activity with the membrane-permeant CA inhibitor, ethoxzolamide. As ethoxzolamide will inhibit CA activity throughout the cytosol (thereby allowing the $\text{CO}_2 \rightleftharpoons \text{HCO}_3^- + \text{H}^+$ interconversion to occur uncatalyzed and at random locations in the cytosol), there is the possibility that pharmacological inhibition could disrupt global pH, and therefore have an additional, unpredicted effect on H⁺ microdomain formation. There are several experiments that could rule out possible global cellular effects of CA inhibition. Overexpression of the catalytically inactive CAII-V143Y has been shown to decrease AE1-mediated Cl⁻/HCO₃⁻ exchange by up to 60%, which is similar to the degree of inhibition observed with ethoxzolamide [32]. CAII-V143Y has a dominant negative effect on anion transport, by competing with

endogenous CAII for binding to the AE1 C-terminus [20, 21]. H⁺ microdomain formation around a deGFP4.AE1 mutant (such as AE1-LDAAA [33]) that does not bind CA could be assessed. Alternatively, β -CAs are less susceptible to acetazolamide inhibition than CAII (an α -CA) (IC₅₀s of 6 x 10⁴ nM and 25 nM, respectively) [34, 35]. Therefore, β -CA could be fused to the C-terminus of deGFP4.AE1, and Cl⁻/HCO₃⁻ exchange assays could be conducted in the presence of acetazolamide, which inhibit cytosolic CAII, with little effect on AE1-localized β -CA. Additionally, these experiments would provide further insight into the bicarbonate transport metabolon.

The major question that needs answering is: How does H⁺ microdomain formation affect nearby protein function? We propose that proteins in close proximity to AE1 would be subjected to a different pH than those more distant from AE1. For example, a kAE1/ILK complex binds nephrin in podocytes, and it has been suggested that kAE1 may establish H⁺ microdomains in the podocyte that function to modulate nearby protein activity or signaling [36]. Specifically, pH-sensitive TRPC (transient receptor potential superfamily of non-selective cation channels) family members co-localize with nephrin in the podocyte [37], where kAE1 activity may alter TRPC activity [36]. It would be fascinating to investigate whether the H⁺ microdomain around AE1 affects TRPC channel activity. In an analogous manner to the studies conducted in this thesis (chapter 4), TRPC channels could be expressed in cells at varying distances away from AE1. Distances could range from immediately adjacent to AE1 (an AE1.TRPC concatamer) to ~1 μ m away, depending on cell type and transfection conditions.

TRPC channel activity could be monitored before, during, and after initiation of AE1-mediated $\text{Cl}^-/\text{HCO}_3^-$ exchange, at different distances. As $[\text{Cl}^-]$, $[\text{HCO}_3^-]$ and $[\text{cation}]$ would be altered in this scenario, careful control experiments would need to be conducted to ensure that the TRCP channel activity measured is specific. It would also be fascinating to examine what effect the H^+ microdomain around AE1 may have on PFK activity, seeing that PFK binds the N-terminus of eAE1, and is exquisitely pH-sensitive [38]. Finally, similar experiments could be conducted using any other pH-regulatory transport protein and pH-sensitive protein pair.

Bibliography

1. Smith KM, Slugoski MD, Cass CE, Baldwin SA, Karpinski E & Young JD (2007) Cation coupling properties of human concentrative nucleoside transporters hCNT1, hCNT2 and hCNT3. *Mol Membr Biol* **24**, 53-64.
2. Smith KM, Slugoski MD, Loewen SK, Ng AM, Yao SY, Chen XZ, Karpinski E, Cass CE, Baldwin SA & Young JD (2005) The broadly selective human Na⁺/nucleoside cotransporter (hCNT3) exhibits novel cation-coupled nucleoside transport characteristics. *J Biol Chem* **280**, 25436-25449.
3. Damaraju VL, Elwi AN, Hunter C, Carpenter P, Santos C, Barron GM, Sun X, Baldwin SA, Young JD, Mackey JR, et al. (2007) Localization of broadly selective equilibrative and concentrative nucleoside transporters, hENT1 and hCNT3, in human kidney. *Am J Physiol Renal Physiol* **293**, F200-211.
4. Slugoski MD, Smith KM, Mulinta R, Ng AM, Yao SY, Morrison EL, Lee QO, Zhang J, Karpinski E, Cass CE, et al. (2008) A conformationally mobile cysteine residue (Cys-561) modulates Na⁺ and H⁺ activation of human CNT3. *J Biol Chem* **283**, 24922-24934.
5. Ritzel MW, Ng AM, Yao SY, Graham K, Loewen SK, Smith KM, Ritzel RG, Mowles DA, Carpenter P, Chen XZ, et al. (2001) Molecular identification and characterization of novel human and mouse concentrative Na⁺-nucleoside cotransporter proteins (hCNT3 and mCNT3) broadly selective for purine and pyrimidine nucleosides (system cib). *J Biol Chem* **276**, 2914-2927.
6. Slugoski MD, Ng AM, Yao SY, Smith KM, Lin CC, Zhang J, Karpinski E, Cass CE, Baldwin SA & Young JD (2008) A proton-mediated conformational shift identifies a mobile pore-lining cysteine residue (Cys-) in human concentrative nucleoside transporter 3. *J Biol Chem* **283**, 8496-8507.
7. Johnson DE, Ai HW, Wong P, Young JD, Campbell RE & Casey JR (2009) Red Fluorescent Protein pH Biosensor to Detect Concentrative Nucleoside Transport. *J Biol Chem* **284**, 20499-20511.
8. Llopis J, McCaffery JM, Miyawaki A, Farquhar MG & Tsien RY (1998) Measurement of cytosolic, mitochondrial, and Golgi pH in single living cells with green fluorescent proteins. *Proc Natl Acad Sci U S A* **95**, 6803-6808.
9. Barros LF & Martinez C (2007) An enquiry into metabolite domains. *Biophys J* **92**, 3878-3884.

10. Tian J & Xie ZJ (2008) The Na-K-ATPase and calcium-signaling microdomains. *Physiology (Bethesda)* **23**, 205-211.
11. Sugimori M, Lang EJ, Silver RB & Llinas R (1994) High-resolution measurement of the time course of calcium-concentration microdomains at squid presynaptic terminals. *Biol Bull* **187**, 300-303.
12. Zaccolo M & Pozzan T (2002) Discrete microdomains with high concentration of cAMP in stimulated rat neonatal cardiac myocytes. *Science* **295**, 1711-1715.
13. Hayakawa K, Tatsumi H & Sokabe M (2008) Actin stress fibers transmit and focus force to activate mechanosensitive channels. *J Cell Sci* **121**, 496-503.
14. Vaughan-Jones RD, Spitzer KW & Swietach P (2006) Spatial aspects of intracellular pH regulation in heart muscle. *Prog Biophys Mol Biol* **90**, 207-224.
15. Swietach P, Zaniboni M, Stewart AK, Rossini A, Spitzer KW & Vaughan-Jones RD (2003) Modelling intracellular H⁺ ion diffusion. *Prog Biophys Mol Biol* **83**, 69-100.
16. Stewart AK, Boyd CA & Vaughan-Jones RD (1999) A novel role for carbonic anhydrase: cytoplasmic pH gradient dissipation in mouse small intestinal enterocytes. *J Physiol* **516 (Pt 1)**, 209-217.
17. Ro HA & Carson JH (2004) pH microdomains in oligodendrocytes. *J Biol Chem* **279**, 37115-37123.
18. Swietach P, Vaughan-Jones RD & Harris AL (2007) Regulation of tumor pH and the role of carbonic anhydrase 9. *Cancer Metastasis Rev* **26**, 299-310.
19. Casey JR, Grinstein S & Orlowski J (2010) Sensors and regulators of intracellular pH. *Nat Rev Mol Cell Biol* **11**, 50-61.
20. Sterling D, Reithmeier RA & Casey JR (2001) A transport metabolon. Functional interaction of carbonic anhydrase II and chloride/bicarbonate exchangers. *J Biol Chem* **276**, 47886-47894.
21. Reithmeier RA (2001) A membrane metabolon linking carbonic anhydrase with chloride/bicarbonate anion exchangers. *Blood Cells Mol Dis* **27**, 85-89.
22. Sterling D & Casey JR (2002) Bicarbonate transport proteins. *Biochem Cell Biol* **80**, 483-497.

23. Spitzer KW, Skolnick RL, Peercy BE, Keener JP & Vaughan-Jones RD (2002) Facilitation of intracellular H^+ ion mobility by CO_2/HCO_3^- in rabbit ventricular myocytes is regulated by carbonic anhydrase. *J Physiol* **541**, 159-167.
24. Fairbanks G, Steck TL & Wallach DFH (1971) Electrophoretic analysis of the major polypeptides of the human erythrocyte membrane. *Biochemistry* **10**, 2606-2617.
25. Errasti-Murugarren E, Molina-Arcas M, Casado FJ & Pastor-Anglada M (2010) The human concentrative nucleoside transporter-3 C602R variant shows impaired sorting to lipid rafts and altered specificity for nucleoside-derived drugs. *Mol Pharmacol* **78**, 157-165.
26. Damaraju VL, Smith KM, Mowles D, Nowak I, Karpinski E, Young JD, Robins MJ & Cass CE (2011) Interaction of fused-pyrimidine nucleoside analogs with human concentrative nucleoside transporters: High-affinity inhibitors of human concentrative nucleoside transporter 1. *Biochem Pharmacol* **81**, 82-90.
27. Wang C, Pimple S & Buolamwini JK (2010) Interaction of benzopyranone derivatives and related compounds with human concentrative nucleoside transporters 1, 2 and 3 heterologously expressed in porcine PK15 nucleoside transporter deficient cells. Structure-activity relationships and determinants of transporter affinity and selectivity. *Biochem Pharmacol* **79**, 307-320.
28. Vaughan-Jones RD, Peercy BE, Keener JP & Spitzer KW (2002) Intrinsic H^+ ion mobility in the rabbit ventricular myocyte. *J Physiol* **541**, 139-158.
29. Coccaro E, Mraiche F, Malo M, Vandertol-Vanier H, Bullis B, Robertson M & Fliegel L (2007) Expression and characterization of the Na^+/H^+ exchanger in the mammalian myocardium. *Mol Cell Biochem* **302**, 145-155.
30. Lang T & Rizzoli SO (2010) Membrane protein clusters at nanoscale resolution: more than pretty pictures. *Physiology (Bethesda)* **25**, 116-124.
31. Tian T, Harding A, Inder K, Plowman S, Parton RG & Hancock JF (2007) Plasma membrane nanoswitches generate high-fidelity Ras signal transduction. *Nat Cell Biol* **9**, 905-914.
32. Fierke CA, Calderone TL & Krebs JF (1991) Functional consequences of engineering the hydrophobic pocket of carbonic anhydrase II. *Biochemistry* **30**, 11054-11063.
33. Dahl NK, Jiang L, Chernova MN, Stuart-Tilley AK, Shmukler BE & Alper SL (2003) Deficient HCO_3^- transport in an AE1 mutant with normal Cl^-

transport can be rescued by carbonic anhydrase II presented on an adjacent AE1 protomer. *J Biol Chem* **278**, 44949-44958.

34. Smith KS & Ferry JG (1999) A plant-type (beta-class) carbonic anhydrase in the thermophilic methanoarchaeon *Methanobacterium thermoautotrophicum*. *J Bacteriol* **181**, 6247-6253.
35. Ho YT, Purohit A, Vicker N, Newman SP, Robinson JJ, Leese MP, Ganeshapillai D, Woo LW, Potter BV & Reed MJ (2003) Inhibition of carbonic anhydrase II by steroidal and non-steroidal sulphamates. *Biochem Biophys Res Commun* **305**, 909-914.
36. Toye AM, Banting G & Tanner MJ (2004) Regions of human kidney anion exchanger 1 (kAE1) required for basolateral targeting of kAE1 in polarised kidney cells: mis-targeting explains dominant renal tubular acidosis (dRTA). *J Cell Sci* **117**, 1399-1410.
37. Cheng H & Harris RC (2010) The glomerulus--a view from the outside--the podocyte. *Int J Biochem Cell Biol* **42**, 1380-1387.
38. Campanella ME, Chu H & Low PS (2005) Assembly and regulation of a glycolytic enzyme complex on the human erythrocyte membrane. *Proc Natl Acad Sci U S A* **102**, 2402-2407.